Harmonized microwave radiometer observations of middle-atmospheric ozone over Switzerland

Inaugural dissertation
of the Faculty of Science,
University of Bern

presented by

Eric Sauvageat

from Jorat-Menthue, VD

Supervisors of the doctoral thesis: Dr. Axel Murk & PD Dr. Klemens Hocke
Institute of Applied Physics

Harmonized microwave radiometer observations of middle-atmospheric ozone over Switzerland

Inaugural dissertation
of the Faculty of Science,
University of Bern

presented by

Eric Sauvageat

from Jorat-Menthue, VD

Supervisors of the doctoral thesis: Dr. Axel Murk & PD Dr. Klemens Hocke
Institute of Applied Physics

Accepted by the Faculty of Science.

The Dean:

Bern, 15. August 2023 Prof. Dr. Marco Herwegh

[1] https://creativecommons.org/licenses/by/4.0/

Summary

This thesis is concerned with ozone measurements in the middle atmosphere over Switzerland. Its main focus is the time series measured by two ground-based microwave radiometers located in Switzerland: The GROund-based Millimeter-wave Ozone Spectrometer (GROMOS) in Bern (46.95° N, 7.44° E, 560 m) and the Stratospheric Ozone MOnitoring RAdiometer (SOMORA) in Payerne (46.82° N, 6.94° E, 491 m). These two instruments have measured hourly ozone profiles in the middle atmosphere ($20-75$ km) for over two decades. As anomalous time periods and inconsistencies in the long-term trends derived from these two instruments were detected, a harmonization project was initiated in 2019. The goal was to fully harmonize the calibration and retrieval routines of GROMOS and SOMORA to better understand and reduce the discrepancies between the two data records. This dissertation presents in detail this harmonization work, the resulting time series and the recent research work done with the harmonized series.

Chapter 1 introduces middle-atmospheric ozone, the quantity of interest of this thesis. In particular, the research background is explained, and the aims and expected impacts of this dissertation are listed.

Chapter 2 lays the basis of passive microwave ground-based radiometry, the ozone measurement technique used throughout this thesis.

The harmonization project between GROMOS and SOMORA is described in Chapter 3. It has been completed for the data from the two instruments from 2009 until 2022 and has been successful at reducing the discrepancies previously observed between the two time series. In the stratosphere and lower mesosphere, the seasonal ozone relative differences between the two instruments are now within 10% and show good correlations ($R > 0.7$), except during summertime. The new time series were validated against satellite measurements from the Microwave Limb Sounder (MLS) and from the Solar Backscatter Ultraviolet Radiometer (SBUV) over Switzerland. Seasonal mean differences with MLS and SBUV are within 10% in the stratosphere and lower mesosphere up to 60 km and increase rapidly above.

The careful harmonization of the processing algorithms explains some of the remaining differences between the two instruments and enables to flag their respective anomalous measurement periods to adapt their consideration in future trend studies. These results are shown in a first peer-reviewed publication reproduced in Chapter 4.

The harmonized calibration and retrieval algorithms have also been applied to the GROMOS data from 1994 to 2009. With a simple homogenization procedure, the time series of GROMOS now extends from 1994 to 2023 and are ready to compute new strato–mesospheric ozone trends. The harmonization of SOMORA data before 2009 is ongoing.

During my thesis, I also investigated a spectral bias affecting the Acqiris AC240 digital spectrometer, widely used in the field of microwave remote sensing and notably as back-end in GROMOS and SOMORA. A negative bias of $\sim 10\%$ was found on the ozone profile retrieved from the AC240 compared to other, more recent digital spectrometers. The bias origin remains unclear, but it can be accounted for by a simple correction scheme. These investigations and results are reproduced in the form of a second peer-reviewed publication in Chapter 5.

At last, I investigated the ozone diurnal cycle in the middle atmosphere above Switzerland. Specifically, I updated the previous observations of the ozone diurnal cycle derived from GROMOS measurements, which had some discrepancies against model data. The strato–mesospheric ozone diurnal cycle is now in better agreement with SOMORA and with different model datasets. Also, I show the first observations of short-term variability of the ozone diurnal cycle. Chapter 6 presents the investigation of the ozone diurnal cycle and its variability over Switzerland in the form of the third and last peer-reviewed publication of this dissertation.

Finally, Chapter 7 presents the conclusions of this thesis and offers an outlook on ongoing and future work done on ozone microwave remote sensing in Switzerland.

Contents

List of Abbreviations

ADC	Analog/Digital Converter
AOS	acousto-optical spectrometer
ARTS	Atmospheric Radiative Transfer Simulator
AVK	averaging kernel
BASCOE	Belgian Assimilation System for Chemical ObsErvations
BDC	Brewer-Dobson circulation
CCM	chemistry climate model
CFC	chlorofluorocarbon
CIRA-86	COSPAR International Reference Atmosphere
DU	Dobson Unit
ECMWF	European Centre for Medium Range Weather Forecasts
ECV	essential climate variable
ENSO	El Niño-Southern Oscillation
ERA5	ECMWF reanalysis dataset, 5th generation
FFTS	fast Fourier-transform spectrometer
FM	forward model
FWHM	full width at half maximum
GDOC	GEOS-GMI Diurnal Ozone Climatology
GHG	greenhouse gas
GROMOS	GROund-based Millimeter-wave Ozone Spectrometer
HITRAN	High-resolution Transmission Molecular Absorption Database
HWHM	half width at half maximum
IAP	Institute of Applied Physics
IF	intermediate frequency
JPL	Jet Propulsion Laboratory
LO	local oscillator
LOTUS	Long-term Ozone Trends and Uncertainties in the Stratosphere
LST	local solar time
MeteoSwiss	Swiss Federal Office for Meteorology and Climatology

MLS	Microwave Limb Sounder
MOD	Merged Ozone Dataset
MOPI	Microwave Ozone Profiling Instrument
MPI	Martin-Puplett interferometer
MWR	microwave radiometer
NASA	National Aeronautics and Space Administration
NCAR	National Center for Atmospheric Research
NDACC	Network for the Detection of Atmospheric Composition Change
NDSC	Network for the Detection of Stratospheric Change
netCDF	Network Common Data Form
NRL	U.S. Naval Research Laboratory
ODS	ozone depleting substance
OEM	Optimal Estimation Method
PSC	polar stratospheric cloud
QBO	Quasi-Biennal Oscillation
RF	radio frequency
RFI	radio frequency interference
RJE	Rayleigh-Jeans Equivalent
SBUV	Solar Backscatter Ultraviolet Radiometer
SOMORA	Stratospheric Ozone MOnitoring RAdiometer
SSW	sudden stratospheric warming
TCO	total column ozone
TEMPERA	temperature radiometer
UV	ultraviolet
VMR	volume mixing ratio
WACCM	Whole Atmosphere Community Climate Model
WIRA-C	Wind Radiometer for Campaigns
WMO	World Meteorological Organization

1 | Ozone in the middle atmosphere

1.1 Introduction

In a time of unprecedented human induced climate change, the monitoring of our environment and notably our atmosphere must remain a priority. Measurements of atmospheric trace gases make it possible to identify, understand, and validate the causes and consequences of many atmospheric phenomena. In addition, measurements are key to accurately predict the future state of the atmosphere and are therefore a starting point to take political actions for the future of our planet.

The earth's atmosphere is often subdivided in different layers based on the vertical temperature profile. Typical temperature profiles from the surface up to ~ 90 km altitude can be seen in Fig. 1.1. The lowest layer, from the surface to the *tropopause*, is called the *troposphere* and is characterized by a nearly steady negative temperature gradient. It is where nearly all weather phenomena occur and where most aerosols and water can be found. Above the troposphere starts the *stratosphere* where the absorption of ultraviolet (UV) radiation from *ozone* (O_3) generates a positive temperature gradient up to the *stratopause*. The positive temperature gradient in the stratosphere results in a strongly stratified layer which largely limits the vertical mixing. The extremely cold tropopause temperatures (as low as $-80°$ C) remove most of the water vapour reaching the tropopause and makes the stratosphere a very dry place. Above the stratosphere is found the *mesosphere*, where the temperature starts decreasing again. This layer is where most meteors end up and where the highest clouds can be found, the so-called noctilucent clouds. The mesosphere ends at the *mesopause*, which also marks the end of the *homosphere*, where all atmospheric gases can be considered well mixed. Beyond this point is found the *thermosphere*, where stratification by molecular mass and ionization starts to dominate. This is the layer where auroras take place.

The *middle atmosphere* covers the region located between ~ 15 and 90 km above the earth' surface. It is comprised of the stratosphere and the mesosphere and contains ~ 20 % of the total air mass. The stratosphere and the mesosphere can be further divided into different sub-layers which are defined in Table 1.1 and will be used throughout this dissertation. Although the stratosphere contains only a small quantity of all atmospheric molecules, it contains ~ 90 % of atmospheric ozone molecules (Wallace and Hobbs, 2006).

Ozone is an essential climate variable (ECV) as defined by the World Meteorological Organization (WMO) and, despite being a minor constituent of our earth's atmosphere ($< 0.0001\%$), it plays a key role in the thermal budget of the stratosphere. By absorbing the high energetic electromagnetic solar radiation (virtually all UV-c and most UV-b), ozone shields our planet from these harmful radiations, consequently allowing life on Earth. It is mostly found in the lower stratosphere between ~ 15 to 25 km, a region often referred to as the *ozone layer*.

In the second half of the 20^{th} century, it was found that anthropogenic emissions of ozone depleting substance (ODS) such as chlorofluorocarbons (CFCs) were threatening the ozone layer (Molina and Rowland, 1974; Crutzen, 1970; Farman et al., 1985; S. Solomon et al., 1986). In fact severe depletion of the ozone layer was observed globally since the 1980s, particularly in the springtime over the Antarctic (S. Solomon, 1999). Given the amplitude of the ozone depletion,

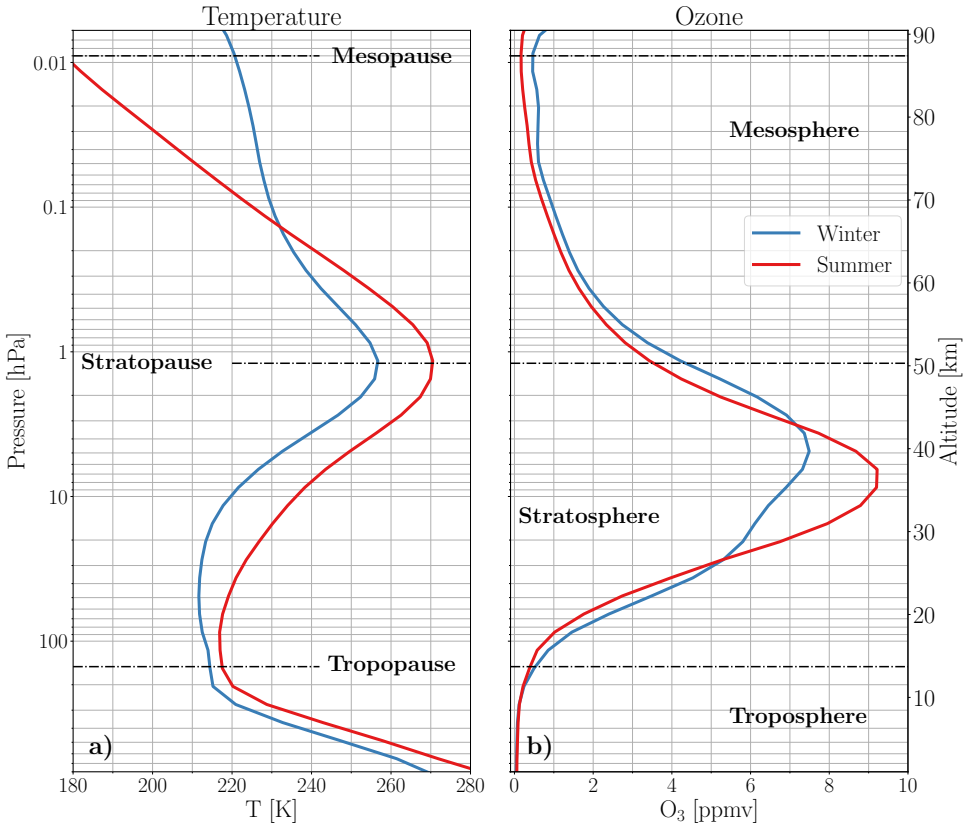

FIGURE 1.1: Mean seasonal temperature (a) and ozone (b) profiles over Bern, Switzerland during the boreal winter and summertime. The ozone data are the measurements from GROMOS, and the temperature are the ones used for the retrievals (see Section 3.2.2).

a large majority of governments worldwide decided to largely ban the production, consumption, and emission of CFCs and other ODS in Montreal in 1987. The resulting *Montreal protocol on Substances that Deplete the Ozone Layer* and its following amendments remain one of the few success stories of international cooperation, and it avoided dramatic depletion of the ozone layer by the end of the 21st century (Newman et al., 2009). Instead, ozone abundances are now expected to recover towards pre-1980 levels during the 21st century and the avoided emissions of CFCs, which are strong greenhouse gases (GHGs), have contributed to significantly reduce the radiative forcing of climate (Velders et al., 2007).

Ozone plays a key role in the stratosphere as it is responsible for the thermal inversion seen above the tropopause (see Fig. 1.1). In fact, the set of photochemical equations governing the abundance of ozone in this layer are exothermic as will be explained in Section 1.2. In addition, their dependency on the availability of sunlight induces a strong diurnal cycle in the thermal forcing of the middle atmosphere, which is also one of the main sources for upper atmospheric tides. The assimilation of ozone data is also important for numerical weather predictions, e.g., for the constraints it provides on incoming UV radiation or on stratospheric constituents (Lahoz et al., 2007). On the other hand, ozone is a powerful GHG and is highly toxic to human health if inhaled. In the troposphere ozone originates from (photo-)chemical reactions between different air pollutants (e.g. car exhaust) and mostly affect cities during warm periods. Whether in the troposphere or in the stratosphere, ozone is a very reactive gas which is subject to natural and anthropogenic influences, leading to strong variations of its abundance with time. Therefore, it

TABLE 1.1: Definition of the pressure ranges and corresponding altitudes used in this dissertation.

Region	**Pressure range** [hPa]	**Altitudes** [km]
Upper mesosphere	$0.1 - 0.01$	$\sim 65 - 80$
Lower mesosphere	$0.9 - 0.1$	$\sim 50 - 65$
Upper stratosphere	$5 - 1$	$\sim 38 - 50$
Mid-stratosphere	$10 - 5$	$\sim 32 - 38$
Lower stratosphere	$50 - 10$	$\sim 22 - 32$
Lowermost stratosphere	$\sim 200 - 50$	$\sim 15 - 22$

is important to monitor its spatio-temporal evolution, from the very local, diurnal variations to the global, multi-decadal trends.

This chapter provides a general introduction to the topic of this dissertation, namely ozone observations in the middle atmosphere. Section 1.2 presents the main photochemical reactions governing the abundance of ozone and its temporal evolution and oscillations. Notably the diurnal variations of middle-atmospheric ozone are introduced in Section 1.3. Section 1.4 lays the theoretical background to understand the geographical distribution and dynamics of ozone in the middle atmosphere, with a focus on the mid-latitudes, region of interest of this dissertation. Section 1.5 provides a basic introduction on the measurement techniques used to monitor ozone in the middle atmosphere and their associated challenges. Section 1.6 introduces the ground-based radiometric measurements performed in Switzerland, which is the main focus of this dissertation. Last, Section 1.7 summarizes the aims and the expected impacts of this work.

1.2 Photochemistry

Ozone (photo-)chemistry in the middle atmosphere is complex, strongly temperature dependent and involves many other chemical species. The chemical equations governing the abundance of ozone in the middle atmosphere can be separated into two distinct families: the *pure oxygen cycle* and the *catalytic depletion cycles*. Here I only give a basic introduction to the main reactions involving ozone, for more details on stratospheric chemistry please refer to Chapter 5 of Brasseur and S. Solomon, 2005.

The set of pure oxygen photochemical reactions leading to the production and destruction of ozone were first described by Chapman, 1930, and they are commonly referred to as the *Chapman cycle*. Together with catalytic depletion cycles involving various species (NO_y, Cl_y, HO_y, ...), they drive the abundance of ozone in the middle atmosphere at multiple time scales. The pure oxygen cycle is a set of chemical equation describing the interaction between solar radiation, molecular oxygen (O_2) and the odd-oxygen family (O_x), composed of oxygen atom (O) and ozone (O_3). They are usually expressed as:

$$O_2 + h\nu \longrightarrow O + O \tag{1.1}$$
$$O + O_2 + M \longrightarrow O_3 + M \tag{1.2}$$
$$O_3 + h\nu \longrightarrow O_2 + O \tag{1.3}$$
$$O_3 + O \longrightarrow O_2 + O_2 \tag{1.4}$$

where M is an inert collision partner and can be any atom or molecule. Eq. 1.1 is a slow source for odd oxygen. It requires solar UV radiation with wavelength lower than 242 nm (UV-c) to break apart an O_2 molecule into two O atoms. Eq. 1.2 is the only known equation to form O_3 in the atmosphere (Brasseur and S. Solomon, 2005). Eq. 1.2 and Eq. 1.3 form a fast cycle continuously destroying and reforming O_3 the middle atmosphere. The net result of these two equations is the conversion of solar energy to kinetic energy resulting in a heating effect and explaining the rise of temperature with height in the stratosphere. Eq. 1.3 also requires solar UV radiation. The photodissociation of O_3 produces an O_2 molecule and an O atom. Depending on the wavelength, it will produce either $O(^3P)$ ($\lambda > 320$ nm) or $O(^1D)$ ($\lambda < 320$ nm), two different states of the O atom. Finally, Eq. 1.4 is a slow sink for ozone and atomic oxygen, referred to as a *cannibalistic reaction*. This reaction is strongly temperature dependent and is more efficient at higher temperatures.

In the second part of the 20$^{\text{th}}$ century, it was discovered that the Chapman cycle overestimates the abundance of ozone in the stratosphere. Therefore, additional sinks for ozone were suggested to explain the observed ozone abundance. It included influences from various oxides, notably of hydrogen (HO_x, Bates and Nicolet, 1950), nitrogen (NO_x, Crutzen, 1970), or chlorine (ClO_x, Stolarski and Cicerone, 1974). Depending on the altitude, all these chemicals were found to destroy ozone by activating catalytic depletion cycles according to the following reactions:

$$\mathrm{X} + \mathrm{O_3} \longrightarrow \mathrm{XO} + \mathrm{O_2} \tag{1.5}$$
$$\mathrm{XO} + \mathrm{O} \longrightarrow \mathrm{X} + \mathrm{O_2} \tag{1.6}$$
$$\mathrm{O} + \mathrm{O_3} \longrightarrow 2\,\mathrm{O_2}\ \text{(Net)} \tag{1.7}$$

where X can be any chemical component acting as a catalyst for ozone destruction, i.e., H, OH, NO, Cl or Br (Brasseur and S. Solomon, 2005).

In practice, the combination of the Chapman and catalytic cycle results in a lifetime of the O_x family which is strongly dependent on the altitude, season, or time of the day, which explains the typical vertical distribution of ozone shown in Fig. 1.1. To summarize, ozone in the lower stratosphere experienced long lifetime (weeks to year) whereas the lifetime is much shorter in the upper stratosphere and mesosphere (hours to days). Therefore, it is usually considered that ozone abundance in the lower stratosphere is dynamically controlled whereas the upper stratosphere and lower mesosphere are closer to photochemical equilibrium (see e.g., Garcia and S. Solomon, 1985; Sakazaki et al., 2013).

1.3 Diurnal cycle

The strong dependence of ozone to the sun's radiation implies that the ozone abundance can vary significantly over a day. These changes are often referred to as *diurnal variations* or as the *ozone diurnal cycle*. Depending on the geographic location and altitude region, ozone varies very differently as a function of the local solar time (LST). In this section I introduce the middle-atmospheric ozone diurnal cycle, focusing on the mid-latitudes, as this is the region of interest of this dissertation (for insight on polar or tropical regions, see Schranz et al., 2018 or Parrish et al., 2014)

In the mesosphere, the importance of the ozone diurnal cycle has been recognized early using photochemical models and from early measurements (e.g., Herman, 1979; Prather, 1981; Vaughan, 1982; Pallister and Tuck, 1983; Zommerfelds et al., 1989). Its main patterns are well known and have been successfully observed and modelled, namely a dramatic ozone depletion

during daytime (reaching nearly complete depletion in the upper mesosphere), when the Chapman cycle is dominated by Eq. 1.3. During the night time, photodissociation stops and ozone is replenished by Eq. 1.2 (Connor et al., 1994; Ricaud et al., 1991; Huang et al., 1997).

Whereas the diurnal cycle signal is quite strong in the mesosphere, it is much weaker in the stratosphere, especially during the wintertime. Models predict a small dip of ozone after sunrise, followed by an accumulation of ozone during daytime and peaking in the afternoon (overall up to 5% diurnal variation at 5 hPa in summer). Nevertheless, even the small stratospheric diurnal cycle needs to be considered when comparing ozone measurement from different observing system or taken at different time of the day (Bhartia et al., 2013; Maillard Barras et al., 2020). This is especially true for satellite time series homogenization as many ozone observing satellites of the past have an orbit drift in LST (e.g. the NASA Solar Backscatter Ultraviolet Radiometer (SBUV), McPeters et al., 2013). In the context of remaining uncertainties on the post-2000 lower stratospheric ozone trends, there has been recently a renewed interest to better characterize the ozone diurnal cycle globally and provide scaling factor to account for it in intercomparison studies or for the creation of merged ozone dataset (Frith et al., 2020; Schanz et al., 2021; Strode et al., 2022).

To validate these new model-based datasets, observations are needed but they remain extremely sparse and challenging, notably because many ozone observing satellites are sun synchronous, measuring two profiles per day. Also, many ground-based ozone measurements techniques rely on the sun as a source of radiation. Using microwave ground-based radiometers, the stratospheric diurnal cycle has been successfully observed at multiple locations (Haefele et al., 2008; Parrish et al., 2014; Studer et al., 2014). However, Parrish et al., 2014 report remaining discrepancies between models and observations in the upper stratosphere and around sunrise.

1.4 Spatio-temporal distribution and dynamics

The production of ozone in the middle atmosphere originates from the oxygen cycle presented in Section 1.2. It is largest in the tropics where the sun's energy is the highest. Whereas the production is highest in the tropics, the actual distribution of ozone around the globe varies significantly in space and time. One reason for these variations are the photochemical processes affecting ozone in the middle atmosphere — which are strongly dependent on the atmospheric composition, sun's radiation and temperature — whereas the remaining variations are due to large scale transport of odd oxygen.

The tropical upper stratosphere is where we found the higher ozone volume mixing ratios (VMRs), however, higher total column ozone (TCO) values[1] are found near the pole as can be seen from Fig. 1.2. This situation is due to the so-called Brewer-Dobson circulation (BDC) named after the two scientists who discovered it in the 20th century (Brewer, 1949; Dobson, 1956). The BDC is a middle atmospheric global circulation patterns which transport ozone-rich air from its source region in the tropics to higher latitudes. It consists of a rising branch at the equator, a meridional circulation towards the poles — larger in the winter hemisphere — and a descending branch above the mid- to high latitudes. An illustration of the BDC is shown in

[1]The abundance of ozone in the atmosphere is expressed with different units depending on the studies or the measurement techniques. The TCO is measured in Dobson Unit (DU), from the name of G. M. B. Dobson, a British physicist and meteorologist who contributed significantly to the early ozone research in the first part of the 20th century. 1 DU is a vertically integrated quantity corresponding to the thickness of a pure ozone layer of 0.01 mm at standard surface pressure and temperature. For ozone vertical profiles in the atmosphere, three other quantities of interest emerge: the ozone partial pressure expressed in pressure units (e.g., Pa or mbar), the ozone number density (in molecules cm^{-3}) and the mixing ratio, either expressed with respect to mass or volume, often in ppm or in ppb. Most remote sensing techniques report ozone mixing ratios, usually in volume, whereas in-situ measurements tend to report the number density or the partial pressure of ozone. One can convert from one to the other at the condition to know about the atmospheric pressure and temperature. In this dissertation, the abundance of ozone will be expressed as VMR in ppmv except otherwise noted.

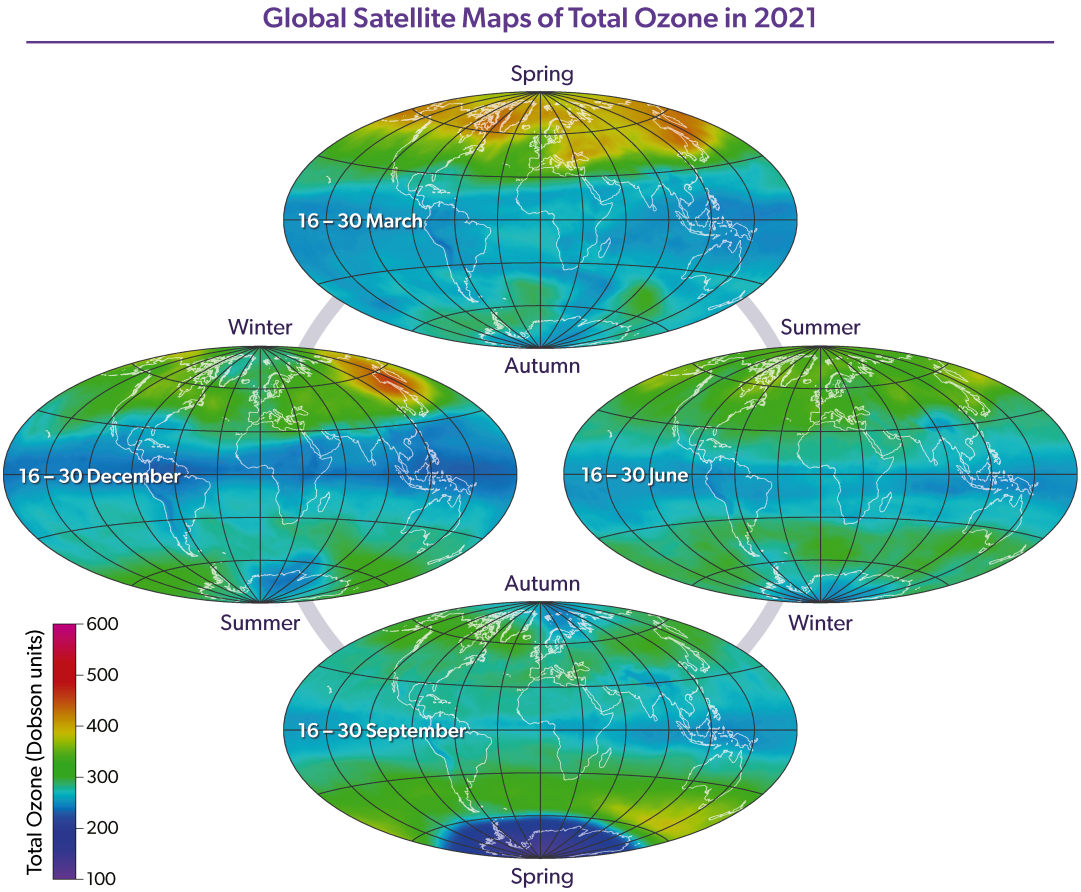

FIGURE 1.2: Global distribution of total column ozone, Figure Q3-1 from Salawitch, R. J. (Lead Author) et al., 2023.

Fig. 1.3 for the summer and winter solstices. The ozone transport through the seasonally varying BDC results in a seasonal dependence of ozone in the mid-latitudes and the polar regions. Its effect can be seen in Fig. 1.2 in the early boreal spring, where TCO values reach a maximum after the stronger transport from the winter branch of the BDC. This is not true in the southern hemisphere, where the lowest TCO values are found in September or October above Antarctica: this is the infamous *ozone hole*.

The ozone hole is caused by strong chemical ozone depletion associated with anthropogenic emissions of halogen source gases, in particular CFCs, a family of powerful ODSs containing carbon, hydrogen, chlorine, and fluorine. CFCs are quite stable molecules that have long enough lifetime to make it to the stratosphere and be transported by large scale motions like the BDC. In the stratosphere, CFCs get photodissociated and converted to so-called *reservoir species*, typically $ClONO_2$ or HCl. The austral winter is characterized by a strong *stratospheric polar vortex*, a low-pressure system centred above the south pole. The polar vortex isolates the polar stratosphere from the mid-latitudes, largely preventing the mixing of air in and out of the vortex and resulting in extremely cold temperatures which can lead to the formation of polar stratospheric clouds (PSCs). In the 1980s, it was discovered that the surface of PSCs triggers heterogeneous chemical reactions with reservoirs species such as $ClONO_2$ and HCl, releasing large amount of *reactive chlorine*, mainly ClO in the polar stratosphere. In late winter, when the sun comes back over the southern polar region, large abundance of ClO dissociate into Cl atoms or react with BrO to initiate strong catalytic ozone depletion cycles. These catalytic reactions result in dramatic ozone depletion over a few weeks, and usually last until mid-October

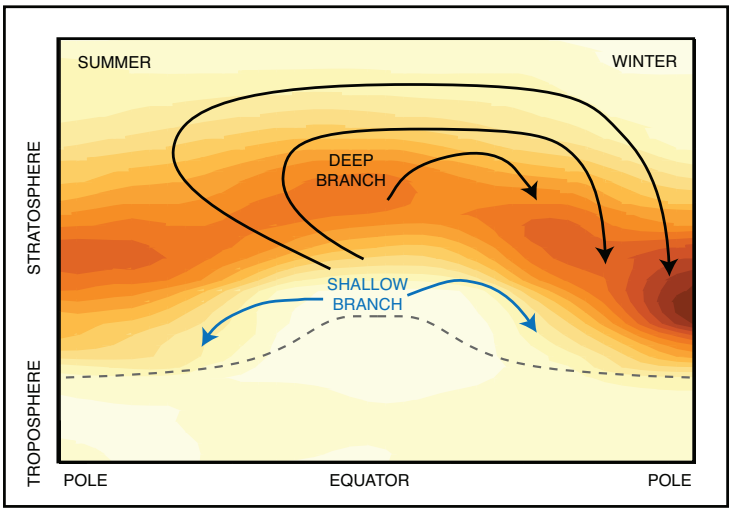

FIGURE 1.3: Schematic illustration of the BDC at solstices, taken from Arblaster, J.M., and N.P Gillett (Lead Authors) et al., 2014. Shading indicates the ozone abundance.

when the temperature rises again and put an end to the large formation of PSCs. Formally, the ozone hole is defined as a region with TCO values less than 220 DU, values which were not observed prior to 1979 (NASA, 2023).

In the northern hemisphere, strong ozone depletion is usually not observed because of higher stratospheric temperatures and of a weaker polar vortex than in the southern hemisphere. On one hand, the higher temperatures prevent the production of PSCs on a large scale, thus largely reducing the heterogeneous chemical conversion of chlorine compounds to their active form. On the other hand, the boreal winter is characterized by large amplitude *planetary waves* (also known as *Rossby waves*). Due to the topology of the northern hemisphere, meridional transport and planetary wave activity are larger than in the southern hemisphere, and thus more prone to perturb or even break the northern polar vortex. These perturbations can result in a weakening or sometimes a reversal of the stratospheric polar vortex winds leading to large-scale subsidence of air in the vortex and to a sudden rise in stratospheric temperatures called a sudden stratospheric warming (SSW) (up to 40 K in a few days, e.g., Shepherd, 2000). The breaking of the polar vortex also mixes mid-latitude, ozone-rich air into the polar regions, reducing the likelihood to form Arctic ozone holes. However, significant Arctic ozone depletion events also happen and have been reported for the first time in 2011 (Manney et al., 2011) and recently in 2020, with new record-low ozone values observed (Manney et al., 2020).

1.4.1 Mid-latitude ozone

The abundance of ozone above Switzerland (Bern) has been shown to follow natural oscillations on a wide range of time scale, from season to years (Calisesi et al., 2005a; Moreira et al., 2016). Strong annual cycle of ozone VMR was identified with amplitude of $\sim 15\%$ in the lower stratosphere, peaking during spring–summer. It is the result of the wintertime ozone transport from the tropics through the BDC. In the upper stratosphere, the annual cycle is reversed, with lower VMRs during spring–summer. This reversal originates from the correlation of the Chapman and catalytic cycles with temperature in this photochemically controlled region. Interannual fluctuations have also been identified in the ozone time series above Bern, notably due to the Quasi-Biennal Oscillation (QBO), El Niño-Southern Oscillation (ENSO) or to the 11 years solar cycle (see Moreira et al., 2016 for more details). Aside these regular fluctuations, large

volcanic eruptions can also impact the ozone abundance, by injecting sulphate aerosols into the stratosphere. The effects of volcanic eruption on stratospheric ozone depend on many parameters (e.g., the aerosol content, the stratospheric temperature, or the chlorine concentration) but they can be significant and last for months to years, e.g., after the Pinatubo eruption in 1991.

In addition, stratospheric ozone abundance has some short-term variability in the range of a few hours to days, which are particularly strong during wintertime (Moreira et al., 2018). These short-term variability during wintertime have been attributed to the meandering of the stratospheric polar vortex and to the planetary-wave-driven meridional transport of polar or subtropical air. Calisesi et al., 2001 showed that the meridional transport of ozone plays a dominant role in some extreme events observed during wintertime. They also note that the photochemistry acts to reduce the ozone changes due to meridional transport. Flury et al., 2009 observed strong decrease of mid-latitude ozone abundance following the major SSW of February 2008. They attributed the lower stratospheric ozone depletion to the transport of ozone-poor air from the polar vortex and the strong upper stratospheric depletion to the increased efficiency of the NO_x cycle caused by the increased stratospheric temperature. A similar depletion was observed during the major SSW from January 2010, when the stratospheric polar vortex overpassed Bern (Scheiben et al., 2012). Using operational analysis data from the European Centre for Medium Range Weather Forecasts (ECMWF), Fig. 1.4 shows an overview of the stratospheric situation following the minor SSW of early January 2015 (Manney et al., 2015). This event was used to investigate the short-term variability of the ozone diurnal cycle (Sauvageat et al., 2023) and exemplify the sometimes complex patterns of stratospheric circulation. In the mesosphere, mid-latitude gravity waves are assumed to induce short-term ozone fluctuations (Hocke et al., 2006). There are also other factors contributing to ozone variability in the mid-latitudes, notably small scale structure known as filament or streamer (Hocke et al., 2017).

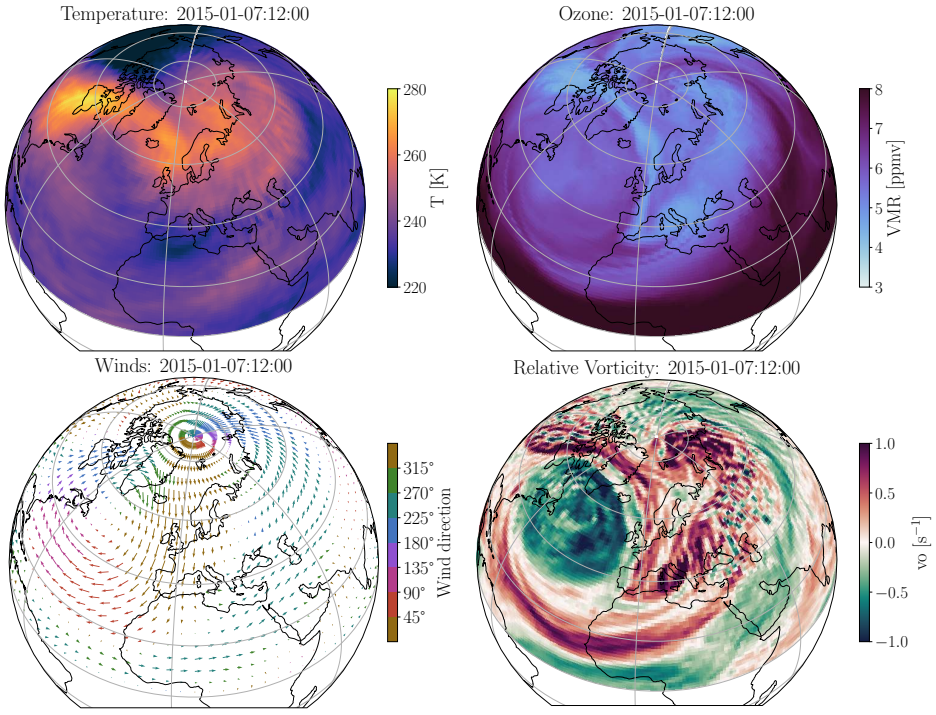

FIGURE 1.4: Overview of the northern hemisphere situation in the upper stratosphere (∼ 5 hPa) following the minor SSW of January 2015. The data are taken from the operational analysis of the ECMWF.

1.4.2 Trends

Ozone trends are a wide topic and I only give here a few facts about the past evolution and future perspectives of strato–mesospheric ozone. The interested reader is directed to the comprehensive review presented in Bernet, 2020.

Following the Montreal Protocol, the reduced ODS emissions have led to a decrease in total chlorine concentration since 1997. Simultaneously, the increasing GHG concentrations (especially of CO_2 and CH_4) are cooling the upper stratosphere (Anderson et al., 2000; P. Solomon et al., 2006). The combination of both factors should in theory lead to an observable recovery or even super recovery of stratospheric ozone concentration (Eyring et al., 2010).

Over the polar regions, the stratospheric ozone abundance has already begun to recover towards pre-industrial levels (S. Solomon et al., 2016). Over the mid-latitudes, the situation is less obvious, and ozone recovery seems to differ depending on the altitude and the geographical area of interest (WMO, 2022; SPARC/IO3C/GAW, 2019; Tummon et al., 2015). In the middle and upper stratosphere, the latest observations agree on a positive trend of ozone concentration despite a high variability in its significance and magnitude (Steinbrecht et al., 2017; Bernet et al., 2019; Godin-Beekmann et al., 2022). These variabilities and remaining uncertainties are illustrated by Fig. 1.5. It shows quite clear recovery of upper stratospheric ozone since the year 2000 and a general good agreement between the models and the measurements in all latitude bands. In contrast, no clear indication of ozone recovery has been reported yet in the lower(most) stratosphere and some observational evidence of further decline in this region were even reported (Ball et al., 2018; Godin-Beekmann et al., 2022). In a context of climate change, there remain also many unknowns regarding the influence of long-term dynamics and composition changes on middle-atmospheric ozone trends depending on the region (Gathen et al., 2021). On one hand, an acceleration of the BDC is expected in the future, which might transport more ozone from its tropical source region to higher latitudes (Butchart, 2014). Also, the cooling trends due to increasing GHG concentrations seem (unfortunately) quite likely to persist in the future. On the other hand, increase of N_2O emission and short-lived halogens not regulated trough the Montreal Protocol might slow down the recovery of ozone. Ravishankara et al., 2009 have shown that surface emission of N_2O might become the dominant ODS in the 21^{st} century and it has recently been shown that very short-lived halogens partly explain the continuous decline of tropical lower stratospheric ozone (Villamayor et al., 2023). Also, the negative response of ozone to increased stratospheric H_2O (through the HO_x depletion cycle) is of concern.

1.5 Measurement techniques

Given the importance of ozone in our atmosphere, it is key to monitor the spatio–temporal evolution of this trace gas. In the stratosphere, ozone measurements are important to assess the success of the Montreal Protocol and to reduce the remaining uncertainties on the future evolution of middle-atmospheric ozone. This is the underlying objective of this dissertation, which aims to improve the quality of long-term measurements of ozone in the middle atmosphere over the mid-latitudes. In this section, I provide a succinct introduction to the different middle-atmospheric measurement techniques (see Hassler et al., 2014 for a complete review).

There exist many different techniques to measure ozone in the middle atmosphere. Nevertheless, there is no single technique, which provides alone sufficient temporal and spatial coverage for satisfying ozone monitoring around the globe. The difficulty to get *in-situ* measurements in the middle atmosphere supported the development of *remote sensing* techniques to measure strato–mesospheric ozone. In fact, most of our current knowledge of this region comes either from simulation studies or remote sensing measurements.

In-situ ozone measurements are difficult in the middle atmosphere and are mostly limited to the lower stratosphere. They are mostly performed by *ozonesondes*, routinely launched (often

weekly) worldwide by national meteorological services. Due to their better accuracy compared to remote sensing techniques, they remain the standard for ozone long-term measurements but have limited spatio-temporal resolution and are limited to lower stratospheric measurements (< 35 km). In-situ measurements are also performed in the stratosphere onboard some high-altitude aircrafts and sometimes in the mesosphere using sounding rockets. However, such measurements are expensive and are only performed on campaigns basis.

The remote sensing techniques use the properties of the ozone molecules to interact with electromagnetic waves at different frequencies (from UV to microwave) to measure ozone abundance. In general, the remote sensing techniques are more complex and less accurate than in-situ measurements because they often need more complex instrumentation and post-processing to derive accurate ozone measurement. However, they are able measure ozone with better spatio–temporal coverage than in-situ measurements. *Active remote sensing* techniques emit themselves the illumination source for the observations (e.g., lidars), whereas *passive remote sensing* techniques rely on extra-terrestrial sources (e.g., sun, stars) or on the thermal microwave emission of the ozone molecule itself. This is the underlying principle of *microwave remote sensing*, which is the technique used in my thesis and will be described in detail in Chapter 2.

Some of the remote sensing techniques only provide information about the TCO above a given location, where more advanced techniques have vertical profiling capabilities. Satellite-based remote sensing provides a near-global coverage, but it often has limited temporal resolution and severe homogenization needs when it comes to long-term monitoring. Ground-based instruments provide only point measurements but can offer a high temporal resolution and are easier to maintain. They currently provide the longest middle-atmospheric ozone time series (Staehelin et al., 1998). In general, there remain many challenges in middle-atmospheric ozone measurement techniques and there is a ceaseless interest for improving the quality of ozone time series (Hubert et al., 2016; Ancellet et al., 2022; Maillard Barras et al., 2022a). It is true for both ground-based and satellite-based datasets and can be understood from Fig. 1.5. This figure highlights the difficulty of detecting long-term trends in the lower stratosphere, partly because of its magnitude, but also because of the large inter-annual ozone variability and the relative scattering between the different measurements.

The need for good quality, stratospheric trace gases measurements (initially focused on ozone) motivated the creation of the Network for the Detection of Stratospheric Change (NDSC) in 1991, which later became the Network for the Detection of Atmospheric Composition Change (NDACC)[2] (De Mazière et al., 2018). This international network aims at regrouping and harmonizing ground-based observations of the atmospheric composition from over 90 research stations worldwide. The main goal of NDACC is to provide long-term datasets of atmospheric trace gases to detect trends and provide validation for satellite- or model-based datasets.

1.6 Strato–mesospheric ozone profiling in Switzerland

The very first measurements of ozone in the atmosphere date back to the 1920s (Dobson and Harrison, 1926; Brönnimann, 2022), with Switzerland having a long history of ground-based ozone measurements, notably with the world longest time series in Arosa/Davos, which started in 1926 (Staehelin et al., 1998). In the 1980s, the Institute of Applied Physics (IAP) of the University of Bern has started to use ground-based microwave radiometry to measure ozone in the middle atmosphere. This passive remote sensing technique uses the emission of the atmospheric molecule in the microwave range to derive vertical profiles, e.g., of ozone or water vapour in the middle atmosphere (Lobsiger et al., 1984; Parrish et al., 1988; Ricaud et al., 1991; Nedoluha et al., 1995). As it does not need any external illumination sources (e.g., sun or stars), it can be used during day and night, which makes it ideal to perform continuous, operational

[2] https://ndacc.larc.nasa.gov

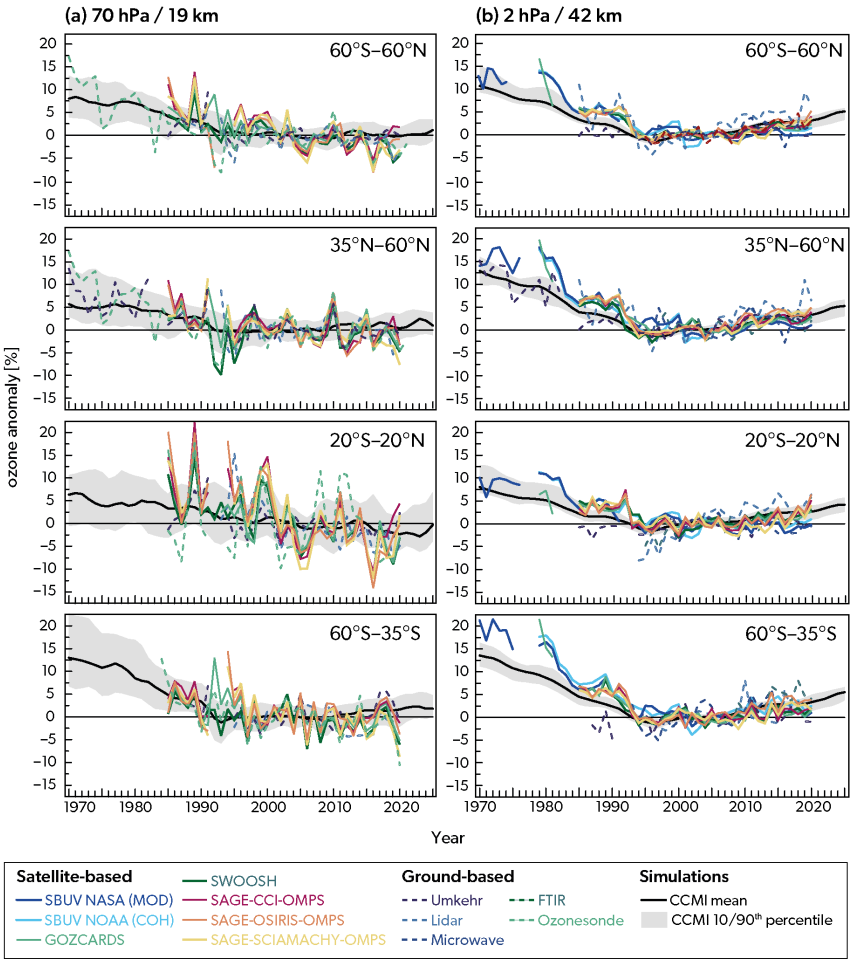

FIGURE 1.5: Annual mean anomalies of simulated and measured ozone in the lowermost (left) and upper stratosphere (right) for 4 latitude bands. Figure 3-9 from Hassler, B. and Young, P. J. (Lead Authors) et al., 2022

measurements, to observe the ozone diurnal cycle, or ozone in the polar region (Raffalski et al., 2005; Palm et al., 2010; Ryan et al., 2016; Schranz et al., 2019)

In the early 1980s, the IAP built a first ozone microwave radiometer (MWR) and in 1994, the institute started operational, continuous measurements of middle-atmospheric ozone from the roof of the "Exakte Wissenschaften (ExWi)" building with the GROund-based Millimeter-wave Ozone Spectrometer (GROMOS). In 1999, the IAP built a second ozone radiometer on behalf of the Swiss Federal Office for Meteorology and Climatology (MeteoSwiss): the Stratospheric Ozone MOnitoring RAdiometer (SOMORA), which started operational measurements in 2000. The two instruments observe the 142 GHz ozone emission line in the stratosphere and mesosphere and have retrieval capabilities from $\sim$ 20 to 80 km. The two instruments are nearly co-located (ca. 40 km), and they have similar sensitivity and viewing angle, meaning that they should essentially measure the same strato–mesospheric ozone profile. In that sense, they provide two independents, nearly co-located, microwave remote sensing measurements of ozone, which is unique worldwide.

GROMOS and SOMORA have been used in numerous studies as reference instrument for ozone measurements in the middle atmosphere, notably for studies on the ozone diurnal cycle, for satellite validation, or for trends studies (Parrish et al., 2014; Hocke et al., 2007; Steinbrecht et al., 2017; Frith et al., 2020). Also, the two instruments are operated within NDACC. An example

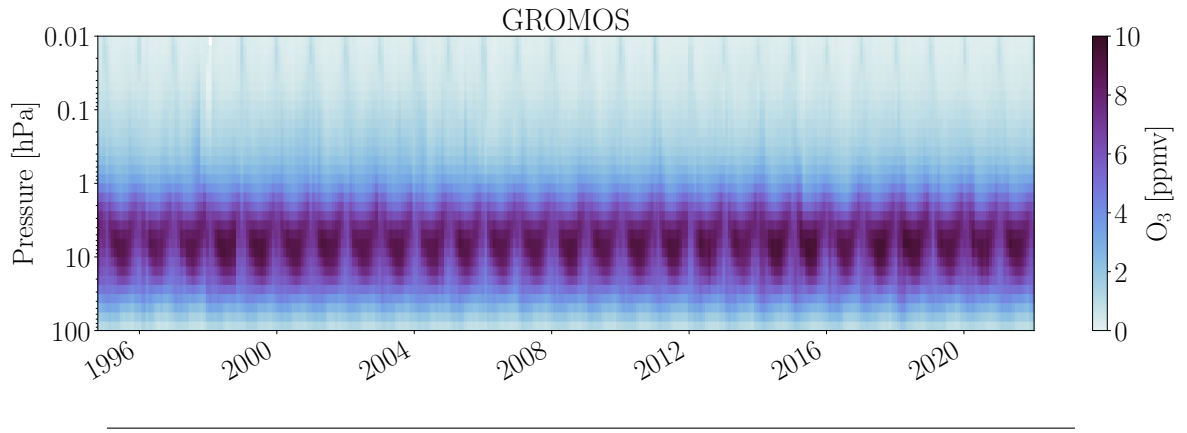

FIGURE 1.6: Ozone time series over Switzerland as measured by the GROMOS microwave radiometer in Bern since the start of the operational measurements in 1994.

of the almost 30 year-long ozone time series measured by GROMOS is shown in Fig. 1.6.

Despite both instruments having similar design, their operational calibration and retrieval algorithms have never been harmonized and showed some substantial differences. In the frame of the Long-term Ozone Trends and Uncertainties in the Stratosphere (LOTUS), SPARC/IO3C/GAW, 2019 found significant discrepancies between the long-term ozone trends of GROMOS and SOMORA. It motivated the work of Bernet et al., 2019, who tried to reconcile the ozone trends of the two instruments, but without formally identifying the cause for the discrepancies. Therefore, in 2019, the IAP and MeteoSwiss decided to act and started a harmonization project with the overall aim to reconcile the ozone time series of GROMOS and SOMORA. This is the main focus of this dissertation and is summarized in the next section.

1.7 Aims and expected impacts of the thesis

This thesis is concerned with ground-based measurements of ozone in the middle atmosphere over Switzerland using microwave radiometry. Following the discovery of systematic discrepancies between GROMOS and SOMORA (Bernet et al., 2019), the main objective of my thesis is to understand and reduce the differences observed between these two ozone time series. To achieve this, a full harmonization of the data processing routine was performed and new time series for the two instruments were obtained. Overall, this work can be further divided into 3 main research objectives, which resulted in the 3 peer-reviewed publications reproduced later in the dissertation. The main research objectives are summarized below.

Research objective 1: Investigate and understand the origin of the discrepancies previously observed between GROMOS and SOMORA. It corresponds quite closely to the main aim of the thesis and represents also the main outcome of my doctoral work. More specifically, the following specific aims were pursued:

- Harmonize and improve the calibration and retrieval routines of GROMOS and SOMORA, including all the outputs.
- Harmonize the data filtering for the two instruments.
- Validate the harmonized time series against external datasets.

The harmonization and validation strategy are presented in detail in Chapter 3 whereas the main results and the associated publication are shown in Chapter 4.

Research objective 2: Assess the reliability of the spectrometer used in ozone remote sensing instrument. Following a preliminary study from Murk and Kotiranta, 2019, the AC240 fast Fourier-transform spectrometer (FFTS) currently used in GROMOS and SOMORA was found to bias the atmospheric spectral measurements compared to more recent digital spectrometers. Therefore, in a study reproduced in Chapter 5, I investigated the spectral properties and the accuracy of the AC240 spectrometer to assess the systematic bias and its effect on the retrieved ozone profiles. The specific aims were:

- Compare the AC240 spectrometer against two other, more recent digital spectrometers during a measurement campaign. My role in this study was to analyse the data from this measurement campaign to assess the systematic bias of the AC240 and investigate if and how it was varying, e.g., if it was sensitive to the atmospheric conditions.
- Quantify the impact of the systematic bias on the ozone retrievals.
- Understand and reproduce the bias to provide a correction for the time series measured with the AC240.

Research objective 3: Compute updated ozone diurnal cycle over Switzerland with the harmonized time series of GROMOS and SOMORA. In fact, the last diurnal cycle study done with GROMOS (Studer et al., 2014) was made with pre-2009 data and showed an overestimated amplitude of the stratospheric cycle. Since then the previous GROMOS ozone retrieval did not show the expected increase of daytime stratospheric ozone in the post-2009 data. Following the renewed interest in stratospheric ozone diurnal cycle consideration, it motivated the idea to provide an update on ozone diurnal cycle observations over Switzerland. This study, presented in Chapter 6, has the following specific aims:

- Use the ozone diurnal cycle as a test signal and as a benchmark for the quality of the new harmonized ozone retrievals.
- Update previous results on middle-atmospheric ozone diurnal cycle over Switzerland.
- Compare and validate the ozone diurnal cycle against three different model-based datasets.
- Investigate the short-term variability of the ozone diurnal cycle, observed for the first time using the harmonized time series of GROMOS and SOMORA.

1.7.1 Expected impacts

From the work presented in this dissertation, the following impacts can be expected:

- Confirm microwave radiometry as a reliable measurement technique within the middle atmospheric ozone community. In fact, while microwave radiometry is widely used for remote sensing of trace gases, the discrepancies found between GROMOS and SOMORA had cast doubt on this technology in the eyes of some members of the community.
- Improve the quality of remote sensing measurement of strato–mesospheric ozone above Switzerland and get a better understanding of the remaining differences between GROMOS and SOMORA.
- Enable accurate stratospheric ozone trend studies based on the harmonized ozone time series of GROMOS and SOMORA.

- Provide consolidated satellite validation data for strato–mesospheric ozone measurements over Switzerland and Central Europe, notably regarding the ozone diurnal cycle.
- Correct and improve the radiometric measurements made with the AC240 around the world, not only for ozone but also for other measurements.

2 | Passive microwave remote sensing of the atmosphere

Microwave radiometry is a passive remote sensing technique relying on the electromagnetic radiation emitted and transmitted in the microwave frequency range to measure some geophysical parameters of interest. This technique is widely used for atmospheric sounding, both space-based and ground-based. Using the spectral characteristics of the microwave radiation, it can be used to derive vertical profile of trace gases (e.g., ozone or water vapour), temperature, or winds in the middle atmosphere.

In this chapter, I introduce the fundamentals of microwave remote sensing, the measurement technique used during my thesis to measure strato–mesospheric ozone. More specifically, Section 2.1 lays the basics of spectroscopy and radiative transfer in the atmosphere at microwave frequencies, whereas Section 2.2 presents the operating principle of passive microwave ground-based radiometers. For more details on passive microwave remote sensing of the atmosphere, the reader is referred to the excellent books of Janssen, 1993 or Ulaby and Long, 2014.

2.1 Spectroscopy and radiative transfer

2.1.1 Microwave absorption and emission

Atoms and molecules in the atmosphere absorb or emit photons when they undergo between different energy levels. Molecular emission and absorption of electromagnetic waves in the microwave range typically results from pure rotational transitions, therefore affecting particles with permanent electrical (or magnetic) dipole moments (e.g., water vapour or ozone). The quantization of the energy levels results in the absorption or emission or photons at frequencies ν_0, specific to each molecule, which results in the concept of *emission lines*.

According to Kirchhoff's law, in condition of local thermal equilibrium, the power absorption and emission due to a specific molecular species i at frequency ν are equal and it can be expressed by the *absorption coefficient* $\alpha(\nu)$:

$$\alpha_i(\nu) = n \sum_j S_j(T) f_j(\nu_0, \nu, p, T) \tag{2.1}$$

where n is the number density of the molecule per unit volume and j identifies a specific line of the molecule of interest. $S_j(T)$ quantifies the strength of the emission line at temperature T, and $f_j(\nu_0, \nu, p, T)$ is a line shape function. The spectral line shape expresses the fact that the emission does not always happen exactly at ν_0 due to different *broadening mechanisms* (Chapter 2 in Janssen, 1993). In the microwave range, the broadening of the emission lines mainly results from two mechanisms: *Doppler* and *pressure broadening*. Compared to these two mechanisms, the natural broadening effect arising from Heisenberg's uncertainty principle is small and can be neglected.

Doppler line broadening arises from the fact that the molecules are constantly in motion, following a Maxwellian velocity distribution. The resulting line shape is Gaussian and can be expressed as

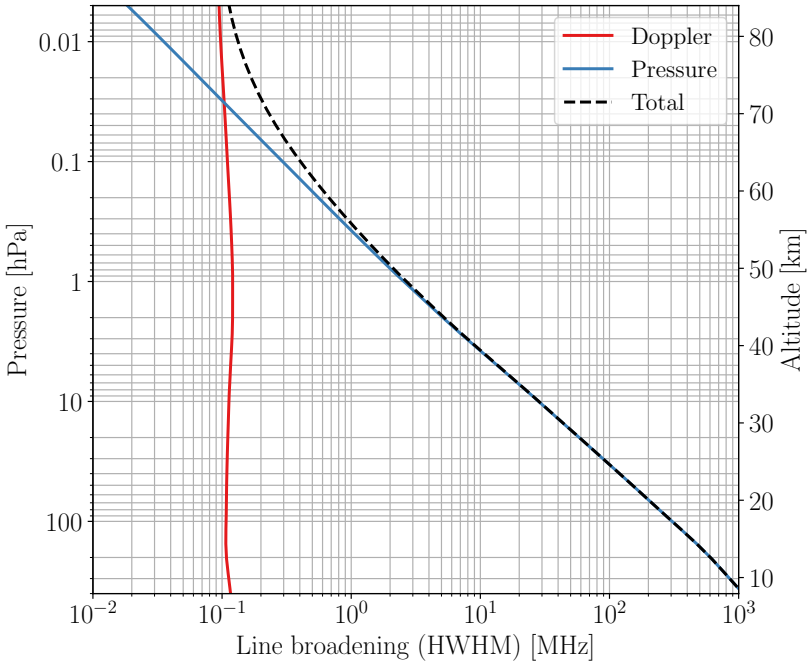

FIGURE 2.1: Line broadening (half width at half maximum (HWHM)) of the 142 GHz ozone emission line calculated for a typical summer atmosphere.

$$f_D(\nu, \nu_0) = \frac{1}{\gamma_D \sqrt{\pi}} \cdot \exp\left[-\left(\frac{\nu - \nu_0}{\gamma_D}\right)^2\right] \tag{2.2}$$

in which the parameter γ_D is

$$\gamma_D = \frac{\nu_0}{c}\sqrt{\frac{2kT}{m}} \tag{2.3}$$

with k being the Boltzmann constant, c the speed of light, m and T respectively the mass and temperature of the molecule involved. From Eq. 2.2 and 2.3, the Doppler broadening increases with temperature and frequency but decreases with the molecular mass. The HWHM of the Doppler line shape is $\gamma_D\sqrt{\ln 2}$ and, despite the temperature dependence of γ_D which changes with altitude, the Doppler broadening is essentially constant with altitude in the range of atmospheric temperature (see Fig. 2.1).

Collisions between the molecules in the atmosphere reduce the lifetime of excited molecules and result in the second broadening mechanisms, the pressure broadening. Pressure broadening usually dominates over Doppler broadening up to the middle atmosphere in the microwave region and its shape can be approximated with, e.g., the Van Vleck-Weisskopf line function:

$$f_{VVW}(\nu, \nu_0) = \frac{1}{\pi} \cdot \frac{\nu}{\nu_0}\left(\frac{\gamma_p}{(\nu_0 - \nu)^2 + \gamma_p^2} + \frac{\gamma_p}{(\nu_0 + \nu)^2 + \gamma_p^2}\right) \tag{2.4}$$

where γ_p is the pressure broadening HWHM:

$$\gamma_p = (\gamma_a \cdot (p - p_i) + \gamma_s \cdot p_i)\left(\frac{T_{ref}}{T}\right)^{\kappa} \tag{2.5}$$

γ_a, γ_s are respectively the air- and the self-broadening coefficients, p_i the partial pressure of the species of interest, and T_{ref} a reference temperature. γ_a, γ_s, κ and T_{ref} can be obtained through spectroscopy catalogues like the High-resolution Transmission Molecular Absorption Database (HITRAN) (Gordon et al., 2022), and are used by radiative transfer software to compute the line shape in combination with the atmospheric composition, temperature, and pressure information. The fact that γ_L depends on pressure is the key for atmospheric profiling by microwave remote sensing, as the atmosphere has monotonically decreasing pressure with altitude. From Eq. 2.4 and 2.5, we note that the pressure broadening line width decreases with decreasing pressure, i.e. with increasing altitude.

Doppler and pressure broadening occur at all levels in the atmosphere but depending on the pressure (i.e. the altitude), the pressure broadening mechanism will dominate over the Doppler broadening, which will enable to retrieve vertical information from the observed line shape. In the microwave frequency range, e.g., near the ozone transition line at 142 GHz, pressure broadening dominates over Doppler broadening up to approximately 75 km, imposing a natural upper boundary for ozone retrievals using this transition line. The contributions of the Doppler and pressure broadening mechanisms to the 142 GHz ozone line are shown in Fig. 2.1.

2.1.2 Radiative transfer

At microwave frequencies, due to the long wavelengths of the radiation of interest, scattering can often be neglected, and it can be considered that incoming radiation arise from the superposed radiation emitted and absorbed by all relevant species. The total absorption coefficient α_ν is the sum of all contributions from the individual absorption coefficient (Eq. 2.1) at frequency ν, plus a so-called *continuum* term which accounts for the broadband emission due to water molecules in the microwave frequency range. The total absorption coefficient is often expressed as

$$\alpha_\nu = \sum_{i=1}^{n} \alpha_i(\nu) + \alpha_{cont}(\nu) \tag{2.6}$$

and describes the total the emission and absorption occurring in the atmosphere at frequency ν. The propagation of radiation along an infinitesimal atmospheric path ds can be described by

$$\frac{dI_\nu}{ds} = -\alpha_\nu(s) I_\nu(s) + \alpha_\nu(s) B_\nu(T(s)) \tag{2.7}$$

This equation, known as the *Schwarzschild's equation*, expresses the change of *spectral radiance* I_ν[1] in a non-scattering medium due to absorption and emission (Janssen, 1993). The first term on the right side of the equation describes the absorption of radiation from the infinitesimal layer (also know as the *Beer-Lambert's law*) and the second term expresses the emission of radiation within the layer following the *Plank's law*. Namely, the spectral radiance due to thermal emission of a blackbody at frequency ν depends solely on its temperature and can be expressed as

$$B_\nu(T) = \frac{2h\nu^3}{c^2} \cdot \frac{1}{e^{\frac{h\nu}{kT}} - 1} \tag{2.8}$$

which has unit of $[\mathrm{Wm^{-2}Hz^{-1}sr^{-1}}]$. Integrating Eq. 2.7 yields the radiance reaching a certain point s_0 (i.e., the ground) after travelling from a point s_∞ through a non-scattering medium in local thermal equilibrium (e.g., the atmosphere):

$$I_\nu(s_0) = I_\nu(s_\infty) e^{-\tau(s_\infty)} + \int_{s_0}^{s_\infty} \alpha_\nu(s) B_\nu(T(s)) e^{-\tau_\nu(s)}\, ds \tag{2.9}$$

[1] Also sometimes called *specific intensity*, *spectral brightness intensity* or simply *radiance*.

with $I_\nu(s_\infty)$ the background spectral radiance which is either an external illumination target (e.g., the sun or the moon) or the *cosmic microwave background*, and τ the *atmospheric opacity* expressed as

$$\tau_\nu(s) = \int_{s_0}^{s} \alpha_\nu(s')\, ds' \tag{2.10}$$

2.1.3 Atmospheric emission spectra

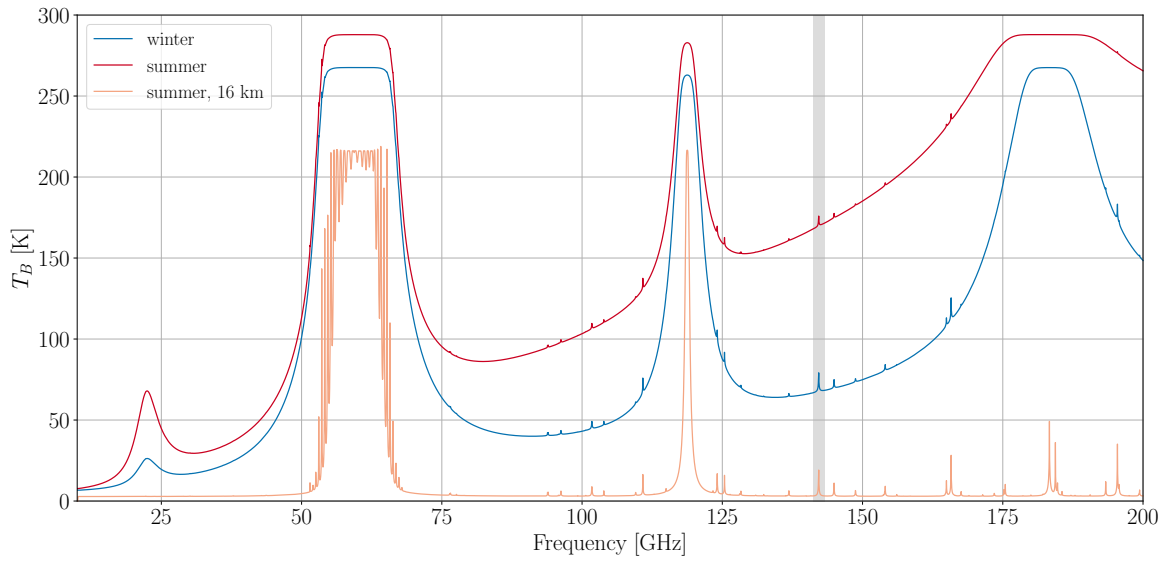

FIGURE 2.2: Atmospheric emission spectra in the mid-latitudes during winter and summer as seen from the surface, respectively at an altitude of 16 km and at an elevation angle of 40° The grey shading highlights the ozone emission line at 142.175 GHz

Nowadays, most radiative transfer calculations are done with dedicated models which essentially solve the above equations for prescribed atmospheric conditions. For my thesis, I have used the Atmospheric Radiative Transfer Simulator (ARTS), an open-source community model focused on the microwave frequency region (Eriksson et al., 2011; Buehler et al., 2018). In addition, ARTS includes useful features to simulate the effect of the microwave receiver on the incoming radiation (Eriksson et al., 2006) and is very flexible with regards to the atmosphere definition.

Using ARTS, it is possible to simulate the atmospheric emission of the different molecules and model the spectral radiance reaching a certain location at a certain frequency. An example of such *atmospheric emission spectra* are shown in Fig. 2.2 in units of *brightness temperature* (see section 2.1.4). This figure shows the atmospheric emission due to oxygen, nitrogen, ozone, and water vapour in the microwave range during typical winter and summer at mid-latitudes. It shows the emission lines of the molecules considered and the strong continuum term resulting from water vapour, increasing towards larger frequencies and larger during summer, when the warmer atmosphere can contain more water vapour. From this simulation, one can understand the effect of the humid troposphere on ground-based microwave observations, especially at millimeter wave frequencies. Simulation of the emission spectra associated with the ozone

transition line at 142 GHz in the middle atmosphere are shown in Fig. 2.3. This figure also illustrates the pressure line broadening mechanism by showing the emission arising from different middle-atmospheric layers, showing the increased broadening of the line at lower altitudes.

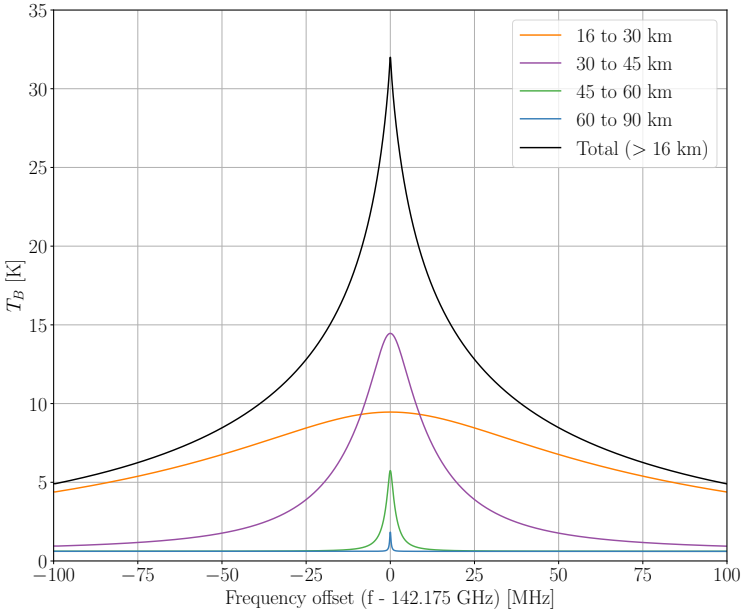

FIGURE 2.3: Simulation of the atmospheric emission spectra from the ozone emission line at 142 GHz. The specific emission due to different middle-atmospheric layers are shown to illustrate the effect of the pressure broadening. The simulation has been performed with ARTS using a mid-latitude winter standard atmosphere. It considers a virtual sensor located at 16 km and looking upward with an elevation angle of 40°.

2.1.4 The brightness temperature

In microwave radiometry, it is customary to convert the spectral radiance in unit of temperature: the *brightness temperature*. However, one needs to be careful because there are different brightness temperature definitions which are sometimes mixed in the literature. Following the nomenclature presented in Han and Westwater, 2000, the *Planck* or *thermodynamic brightness temperature* is defined as the inverse of the Planck's function (Eq. 2.8):

$$T_B = B_\nu^{-1}(I_\nu) = \frac{h\nu}{k} \frac{1}{\ln(\frac{2h\nu^3}{c^2 I_\nu} + 1)} \tag{2.11}$$

It corresponds to the physical temperature a blackbody should have to emit the observed radiance I_ν. Using this definition, it follows that the brightness temperature of blackbodies equals their physical temperature.

In the microwave region, in the limit where $h\nu \ll kT$, it is possible to expand Eq. 2.8 to get a linear relationship between the spectral radiance of a blackbody and its physical temperature:

$$B_\nu(T) \approx \frac{2\nu^2 k}{c^2} \cdot T \tag{2.12}$$

It is known as the *Rayleigh-Jeans approximation*, and it offers another possibility to define the brightness temperature essentially as a scaling of Eq. 2.12:

$$T_B^{(RJE)} \doteq \frac{c^2}{2k\nu^2} I_\nu \tag{2.13}$$

This scaling corresponds to the so-called Rayleigh-Jeans Equivalent (RJE) brightness temperature and provides a linear relationship between the spectral radiance and the physical temperature of a blackbody, which is often used to express Eq. 2.9 in temperature units.

The two brightness temperature definition are fully valid, but they systematically deviate from each other, especially when considering observation of low temperature target (e.g., cold sky), i.e. when $h\nu \not\ll kT$ and where Rayleigh-Jeans approximation is not valid. This is the case in the frequency range considered and, in the rest of this dissertation, all the results will be converted and plotted in units of thermodynamic brightness temperature.

2.2 Microwave radiometry

2.2.1 Operating principle

Microwave radiometers (MWRs) are passive remote sensing instruments measuring the electromagnetic radiation emitted, transmitted, and attenuated through a medium (e.g., the Earth's atmosphere) in the microwave frequency range (300 MHz to 300 GHz). The goal of a radiometer is to receive and quantify accurately the incoming radiation intensity corresponding to $I_\nu(s_0)$ in Eq. 2.9. From the combination of the measured incoming radiation and of a radiative transfer model like ARTS, it is then possible to infer some properties of the medium that emitted, transmitted, or attenuated the radiation (Janssen, 1993). Ground-based MWRs have been used since the end of the 20$^{\text{th}}$ century to measure middle-atmospheric temperature, wind or trace gas profiles (Parrish et al., 1992; Tsou et al., 1995; Nedoluha et al., 1995; Rüfenacht et al., 2012; Tschanz et al., 2013; Hagen et al., 2018; Krochin et al., 2022).

In my thesis, I have used *total power radiometers*, which are the simplest type of radiometer and for which a simplified diagram can be seen in Fig. 2.4. Its main working principle is quickly described in following. MWRs use an *antenna* to receive the electromagnetic radiation power at a *radio frequency (RF)*. Often, MWRs use a rotating mirror to switch between the target of interest (e.g., the atmosphere) and the calibration targets. Most radiometers use *superheterodyne receiver* where, after amplification and filtering, the RF radiation is *down-converted* to a lower *intermediate frequency (IF)*. A signal generator produces a *local oscillator (LO)* frequency which is mixed with the RF in a *mixer*. The mixing process results in a lower frequency signal which is proportional to the amplitude of the RF signal but is easier to process further. After mixing, the signal is usually filtered, further amplified and then undergoes a real-time spectral analysis in a *spectrometer*. Nowadays, the spectral analysis is often done digitally: an Analog/Digital Converter (ADC) samples the IF time signal which is then processed in real-time with dedicated algorithms (e.g., FFT) to compute the power spectrum of the signal. As will be shown later in this dissertation, this step is challenging and key to get accurate radiometric measurements. After the spectral decomposition, the signal is usually integrated to reduce the *noise level* and recorded on a computer. For more details on receiver techniques and microwave radiometry in general, the reader is redirected to chapter 6 and 7 in Ulaby and Long, 2014 or chapter 1 in Janssen, 1993.

2.2.2 Calibration

The raw radiometer output P_{out} (often in voltage or in instrument specific units, e.g., spectrometer counts) to an incoming radiation power can be derived from the *Johnson-Nyquist Noise* (Nyquist, 1928) and expressed as

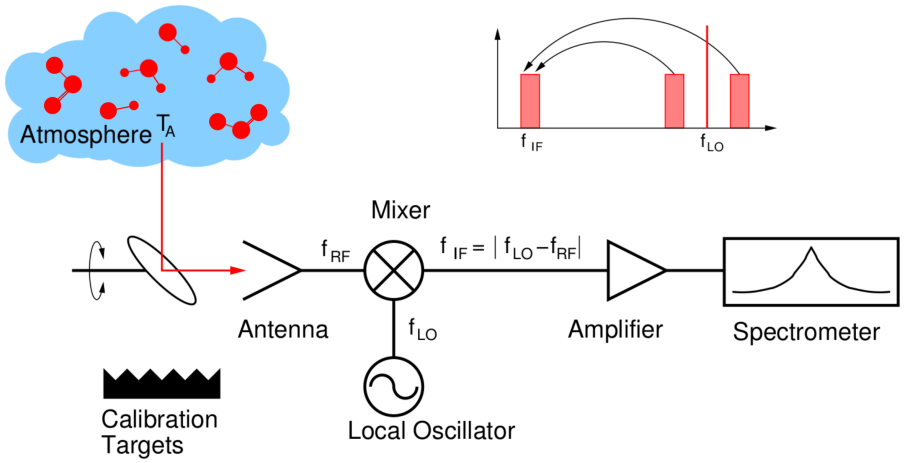

FIGURE 2.4: Simplified diagram of a MWR, courtesy of A. Murk. See text for the description of the different components.

$$P_{out}(\nu) = k\Delta\nu G(\nu) T_{sys}(\nu) \tag{2.14}$$

with $\Delta\nu$ the *bandwidth*, typically the width of a spectrometer channel, G the radiometer gain[2] and T_{sys} the *system noise temperature* (Chapter 7 in Ulaby and Long, 2014).

In microwave radiometry, the system temperature T_{sys} is the sum of the *receiver noise temperature* T_{rec} (often T_N) and of the *antenna temperature* T_a:

$$T_{sys} = T_{rec} + T_a \tag{2.15}$$

The antenna temperature is the convolution of the antenna pattern with the actual brightness temperature of the observed scene. For ground-based observations of the atmosphere, it should correspond to the brightness temperature of the sky ($T_{B,sky}$) and is the quantity of interest. T_{rec} corresponds to the thermal noise added by the components within the receiver and is often higher than T_a.

The goal of the calibration is to convert the spectrometer power measurements (counts) into physical units (e.g., spectral radiance or brightness temperature). Assuming a linear transfer characteristic curve between a hot and a cold calibration loads of known temperatures (Fig. 2.5), two parameters can be determined, namely the gain of the radiometer and an offset, corresponding to the noise power generated by the receiver, i.e., T_{rec}. Combining Eq. 2.14 and Eq. 2.15, it is possible to write:

$$T_A = \frac{P_{out}}{k\Delta\nu G} - T_{rec} = C \cdot (P_{out} - P_0) \tag{2.16}$$

where $P_0 = T_{rec}/C$ is the noise power generated by the instrument in the absence of any atmospheric signal. From the observation of two calibration targets (a *hot* at temperature T_h and a *cold* one at T_c) with known emissivity, it is then possible to get the calibration parameter C as

$$C = \frac{T_{B,h} - T_{B,c}}{P_h - P_c} \tag{2.17}$$

and to compute the T_{rec} as

[2]Note that from now on, the frequency dependence of the gain, power and brightness temperature will be implicitly assumed.

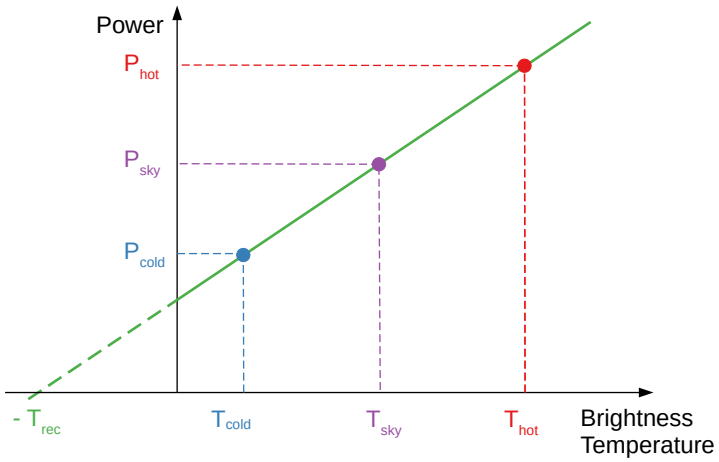

FIGURE 2.5: Calibration characteristic curve of a total power microwave radiometer where the x-axis can be expressed in the different units for the incoming radiation (e.g., brightness temperature, specific intensity, ...)

$$T_{rec} = \frac{P_c T_{B,h} - P_h T_{B,c}}{P_h - P_c} = \frac{T_{B,h} - Y T_{B,c}}{Y - 1} \tag{2.18}$$

where the so-called *Y-factor* is introduced, simply expressing the ratio between the power counts from the two calibration loads:

$$Y = \frac{P_h}{P_c} \tag{2.19}$$

Finally, Eq. 2.20 is used to directly convert the power output of the spectrometer to units of atmospheric radiation, e.g., spectral radiance, or brightness temperature:

$$T_{B,sky} = (T_{B,h} - T_{B,c}) \cdot \frac{P_{sky} - P_c}{P_h - P_c} + T_{B,c} \tag{2.20}$$

where it is assumed that $T_{B,sky}$ is the observed brightness temperature when looking at the sky with corresponding power P_{sky} measured by the spectrometer. Note that Eq. 2.20 is expressed with the spectral radiance or with $T_B^{(RJE)}$ without making any approximations as the two are linearly related (Eq. 2.13). However, directly using the physical temperature of the calibration loads as is often done introduces a (small) bias in the calibration.

In practice, because of the high thermal sensitivity of microwave receivers, the calibration is done continuously by switching at regular intervals between the calibration loads and the atmosphere. Also, the noise power measurement possesses a statistical uncertainty which is related to the bandwidth and to the integration time t_{int} of the measurement. This statistical uncertainty is expressed by the *radiometer noise formula* which is a surrogate for the sensitivity of a radiometer. It essentially quantifies the smallest change of radiation power detectable by the instrument (neglecting gain variations):

$$\frac{\Delta P}{P} = \frac{\Delta T}{T_{sys}} = \frac{1}{\sqrt{\Delta\nu \cdot t_{int}}} \tag{2.21}$$

Beyond the inherent statistical uncertainty from the noise measurement, it should be noted that any divergence from a purely linear transfer characteristics curve will introduce a bias in the determination of $T_{B,sky}$ (see e.g., Sauvageat et al., 2021).

2.2.3 Retrieval

In the microwave frequency range, the pressure broadening effect acting on atmospheric emission lines is used to retrieve information on atmospheric vertical profile from the calibrated microwave emission spectra (Rodgers, 1976). This so-called *retrieval* from MWR measurements has been successfully applied on temperature, wind and trace gases like O_3, CO or H_2O (Janssen, 1993). Among the different retrieval techniques, I selected the Optimal Estimation Method (OEM) following the formalism described by Rodgers, 2000. This statistical method extracts the best estimate of an atmospheric profile from a set of measurements with noise, some a priori knowledge and a forward model. In addition, the OEM enables to characterize the error budget of the retrievals. It is widely used to solve atmospheric inversion problems and has been successfully applied to strato–mesospheric ozone retrievals since many years, both on ground-based and satellite MWRs. In this section I present succinctly the retrieval method while the details of its application to my project are presented in section 3.2.2. For more detailed information on the OEM or its application to ozone profiling instruments, the reader is redirected to e.g., Parrish et al., 1988; Parrish, 1994; Tsou et al., 1995; Rodgers, 2000.

Forward model

In the case of ground-based microwave radiometry, the forward model (FM) describes the radiative transfer physic between the trace gas emission and the instrument's receiver (operator F below). The goal of the FM is to simulate the radiometric measurements ($\boldsymbol{y}$)[3] from a given atmospheric state ($\boldsymbol{x}$), a set of FM parameters ($\boldsymbol{b}$), and error sources ($\boldsymbol{\epsilon}$). It describes the emission, extinction, and transmission of microwave radiation between the ozone molecules and the receiver, and it can be mathematically described by Eq. 2.22:

$$\boldsymbol{y} = F(\boldsymbol{x}, \boldsymbol{b}) + \boldsymbol{\epsilon} \tag{2.22}$$

After running the FM, the simulated atmospheric spectrum can be compared with the actual measurements. Based on a cost function, the state vector $\boldsymbol{x}$ can then be updated, and the FM run again to yield an improved simulated spectrum providing a better match with the observations. This iterative process is referred to as an atmospheric *inversion* or a *retrieval*.

Optimal Estimation Method

The inversion of microwave atmospheric emission spectra is ill-posed because the available measurements are usually not able to fully resolve the atmospheric profile that would reproduce the observations. It means that, even in the case of a perfect knowledge of the atmospheric radiative transfer physics and sensor's influence on the observations, it would usually not be possible to retrieve a unique atmospheric profile matching the measurements. Therefore, there is a need to combine the measurements with some additional knowledge, for instance on the state of the atmosphere or the expected shape of the solution. The OEM is a technique to invert atmospheric emission spectra by combining the measurements with these additional information (so-called *a priori information*) in a statistically optimal way.

To solve the inverse problem, the OEM relies on Bayes' probability theorem, and it tries to find an estimate of the true state by minimizing the following cost function:

$$C = [\boldsymbol{y} - F(\hat{\boldsymbol{x}})]^T \boldsymbol{S_y^{-1}} [\boldsymbol{y} - F(\hat{\boldsymbol{x}})] + [\hat{\boldsymbol{x}} - \boldsymbol{x_a}]^T \boldsymbol{S_a^{-1}} [\hat{\boldsymbol{x}} - \boldsymbol{x_a}] \tag{2.23}$$

where $\hat{\boldsymbol{x}}$ is the estimated atmospheric profile of interest and $\boldsymbol{x_a}$ is the a priori profile. $\boldsymbol{S_y}$ and $\boldsymbol{S_a}$ are respectively the measurement and a priori covariance matrix which are defined by the user.

[3] in the following equations, bold letters represent vectors or matrices.

These covariance matrices account respectively for the measurement and atmospheric noise and have a considerable influence on the retrieval result and its error budget.

The best estimate of the atmospheric profile $\hat{x}$ is computed iteratively with e.g., the Gauss-Newton algorithm using Eq. 2.24:

$$\hat{\boldsymbol{x}}_{i+1} = \hat{\boldsymbol{x}}_i + (\boldsymbol{S}_a^{-1} + \boldsymbol{K}_i^T \boldsymbol{S}_y^{-1} \boldsymbol{K}_i)^{-1} [\boldsymbol{K}_i^T \boldsymbol{S}_y^{-1} (\boldsymbol{y} - F(\boldsymbol{x}_i)) - \boldsymbol{S}_a^{-1} (\boldsymbol{x}_i - \boldsymbol{x}_a)] \tag{2.24}$$

where K is the so-called *Jacobian matrix* computed with the FM. It corresponds to the derivative of F with respect to x and essentially describes the sensitivity of the FM to changes in the atmospheric profile (see e.g., Fig. 3.3). From the covariance and the Jacobian matrices, the sensitivity of the retrieved state to the measurement, also called the *gain matrix*, is computed with:

$$\frac{\partial \hat{\boldsymbol{x}}}{\partial \boldsymbol{y}} = \boldsymbol{G} = (\boldsymbol{K}^T \boldsymbol{S}_y^{-1} \boldsymbol{K} + \boldsymbol{S}_a^{-1})^{-1} \boldsymbol{K}^T \boldsymbol{S}_y^{-1} \tag{2.25}$$

And the averaging kernel (AVK) $\boldsymbol{A}$, which is the sensitivity of $\hat{\boldsymbol{x}}$ to changes in the unknown true state $\boldsymbol{x}$ can then be computed by

$$\frac{\partial \hat{\boldsymbol{x}}}{\partial \boldsymbol{x}} = \boldsymbol{A} = \frac{\partial \hat{\boldsymbol{x}}}{\partial \boldsymbol{y}} \frac{\partial \boldsymbol{y}}{\partial \boldsymbol{x}} = \boldsymbol{G}\boldsymbol{K} \tag{2.26}$$

The AVKs are critical in any type of remote sensing retrievals, and they form an integral part of the resulting profile. They characterize the smoothing of the retrieved profile compared to the true profile and are therefore used as a surrogate for the vertical resolution of the retrieved profile. The vertical resolution of the retrieved profile is typically expressed by computing the full width at half maximum (FWHM) of the AVK, whereas the difference between the peak of the AVKs and their nominal altitude give the vertical offset of the retrieved profile. Also, the sum of the AVKs at each pressure level yields the *measurement response* (or *measurement contribution*) of the retrieval, which quantifies the information content due to the measurement and to the a priori in the retrieved profile.

Retrieval errors

One advantage of the OEM is that it enables to characterize the error budget of the retrievals. As a first estimate, the total error is composed of two main components: the so-called *smoothing error* and *measurement error* (sometimes called *retrieval noise*).

The smoothing error describes the error arising from the limited vertical resolution of the instrument. In fact, radiometers are not able to resolve small scale vertical changes of the true profile and can only retrieve a smoothed version of the true profile. The amplitude of the smoothing error can give an impression of the vertical resolution of the observing system and is large compared to other error sources. However, this error can be neglected when comparing against other instruments if the AVKs of the MWR are considered. The AVKs are used to smooth the higher resolution profile to mimic the effect of the limited vertical resolution of the MWR, an operation referred as *averaging kernel smoothing* (see Rodgers and Connor, 2003; Calisesi et al., 2005b). The AVK smoothing also enables to remove the influence of the a priori and is applied with Eq. 2.27.

$$\boldsymbol{x_c} = \boldsymbol{x_a} + \boldsymbol{A}(\boldsymbol{x} - \boldsymbol{x_a}) \tag{2.27}$$

where $\boldsymbol{x}$ is the higher resolution profile (e.g., a satellite or a model dataset), $\boldsymbol{x_a}$ is the a priori profile of the MWR retrievals, $\boldsymbol{A}$ are the AVKs and $\boldsymbol{x_c}$ is the resulting convolved profile.

The measurement error is a consequence of the noise present in the measurements and is by essence *random*. This error impacts mostly the higher altitudes and can set an upper altitude

limit to the retrieval capabilities of the observing system. The measurement error can be reduced using a longer integration time or by reducing the receiver noise temperature of the instrument (e.g., by cooling the receiver chain).

Overall, the total error covariance matrix of the retrieval can be computed as the sum of the smoothing error covariance matrix ($\boldsymbol{S_s}$) and the retrieval noise covariance matrix ($\boldsymbol{S_o}$).

$$\boldsymbol{S_{\hat{x}}} = \boldsymbol{S_s} + \boldsymbol{S_o} = (\boldsymbol{A} - \boldsymbol{I})\boldsymbol{S_a}(\boldsymbol{A} - \boldsymbol{I}) + \boldsymbol{G}\boldsymbol{S_y}\boldsymbol{G^T} \tag{2.28}$$

Note that to provide a realistic error budget to the retrieval, $\boldsymbol{S_y}$ should also consider any errors caused by corrections applied between the simulated and the true observations (e.g., tropospheric or windows correction). It is important to keep in mind that this is usually not the case and that further error sources need to be considered to provide a comprehensive error budget. In addition, error due to the FM parameters, the temperature of the calibration targets, or the pointing angle must be accounted for and can result in so-called *systematic error*. Such errors can result in a systematic biasing of the retrieved profile and will be discussed further in the context of GROMOS and SOMORA in Chapter 3.

3 | Microwave radiometer observations of ozone in Switzerland

This chapter describes the GROMORA project (an awkward combination of **GROM**OS and SO**MORA**) which forms the core of my doctoral thesis. The project started in 2019, in a collaboration between the IAP and MeteoSwiss. Its main goal was to better understand the cause of observed discrepancies between GROMOS and SOMORA and between these instruments and other ozone time series. The project resulted in harmonized calibration and retrieval algorithms for GROMOS and SOMORA and in fully reprocessed ozone time series for the two instruments. The new time series are now in better agreement, at least for the decade 2010 to 2020, compared to the series retrieved with the previous algorithms. In addition to the new time series, the harmonized code has been published along with two internal reports documenting the new calibration and retrieval algorithms (Sauvageat, 2021; Sauvageat, 2022b). For the sake of conciseness, I decided not to include the full reports in this dissertation, but I have reused some relevant parts of them in the present chapter.

The chapter is organized as follows: first I introduce GROMOS and SOMORA in Section 3.1, then I present the harmonization strategy used to produce the new calibration and retrieval algorithms in Section 3.2. The validation strategy for the new time series will be introduced in Section 3.3.

3.1 GROMOS and SOMORA

The GROund-based Millimeter-wave Ozone Spectrometer (GROMOS) and the Stratospheric Ozone MOnitoring RAdiometer (SOMORA) are two ground-based passive microwave radiometers (MWRs) measuring ozone in the middle atmosphere. GROMOS is operated by the IAP at the University of Bern (46.95° N, 7.44° E) whereas SOMORA is operated by MeteoSwiss in Payerne (46.82° N, 6.94° E). The location and approximate field-of-view of the two instruments can be seen in Fig. 3.1 and the two instruments are shown in Fig. 3.2. Their main properties are summarized in Table 3.1. GROMOS and SOMORA are part of the NDACC, and they operate continuously since 1994 (GROMOS) and 2000 (SOMORA). The two instruments are single sideband, total-power radiometers which observe the rotational transition line of ozone at 142.175 GHz and provide continuous ozone profiles with hourly time resolution at altitudes between 20 and 75 km. GROMOS and SOMORA have been designed at the IAP and in addition to using similar technologies, their geographic proximity (ca. 40 km) makes them unique in the world of passive microwave observations. This proximity also makes them important for the validation of the technology within the stratospheric ozone community. Notably, the two instruments have been extensively used for estimating long-term trends, and as satellite validation datasets for strato–mesospheric ozone.

3.1.1 Some historical background

In the following, I will try to present succinctly the history of the two instruments and the reasons that lead to this dissertation. I will not provide a full description of the hardware of

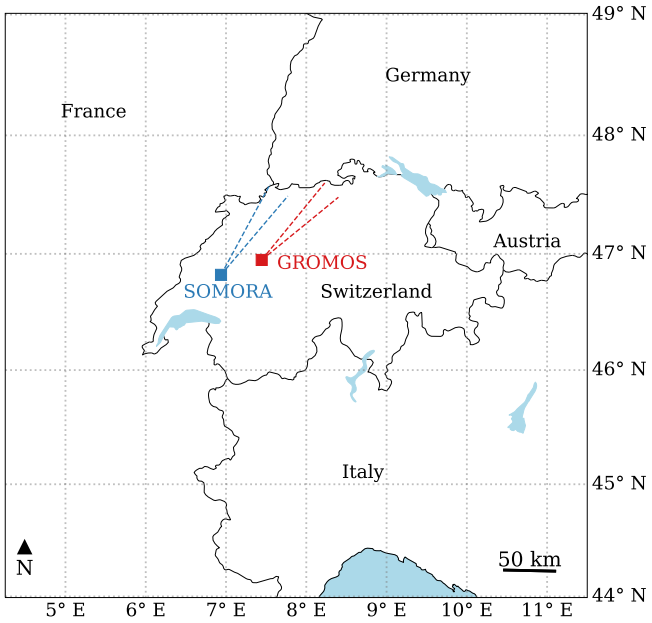

FIGURE 3.1: Geographic location of GROMOS and SOMORA microwave radiometers. The dashed lines indicate the approximate field-of-view of the two instruments, reproduced from Sauvageat et al., 2022b.

the two instruments as it would be redundant to earlier internal reports and dissertation. In addition, no hardware modification was performed in the frame of this thesis, therefore, for technical description of GROMOS and SOMORA, the interested reader is redirected to the relevant references given below.

GROMOS history starts in the 1980's with a first working prototype developed at the IAP of the University of Bern, which started operating in 1981 (Lobsiger et al., 1984; Lobsiger, 1987). However, this first version of the instrument was used only on campaign basis. Building on this first prototype, an updated version of the instrument started operational measurements of ozone in 1994 for which a description is available in Peter, 1997. Until 2009, GROMOS provided continuous measurement of strato–mesospheric ozone profiles using a filter bank spectrometer.

SOMORA was developed and tested at the end of the 1990s by the IAP (Rindlisbacher, 1999) and started operation in 2000, first in Bern and since 2002 at MeteoSwiss in Payerne. Until 2009, SOMORA used two acousto-optical spectrometer (AOS) for the spectral measurement of the ozone emission line.

Between 2000 and 2005, GROMOS and SOMORA each used a home-made retrieval software inspired from the older GROMOS algorithm (Calisesi, 2003). Following a change of the front-end on SOMORA in 2005, its retrieval software needed an update. Therefore, a new retrieval algorithm based on the first version of the Atmospheric Radiative Transfer Simulator (ARTS) and its accompanying QPack package (Eriksson et al., 2005) was introduced for the two instruments and the full time series were reprocessed (Vasic, 2005; Maillard Barras et al., 2009).

In 2009, a spectrometer update was made on GROMOS and SOMORA. On the two instruments, the old spectrometers were replaced by the Acqiris AC240, a new digital real-time fast Fourier-transform spectrometer (FFTS). After 2009, the two instruments were therefore running with the same spectrometer and the same radiative transfer model. However, there were still some differences in the way the calibration and quality control were made, and especially in the

(I) GROMOS (II) SOMORA

FIGURE 3.2: Pictures of GROMOS and SOMORA MWRs at the University of Bern (a) and at MeteoSwiss in Payerne (b). The two instruments are each in a temperature-controlled room and use a rotating mirror to constantly switch between the hot and cold calibration targets and the atmosphere. The atmospheric observations are done through a styrofoam window which is almost transparent for the incoming microwave radiation.

retrieval setup. Notably, all a priori data were different, and the retrievals were based on two different version of ARTS (version 1 for SOMORA and version 2 for GROMOS).

There have been multiple studies that performed comparison of GROMOS and SOMORA in their 20 years of co-existence. It was generally found that the two instruments agree within 10% at altitudes between 25 to 45 km and within 15% between 45 and 65 km (Bernet et al., 2019; Maillard Barras et al., 2020). The two instruments have also been compared to other independent datasets, both ground-based (e.g., lidars or ozonesondes) and satellite-based (Dumitru et al., 2006; Hocke et al., 2007; Studer et al., 2013; Bernet et al., 2019; Petropavlovskikh et al., 2019).

Despite this general good agreement, most studies have noticed some differences between GROMOS and SOMORA which have raised concerns in the community. In fact, some systematic biases were detected between GROMOS and SOMORA time series, for which no explanations could be found. In addition, some anomalous time periods have been identified in the GROMOS time series and have been shown to affect the ozone trends derived from this instrument (Bernet et al., 2019). For SOMORA, the same analysis has been performed and suggested the presence of anomalies in the time series as well.

While GROMOS and SOMORA are technically similar, there were some significant differences in the way their data are processed, not only in the retrievals but also during the calibration. It made it difficult to compare the calibrated and integrated spectra, and therefore to identify the potential error sources arising during the calibration. For these reasons, in November 2019, MeteoSwiss and the IAP decided to act and hired me to try understanding and solve the discrepancies between the two instruments. After some preliminary work with the older routines, it became clear that a full harmonization of the data processing from the two instruments would be beneficial. The goal was to keep two independent ozone profiling radiometers in Switzerland but with a completely harmonized processing from the raw data (level 0) to the ozone profiles (level 2) for these two instruments.

3.2 Harmonization of GROMOS and SOMORA data processing

This section summarizes the harmonization strategy applied to the data processing of GROMOS and SOMORA. Section 3.2.1 deals with the calibration of the radiometric measurements (level 0 to level 1) and Section 3.2.2 with the ozone profile retrievals (level 1 to level 2). For more details

TABLE 3.1: GROMOS and SOMORA microwave radiometers, adapted from Sauvageat et al., 2022b

	GROMOS	**SOMORA**
Location	Bern	Payerne
Latitude	46.95° N	46.82° N
Longitude	7.44° E	6.94° E
Altitude	560 m	491 m
Azimuth angle	45°	34°
Elevation angle	40°	39°
Observation frequency	142.175 GHz	
Intermediate frequency	3.7 GHz	7.1 GHz
Setup before 2009		
Spectrometer	filter banks	2 x AOS
Bandwidth	1.2 GHz (46 channels)	1 GHz (3068 channels)
Frequency resolution	100 MHz to 212 kHz	979.4 – 24.45 kHz
T_{rec}	$\sim$ 3000 K	$\sim$ 2100 K
Setup after 2009		
Spectrometer	Digital FFTS Acqiris AC240	
Bandwidth	1 GHz (32768 channels)	1 GHz (16384 channels)
Frequency resolution	30.52 kHz	61.04 kHz
T_{rec}	$\sim$ 2750 K	$\sim$ 2550 K

on either part, the reader is redirected to the internal reports containing all the information about the new calibration (Sauvageat, 2021) or retrieval (Sauvageat, 2022b) routines.

3.2.1 Calibration setup

The first step of the harmonization was logically concerned with the calibration of the radiometric raw measurements. GROMOS and SOMORA use the same calibration scheme, the *hot-cold calibration* which was introduced in Section 2.2.2. The two instruments use a rotating mirror to continuously switch between a hot, a cold calibration target and the atmospheric observations. The hot calibration target is a heated blackbody at $\sim$ 40° C while the cold target consists of a blackbody immersed into a liquid nitrogen (LN_2) dewar. The two instruments also perform regular *tipping curve* calibration, but they are only used for validation purpose and will not be described here (see Ingold et al., 1998 for more details).

In essence, the harmonization of the calibration procedure is straight forward and essentially involves a single formula (Eq. 2.20). The difficulty resides in the appropriate filtering of the data and the understanding of the processes that can alter the calibration results (e.g., LN_2 refills). For the harmonized calibration routine, it was decided to perform the calibration in two steps: a first *calibration* step where 10 minutes averaged voltage measurements are converted into brightness temperature followed by an *integration* step, which combines the 10 minutes calibrated spectra into hourly integrated spectra. The 10 minutes calibrated spectra are the *level 1a* and

the hourly integrated values are the *level 1b* and are the results of the calibration routine. The idea behind this two-step process is to have a better control over the data quality and a greater flexibility of the routine. Note that already during the calibration (level 0 to level 1a), basic quality checks are done on each single raw spectrum to check for outliers. Therefore the 10 minutes calibrated spectra should be already preserved against technical issues that could affect individual spectra (e.g. numerical errors). Unlike the previous calibration routines, it was decided to use Eq. 2.20 in its original form before converting the resulting intensity in thermodynamic brightness temperatures using Eq. 2.11. It enables to keep the best possible accuracy for the measured sky spectral intensity, while keeping its historical (and somehow much easier to visualize) units.

The *calibration time* (10 minutes) and *integration time* (1 hour) were selected based on the capabilities of the two instruments and on the atmospheric variability expected over Switzerland. In fact, tropospheric conditions significantly affect the radiometric measurements and can sometimes prevent the observation of the stratospheric ozone line. In this case, it is desirable to remove the calibrated spectra recorded during bad conditions and integrate only the good quality spectra during a given hour. Similarly, LN_2 refills of the dewar, typically lasting for $\sim$ 20 minutes, often alter the results of the calibration. The two steps calibration routine enables to remove the spectra recorded during the refills while keeping a valid hourly integrated spectrum during this hour.

Depending on the time resolution and measurement accuracy required, this two steps calibration procedure also enables to change the integration time easily, without having to run the full calibration again. It has proven particularly useful as the first calibration step involves the reading of the raw measurements and is the most computer intensive part. The calibrated (level 1a) and integrated (level 1b) spectra are finally saved separately in daily Network Common Data Form (netCDF) files along with many useful diagnostic quantities which are then used during the retrieval process or to identify potential anomalous periods. The set of flags designed for the calibrated and integrated spectra are shown in Fig. A.3 for a full year of GROMOS measurements. Daily diagnostics plots are also produced and saved along the level 1 files for quality checks.

3.2.2 Retrieval setup

As introduced in Section 2.2.3, once the radiometric measurements are calibrated and integrated, they can be used to infer the quantity and vertical distribution of ozone that is present above the instrument during the measurement time. To do this, we need to solve the inverse problem to find the ozone profile that resulted in the radiometric spectra, a process referred to as *retrieval*.

To perform the retrieval, the radiometric measurements are compared against the forward model, which simulates the atmospheric emission and performs the radiative transfer simulations of the atmosphere. In the frame of this project, I used the latest stable version of ARTS (v. 2.4, Buehler et al., 2018). ARTS offers a fully integrated OEM retrieval environment and includes many tools to help simulate and retrieve the sensor's influence on the radiometric measurements (Eriksson et al., 2006). Providing the right set of a priori and instrumental knowledge to the algorithm, it is possible to retrieve hourly ozone profiles at altitude between $\sim$ 20 and 75 km, depending on the tropospheric conditions (i.e., also on the season).

In practice, the full retrieval outputs are a combination of different quantities depending on the user's interests. It includes of course the atmospheric profile of interest (e.g., ozone) but can also include further quantities like a water vapour continuum term or some instrumental parameters. The different retrieval quantities defined for GROMOS and SOMORA are described below, whereas Table 3.2 lists the main parameters used in the new harmonized GROMORA retrievals.

For the upload of GROMOS and SOMORA data to NDACC, two different retrieval types are performed: the "rapid delivery" retrieval, which aims to be a near real-time product, and the "consolidated" retrieval, which is the final product and is usually uploaded at a later stage after a more rigorous quality control.

Atmosphere, spectroscopy, and forward model

ARTS offers many possibilities to define the atmospheric state, a priori data and simulation grids. I use one-dimensional pressure, temperature, and altitude profiles from the ECMWF. Depending on the version of the retrievals, I select either the operational analyses (for rapid delivery retrievals) or the latest reanalysis product: the ECMWF reanalysis dataset, 5th generation (ERA5) dataset (for consolidated retrievals). The ECMWF datasets are limited to approximately 70 km altitude and therefore, I complete it with a COSPAR International Reference Atmosphere (CIRA-86) monthly climatology up to 112 km.

As atmospheric species, I include ozone, water vapour, oxygen, and nitrogen. For ozone, I use the spectroscopic database from Perrin et al., 2005, which is provided with ARTS and is derived from the HITRAN and Jet Propulsion Laboratory (JPL) spectroscopic databases. For water vapour, I use the "H2O-PWR98" complete absorption model for water vapour provided by ARTS and based on Rosenkranz, 1998. For oxygen and nitrogen, I take some standard parametrizations provided by ARTS, respectively "O2-PWR93" and "N2-SelfContStandardType" (for more information, see Buehler et al., 2005 or the ARTS user guide[1]).

The simulation frequency grids have been defined to cover the range of GROMOS and SOMORA spectrometers with a refined frequency resolution around the ozone line centre. It matches the spectrometer resolution at the line centre to optimize retrievals at higher altitudes, whereas the spectral resolution is coarser on the line wings to limit computation time.

The forward model also computes the *weighting functions* or *Jacobians*. They indicate the sensitivity of the spectrum to changes in the ozone profile and are shown in Fig. 3.3. In general, the weighting functions of GROMOS and SOMORA are expected to be similar as they are generated with the same forward model and nearly identical atmospheric conditions. Only minor differences are introduced by their different frequency resolution. The two instruments are sensitive to ozone changes approximately up to the mesopause ($\sim$ 80 km), which also corresponds to the limit where pressure broadening dominates over Doppler broadening (see Fig. 2.1). This explains why, despite their different frequency resolution, GROMOS and SOMORA have the same upper altitude limit.

Measurement noise and sensor considerations

To perform meaningful retrievals, it is important to consider the influence of the sensor on the atmospheric emission spectrum. However, it is a complex task requiring the simulation of many instrumental components, most of which have unknown effects on the atmospheric spectra. In addition, most of them are time (e.g. seasonal) or frequency dependent.

The first error source arising from the instrument is the *measurement noise* present in every spectrum. The noise originates partly from thermal emission of the receiver components and is present in any remote sensing system. In addition, the atmosphere itself also adds noise to the measurement, notably though the tropospheric water continuum, which can dampen quite significantly the stratospheric ozone signal, and which depends strongly on the atmospheric conditions. In microwave radiometry, the noise level is reduced through integration of the calibrated spectrum, but it is still important especially as the received radiation power is small. The quantification of the measurement noise is a key step for OEM retrievals because it defines, together

[1] https://www.radiativetransfer.org/

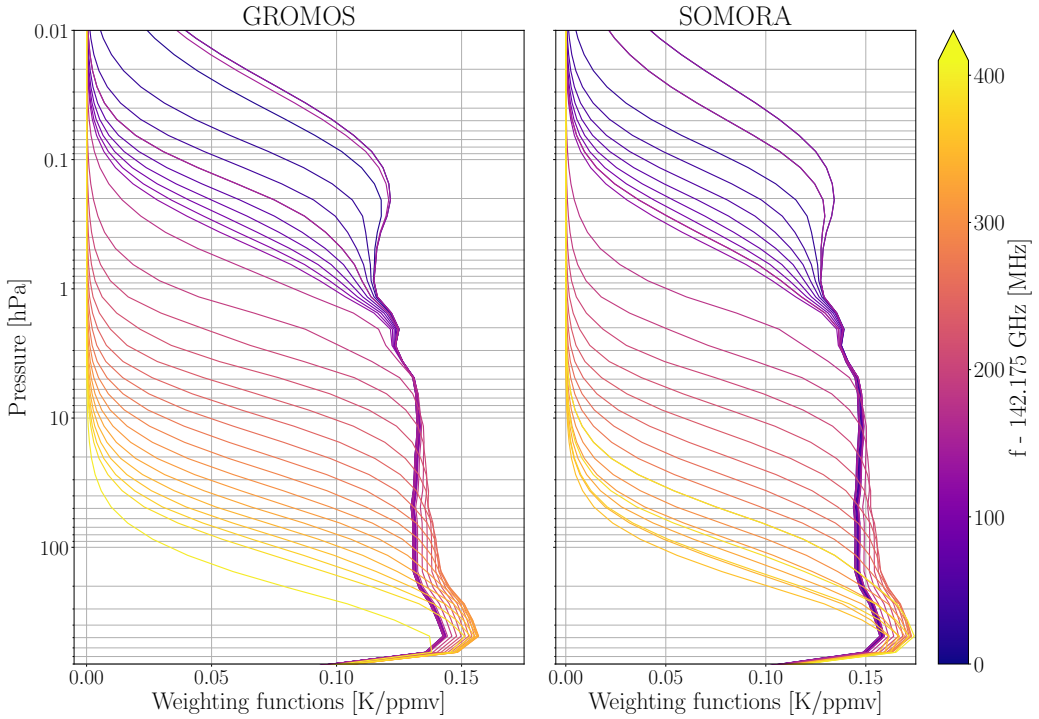

FIGURE 3.3: Weighting functions (Jacobians) obtained from GROMOS and SOMORA forward model. Each line represents the sensitivity of a certain frequency channel to changes in the vertical ozone profile. Purple colours indicate channels near the line centre, which are sensitive higher in the atmosphere, whereas yellow colours indicate channels on the line wing only sensitive to lower altitudes.

with the a priori covariance, the information that can be extracted from the measurement at each pressure level.

The measurement noise is computed individually for each integrated spectrum $\boldsymbol{y}$ based on the observed noise level and it is considered to be uncorrelated between the different channels (i.e., $\boldsymbol{S_y}$ is a diagonal matrix). More specifically, I use the variance of the differences between the neighbouring channels ($\sigma^2_{\Delta \boldsymbol{y}}$) after removal of any spurious FFTS channels. This variance should be twice the simple variance of the measurement vector ($\sigma^2_{\Delta \boldsymbol{y}} = 2\sigma^2_{\boldsymbol{y}}$) and therefore, the noise covariance matrix for each retrieval is defined as

$$(\boldsymbol{S_y})_{ii} = \frac{1}{2}\sigma^2_{\Delta \boldsymbol{y}} \tag{3.1}$$

It results in slightly higher noise level for GROMOS ($\sigma_y \approx 0.7$ K) than SOMORA ($\sigma_y \approx 0.5$ K) because GROMOS has a higher receiver noise temperature and a higher frequency resolution.

ARTS has dedicated built-in functions that can model the influence of the most relevant components on the atmospheric observations (Eriksson et al., 2006). For GROMOS and SOMORA after 2009, I included the effect of the FFTS channel response ($|\frac{\sin(x)}{x}|^2$) and the effect of the sideband ratio. GROMOS and SOMORA both have double sideband mixers and a Martin-Puplett interferometer (MPI) for the sideband rejection (Calisesi, 2003; Peter, 1997). Therefore, the sideband response is assumed to follow a sinusoidal dependence and can be modelled based on previous measurements performed on each instrument.

There are other sensors or external influences which are difficult to estimate and correct

during the calibration process or to simulate accurately for each spectrum. This is the case for the instrumental baselines and the tropospheric absorption. The instrumental baselines are modulation of the atmospheric spectrum due to the observing system. They can arise during the mixing process, the sideband filtering or can be due to undesired reflections, typically when observing the calibration targets. Because these quantities can vary with time and are difficult to simulate or correct beforehand, they have been included as additional retrieval quantities and are described in the next section.

Retrieval quantities

In ARTS, it is possible to have multiple retrieval quantities, which are all added to the state vector $\boldsymbol{x}$. It can be some additional atmospheric unknown quantities (e.g., wind or tropospheric continuum), or some unknown sensors influence on the observations. In principle, the inversion problem is the same as with a single retrieval quantity. For each retrieval quantity, it is needed to define a corresponding a priori and covariance matrix. In this section, I describe the retrieval quantities used for the GROMORA retrievals and briefly discuss the reasons for their addition.

Ozone: The main retrieval quantity is vertical profiles of hourly ozone VMR in the middle atmosphere. As a priori I work with monthly mean ozone profiles from free-running simulations from Whole Atmosphere Community Climate Model (WACCM), version 4 in the configuration described by Schanz et al., 2014. WACCM is a fully coupled global chemistry climate model (CCM) developed at the National Center for Atmospheric Research (NCAR) which simulates the atmosphere from the surface to $\sim$ 150 km altitude, with a vertical resolution between 1.1 and 2 km in the middle-atmosphere. WACCM was run with a horizontal resolution of 4° latitude by 5° longitude and for the retrieval, I select the closest grid point to both Bern and Payerne, which corresponds to 45° N and 5° E. The model was run with the pre-defined free-running "F 2000" scenario, simulating a perpetual year 2000 but without data nudging. Further, depending on the LST, I use either the daytime or night-time a priori ozone profile as shown in Fig. A.1. The reason for using these simulations was to make sure that the a priori profiles would not depend on any measurements used for the validation of the new harmonized retrievals (e.g., with measurement from the Microwave Limb Sounder (MLS) as done previously).

The a priori covariance matrix for ozone varies with altitude and is constant for all days and hours. Under 1 hPa ($\sim$ 50 km), it is a fraction of a yearly mean ozone profile obtained from WACCM. Above, it has been adapted to optimize the information content from the measurement in the lower mesosphere. To account for the vertical coupling of the atmosphere, it includes exponentially decreasing covariances between the pressure levels that are computed as

$$(\boldsymbol{S_a})_{i,j} = \sigma_a(z_i)\sigma_a(z_j)\exp\left(-\frac{|z_i - z_j|}{h}\right) \tag{3.2}$$

For the GROMORA retrievals, I set a correlation length $h = 1$ km and a cut-off value has been applied, which suppresses any covariances as soon as it is under a certain threshold. The ozone a priori covariance matrix is shown in Fig. A.2.

Tropospheric contribution: Around the 142 GHz ozone transition line, the tropospheric water continuum contributes significantly to the observed spectra and must be considered during the inversion process. It is often accounted for with a so-called *tropospheric correction* (Ingold et al., 1998). Such a correction is widely used but their impact on the ozone line can be difficult to quantify, therefore it was decided to include the tropospheric water vapour as a retrieval quantity, as done previously for such retrievals (e.g., Palm et al., 2010). In practice, I use the ECMWF humidity profile as a priori and retrieve a tropospheric continuum value from each measured spectrum. Note that I retrieve only a scaling factor of the a priori water vapour profile

so that the retrieved value for the continuum have no physical meaning without the a priori. The goal here is not to retrieve meaningful tropospheric water vapour profile (for which the instrument has anyway no sensitivity) but only to fit and remove the continuum contribution from the observed stratospheric ozone line.

Instrumental contributions: A frequency shift is also retrieved for each spectrum. The reason for including such a retrieval quantity is because the local oscillators of both GROMOS and SOMORA are not perfectly stable and even a slight shift of the reference frequency can have significant bias on the retrievals, especially on the higher altitudes.

Despite mitigation of baselines using different techniques (e.g., continuous mirror wobbling, non-perpendicular aspect of cold load), it is often necessary to retrieve some instrumental baselines as well (Palm et al., 2010). In the case of GROMOS and SOMORA, I include a second-order polynomial and sinusoidal baselines with different period. To avoid the degradation of the retrievals with the addition of too many baselines, I performed a first processing of the full time series without the sinusoidal baselines and used the residuals to find the appropriate baseline periods for each instrument. The baseline periods remain the same on timescale of month to years so that, in practice, only a few period changes are made during the full extent of the time series for each instrument. The details of which baseline periods have been used for which years can be found in the documentation provided with the time series (see Chapter 4).

TABLE 3.2: Main retrievals parameters used in the new harmonized routine for GROMOS and SOMORA retrievals.

	source/type
Forward model	ARTS (Buehler et al., 2005; Eriksson et al., 2011)
Atmospheric species	O_3, H_2O, O_2 and N_2
Spectroscopy	Perrin et al., 2005 (JPL & HITRAN)
Atmospheric state	1D ECMWF & CIRA-86
O_3 a priori	WACCM, monthly, day/night
H_2O a priori	ECMWF
Modelling grid	$\sim 1 - 112$ km, 2 km resolution
Retrieval grid	$\sim 1 - 95$ km, 2 km, resolution

Level 2

Similarly as for the level 1 files, the outputs of the retrieval routine (i.e., the hourly ozone profiles and diagnostic quantities) are stored in daily netCDF files. The level 2 files hold not only the hourly retrieved ozone profiles, but also the other retrieved quantities and some diagnostics saved during the OEM retrievals. For instance, it holds the measured and fitted spectra (see an example in Fig. 3.4I for GROMOS and in Fig. 3.5I for SOMORA), the noise level of the spectra and all relevant geolocation information. For all retrieved quantities, it always includes the a priori value, grid and error estimations extracted from the OEM. Other typical diagnostic quantities available in the level 2 files include (see Section 2.2.3 for all definitions):

- the AVK matrix and the measurement response,
- the smoothing and measurement error profiles,
- the FWHM of the AVK, corresponding to the vertical resolution of the retrieved profile,

- the AVK vertical offset.

An example of hourly retrieved ozone profiles with these diagnostic quantities can be seen in Fig. 3.4II for GROMOS and Fig. 3.5II for SOMORA. Example of yearly concatenated diagnostic plots for GROMOS are shown in Fig. A.4 and Fig. A.5.

Retrieval errors

As mentioned in Section 2.2.3, the OEM provides two main error components of the retrievals: the smoothing and the measurement error. However, these errors do not include any systematic error sources arising either from the instrument or from the radiative transfer model. To get an estimation of the total error budget for both instruments, a simple sensitivity analysis has been performed on a set of parameters known to introduce systematic biases in the retrievals.

On the instrument side, it includes potential pointing errors, change of the LN_2 target emissivity (i.e. of brightness temperature, especially before/after refills), error in the sideband suppression ratio or uncertainties in the window transmittance. On the atmospheric side, it includes potential errors from the spectroscopic parameters, namely the line intensity and the continuum model used in the forward model. This analysis is presented in Sauvageat et al., 2022b, which is reprinted in Chapter 4.

The main conclusions from the sensitivity analysis are that the total relative uncertainties depend on the tropospheric conditions, with higher uncertainties at higher opacities. Systematic error dominates the uncertainty budget up to ~ 2 hPa, whereas the measurement error becomes quickly dominant above this pressure level. The relative uncertainty in the stratosphere is slightly higher for GROMOS ($9-10\%$) than for SOMORA ($7-8\%$) due to its lower intermediate frequency which increases the sensitivity of GROMOS to the sideband suppression ratio. At higher tropospheric opacities, the total relative uncertainties in the stratosphere increase to $12-15\%$ for GROMOS and $10-12\%$ for SOMORA. Overall these values are aligned with previous error budgets for GROMOS and SOMORA (Calisesi, 2003) and are typical for ground-based ozone MWRs (e.g., Palm et al., 2010; Kopp et al., 2002),

3.3 Validation

Due to their geographic proximity and similar viewing geometry, GROMOS and SOMORA can be compared directly. In this regard, great care has been taken to keep the processing of the data from the two instruments independent. Although the two instruments rely on the same calibration, retrieval algorithms and set of a priori data, they do not use the measurements of the other at all. In that sense, the measurements from GROMOS and SOMORA are considered independent of each other and can therefore be cross-validated against each other.

Despite their independence, GROMOS and SOMORA measurements would still be affected by any bias introduced in the calibration, the retrieval routines and, to a less extent though, by the a priori data. Therefore, further validation of the harmonized ozone time series was performed by comparing their observations with co-located satellite measurements. Namely, I used two satellite-based datasets of strato–mesospheric ozone for the validation which are succinctly described below. The results of these validations are shown in Chapter 4.

3.3.1 Aura MLS

As the main validation dataset for the harmonized GROMORA retrievals, I use ozone measurements from the Microwave Limb Sounder (MLS) instrument onboard the Aura spacecraft (Waters et al., 2006; Froidevaux et al., 2008). It is operated since 2004 by the National Aeronautics and Space Administration (NASA) in the frame of the Earth Observing System and

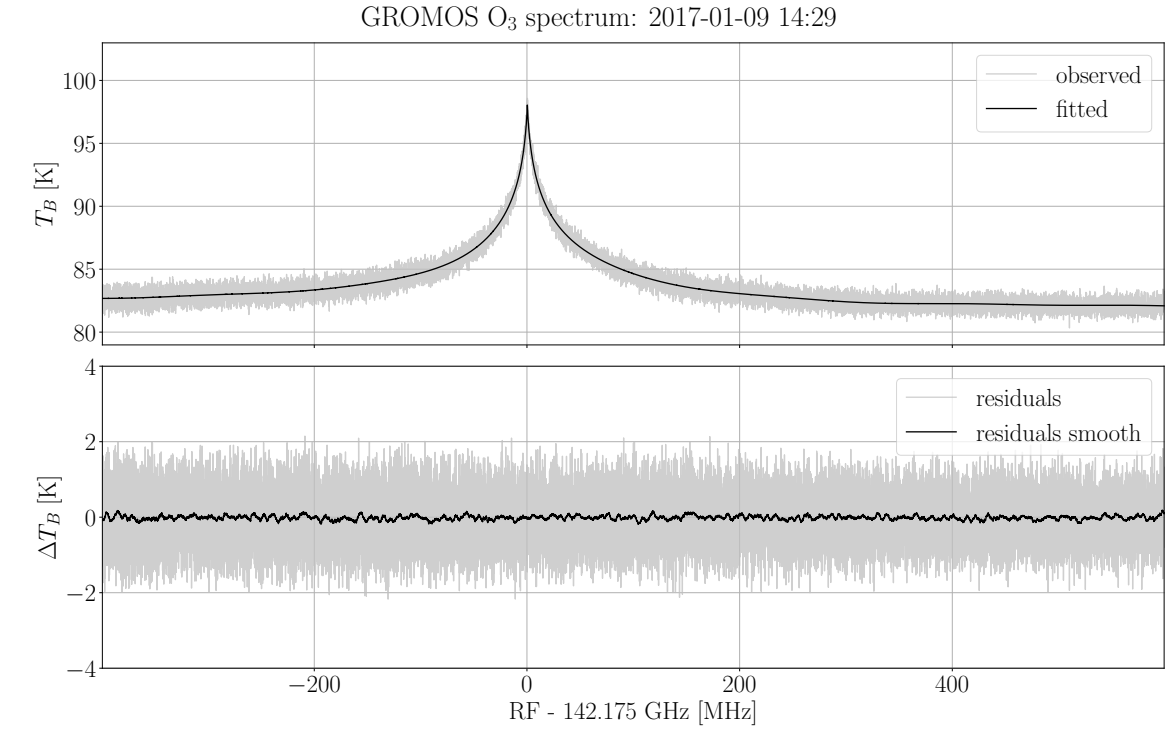

(I) Measured and fitted ozone emission spectra

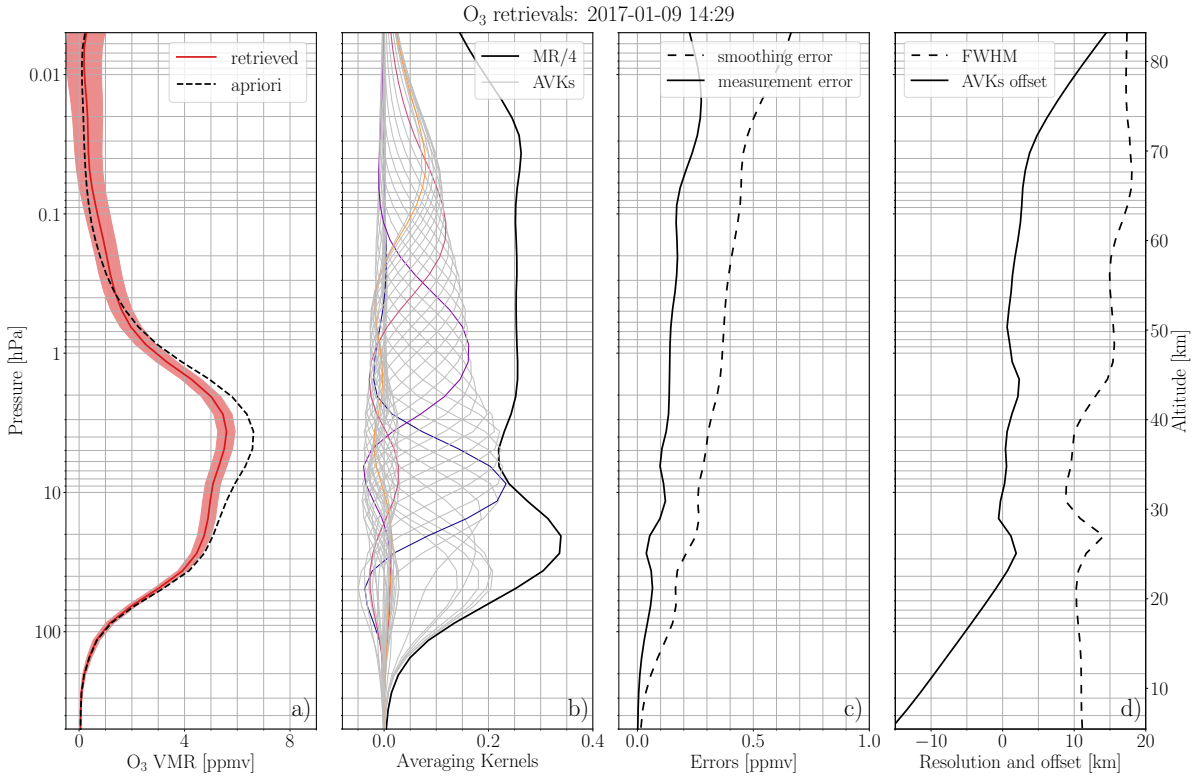

(II) Retrieved ozone profiles and diagnostic quantities (see text for details).

FIGURE 3.4: Example of hourly ozone retrievals from GROMOS.

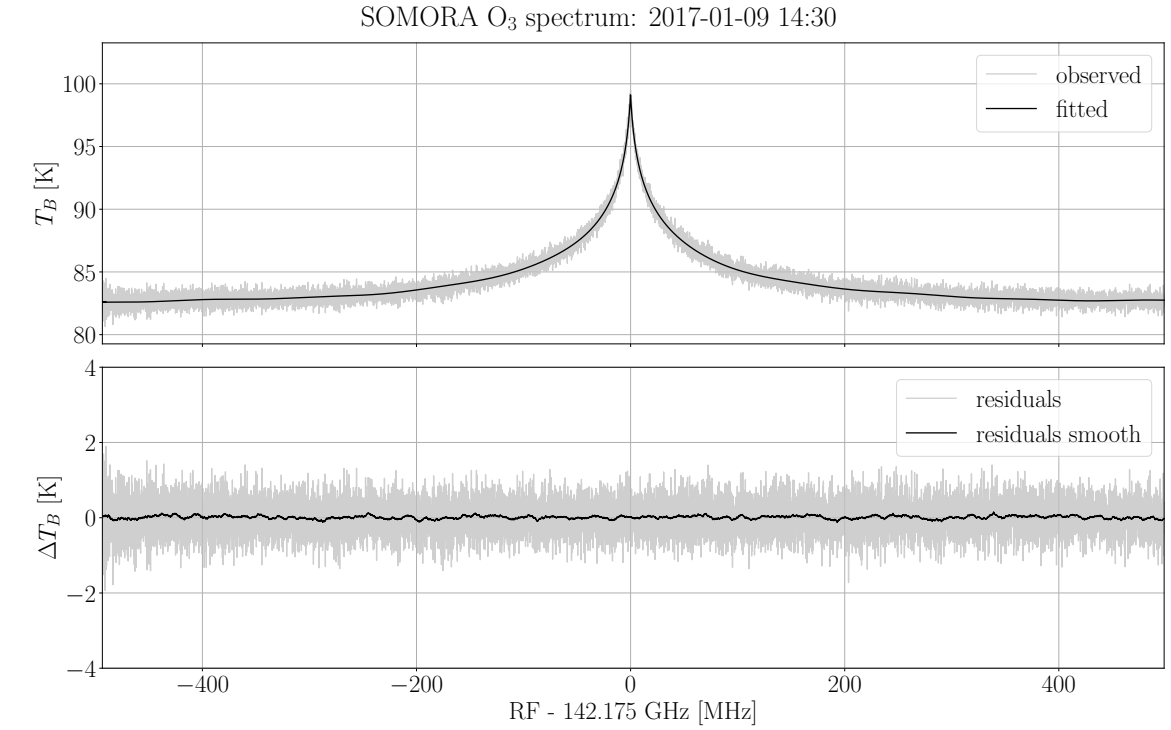

(I) Measured and fitted ozone emission spectra.

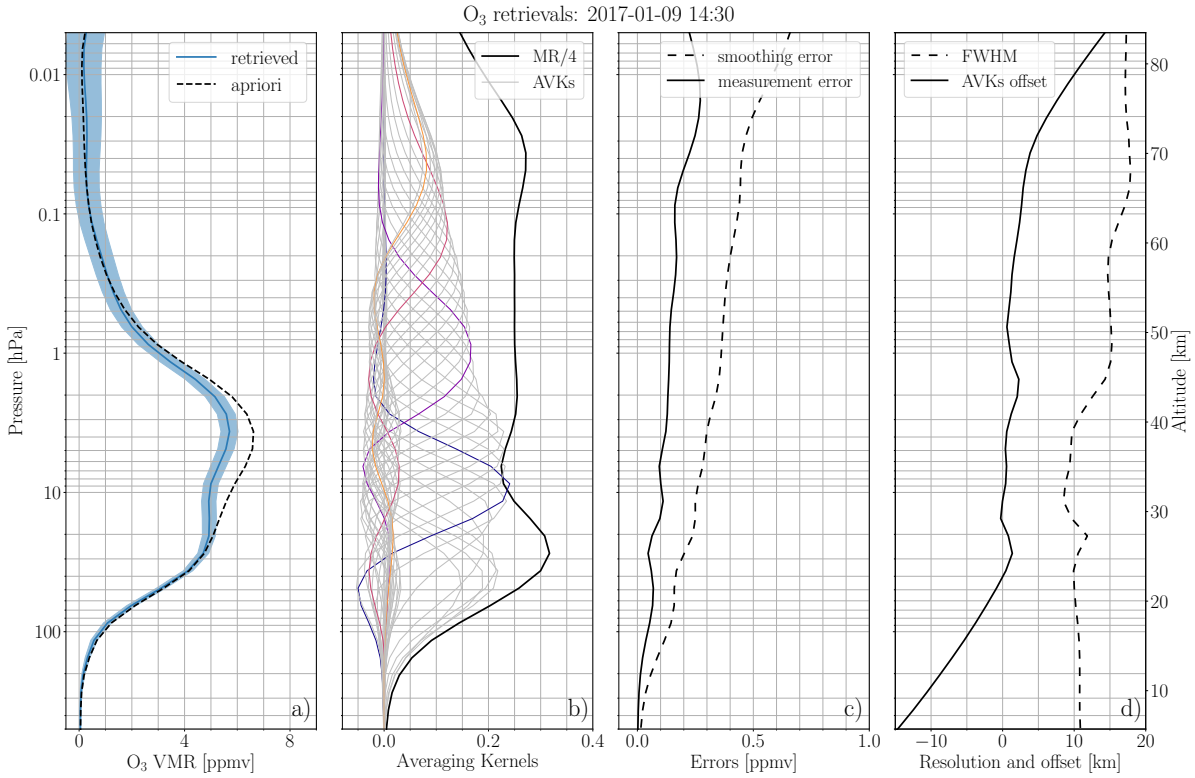

(II) Retrieved ozone profiles and diagnostic quantities (see text for details).

FIGURE 3.5: Example of hourly ozone retrievals from SOMORA.

has been used extensively for ozone profile validation globally and against many other observing systems (e.g., Boyd et al., 2007; Livesey et al., 2008; Hubert et al., 2016).

MLS is a passive microwave radiometer observing the ozone emission line around 240 GHz in a limb sounding geometry. It follows a sun-synchronous orbit and overpasses Switzerland twice a day around 02:20 and 13:10 LST. In my work I have used the latest level 2 ozone retrievals (v5) and the recommended data screening from Livesey et al., 2022. It results in ozone VMR profiles between 261 to 0.001 hPa with a typical vertical resolution ranging from ~ 2.5 km in the lower stratosphere increasing to ~ 5.5 km at the mesopause with an accuracy of $5-10$ % in the stratosphere increasing up to 100 % at 0.01 hPa. Its horizontal resolution ranges between 300 and 500 km.

For the validation of GROMOS and SOMORA time series, I use all co-located MLS observations on the period 2009-2022. As spatial co-location criteria, I use $\pm 3.6°$ in latitude and $\pm 10.5°$ in longitude from Bern, an area corresponding to Central Europe. As temporal criteria, I keep all profiles measured within a 3-hour time window around the MLS overpass time. Then, I keep only the time windows where both MLS and the MWRs have co-located profiles with sufficient data quality. As the vertical resolution of the radiometers is quite coarse (~ 10 km up to 3 hPa and ~ 15 km above) compared to the vertical resolution from the MLS measurements, the higher resolved MLS profiles are convolved with each radiometer's AVKs for the comparisons using Eq. 2.27.

3.3.2 SBUV

In addition to MLS, I also use the latest release of the Merged Ozone Dataset (MOD) derived from the Solar Backscatter Ultraviolet Radiometer (SBUV, retrievals v8.7, Frith et al., 2020; Ziemke et al., 2021). This dataset provides daily overpasses over many ground-based ozone measurement stations, including Payerne in Switzerland which I used as the reference for the comparisons with GROMOS and SOMORA. It provides stratospheric ozone VMR profiles from 50 to 0.5 hPa merged according to the new MOD v2, Release 1 derived from SBUV (and SBUV/2) and adjusted for the diurnal cycles to an equivalent local measurement time of 1:30 PM. The vertical resolution from the SBUV retrievals is $\sim 6-7$ km in the middle and upper stratosphere (McPeters et al., 2013; Bhartia et al., 2013) which is closer to the vertical resolution of GROMOS and SOMORA in this region. For this reason, contrary to MLS, I did not apply any AVK smoothing to the SBUV measurements.

4 | Harmonized ozone retrievals for GROMOS and SOMORA

This chapter presents the main outcome of the harmonization project between GROMOS and SOMORA. It summarises the main results obtained from the project, which were peer-reviewed and published in Sauvageat et al., 2022b. It focuses on the post 2009 period, where the two instruments used the Acqiris AC240 digital spectrometer as back-end. The publication presents the harmonization of the calibration and retrieval algorithms from GROMOS and SOMORA and the resulting time series for the period 2009-2022. It also characterizes the new retrievals and associated uncertainties. Note that at the time of publication, the spectral bias of the AC240 (Sauvageat et al., 2020) was not fully assessed yet and therefore, no correction has been applied to the time series used in the following publication. The influence of the spectrometer bias on the results presented here is discussed in Section 7.2.1

A careful cross-comparison of the two instruments is performed and validation is provided against two satellite datasets, the MLS aboard the Aura satellite and the SBUV MOD. In addition, the new time series are compared with the series from the previous version of the calibration and retrieval algorithms to assess the improvement from the harmonized data processing.

Overall, a good agreement is found between GROMOS and SOMORA on the period 2009-2022, with seasonal ozone relative differences lower than 10% and good correlation ($R > 0.7$) between the two time series in most of the middle atmosphere ($\sim$ 25 to 70 km). An exception occurs during summertime, where the correlation is found to be lower than for the other seasons. A potential reason for the summer bias on SOMORA could be a seasonal change in the instrumental baselines, not considered in the retrievals but it is still to be confirmed. Compared to the previous data processing, the agreement between GROMOS and SOMORA has significantly improved, especially above 60 km. The mean relative ozone difference against satellite measurements above Switzerland are within 10% between $\sim$ 20 and 60 km. In summer, we observed a systematic bias from SOMORA against MLS which is consistent with the lower correlation found in summer between GROMOS and SOMORA.

4.1 Publication: Harmonized retrievals of Swiss ozone radiometers

Overall, the harmonization project of GROMOS and SOMORA have resulted in multiple outputs referenced below. First, two internal research reports detailing respectively the new calibration and retrieval routines written for the two instruments can be found on the Bern Open Repository and Information System (BORIS). Second, the new harmonized datasets from GROMOS and SOMORA can be found on BORIS-portal[1] along with a detailed documentation of the two time series for the period 2009-2021. The harmonized calibration and retrieval routines have been published and are freely available. The latest version is available on GitHub[2] whereas the release corresponding to the published article is archived at Sauvageat, 2022a. In addition to the main

[1] https://boris-portal.unibe.ch/cris/project/pj00023
[2] https://github.com/leric2/GROMORA-harmo

code, many useful functions to deal with the level 2 data can be found on GitHub[3] and even more on the Git server of the IAP (accessible on request to the sysadmin).

This project was first presented at the 2021 Quadrennial Ozone Symposium (QOS), then the description and results of the harmonization were peer-reviewed and published in *Atmospheric Measurement Techniques*.

Calibration report:

Sauvageat, E. (2021). *Calibration routine for ground-based passive microwave radiometer: a user guide*. Research Report No. 2021-01-MW. Institute of Applied Physics, University of Bern. DOI: 10.48350/164418.

Retrieval report:

Sauvageat, E. (2022b). *Harmonized ozone profile retrievals from GROMOS and SOMORA*. Research Report No. 2022-01-MW. Institute of Applied Physics, University of Bern. DOI: 10.48350/170121.

Code:

Sauvageat, E. (2022a). *GROMORA-harmo: calibration and retrieval code for Swiss ozone microwave radiometers*. Version 2. DOI: 10.5281/zenodo.6799357.

Citation of the peer-reviewed publication:

Sauvageat, E., Maillard Barras, E., Hocke, K., Haefele, A., and Murk, A. (2022b). "Harmonized retrieval of middle atmospheric ozone from two microwave radiometers in Switzerland". In: *Atmospheric Measurement Techniques* 15.21, pp. 6395–6417. DOI: 10.5194/amt-15-6395-2022.

[3] https://github.com/leric2/gromora_analysis

Atmos. Meas. Tech., 15, 6395–6417, 2022
https://doi.org/10.5194/amt-15-6395-2022

Atmospheric Measurement Techniques
Open Access
EGU

Harmonized retrieval of middle atmospheric ozone from two microwave radiometers in Switzerland

Eric Sauvageat[1,2], **Eliane Maillard Barras**[3], **Klemens Hocke**[1,2], **Alexander Haefele**[3], **and Axel Murk**[1,2]

[1]Institute of Applied Physics, University of Bern, Bern, Switzerland
[2]Oeschger Centre for Climate Change Research, University of Bern, Bern, Switzerland
[3]Federal Office of Meteorology and Climatology, MeteoSwiss, Payerne, Switzerland

Correspondence: Eric Sauvageat (eric.sauvageat@unibe.ch)

Received: 13 July 2022 – Discussion started: 15 July 2022
Revised: 28 September 2022 – Accepted: 5 October 2022 – Published: 8 November 2022

Abstract. We present new harmonized ozone time series from two ground-based microwave radiometers in Switzerland: GROMOS and SOMORA. Both instruments have measured hourly ozone profiles in the middle atmosphere (20–75 km) for more than 2 decades. As inconsistencies in long-term trends derived from these two instruments were detected, a harmonization project was initiated in 2019. The goal was to fully harmonize the data processing of GROMOS and SOMORA to better understand and possibly reduce the discrepancies between the two data records. The harmonization has been completed for the data from 2009 until 2022 and has been successful at reducing the differences observed between the two time series. It also explains the remaining differences between the two instruments and flags their respective anomalous measurement periods in order to adapt their consideration for future trend computations.

We describe the harmonization and the resulting time series in detail. We also highlight the improvements in the ozone retrievals with respect to the previous data processing. In the stratosphere and lower mesosphere, the seasonal ozone relative differences between the two instruments are now within 10 % and show good correlation ($R > 0.7$) (except during summertime). We also perform a comparison of these new data series against measurements from the Microwave Limb Sounder (MLS) and Solar Backscatter Ultraviolet Radiometer (SBUV) satellite instruments over Switzerland. Seasonal mean differences with MLS and SBUV are within 10 % in the stratosphere and lower mesosphere up to 60 km and increase rapidly above that point.

1 Introduction

Ozone is a trace gas of great importance in the earth's atmosphere. It shields the surface of our planet from most of the sun's harmful ultraviolet radiation by absorbing it in the stratosphere (the "ozone layer") and consequently allowing life out of water. In the second half of the 20th century, it was suggested that anthropogenic emissions of certain chemical compounds, the commonly called ozone-depleting substances (ODSs), were threatening this protective layer (Molina and Rowland, 1974; Crutzen, 1970; Farman et al., 1985; Solomon et al., 1986). As a result, severe depletion of the ozone layer was observed in the springtime over the Antarctic and led to the banning of ODS emissions formalized in the Montreal Protocol in 1987.

Since then, there has been an increased interest in the monitoring of ozone in the middle atmosphere to assess the effect of the Montreal Protocol. The reduction of ODS emissions has led to a decrease in total chlorine concentration since 1997, whereas the increasing greenhouse gases concentration is cooling the upper stratosphere (Anderson et al., 2000; Solomon et al., 2006). From the existing knowledge in middle-atmospheric chemistry, the combination of both factors should lead to an observable recovery or even super recovery of ozone concentration at these altitudes (Eyring et al., 2010). In fact, over the polar regions, the stratospheric ozone concentrations have already begun their recovery towards pre-industrial levels (Solomon et al., 2016). Over the mid-latitudes, the situation is less obvious, and ozone recovery seems to differ depending on the altitude and the geographical area of interest (Braesicke et al., 2018; Petropavlovskikh et al., 2019; Tummon et al., 2015). In the

Published by Copernicus Publications on behalf of the European Geosciences Union.

upper stratosphere, the latest observations agree on a positive trend of ozone concentration despite a high variability in its significance and magnitude (Fahey et al., 2018; Steinbrecht et al., 2017; Bernet et al., 2019; Godin-Beekmann et al., 2022). In contrast, no clear indication of ozone recovery has been reported yet in the lower stratosphere and some observational evidence of further decline in this region were even reported (Ball et al., 2018). In the context of climate change, there also remain many unknowns regarding the influence of long-term dynamic and composition changes on middle-atmospheric ozone trends depending on the region (von der Gathen et al., 2021). In regards to these uncertainties, there is still a high need for accurate and long-term time series in the research field.

Microwave ground-based radiometers (MWRs) provide continuous, all-weather measurements of ozone in the middle atmosphere and are therefore well suited to estimate long-term trends and cross-validate satellite measurements (Hocke et al., 2007). Compared to other ground-based measurement techniques, they are able to retrieve ozone profiles from the stratosphere well into the mesosphere with a high temporal resolution but at the cost of a quite low vertical resolution.

In Switzerland, two ozone MWRs have operated for more than 20 years in the vicinity of each other (ca. 40 km): the GROund-based Millimeter-wave Ozone Spectrometer (GROMOS) in Bern and the Stratospheric Ozone MOnitoring RAdiometer (SOMORA) in Payerne (Fig. 1). They operate in the frame of the Network for the Detection of Atmospheric Composition Change (NDACC) (De Mazière et al., 2018). Such long-term time series of two ozone MWRs combined in such geographic proximity is unique worldwide and therefore offers the opportunity for extensive cross-validations. It also allows for more thorough investigation of measurement uncertainties, possible instrumental failures, and calibration and retrieval errors.

During the first phase of the activity "Long-term Ozone Trends and Uncertainties in the Stratosphere" (LOTUS), inconsistencies were found in ozone trend estimates from these two radiometers (Petropavlovskikh et al., 2019). In addition, Bernet et al. (2019) identified some anomalous periods in the Bern time series and highlighted the need to account for these anomalies to compute more accurate trends. However, Bernet et al. (2019) did not investigate the reasons for such anomalies, and the differences between these two time series remained unexplained. Due to their geographic proximity and similar observation geometry, the differences are too big to be geophysical. The data processing, however, was quite different between the instruments, and therefore it was decided to reprocess both time series with new and harmonized algorithms. A harmonization project was initiated jointly by the operators of these two instruments in 2019 with the goal to better understand their differences.

We present and validate here the new harmonized time series for GROMOS and SOMORA focusing on the time period from the month of September 2009 until December

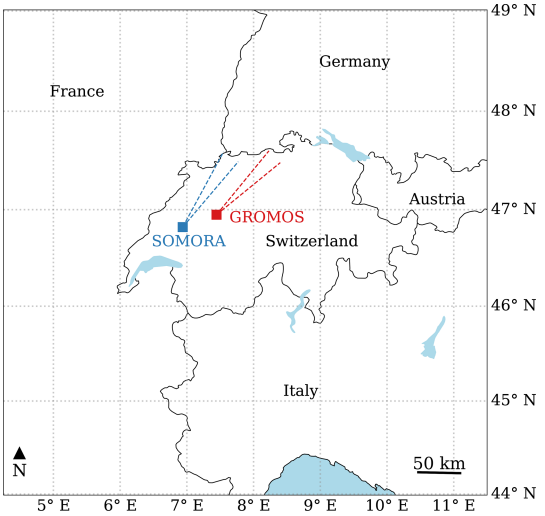

Figure 1. Location of GROMOS and SOMORA, with their approximate viewing directions.

2021. We present the harmonization process applied to the data processing of the two radiometers, including a short description of the new calibration and retrieval routines. We also show the improvements resulting from this harmonization by comparing the new series with their previous versions. As a validation, we performed a cross-comparison between the two instruments and compared them against satellite dataset, namely from the Microwave Limb Sounder (MLS) and the Solar Backscatter Ultraviolet Radiometer (SBUV).

A detailed description of the calibration and retrievals routines has been published in the form of two research reports available on the publication database of the University of Bern (Sauvageat, 2021, 2022a), and a full documentation of the time series is available together with the data.

This paper is organized as follows. Section 2 presents the instruments, highlighting their similarities and differences. Section 3 presents the harmonization procedure applied to the calibration and retrieval routines. Section 4 presents the new harmonized ozone time series, whereas Sect. 5 presents comparisons and cross-validations against satellite measurements. Section 6 summarizes the main conclusions and gives an outlook.

2 Ozone microwave radiometry in Switzerland

Passive microwave radiometry uses the electromagnetic radiation emitted and transmitted in the microwave frequency region to derive geophysical quantities of interest. It makes this technique suitable for both surface observation of the earth from space and sounding of atmospheric trace gases,

temperature or winds from satellites or ground-based instruments. Unlike other techniques, MWRs do not require UV/VIS emitting sources (e.g. sun or stars) and are able to measure during day and night. In addition, the pressure broadening effect at microwave frequencies enables the retrieval of vertical profiles of temperature, winds and abundances (e.g. Parrish et al., 1988; Connor et al., 1994; Rüfenacht et al., 2012; Krochin et al., 2022).

Ozone possesses many rotational transition lines in the microwave region. Its emission lines at 110.836 and 142.175 GHz are most often used for ground-based observations because of their line intensity and the limited effect of water vapour absorption at these frequencies.

GROMOS and SOMORA have been designed and built at the Institute of Applied Physics (IAP) at the University of Bern with quite similar components (Calisesi, 2003; Peter, 1997). They observe the ozone emission line around 142 GHz to retrieve hourly ozone profiles in the stratosphere and lower mesosphere ($\sim$ 20 to 75 km) using the optimal estimation method. GROMOS has been operated by IAP in Bern since 1994, and SOMORA has been operated by the Federal Office of Meteorology and Climatology (MeteoSwiss) in Payerne since 2000 (see locations given in Fig. 1). Both instruments are located on the Swiss Plateau, approximately 40 km from each other, where they experience similar atmospheric conditions. This can be seen by looking at the seasonal distribution of tropospheric opacities at the two sites shown in Fig. A1. The main characteristics of the two instruments are summarized in Table 1.

2.1 Spectrometers

The spectrometer is a key component of any MWR and can significantly influence its retrieval capabilities. Since 2009, both instruments use the same spectrometer, namely the Acqiris AC240 which is a digital fast Fourier transform (FFT) spectrometer (Benz et al., 2005; Muller et al., 2009). On SOMORA, it replaced an acousto-optical spectrometer in September 2009, whereas on GROMOS it replaced discrete filter banks in July 2009. In both cases, the time series were homogenized using an overlap period of roughly 2 years, and the pre-2009 time series were corrected with respect to the FFT spectrometer time series (e.g. Moreira et al., 2015; Maillard Barras et al., 2020). Whereas both instruments use the same digitizer with the same bandwidth of 1 GHz, it should be noted that the frequency resolution is 2 times higher for GROMOS than for SOMORA because GROMOS uses an inphase quadrature (IQ) down-converter and digital sideband separation, which results in twice the number of channels (Murk et al., 2009). As a result, GROMOS could be more sensitive to ozone at higher altitudes. However, we do not see any significant difference in vertical sensitivity compared to SOMORA, possibly because of the high receiver noise, which could act as a limiting factor for extending the altitude coverage of the two instruments.

The AC240 is still being used in many MWRs; however, it is ageing and has recently been shown to produce a spectral bias compared to more recent spectrometers, most likely impacting ozone retrievals as well (Sauvageat et al., 2021). In this contribution, we only focus on the period where both instruments use the AC240, namely from September 2009 to end of 2021. Therefore, both time series should be similarly impacted by the spectrometric bias and thus should not affect the results of the comparisons between GROMOS and SOMORA. This might, however, influence the comparisons against the satellite observations, but there is unfortunately no way to confirm the amplitude of the bias on the ozone profiles at the moment.

3 Harmonization process

Discrepancies were identified between the GROMOS and SOMORA data series and trends (Bernet et al., 2019; Petropavlovskikh et al., 2019; Maillard Barras et al., 2020) for which no explanations could be found. To better understand these discrepancies, it was decided to perform a full harmonization of the data processing of GROMOS and SOMORA, from the raw data (level 0) to the ozone profiles (level 2). The idea was to harmonize the whole processing chain, including the inputs and outputs of the routine, while keeping the two data series fully independent.

The harmonization project can be separated into two distinct parts: the calibration of the radiometric data (level 0 to 1) and the retrievals of ozone profiles (level 1 to 2). Section 3.1 will briefly describe the new calibration and integration routines (see Sauvageat, 2021 for details), whereas Sect. 3.2 will describe the retrievals of ozone profiles from the calibrated spectra.

3.1 Calibration

GROMOS and SOMORA are both total power radiometers with superheterodyne receivers. They measure the atmospheric ozone emission line around 142.175 GHz and use the heterodyne principle to down convert the incoming radiation (RF signal) to an intermediate frequency (IF) by mixing with a local oscillator frequency (LO) which allows for easier signal processing.

The operation of microwave radiometers requires continuous calibration because their receivers are never perfectly stable (e.g. Ulaby and Long, 2014, chap. 7). Both instruments use a so-called hot–cold calibration scheme: using a rotating mirror fixed on a path length modulator, they are continuously switching between the atmospheric observation, a hot and a cold calibration target. In both instruments, a heated black-body kept at a constant temperature ($T_{\mathrm{hot}} \approx 310$ K) is used as hot load, whereas liquid nitrogen (LN2) observation is used as cold load. Both instruments use a Martin–Pupplet interferometer (MPI) to suppress the contribution of the un-

Table 1. GROMOS and SOMORA microwave radiometers.

	GROMOS	SOMORA
Location	Bern	Payerne
Latitude	46.95° N	46.82° N
Longitude	7.44° E	6.94° E
Altitude	560 m	491 m
Azimuth angle	45°	34°
Elevation angle	40°	39°
Observation frequency	142.175 GHz	142.175 GHz
Spectrometer	Acqiris AC240	Acqiris AC240
Bandwidth	1 GHz (32 768 channels)	1 GHz (16 384 channels)
Intermediate frequency	3.7 GHz	7.1 GHz
Frequency resolution	30.52 kHz	61.04 kHz
T_{rec}	$\sim$ 2750 K	$\sim$ 2550 K

desired sideband. The pathlength modulator is used to mitigate the standing waves between the receiver and the calibration targets, which are otherwise causing systematic baseline errors on the calibrated spectra. In parallel to the hot–cold calibration scheme, the instruments also perform tipping curve calibration (Ingold et al., 1998) as cross-validation for the LN2 calibration. Assuming linear transfer characteristics, the atmospheric spectral radiance can then be determined and further converted to brightness temperature using Planck's law (e.g. Ulaby and Long, 2014, chap. 6).

Despite similar designs and raw data contents, the previous calibration routines for GROMOS and SOMORA were different. Therefore, a new routine was designed to harmonize the calibration between the two instruments. The calibration essentially converts the raw spectrometer measurements to radiance intensity and integrates them together on a chosen integration time. For this new routine, the calibration results in two different data levels, namely the calibrated spectrum (level 1a) and the integrated spectrum (level 1b).

Harmonized quality control was introduced in order to identify spurious instrumental signals. It flags the most common technical problems at level 1a (e.g. noise temperature jumps, LN2 refills, LO frequency shifts) and combines them into a single instrumental flag value for level 1b (Sauvageat, 2021).

Considering instrumental issues and technical interruptions for maintenance (e.g. for LN2 refilling or instrument repairs), GROMOS and SOMORA provided good-quality hourly spectra for 87 % and 89 % of the measurements performed between 2009 and 2021, respectively. This results in more than 80 000 h of comparable retrieved ozone profiles.

3.2 Retrieval setup

In the microwave frequency range, the pressure-broadening effect of atmospheric emission lines is used to retrieve information on the atmospheric constituent profile from the calibrated microwave emission spectra. This so-called retrieval is a well-validated technique that has been successfully applied to temperature; wind; and many trace gases like O_3, CO, or H_2O (Janssen, 1993, chap. 7). Among the different retrieval techniques, we selected the optimal estimation method (OEM) following the formalism described by Rodgers (2000). This statistical method extracts the best estimate of an atmospheric profile from a set of measurements with noise, a priori information and a forward model. In addition, the OEM enables the characterization of the error budget of the retrievals (Fig. 3). In the following, we will briefly present and discuss the new harmonized retrieval setup used for GROMOS and SOMORA. More information on this setup is available in Sauvageat (2022a). For detailed information on the OEM or its application to ozone profiling instruments, the reader is redirected to Parrish et al. (1992) or Tsou et al. (1995).

3.2.1 Forward model

In the case of ground-based microwave radiometry, the forward model (FM) describes the radiative transfer physics between trace gas emissions and the instrument's receiver. We used the Atmospheric Radiative Transfer Simulator 2.4 (ARTS), an open-source software with a special focus on microwave radiative transfer simulations (Eriksson et al., 2011; Buehler et al., 2018). In addition, it offers a fully integrated OEM retrieval environment and includes many tools to help simulate and retrieve the sensor's influence on the radiometric measurements (Eriksson et al., 2006).

ARTS offers many possibilities to define the atmospheric state, a priori data and simulation grids. We use one-dimensional pressure and temperature profiles from the European Centre for Medium-Range Weather Forecasts (ECMWF) daily operational analysis (6 h time and 1.125° spatial resolution). This dataset is limited to approximately 70 km altitude, and we therefore extend it using the COSPAR International Reference Atmosphere (CIRA-86) climatology at upper altitudes (Chandra et al., 1990). The frequency

Table 2. Main parameters used in GROMOS and SOMORA retrievals.

Forward model	ARTS
Species	O_3, H_2O, O_2 and N_2
Spectroscopy	Perrin (JPL and HITRAN)
Atmospheric state	1D ECMWF and CIRA 86
O_3 a priori	WACCM
H_2O a priori	ECMWF
FM grid	$\sim$ 1–112 km, 2 km resolution
Retrieval grid	$\sim$ 1–95 km, 2 km resolution

grids have been defined to cover the range of GROMOS and SOMORA spectrometers with a refined frequency resolution around the ozone line: it matches the spectrometer resolution at the line centre to optimize retrievals at higher altitudes, whereas the spectral resolution is coarser on the line wings to limit computation time.

As atmospheric species, we use ozone, water vapour, oxygen and nitrogen. For ozone, we use the spectroscopic database from Perrin et al. (2005), which is provided with ARTS 2.4 and is derived from the HITRAN and JPL spectroscopic databases. For water vapour, oxygen and nitrogen, we use the parameterizations provided within ARTS (see Buehler et al., 2005). A summary of the main retrieval parameters used for GROMOS and SOMORA can be found in Table 2, and more details are provided in Sauvageat (2022a).

3.2.2 Ozone retrieval

The main retrieval quantity is hourly ozone volume mixing ratio (VMR) from the stratosphere to the lower mesosphere, i.e. between $\sim$ 100 and 0.01 hPa. The a priori are monthly ozone profiles extracted from free-running simulations of the Whole Atmosphere Community Climate Model (WACCM) as described in Schanz et al. (2014). Further, depending on the local solar time, we either use a daytime or nighttime a priori ozone profile. The a priori covariance matrix for ozone varies with atmospheric pressure in order to optimize the information from the measurements in the stratosphere and lower mesosphere. It includes exponentially decreasing covariances between pressure levels to reflect the vertical coupling of the atmosphere.

3.2.3 Sensor and noise

The accuracy of the retrievals can be improved by taking the systematic characteristics of the instrument into account. ARTS has dedicated built-in functions that can model the influence of the most relevant components on the atmospheric observations (Eriksson et al., 2006). For GROMOS and SOMORA, we included the effect of the FFT spectrometer channel response $\left(\left|\frac{\sin(x)}{x}\right|^2\right)$ and the effect of the sideband ratio (Murk and Kotiranta, 2019).

The measurement noise is an important quantity for OEM retrievals because it defines, together with the a priori covariance, the information that can be extracted from the measurement at each pressure level. The noise covariance matrix is computed independently for each instrument and each retrieval based on the noise level observed on the integrated spectrum and is considered to be uncorrelated between the different channels in a similar way to the method explained in Krochin et al. (2022). It is slightly higher for GROMOS ($\approx$ 0.7 K) than SOMORA ($\approx$ 0.5 K) because GROMOS has a higher receiver noise temperature and a higher frequency resolution.

3.2.4 Additional retrieval quantities

There are other sensors or external influences that are difficult to estimate and correct during the calibration process or to simulate accurately for each spectrum. This is the case for the instrumental baselines and the tropospheric absorption. The instrumental baselines are a modulation of the atmospheric spectrum due to the observing system. They can arise during the mixing process and the sideband filtering or can be due to undesired reflections, typically when observing the calibration targets. In ARTS, it is possible to consider them as unknown and add them as additional retrieval quantities.

Around the 142 GHz ozone line, the tropospheric water continuum contributes significantly to the observed spectra and has to be considered during the inversion process. One simple correction method is the so-called tropospheric correction (Ingold et al., 1998), but it is certainly a better solution – also in view of assessment of the error propagation – to include the tropospheric water vapour as a retrieval quantity within ARTS, as has been done previously for such retrievals (e.g. in Palm et al., 2010). A frequency shift was also retrieved for each spectrum because the local oscillators of both GROMOS and SOMORA are not perfectly stable and even a slight shift of the reference frequency can bias the ozone profile retrievals.

Despite mitigation of instrumental baselines using different techniques (e.g. mirror wobbling, non-perpendicular aspect of cold load), it is often necessary to retrieve some instrumental baselines as well (Palm et al., 2010). In the case of GROMOS and SOMORA, we include a second-order polynomial and different sinusoidal baselines. In order to avoid the degradation of the retrievals with the addition of too many sinusoidal baselines, we first processed the full time series without any sinusoidal baselines and used the residuals to compute the main sinusoidal baseline periods for each instrument. We observed that the sinusoidal baseline periods remain similar on timescales of months to years, so in practice only a few period changes were applied during the full extent of the time series for each instrument (see Sauvageat, 2022a, for details).

3.2.5 Retrieval results

For each retrieval quantity, the OEM returns the statistical best estimates of the results, and ARTS returns the corresponding fitted atmospheric spectrum, which can be compared against the MWR observation to evaluate the goodness of the fit. Figure 2 shows examples of hourly integrated spectra from GROMOS and SOMORA together with their fitted measurement spectra.

Figure 3 shows the corresponding ozone retrievals and main diagnostic quantities for the spectra shown in Fig. 2. It includes the averaging kernels (AVKs), which are a measure of the sensitivity of the retrieval to the true ozone profile at each pressure level. The sum of the AVKs at each level defines the measurement response (MR). It is an indication of the measurement contribution to the retrieved profile, whereas the remaining information comes from the a priori. In microwave remote sensing, a MR of 80 % is often used to define the lower and upper boundaries of the retrievals in order to limit the influence of the a priori on the results. Also included as diagnostic quantities are the smoothing and measurement errors computed by the OEM as defined by Rodgers (2000). The smoothing error is a consequence of the limited resolution of the instrument, whereas the measurement error arises from the noisy nature of the observations. Finally, we show the full width at half maximum (FWHM) of the AVKs at each level and the altitude offset (in kilometres) between the AVK maximum and its corresponding altitude. Both together give an indication on the altitude resolution and the vertical offset between the true and retrieved profiles.

3.3 Uncertainty budget

The retrieval errors presented above do not include systematic errors that can arise during the calibration or the retrievals. It is cumbersome to estimate all possible errors on such complex measurement setup and therefore, we decided to perform a sensitivity analysis on the most important error sources using two reference time periods with low ($\tau \approx 0.15$) and high ($\tau \approx 1.3$) atmospheric opacities. The uncertainties considered in our study are listed in Table 3 as well as the perturbations used for the sensitivity analysis. These were determined in different ways for each error source, deriving it either from measurement (e.g. T_{cold}, sideband ratio, window transmittance) or empirical values (e.g. pointing, spectroscopy).

The uncertainty budget for GROMOS and SOMORA is presented in Fig. 4 in the case of low tropospheric opacities. The high-opacity cases for both instruments can be seen in Appendix B (Fig. B1).

In general, the sensitivity of GROMOS and SOMORA to the different perturbations is very similar. A notable exception is the higher sensitivity of GROMOS to the sideband path length, which is a consequence of its lower intermediate frequency. For both instruments, the total uncertainty is dominated by systematic errors below 2 hPa, whereas the measurement noise becomes quickly dominant above this point. In relative terms, the uncertainty is approximately 9 %–10 % for GROMOS and 7 %–8 % for SOMORA up to the stratopause and then increases significantly in the mesosphere.

In the case of high tropospheric opacity, the ozone emission line gets more attenuated by the tropospheric water vapour absorption. The AVKs get degraded, reducing the sensitivity of the retrievals and leading to higher uncertainties than at lower opacities. As can be seen in Fig. B1, the atmospheric temperature profile becomes the dominant contribution to the uncertainties below 1 hPa at higher opacity. This is likely due to the increased importance of the water vapour continuum retrieval, which is itself strongly dependent on tropospheric humidity and temperature. In the higher-opacity case, the total relative uncertainty in the stratosphere is 12 %–15 % for GROMOS and 10 %–12 % for SOMORA. In view of the perturbations and error sources considered in this study, these values compare well with similar ozone radiometers at other locations reported in the literature (e.g. Palm et al., 2010; Kopp et al., 2002).

4 Harmonized ozone time series

Using the new calibration and retrieval routines described previously, we have reprocessed the GROMOS and SOMORA data series for the time where they both use the AC240 spectrometer, i.e. from the end of 2009 until 2021. Figure 5 shows weekly averaged ozone profiles for GROMOS and SOMORA for the decade 2010–2020. It shows the consistency of the measurements and highlights the very few large interruptions happening on both instruments during this period. Most interruptions are due to instrumental issues (e.g. LN2 refilling or LO frequency stability) or atmospheric conditions (e.g. high tropospheric opacity masking the ozone emission line), and they usually last for a few hours at most. The longer interruptions result from cold load issues or hardware changes, which can last for a few days or weeks.

To validate these two data series, we first present a cross-comparison of the GROMOS and SOMORA data series and show the improvement resulting from the reprocessing compared to the previous retrieval version. We then compare both instruments against satellite-based ozone observations from MLS and SBUV above Switzerland.

4.1 Cross-comparison between GROMOS and SOMORA

GROMOS and SOMORA are located close to each other, have similar viewing directions, and experience similar tropospheric conditions during all seasons (Fig. A1). In addition, they have similar altitude range and sensitivity and can

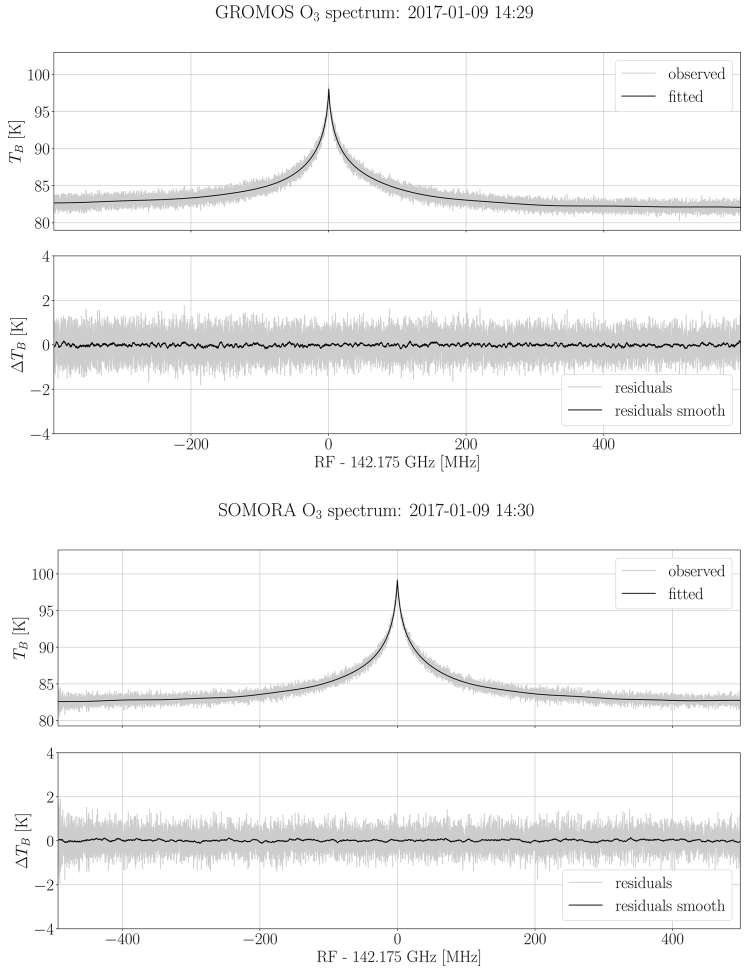

Figure 2. Integrated and fitted spectrum for GROMOS and SOMORA, binned to the same spectral resolution. The lower panels show the residuals, i.e. the differences between the measurement and the fitted spectrum. The smoothed residuals are computed using a running mean over 128 channels.

Table 3. Potential error sources and the perturbations used for the sensitivity analysis.

Pointing	error on the zenith angle	1°
T_{cold}	cold calibration target temperature	2 K
Window transmittance	transmittance of the windows in front of the instrument	3 %
T_{profile}	constant offset in atmospheric temperature profile	5 K
Spectroscopy	error in spectroscopic line intensity	3 %
Sideband ratio	error in MPI path length difference	0.05 mm

therefore be used for direct cross-validation of their time series. The upper panel in Fig. 6 shows the weekly mean relative differences between GROMOS and SOMORA harmonized data series (note that the lower panel of this figure will be discussed in Sect. 4.2). In general, GROMOS and SOMORA agree well in most of the middle atmosphere, with relative differences mostly lower than 10 % in the stratosphere and lower mesosphere (from ∼ 50 to 0.1 hPa), increasing towards lower and higher altitudes. The higher relative differences at lower and higher altitudes are partly explained by the shape of the ozone VMR profile when intensity is at its maximum in the stratosphere. In general, the

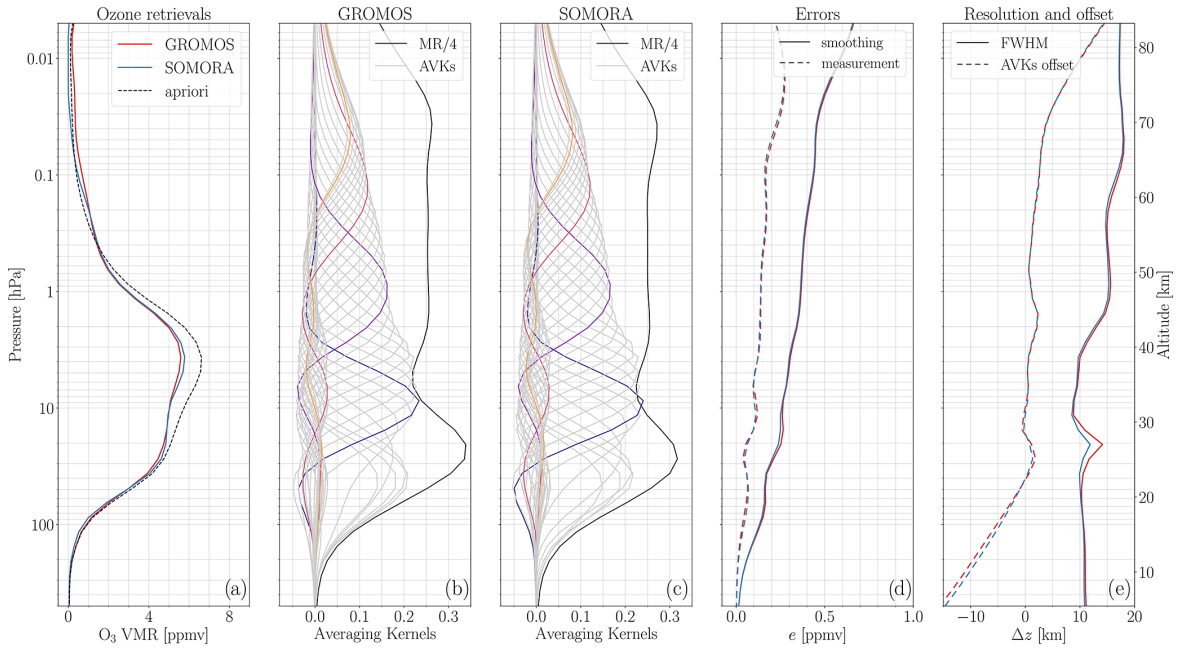

Figure 3. Example of GROMOS and SOMORA hourly ozone retrievals on 9 January 2017 around 14:30 UT with a tropospheric opacity $\tau \approx 0.4$: panel **(a)** shows the a priori and retrieved ozone profiles, panels **(b)** and **(c)** show the GROMOS and SOMORA averaging kernels together with their MR (divided by 4 to fit in the same plots), panel **(d)** shows the smoothing and measurement error, and panel **(e)** shows the full width at half maximum (FWHM) and the offset between the AVKs peak and the actual altitude contribution. All quantities are retrieved on pressure levels, and approximated altitudes are indicated on the right. See the text for more details on each diagnostic quantity.

lower altitudes are also the most impacted by instrumental baselines, which explains the increase in the differences below 50 hPa, whereas at higher altitudes the instrumental noise becomes the dominant factor and the sensitivity of the radiometers decreases quickly. In addition, the diurnal ozone variations typically become much larger in the mesosphere (e.g. around 20 % compared to a few percent in the stratosphere; Haefele et al., 2008).

We also see some oscillatory patterns in the relative differences, some of which can be identified as clear seasonal patterns (e.g. in the lower stratosphere between 2014 and 2017). These seasonal differences are highlighted in Fig. 7, which shows seasonal ozone profile comparisons between GROMOS and SOMORA. The mean seasonal differences between the two instruments are lower than 10 % at all seasons and throughout most of the middle atmosphere and show a negative ozone bias from GROMOS in the upper mesosphere ($p < 0.05$ hPa). In the stratosphere and lower mesosphere, the ozone profiles are well correlated with Pearson's R coefficients mostly above 0.7 at most pressure levels and seasons (Fig. 7). However, this is not the case during summer, where we find significantly lower correlation between GROMOS and SOMORA ozone profiles.

Table 4. Definition of the pressure ranges and corresponding altitudes used in this study.

Region	Pressure range (hPa)	Approximate altitudes (km)
Upper mesosphere	0.1–0.01	∼ 65–80
Lower mesosphere	0.9–0.1	∼ 50–65
Upper stratosphere	5–1	∼ 38–50
Lower stratosphere	50–10	∼ 22–32

Figure 8 shows scatter plots of their differences in three pressure level domains corresponding approximately to the lower stratosphere, the upper stratosphere and the lower mesosphere (see Table 4 for the definitions). It shows the net difference in atmospheric opacity between the winter and the summer and highlights the higher ozone variability during the wintertime. Figure 8 confirms the general good agreement between GROMOS and SOMORA in the middle atmosphere and corroborates the existence of a seasonal bias between the instruments during summertime.

During the summertime, the warmer and wetter troposphere results in a higher opacity. This attenuates the ozone spectral line and thus decreases the retrieval sensitivity dur-

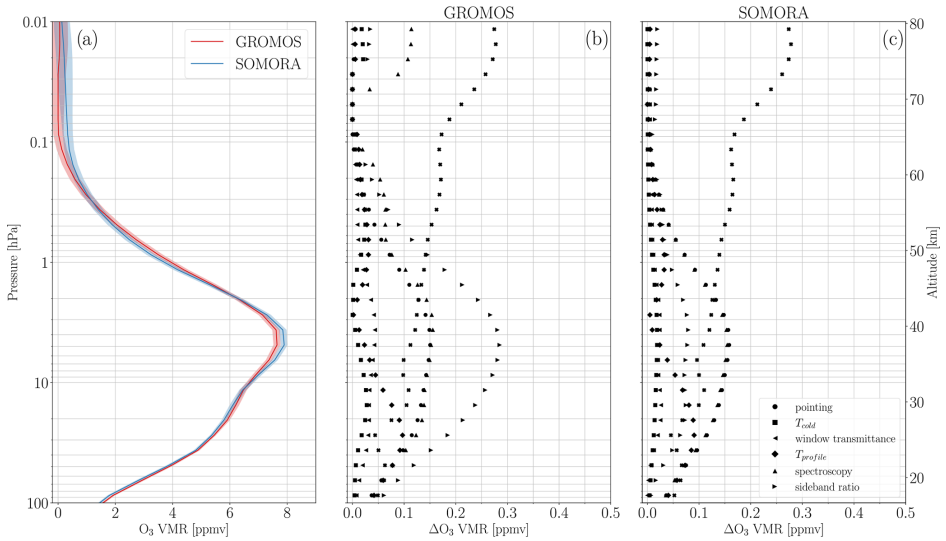

Figure 4. Uncertainty budget for GROMOS and SOMORA in a low-opacity case ($\tau \approx 0.15$). Panel **(a)** shows the reference ozone profile chosen for the sensitivity analysis. Panels **(b)** and **(c)** show the ozone VMR uncertainties arising from the error sources listed in Table 3.

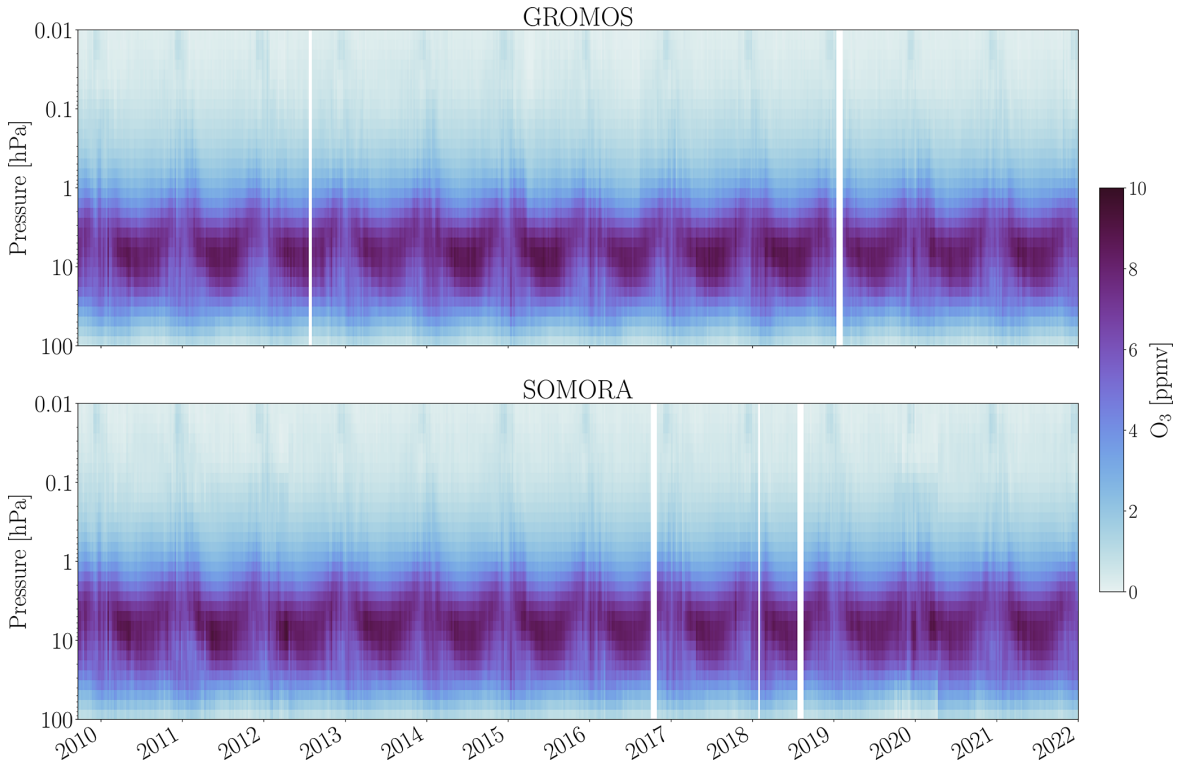

Figure 5. Weekly averaged ozone volume mixing ratio (VMR) profiles for GROMOS and SOMORA.

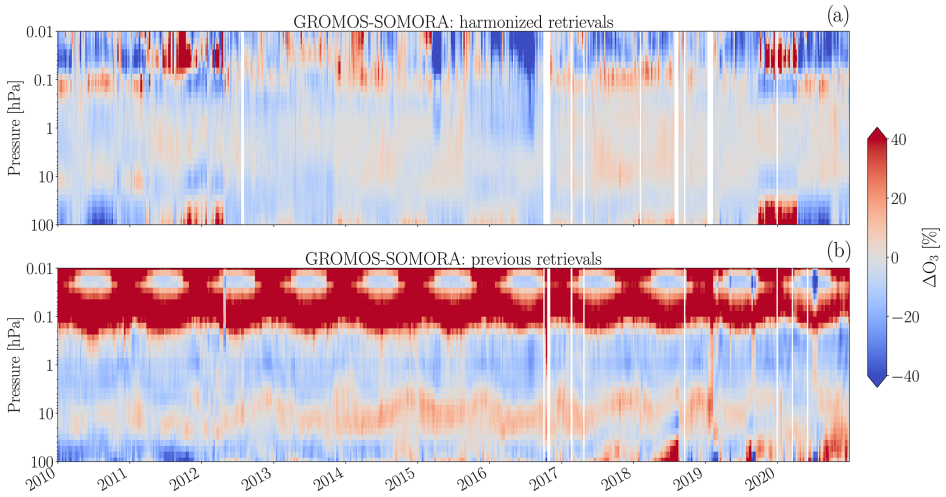

Figure 6. Weekly ozone relative difference between the new **(a)** and previous **(b)** GROMOS and SOMORA series.

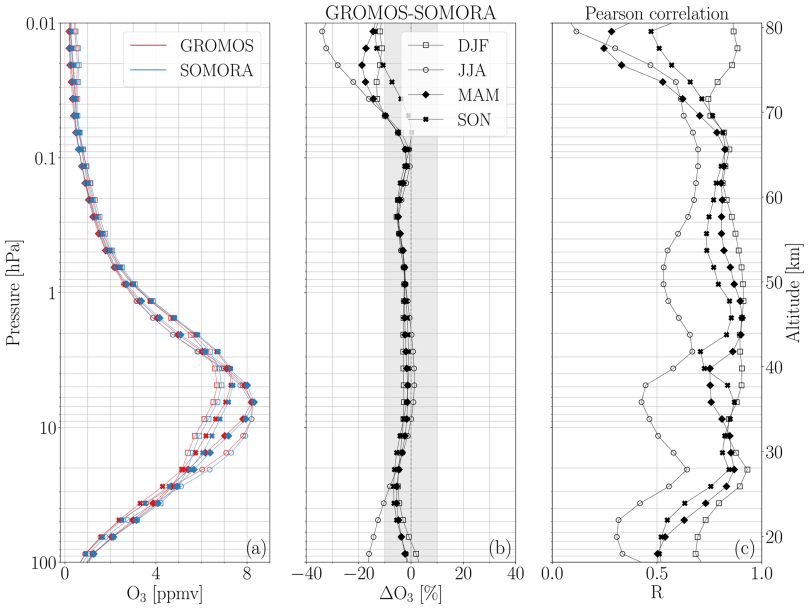

Figure 7. Mean seasonal ozone VMR profiles **(a)** and their mean relative differences **(b)** and correlations **(c)**. The shaded area in panel **(b)** indicates the $\pm 10\,\%$ interval.

ing summer. As discussed in Sect. 3.3, a higher tropospheric opacity also results in larger uncertainties in the retrieved ozone profile. In case of very hot and humid conditions, the troposphere can become optically thick at 142 GHz, which can prevent the retrieval of ozone profiles. It can be seen in Fig. A1, which shows higher tropospheric opacity in summertime than during the other seasons. However, Fig. A1 also shows that the difference in tropospheric opacity at the two sites remains constant, independent of the season. In addition, we investigated the correlations between GROMOS and SOMORA considering only profiles measured at low tropospheric opacity ($\tau \leqslant 1$) and did not see any significant changes in the results. For these reasons, we believe that the summer bias does not result from the higher tropospheric opacities affecting this season.

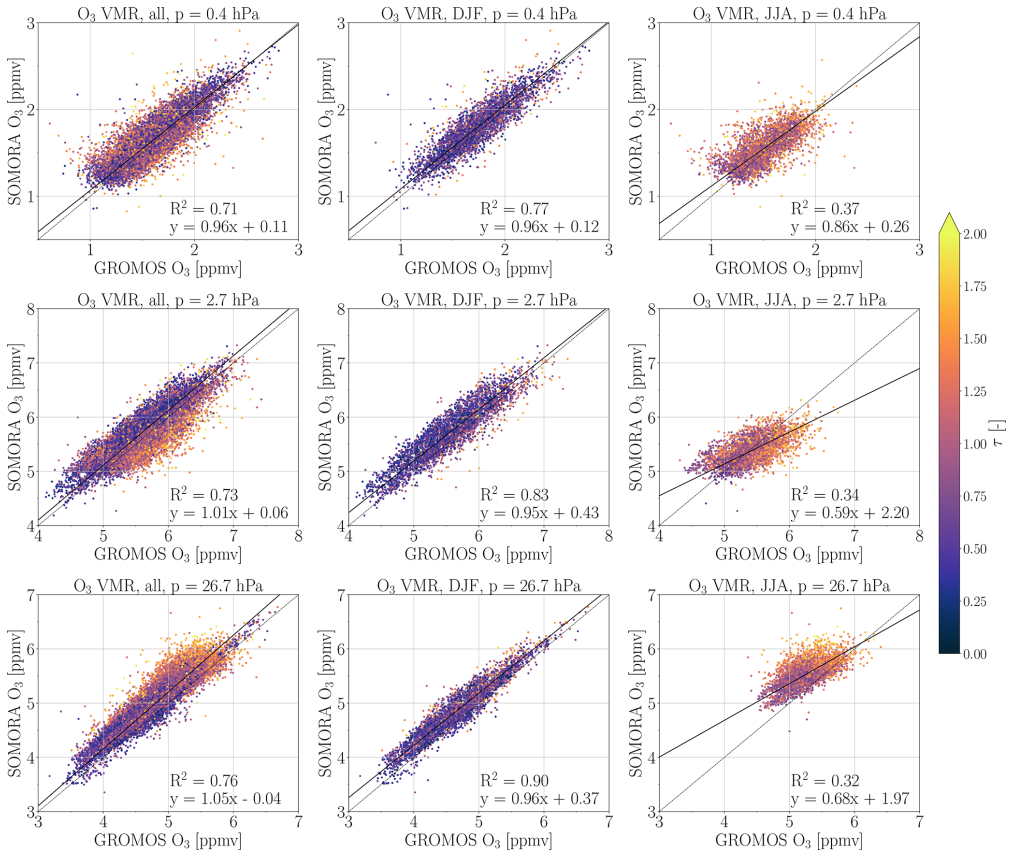

Figure 8. Mean ozone VMR for three different levels for the whole series (left column), the boreal winter season (middle column) and the boreal summer (right column). The three pressure levels correspond approximately to the lower stratosphere ($10 < p < 50$ hPa), upper stratosphere ($1 < p < 5$ hPa) and lower mesosphere ($0.1 < p < 0.9$ hPa). All data points are colour coded based on the atmospheric opacity (τ) computed at SOMORA measurement time and location. The linear regression coefficients and their coefficient of determination R^2 are indicated on each subplot.

The reasons for the summer seasonal bias remain unclear, but we assume that they result from seasonal temperature and humidity cycles in the troposphere. Indeed, despite controlled room temperature for both instruments, the higher summer temperatures still influence the room and window temperatures and consequently the instruments (e.g. receiver noise temperature or instrumental baselines). We believe that the hardware components of GROMOS and SOMORA have different sensitivity to such influences, which could explain the seasonal patterns observed in their relative differences and the lower correlation of the ozone profiles during summer.

In addition to these seasonal effects, Fig. 6 highlights some sudden changes in the differences between the two instruments, most of which can be related to a specific instrumental issue on either instrument. It can be seen for instance in April 2012, where the cold load observation angle was changed on SOMORA, reducing its baseline significantly. Another example is the strong negative ozone differences during summer 2016, which were due to a frequency lock problem in GROMOS. Finally, the large flagged period starting at the end of 2019 marks the beginning of several instrumental issues on SOMORA that were finally solved by the replacement of the LO baseband converter in September 2020. All of these issues have been identified and documented and are flagged accordingly in the new ozone data series. A detailed documentation of the time series can be found together with the data.

4.2 Comparison with previous retrievals

Computing trends for GROMOS and SOMORA is out of scope of this contribution but we would still like to provide some first elements toward answering whether this

harmonization can help solving the discrepancies previously found between both instruments (Bernet et al., 2019; Petropavlovskikh et al., 2019). Therefore, we compare our new harmonized ozone time series with the previous data version of GROMOS and SOMORA.

Figure 6 shows the weekly relative differences between the new harmonized series (upper panel) and the previous retrievals (lower panel) from 2010 to 2021. It highlights the significant improvements introduced by the harmonization process in most of the pressure range covered by the radiometers. Among other changes, it corrects the strong positive ozone bias from GROMOS seen in the mesosphere and reduces the stratospheric ozone difference clearly visible in many years of the previous data series at ~ 10 hPa. The differences between the previous series also showed a quite strong seasonal signal. As the previous processing was different between the two instruments, in particular in the way it was treating the tropospheric attenuation, it gives some confidence that the remaining seasonal bias in the new series is not an artefact introduced by the new retrieval method.

Although the harmonized retrievals improve most of the time period considered, it seems that the problems seen on SOMORA in 2020 are less well treated in the new processing. Indeed, in the previous processing the sine baseline periods were adapted daily during this time whereas the new processing only considered fixed periods. It indicates that the instrumental baselines on SOMORA varied significantly during this period and highlights the need to treat it carefully for further analysis.

From Fig. 6, it is clear that the harmonized processing significantly reduces the differences between the GROMOS and SOMORA ozone time series. However, the question remains if it can solve the discrepancies found between their respective trends. Of course, the full reprocessing of the series (including the decade 2000–2010) would be needed to fully answer this question, but we present some preliminary results showing the temporal evolution of the ozone differences between both series in Fig. 9. It shows the weekly mean differences between GROMOS and SOMORA with the previous and new retrieval algorithms in three pressure ranges. Ideally, these differences should be constant to guarantee similar trends from both instruments. Simple linear regressions have been performed on these data and indicate smaller drift intensities at all pressure ranges from the new data processing that are significant above 10 hPa.

As a consequence, the future trends to be derived for this decade from the new series should be in better agreement than with the previous retrievals. However, even with the new series, we still observe a drift between both instruments in the stratosphere, which calls for a careful treatment of spurious data periods for the next trends analysis, as done in Bernet et al. (2021).

5 Comparison with satellites

Attention was paid to keep GROMOS and SOMORA data processing fully independent. However, they would be both impacted by any bias introduced by the calibration or retrieval algorithms and therefore, we provide further validation by comparing their observations with satellite measurements.

5.1 Aura MLS

As the main validation dataset, we use ozone measurements from the Microwave Limb Sounder (MLS) on the Aura satellite launched in 2004 (Waters et al., 2006). It is operated by the National Aeronautics and Space Administration (NASA) in the frame of the Earth Observing System and has been used extensively for ozone profile validation over many regions and against many other observing systems (e.g. Boyd et al., 2007; Livesey et al., 2008; Hubert et al., 2016).

MLS is a passive microwave radiometer observing the ozone emission line around 240 GHz in a limb sounding geometry. It follows a sun-synchronous orbit which results in two overpasses per day around 01:00 and 13:00 UTC over central Europe. In this work, we have used the latest level 2 ozone retrievals (version 5) and the recommended data screening described in Livesey et al. (2022). It results in ozone VMR profiles between 261 to 0.001 hPa with a typical vertical resolution ranging from ~ 2.5 km in the lower stratosphere increasing to ~ 5.5 km at the mesopause with an accuracy of 5 %–10 % in the stratosphere increasing up to 100 % at 0.01 hPa.

For the following comparisons, we extracted co-located MLS observations to GROMOS and SOMORA. As spatial coincidence criteria, we use $\pm 3.6°$ in latitude and $\pm 10.5°$ in longitude from Bern, an area corresponding approximately to Central Europe. As temporal criteria, we averaged the MWR and the MLS profiles within 3 h time windows and keep only the time windows where both MLS and the MWR have profiles with sufficient data quality.

The MLS vertical resolution of ozone retrievals is much lower than the one from the MWRs. It means that the MWRs will essentially observe a smoothed vertical profile compared to the MLS observations. Therefore, the higher-resolved MLS profiles are convolved with the MWR averaging kernels for the comparisons (see Connor et al., 1994; Tsou et al., 1995). This AVKs smoothing also enables the removal of the influence of the a priori and follows Eq. (1):

$$\boldsymbol{x}_\mathrm{c} = \boldsymbol{x}_\mathrm{a} + \mathbf{A}(\boldsymbol{x} - \boldsymbol{x}_\mathrm{a}), \tag{1}$$

where $\boldsymbol{x}$ is the higher-resolution profile (MLS), $\boldsymbol{x}_\mathrm{a}$ is the a priori profile from the MWR retrievals, $\mathbf{A}$ are the averaging kernels and $\boldsymbol{x}_\mathrm{c}$ is the resulting convolved profile.

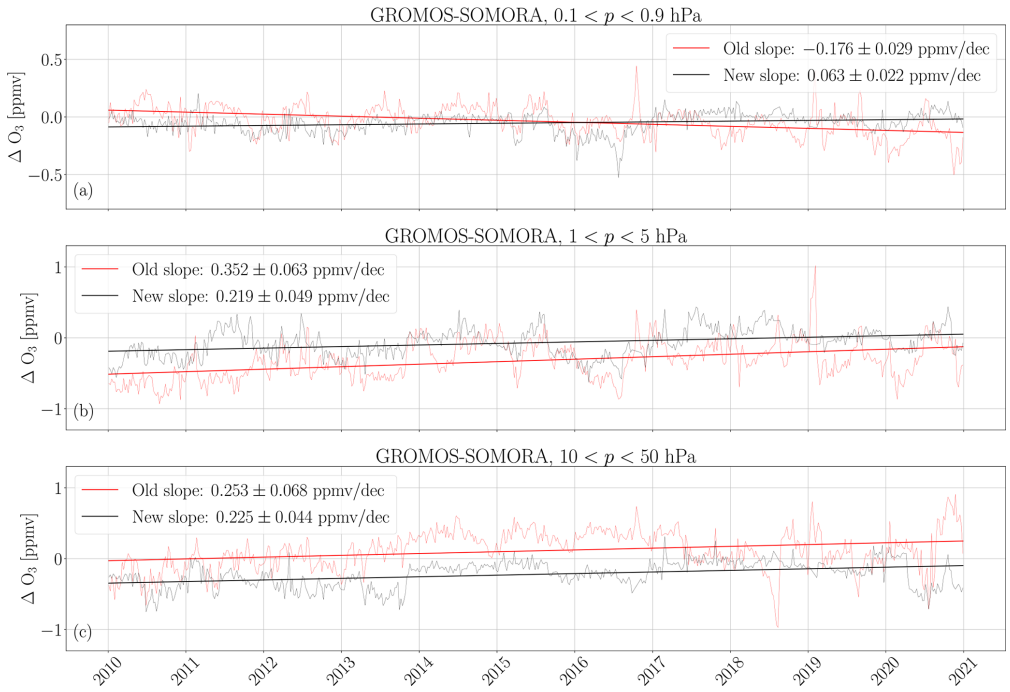

Figure 9. Weekly ozone differences between the previous and the new GROMOS and SOMORA series for the three pressure levels defined in Table 4: **(a)** lower mesosphere, **(b)** upper stratosphere and **(c)** lower stratosphere. A linear fit of the differences is shown as a straight line for the previous and the new series. The slope values are indicated with a 95 % confidence interval.

5.2 SBUV/2

In addition to MLS, we also use the latest release of the Solar Backscatter Ultraviolet Radiometer (SBUV/2) Merged Ozone Dataset (MOD) (Frith et al., 2020; Ziemke et al., 2021). This dataset provides daily overpasses over many ground-based ozone measurement stations, including Payerne in Switzerland. It provides stratospheric ozone VMR profiles from 50 to 0.5 hPa merged according to the new MOD v2 Release 1 derived from SBUV and adjusted for the diurnal cycles to an equivalent local measurement time of 13:30. The vertical resolution from the SBUV retrievals is ∼6–7 km in the middle and upper stratosphere (McPeters et al., 2013; Bhartia et al., 2013), which is closer to the vertical resolution of GROMOS and SOMORA in this region. For this reason, contrary to MLS, we do not apply any AVK smoothing to the SBUV measurements for the following comparisons.

5.3 Time series

Figure 10 shows weekly averaged GROMOS and SOMORA time series together with SBUV and MLS measurements on three pressure ranges corresponding to the lower stratosphere, upper stratosphere and lower mesosphere. It shows the consistencies of the GROMOS and SOMORA time series and highlights the good agreement of both MWRs with both satellite datasets during the last decade. As these time series are already averaged on given pressure ranges, we did not apply any AVK smoothing on the MLS data at this stage. It is also important to keep in mind that the SBUV daily dataset is adjusted to daytime (13:30), whereas both MLS and the MWRs have both daytime and night-time measurements.

In the stratosphere, clear seasonal patterns are well captured by all datasets, and the higher winter ozone variability is clearly visible at all pressure levels. On timescales of a few weeks, we can see that all four datasets are able to capture the larger ozone variations well not only in the stratosphere but also in the mesosphere where these variations become relatively small compared to the amplitude of the ozone diurnal cycle.

We can see a slight bias of the SOMORA data series in the lower stratosphere. It is especially visible before 2014 and after 2019, as has been mentioned previously. This plot also helps to identify some remaining spurious time periods in the new harmonized series (e.g. GROMOS data in summer 2016). From a qualitative point of view, we do not observe large drifts from any of the datasets with respect to the others. More work will be needed to confirm the stability from both

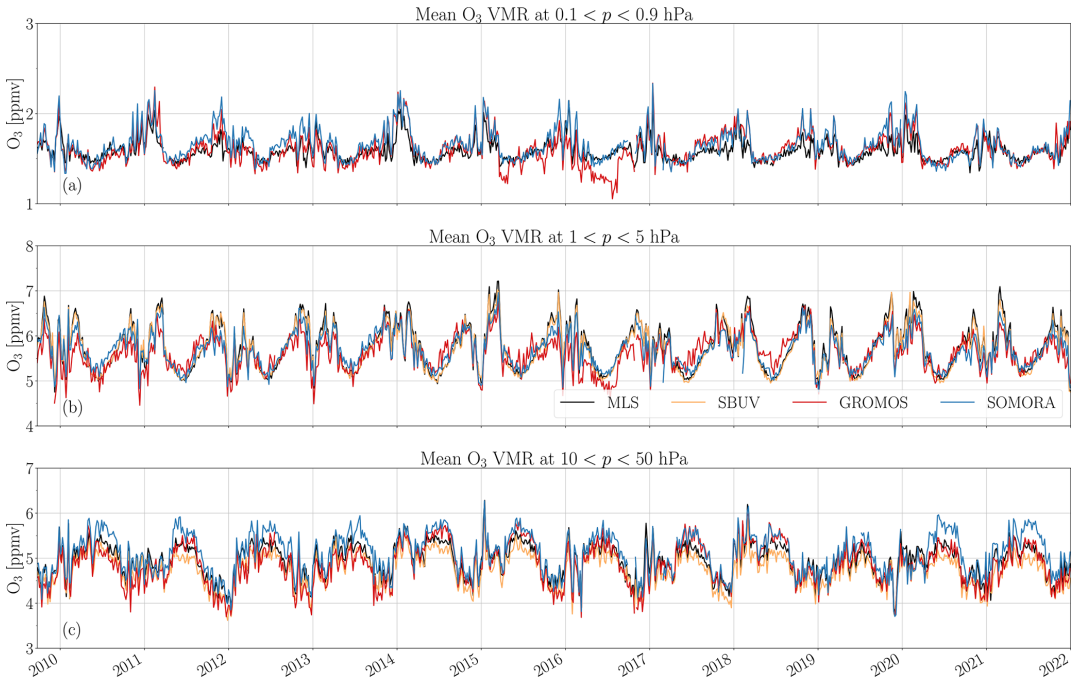

Figure 10. Weekly averaged ozone VMR from MLS, SBUV, GROMOS and SOMORA at three pressure intervals: **(a)** lower mesosphere, **(b)** upper stratosphere and **(c)** lower stratosphere. The SBUV dataset extends only up to 0.5 hPa and is therefore not shown in panel **(a)**.

MWRs, but it gives some confidence that both instruments can be used for trends analysis in the decade 2010–2020.

5.4 Profile comparisons

As quantitative validation, we show seasonal comparisons of MWRs profiles with the satellite datasets. In the following, we mostly focus on the MLS time series because it covers the same altitude range as the MWRs and because SBUV only provides daytime measurements. For the period between 2009 and 2021, we obtain more than 7100 colocated profiles between MLS and each MWR, giving approximately 1700 profiles per meteorological season. Figures 11 and 12 show comparisons between winter (resp. summer) ozone profiles measured by GROMOS, SOMORA, SBUV and MLS. Both figures show the mean seasonal ozone profile from each dataset and the relative differences between MLS and the MWRs with and without AVK convolution. The comparisons for spring and autumn are shown in Appendix C (Figs. C1 and C2).

Both GROMOS and SOMORA show very good agreement with MLS at all seasons and altitudes, with the exception of SOMORA during summertime. Mean seasonal relative differences between the two instruments and colocated MLS profiles are within 10 % in the stratosphere and lower mesosphere (up to ∼ 60 km), corresponding to the expected uncertainties of the MWRs. Above in the mesosphere, the relative differences between the MWRs and MLS grow rapidly and show some oscillations. For most of the mesosphere, the mean seasonal relative differences stay below 50 % for both instruments, but given the errors reported for the MWRs and MLS at these altitudes, we will focus our discussion on the region from ∼ 20 to 60 km. The relative differences with SBUV (not shown) are very similar to those with MLS and are below 10 % in the whole stratosphere for the two instruments.

Figure 12 again reveals the summer bias mentioned previously. Taking MLS as a reference, this plot indicates that the summer bias in the lower stratosphere is the result of an overestimation of ozone by SOMORA during this season. The reason for this could be a seasonal change in the instrumental baselines that is not taken into account in the retrieval. For both instruments, the differences with the convolved MLS profiles are still smaller in autumn and winter than in spring and summer when the absorption by the troposphere is stronger.

Moreira et al. (2017) compared the previous GROMOS retrieval dataset to MLS between 2009 and 2016. Similar agreement was found in the middle stratosphere; however, this quickly degraded at lower and higher altitudes. This is in accordance with the results shown in Fig. 6 and confirms the improvement brought by the new data processing.

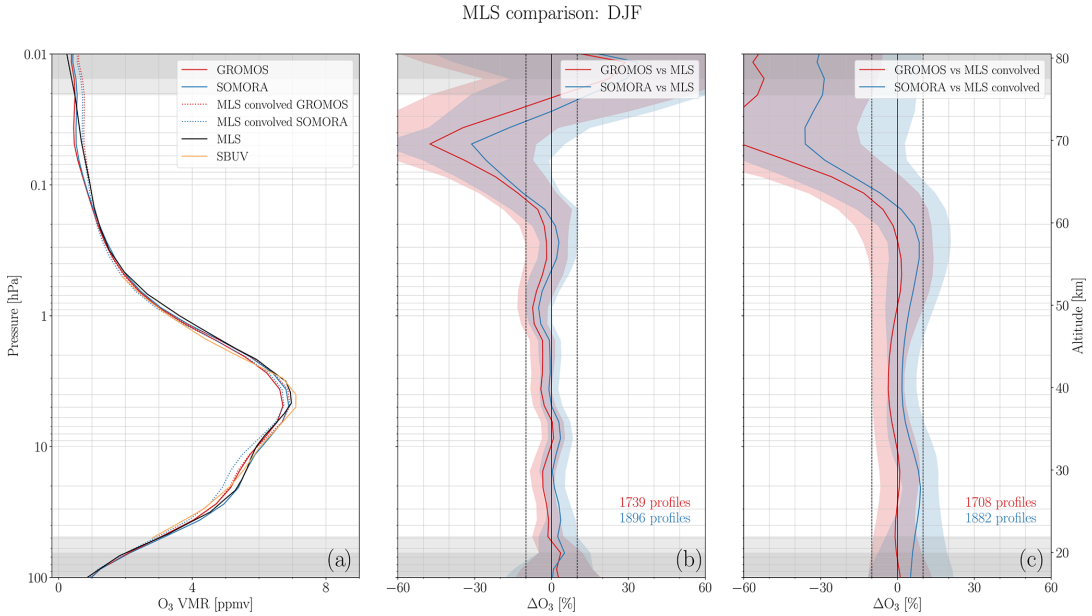

Figure 11. Seasonal comparison with MLS and SBUV during winter months (December, January and February). Panel **(b)** shows the relative differences with MLS, whereas panel **(c)** shows the relative differences with the convolved MLS profiles. The coloured areas show the standard deviation of the differences with MLS, and the grey shading indicates the limits where the a priori contribution exceeds 20 %. The dashed vertical lines indicate the ±10 % interval.

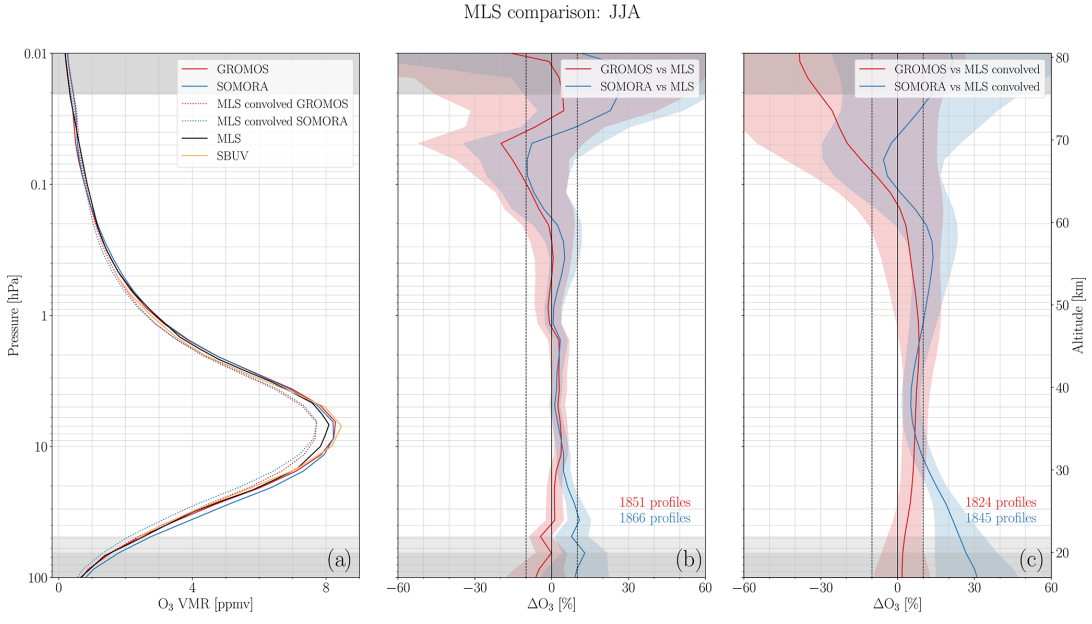

Figure 12. The same as Fig. 11 but for summer (June, July and August).

Table 5. Mean relative VMR differences ((MWR − MLS) / MWR) between MWRs and MLS at three pressure ranges, with and without AVK convolution. In parentheses we show the standard deviations of the VMR relative differences in each pressure range.

Pressure range (hPa)	$\Delta O_{3,\text{GROMOS}}$ (%)	$\Delta O_{3,\text{GROMOS, convolved}}$ (%)	$\Delta O_{3,\text{SOMORA}}$ (%)	$\Delta O_{3,\text{SOMORA, convolved}}$ (%)
0.9–0.1	−4.1 (3.2)	−0.9 (4.0)	−0.9 (4.0)	+5.6 (4.3)
5–1	−1.7 (1.1)	+2.5 (0.1)	−0.3 (0.8)	+5 (0.8)
50–10	−0.7 (1.0)	+2.0 (1.4)	+4.2 (1.2)	+11.6 (1.4)

SOMORA showed similar agreement with MLS in the range 25 to 0.1 hPa between 2004 and 2015 (Maillard Barras et al., 2020). Below 25 hPa, SOMORA showed a positive bias compared to other datasets that gives confidence that this bias is not related to the new data processing.

Similar comparisons between MWR and MLS has been performed at various locations (e.g. Boyd et al., 2007; Palm et al., 2010; Ryan et al., 2016) and showed similar results to the ones obtained in our study. This is confirmed by the mean ozone VMR relative differences between MWR and MLS given in Table 5 for the middle atmosphere. Averaged over these pressure ranges and the entire time period, the differences between MLS and the MWRs are less than 5 % in the stratosphere and lower mesosphere.

Overall, SOMORA and GROMOS profiles are in better accordance with the non-convolved MLS than with the convolved MLS profiles. This can be seen for both instruments and at the three pressure ranges from the seasonal plots and in Table 5. It is not entirely clear why these differences are larger with the convolved MLS profiles, but it does not result from sampling differences (not shown). As it seems especially visible in SOMORA in the lower stratosphere, it could potentially arise from instrumental baselines impacting the AVKs.

6 Conclusions

New harmonized data series from two Swiss ozone ground-based microwave radiometers are now available from 2009 to 2021. The reprocessing provides a full harmonization at all levels, from the calibration of the raw data to the retrieval of the ozone profiles. It includes the data inputs and outputs, the systematic flagging, the output temporal resolution and the retrieval grids. The harmonization makes the comparison and the identification of biases easier than in the past. It significantly improves the agreement between the two instruments in this time period and reduces the long-term drift of their differences. It should help to resolve the discrepancies previously found in the trend estimates derived from these two time series.

However, despite these significant improvements, systematic differences remain between the two instruments. They include a seasonal bias, mostly visible in the lower stratosphere in summer, as well as a negative ozone bias of GROMOS in the upper mesosphere. Further work is needed to fully understand these systematic biases but they probably both arise from instrumental sources as they were already seen in the previous retrieval versions. In addition, limited anomalous time periods still remain on both instruments but most of their causes are now identified and documented. The new harmonized data series are also compared against two independent and co-located satellite datasets. Both instruments show a good agreement with SBUV and MLS, with mean relative differences below 10 % in most of the stratosphere and lower mesosphere (up to $\sim$ 60 km).

The new retrieval products of ozone profiles at Bern and Payerne are available and will be submitted to NDACC. We also plan to extend the harmonization process to the older observations from these two instruments in order to provide the full harmonized ozone time series since 1994 (GROMOS) and 2000 (SOMORA). The collocation of two harmonized time series with high temporal resolution also opens the way to unique short-term ozone variations analyses.

Appendix A: Opacities

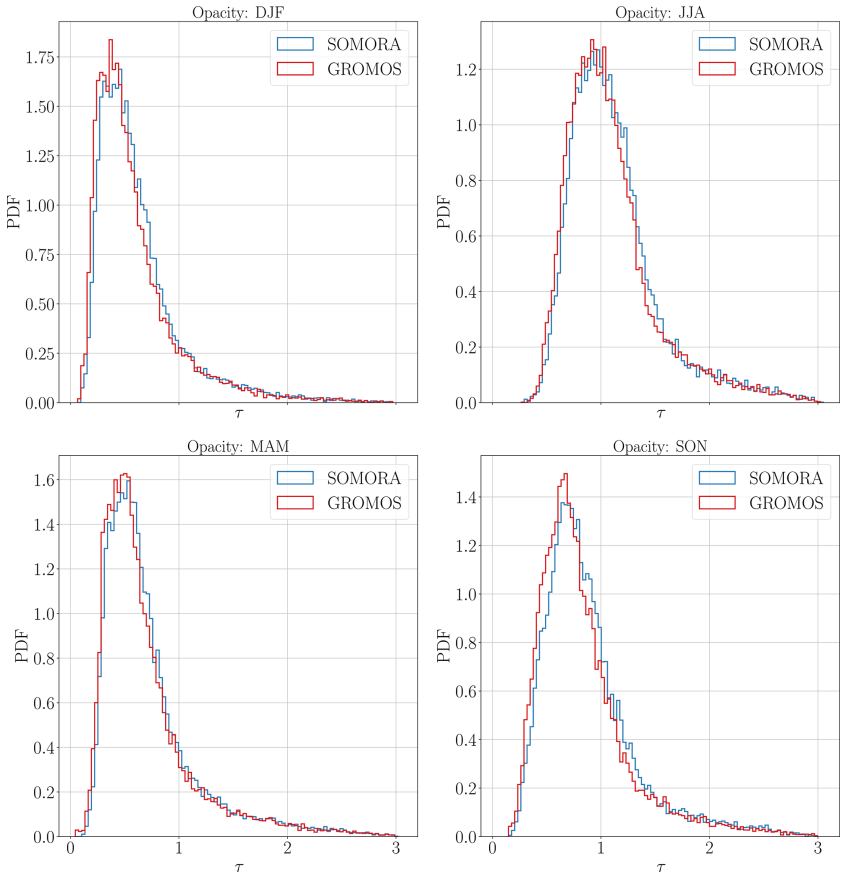

Figure A1. Seasonal comparisons of hourly tropospheric opacities in Bern (GROMOS) and Payerne (SOMORA) from 2009 to 2021.

Appendix B: Uncertainty budget at high atmospheric opacities

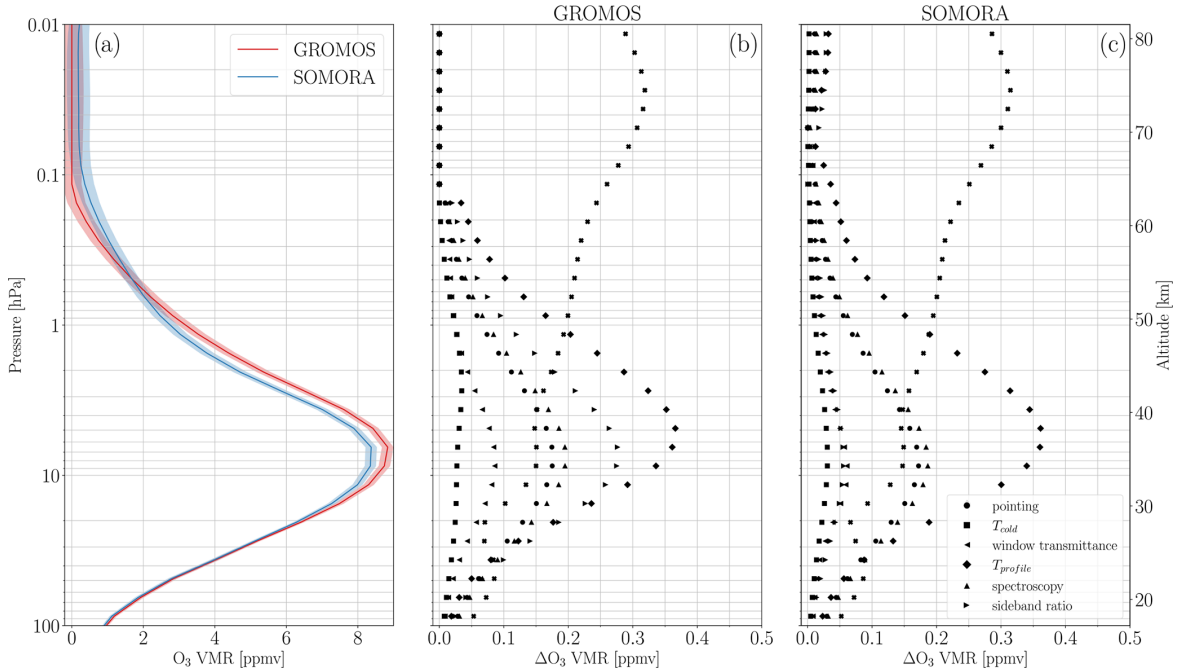

Figure B1. Uncertainty budget for GROMOS and SOMORA in the high-opacity case ($\tau \approx 1.3$). Panel **(a)** shows the reference ozone profile chosen for the sensitivity analysis. Panels **(b)** and **(c)** show the ozone VMR uncertainties arising from the error sources listed in Table 3.

Appendix C: Seasonal comparison with MLS and SBUV

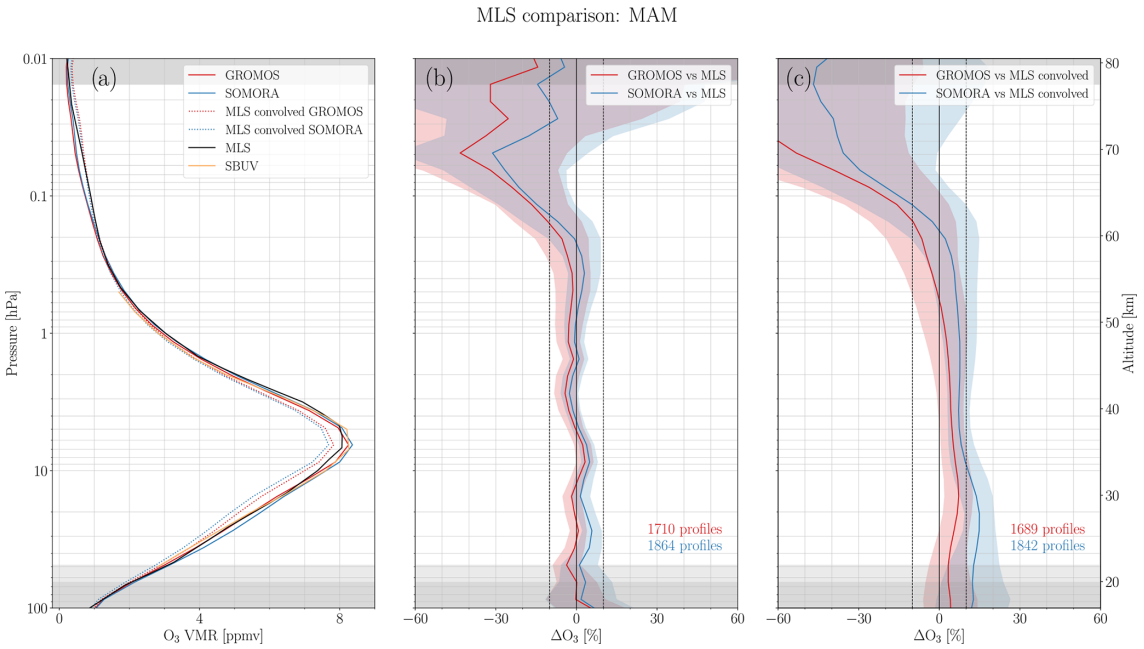

Figure C1. The same as Fig. 11 but for spring (March, April and May).

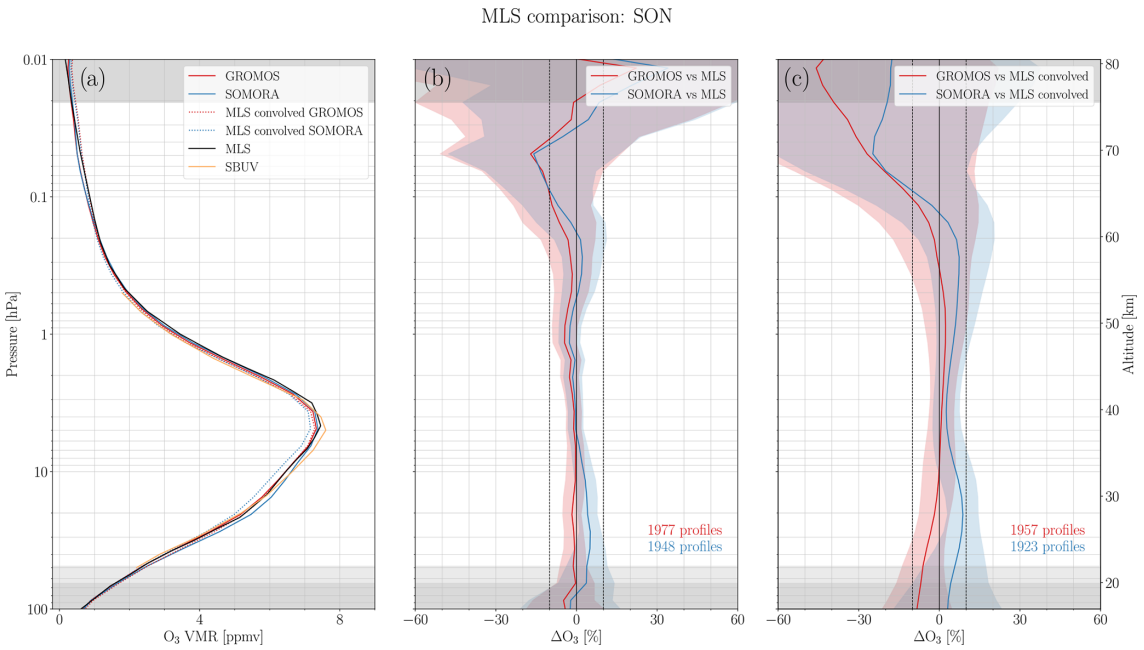

Figure C2. The same as Fig. 11 but for autumn (September, October and November).

Code and data availability. The GROMOS and SOMORA level 2 data are available from the Bern Open Repository and Information System (University of Bern, 2022) in the form of yearly netCDF files: GROMOS data can be found at https://doi.org/10.48620/65 (Sauvageat et al., 2022), and SOMORA data can be found at https://doi.org/10.48620/119 (Maillard Barras et al., 2022). The new harmonized calibration and retrieval routines are freely available at https://doi.org/10.5281/zenodo.6799357 (Sauvageat, 2022b). The analysis code reproducing all the results presented in this paper can be found at https://doi.org/10.5281/zenodo.7185298 (Sauvageat, 2022c). MLS v5 data are available from the NASA Goddard Space Flight Center Earth Sciences Data and Information Services Center (GES DISC): https://doi.org/10.5067/Aura/MLS/DATA2516 (Schwartz et al., 2020). The SBUV MOD dataset is available at https://acd-ext.gsfc.nasa.gov/Data_services/merged/ (NASA Goddard Earth Sciences Data and Information Services Center, 2022).

Author contributions. ES performed the harmonization project, carried out the data analysis and prepared the manuscript. EMB provided the SOMORA data and helped with the data analysis. KH provided the GROMOS data and helped with the data analysis. AH conceived the project and provided advice on the data analysis. AM conceived the project and helped with the data analysis. All of the authors discussed the scientific findings and provided valuable feedback for the manuscript editing.

Competing interests. The contact author has declared that none of the authors has any competing interests.

Disclaimer. Publisher's note: Copernicus Publications remains neutral with regard to jurisdictional claims in published maps and institutional affiliations.

Special issue statement. This article is part of the special issue "Atmospheric ozone and related species in the early 2020s: latest results and trends (ACP/AMT inter-journal SI)". It is a result of the 2021 Quadrennial Ozone Symposium (QOS) held online on 3–9 October 2021.

Acknowledgements. The authors acknowledge all of the people that took care of GROMOS and SOMORA over more than 20 years, in particular Nik Jaussi, Andres Luder and Tobias Plüss. In addition, they would like to thank the numerous developers that contributed to the free and open-source tools used for the data analysis and visualization, in particular xarray (Hoyer and Hamman, 2017), Matplotlib (Hunter, 2007), Typhon and pyretrievals, and the ARTS community for their precious help and support.

Financial support. This work has been supported by MeteoSwiss and the Swiss Global Atmospheric Watch programme.

Review statement. This paper was edited by Corinne Vigouroux and reviewed by Giovanni Muscari and one anonymous referee.

References

Anderson, J., Russell III, J., Solomon, S., and Deaver, L.: Halogen Occultation Experiment confirmation of stratospheric chlorine decreases in accordance with the Montreal Protocol, J. Geophys. Res.-Atmos., 105, 4483–4490, 2000.

Ball, W. T., Alsing, J., Mortlock, D. J., Staehelin, J., Haigh, J. D., Peter, T., Tummon, F., Stübi, R., Stenke, A., Anderson, J., Bourassa, A., Davis, S. M., Degenstein, D., Frith, S., Froidevaux, L., Roth, C., Sofieva, V., Wang, R., Wild, J., Yu, P., Ziemke, J. R., and Rozanov, E. V.: Evidence for a continuous decline in lower stratospheric ozone offsetting ozone layer recovery, Atmos. Chem. Phys., 18, 1379–1394, https://doi.org/10.5194/acp-18-1379-2018, 2018.

Benz, A. O., Grigis, P. C., Hungerbühler, V., Meyer, H., Monstein, C., Stuber, B., and Zardet, D.: A broadband FFT spectrometer for radio and millimeter astronomy, Astron. Astrophys., 442, 767–773, https://doi.org/10.1051/0004-6361:20053568, 2005.

Bernet, L., von Clarmann, T., Godin-Beekmann, S., Ancellet, G., Maillard Barras, E., Stübi, R., Steinbrecht, W., Kämpfer, N., and Hocke, K.: Ground-based ozone profiles over central Europe: incorporating anomalous observations into the analysis of stratospheric ozone trends, Atmos. Chem. Phys., 19, 4289–4309, https://doi.org/10.5194/acp-19-4289-2019, 2019.

Bernet, L., Boyd, I., Nedoluha, G., Querel, R., Swart, D., and Hocke, K.: Validation and Trend Analysis of Stratospheric Ozone Data from Ground-Based Observations at Lauder, New Zealand, Remote Sens., 13, 109, https://doi.org/10.3390/rs13010109, 2021.

Bhartia, P. K., McPeters, R. D., Flynn, L. E., Taylor, S., Kramarova, N. A., Frith, S., Fisher, B., and DeLand, M.: Solar Backscatter UV (SBUV) total ozone and profile algorithm, Atmos. Meas. Tech., 6, 2533–2548, https://doi.org/10.5194/amt-6-2533-2013, 2013.

Boyd, I. S., Parrish, A. D., Froidevaux, L., Clarmann, T. v., Kyrölä, E., Russell, J. M., and Zawodny, J. M.: Ground-based microwave ozone radiometer measurements compared with Aura-MLS v2.2 and other instruments at two Network for Detection of Atmospheric Composition Change sites, J. Geophys. Res.-Atmos., 112, D24S33, https://doi.org/10.1029/2007JD008720, 2007.

Braesicke, P., Neu, J., Fioletov, V., Godin-Beekmann, S., Hubert, D., Petropavlovskikh, I., Shiotani, M., and Sinnhuber, B.-M.: Global Ozone: Past, Present, and Future, chap. 3 in: Scientific Assessment of Ozone Depletion: 2018, Global Ozone Research and Monitoring Project – Report No. 58, World Meteorological Organization, Geneva, Switzerland, ISBN: 978-1-7329317-1-8, 2018.

Buehler, S. A., Eriksson, P., Kuhn, T., von Engeln, A., and Verdes, C.: ARTS, the atmospheric radiative transfer simulator, J. Quant. Spectrosc. Ra., 91, 65–93, https://doi.org/10.1016/j.jqsrt.2004.05.051, 2005.

Buehler, S. A., Mendrok, J., Eriksson, P., Perrin, A., Larsson, R., and Lemke, O.: ARTS, the Atmospheric Radiative Transfer Simulator – version 2.2, the planetary toolbox edition, Geosci.

Model Dev., 11, 1537–1556, https://doi.org/10.5194/gmd-11-1537-2018, 2018.

Calisesi, Y.: The Stratospheric Ozone Monitoring Radiometer SOMORA: NDSC Application Document, Research report no. 2003-11, Institute of Applied Physics, University of Bern, Switzerland, 2003.

Chandra, S., Fleming, E. L., Schoeberl, M. R., and Barnett, J. J.: Monthly mean global climatology of temperature, wind, geopotential height and pressure for 0–120 km, Adv. Space Res., 10, 3–12, 1990.

Connor, B. J., Siskind, D. E., Tsou, J., Parrish, A., and Remsberg, E. E.: Ground-based microwave observations of ozone in the upper stratosphere and mesosphere, J. Geophys. Res.-Atmos., 99, 16757–16770, https://doi.org/10.1029/94JD01153, 1994.

Crutzen, P. J.: The influence of nitrogen oxides on the atmospheric ozone content, Q. J. Roy. Meteor. Soc., 96, 320–325, https://doi.org/10.1002/qj.49709640815, 1970.

De Mazière, M., Thompson, A. M., Kurylo, M. J., Wild, J. D., Bernhard, G., Blumenstock, T., Braathen, G. O., Hannigan, J. W., Lambert, J.-C., Leblanc, T., McGee, T. J., Nedoluha, G., Petropavlovskikh, I., Seckmeyer, G., Simon, P. C., Steinbrecht, W., and Strahan, S. E.: The Network for the Detection of Atmospheric Composition Change (NDACC): history, status and perspectives, Atmos. Chem. Phys., 18, 4935–4964, https://doi.org/10.5194/acp-18-4935-2018, 2018.

Eriksson, P., Ekström, M., Melsheimer, C., and Buehler, S. A.: Efficient forward modelling by matrix representation of sensor responses, Int. J. Remote Sens., 27, 1793–1808, 2006.

Eriksson, P., Buehler, S., Davis, C., Emde, C., and Lemke, O.: ARTS, the atmospheric radiative transfer simulator, version 2, J. Quant. Spectrosc. Ra., 112, 1551–1558, https://doi.org/10.1016/j.jqsrt.2011.03.001, 2011.

Eyring, V., Cionni, I., Bodeker, G. E., Charlton-Perez, A. J., Kinnison, D. E., Scinocca, J. F., Waugh, D. W., Akiyoshi, H., Bekki, S., Chipperfield, M. P., Dameris, M., Dhomse, S., Frith, S. M., Garny, H., Gettelman, A., Kubin, A., Langematz, U., Mancini, E., Marchand, M., Nakamura, T., Oman, L. D., Pawson, S., Pitari, G., Plummer, D. A., Rozanov, E., Shepherd, T. G., Shibata, K., Tian, W., Braesicke, P., Hardiman, S. C., Lamarque, J. F., Morgenstern, O., Pyle, J. A., Smale, D., and Yamashita, Y.: Multi-model assessment of stratospheric ozone return dates and ozone recovery in CCMVal-2 models, Atmos. Chem. Phys., 10, 9451–9472, https://doi.org/10.5194/acp-10-9451-2010, 2010.

Fahey, D., Newman, P. A., Pyle, J. A., Safari, B., Chipperfield, M. P., Karoly, D., Kinnison, D. E., Ko, M., Santee, M., and Doherty, S. J.: Scientific Assessment of Ozone Depletion: 2018, Global Ozone Research and Monitoring Project-Report No. 58, ISBN: 978-1-7329317-1-8, 2018.

Farman, J. C., Gardiner, B. G., and Shanklin, J. D.: Large losses of total ozone in Antarctica reveal seasonal ClO_x/NO_x interaction, Nature, 315, 207–210, 1985.

Frith, S. M., Bhartia, P. K., Oman, L. D., Kramarova, N. A., McPeters, R. D., and Labow, G. J.: Model-based climatology of diurnal variability in stratospheric ozone as a data analysis tool, Atmos. Meas. Tech., 13, 2733–2749, https://doi.org/10.5194/amt-13-2733-2020, 2020.

Godin-Beekmann, S., Azouz, N., Sofieva, V. F., Hubert, D., Petropavlovskikh, I., Effertz, P., Ancellet, G., Degenstein, D. A., Zawada, D., Froidevaux, L., Frith, S., Wild, J., Davis, S., Steinbrecht, W., Leblanc, T., Querel, R., Tourpali, K., Damadeo, R., Maillard Barras, E., Stübi, R., Vigouroux, C., Arosio, C., Nedoluha, G., Boyd, I., Van Malderen, R., Mahieu, E., Smale, D., and Sussmann, R.: Updated trends of the stratospheric ozone vertical distribution in the 60° S–60° N latitude range based on the LOTUS regression model , Atmos. Chem. Phys., 22, 11657–11673, https://doi.org/10.5194/acp-22-11657-2022, 2022.

Haefele, A., Hocke, K., Kämpfer, N., Keckhut, P., Marchand, M., Bekki, S., Morel, B., Egorova, T., and Rozanov, E.: Diurnal changes in middle atmospheric H_2O and O_3: Observations in the Alpine region and climate models, J. Geophys. Res.-Atmos., 113, D17303, https://doi.org/10.1029/2008JD009892, 2008.

Hocke, K., Kämpfer, N., Ruffieux, D., Froidevaux, L., Parrish, A., Boyd, I., von Clarmann, T., Steck, T., Timofeyev, Y. M., Polyakov, A. V., and Kyrölä, E.: Comparison and synergy of stratospheric ozone measurements by satellite limb sounders and the ground-based microwave radiometer SOMORA, Atmos. Chem. Phys., 7, 4117–4131, https://doi.org/10.5194/acp-7-4117-2007, 2007.

Hoyer, S. and Hamman, J.: xarray: N-D labeled Arrays and Datasets in Python, Journal of Open Research Software, 5, 10, https://doi.org/10.5334/jors.148, 2017.

Hubert, D., Lambert, J.-C., Verhoelst, T., Granville, J., Keppens, A., Baray, J.-L., Bourassa, A. E., Cortesi, U., Degenstein, D. A., Froidevaux, L., Godin-Beekmann, S., Hoppel, K. W., Johnson, B. J., Kyrölä, E., Leblanc, T., Lichtenberg, G., Marchand, M., McElroy, C. T., Murtagh, D., Nakane, H., Portafaix, T., Querel, R., Russell III, J. M., Salvador, J., Smit, H. G. J., Stebel, K., Steinbrecht, W., Strawbridge, K. B., Stübi, R., Swart, D. P. J., Taha, G., Tarasick, D. W., Thompson, A. M., Urban, J., van Gijsel, J. A. E., Van Malderen, R., von der Gathen, P., Walker, K. A., Wolfram, E., and Zawodny, J. M.: Ground-based assessment of the bias and long-term stability of 14 limb and occultation ozone profile data records, Atmos. Meas. Tech., 9, 2497–2534, https://doi.org/10.5194/amt-9-2497-2016, 2016.

Hunter, J. D.: Matplotlib: A 2D graphics environment, IEEE Ann. Hist. Comput., 9, 90–95, 2007.

Ingold, T., Peter, R., and Kämpfer, N.: Weighted mean tropospheric temperature and transmittance determination at millimeter-wave frequencies for ground-based applications, Radio Sci., 33, 905–918, https://doi.org/10.1029/98RS01000, 1998.

Janssen, M. A., ed.: Atmospheric remote sensing by microwave radiometry, chap. 7, Wiley series in remote sensing, Wiley, New York, 358–375, ISBN: 0-471-62891-3, 1993.

Kopp, G., Berg, H., Blumenstock, T., Fischer, H., Hase, F., Hochschild, G., Höpfner, M., Kouker, W., Reddmann, T., Ruhnke, R., Raffalski, U., and Kondo, Y.: Evolution of ozone and ozone-related species over Kiruna during the SOLVE/THESEO 2000 campaign retrieved from ground-based millimeter-wave and infrared observations, J. Geophys. Res., 108, 8308, https://doi.org/10.1029/2001JD001064, 2003

Krochin, W., Navas-Guzmán, F., Kuhl, D., Murk, A., and Stober, G.: Continuous temperature soundings at the stratosphere and lower mesosphere with a ground-based radiometer considering the Zeeman effect, Atmos. Meas. Tech., 15, 2231–2249, https://doi.org/10.5194/amt-15-2231-2022, 2022.

Livesey, N. J., Filipak, M. J., Froidevaux, L., Read, W. G., Lambert, A., Santee, M. L., Jiang, J. H., Pumphrey, H. C., Waters, J. W., Cofield, R. E., Cuddy, D. T., Daffer, W. H., Drouin, B.

J., Fuller, R. A., Jarnot, R. F., Jiang, Y. B., Knosp, B. W., Li, Q. B., Perun, V. S., Schwartz, M. J., Snyder, W. V., Stek, P. C., Thurstans, R. P., Wagner, P. A., Avery, M., Browell, E. V., Cammas, J.-P., Christensen, L. E., Diskin, G. S., Gao, R.-S., Jost, H.-J., Loewenstein, M., Lopez, J. D., Nedelec, P., Osterman, G. B., Sachse, G. W., and Webster, C. R.: Validation of Aura Microwave Limb Sounder O_3 and CO observations in the upper troposphere and lower stratosphere, J. Geophys. Res., 113, D15S02, https://doi.org/10.1029/2007JD008805, 2008.

Livesey, N. J., Read, W. G., Wagner, P. A., Froidevaux, L., Santee, M. L., Schwartz, M. J., Lambert, A., Valle, L. F. M., Pumphrey, H. C., Manney, G. L., Fuller, R. A., Jarnot, R. F., Knosp, B. W., and Lay, R. R.: Earth Observing System (EOS) Aura Microwave Limb Sounder (MLS) Version 5.0x Level 2 and 3 data quality and description document, Tech. rep., https://mls.jpl.nasa.gov/eos-aura-mls/data-documentation, last access: 20 April 2022.

Maillard Barras, E., Haefele, A., Nguyen, L., Tummon, F., Ball, W. T., Rozanov, E. V., Rüfenacht, R., Hocke, K., Bernet, L., Kämpfer, N., Nedoluha, G., and Boyd, I.: Study of the dependence of long-term stratospheric ozone trends on local solar time, Atmos. Chem. Phys., 20, 8453–8471, https://doi.org/10.5194/acp-20-8453-2020, 2020.

Maillard Barras, E., Sauvageat, E., Haefele, A., Hocke, K., and Murk, A.: Harmonized middle atmospheric ozone time series from SOMORA, BORIS [data set], https://doi.org/10.48620/119, 2022.

McPeters, R. D., Bhartia, P., Haffner, D., Labow, G. J., and Flynn, L.: The version 8.6 SBUV ozone data record: An overview, J. Geophys. Res.-Atmos., 118, 8032–8039, https://doi.org/10.1002/jgrd.50597, 2013.

Molina, M. J. and Rowland, F. S.: Stratospheric sink for chlorofluoromethanes: chlorine atom-catalysed destruction of ozone, Nature, 249, 810–812, https://doi.org/10.1038/249810a0, 1974.

Moreira, L., Hocke, K., Eckert, E., von Clarmann, T., and Kämpfer, N.: Trend analysis of the 20-year time series of stratospheric ozone profiles observed by the GROMOS microwave radiometer at Bern, Atmos. Chem. Phys., 15, 10999–11009, https://doi.org/10.5194/acp-15-10999-2015, 2015.

Moreira, L., Hocke, K., and Kämpfer, N.: Comparison of ozone profiles and influences from the tertiary ozone maximum in the night-to-day ratio above Switzerland, Atmos. Chem. Phys., 17, 10259–10268, https://doi.org/10.5194/acp-17-10259-2017, 2017.

Muller, S. C., Murk, A., Monstein, C., and Kampfer, N.: Intercomparison of digital fast Fourier transform and acoustooptical spectrometers for microwave radiometry of the atmosphere, IEEE T. Geosci. Remote, 47, 2233–2239, 2009.

Murk, A. and Kotiranta, M.: Characterization of digital real-time spectrometers for radio astronomy and atmospheric remote sensing, in: Proceedings of the International Symposium on Space THz Technology, Gothenburg, Sweden, 15–17 April 2019, vol. 15, ISBN: 9781713803225, 2019.

Murk, A., Treuttel, J., Rea, S., and Matheson, D.: Characterization of a 340 GHz Sub-Harmonic IQ Mixer with Digital Sideband Separating Backend, in: Proceedings of the 5th ESA Workshop on Millimetre Wave Technology and Applications, ESTEC, Noordwijk, Netherland, 469–476, https://doi.org/10.7892/boris.37596, 2009.

NASA Goddard Earth Sciences Data and Information Services Center: SBUV Merged Ozone Data Set (MOD), NASA [data set] https://acd-ext.gsfc.nasa.gov/Data_services/merged/, last access: 1 November 2022.

Palm, M., Hoffmann, C. G., Golchert, S. H. W., and Notholt, J.: The ground-based MW radiometer OZORAM on Spitsbergen – description and status of stratospheric and mesospheric O_3-measurements, Atmos. Meas. Tech., 3, 1533–1545, https://doi.org/10.5194/amt-3-1533-2010, 2010.

Parrish, A., deZafra, R. L., Solomon, P. M., and Barrett, J. W.: A ground-based technique for millimeter wave spectroscopic observations of stratospheric trace constituents, Radio Sci., 23, 106–118, https://doi.org/10.1029/RS023i002p00106, 1988.

Parrish, A., Connor, B. J., Tsou, J. J., McDermid, I. S., and Chu, W. P.: Ground-based microwave monitoring of stratospheric ozone, J. Geophys. Res.-Atmos., 97, 2541–2546, https://doi.org/10.1029/91JD02914, 1992.

Perrin, A., Puzzarini, C., Colmont, J.-M., Verdes, C., Wlodarczak, G., Cazzoli, G., Buehler, S., Flaud, J.-M., and Demaison, J.: Molecular Line Parameters for the "MASTER" (Millimeter Wave Acquisitions for Stratosphere/Troposphere Exchange Research) Database, J. Atmos. Chem., 51, 161–205, https://doi.org/10.1007/s10874-005-7185-9, 2005.

Peter, R.: The Ground-based Millimeter-wave Ozone Spectrometer – GROMOS, Research report no. 97-13, Institute of Applied Physics, University of Bern, Switzerland, 1997.

Petropavlovskikh, I., Godin-Beekmann, S., Hubert, D., Damadeo, R., Hassler, B., and Sofieva, V.: SPARC/IO3C/GAW report on Long-term Ozone Trends and Uncertainties in the Stratosphere, SPARC Report No. 9, GAW Report No. 241, WCRP-17/2018, International Project Office at DLR-IPA, https://doi.org/10.17874/f899e57a20b, 2019.

Rodgers, C. D.: Inverse Methods for Atmospheric Sounding: Theory and Practice, World Scientific Publishing Co. Pte. Ltd., ISBN: 981-02-2740-X, 2000.

Rüfenacht, R., Kämpfer, N., and Murk, A.: First middle-atmospheric zonal wind profile measurements with a new ground-based microwave Doppler-spectro-radiometer, Atmos. Meas. Tech., 5, 2647–2659, https://doi.org/10.5194/amt-5-2647-2012, 2012.

Ryan, N. J., Walker, K. A., Raffalski, U., Kivi, R., Gross, J., and Manney, G. L.: Ozone profiles above Kiruna from two ground-based radiometers, Atmos. Meas. Tech., 9, 4503–4519, https://doi.org/10.5194/amt-9-4503-2016, 2016.

Sauvageat, E.: Calibration routine for ground-based passive microwave radiometer: a user guide (Research Report 2021-01-MW), University of Bern, Institute of Applied Physics, Bern, https://doi.org/10.48350/164418, 2021.

Sauvageat, E.: Harmonized ozone profile retrievals from GROMOS and SOMORA (Research Report 2022-01-MW), Institute of Applied Physics, University of Bern, https://doi.org/10.48350/170121, 2022a.

Sauvageat, E.: leric2/GROMORA-harmo: GROMORA v2.0 (gromora_v2), Zenodo [code], https://doi.org/10.5281/zenodo.6799357, 2022b.

Sauvageat, E.: leric2/gromora_analysis: AMT_paper (AMT_paper), Zenodo [code], https://doi.org/10.5281/zenodo.7185298, 2022c.

Sauvageat, E., Albers, R., Kotiranta, M., Hocke, K., Gomez, R. M., Nedoluha, G. E., and Murk, A.: Comparison of Three High Resolution Real-Time Spectrometers for Microwave Ozone Profiling Instruments, IEEE J. Sel. Top. Appl., 14, 10045–10056, https://doi.org/10.1109/JSTARS.2021.3114446, 2021.

Sauvageat, E., Murk, A., Hocke, K., Maillard Barras, E., and Haefele, A.: Harmonized middle atmospheric ozone time series from GROMOS, BORIS [data set], https://doi.org/10.48620/65, 2022.

Schanz, A., Hocke, K., and Kämpfer, N.: Daily ozone cycle in the stratosphere: global, regional and seasonal behaviour modelled with the Whole Atmosphere Community Climate Model, Atmos. Chem. Phys., 14, 7645–7663, https://doi.org/10.5194/acp-14-7645-2014, 2014.

Schwartz, M., Froidevaux, L., Livesey, N. and Read, W.: MLS/Aura Level 2 Ozone (O3) Mixing Ratio V005, Greenbelt, MD, USA, Goddard Earth Sciences Data and Information Services Center (GES DISC) [data set], https://doi.org/10.5067/Aura/MLS/DATA2516, 2020.

Solomon, P., Barrett, J., Mooney, T., Connor, B., Parrish, A., and Siskind, D. E.: Rise and decline of active chlorine in the stratosphere, Geophys. Res. Lett., 33, L18807, https://doi.org/10.1029/2006GL027029, 2006.

Solomon, S., Garcia, R. R., Rowland, F. S., and Wuebbles, D. J.: On the depletion of Antarctic ozone, Nature, 321, 755–758, 1986.

Solomon, S., Ivy, D. J., Kinnison, D., Mills, M. J., Neely III, R. R., and Schmidt, A.: Emergence of healing in the Antarctic ozone layer, Science, 353, 269–274, 2016.

Steinbrecht, W., Froidevaux, L., Fuller, R., Wang, R., Anderson, J., Roth, C., Bourassa, A., Degenstein, D., Damadeo, R., Zawodny, J., Frith, S., McPeters, R., Bhartia, P., Wild, J., Long, C., Davis, S., Rosenlof, K., Sofieva, V., Walker, K., Rahpoe, N., Rozanov, A., Weber, M., Laeng, A., von Clarmann, T., Stiller, G., Kramarova, N., Godin-Beekmann, S., Leblanc, T., Querel, R., Swart, D., Boyd, I., Hocke, K., Kämpfer, N., Maillard Barras, E., Moreira, L., Nedoluha, G., Vigouroux, C., Blumenstock, T., Schneider, M., García, O., Jones, N., Mahieu, E., Smale, D., Kotkamp, M., Robinson, J., Petropavlovskikh, I., Harris, N., Hassler, B., Hubert, D., and Tummon, F.: An update on ozone profile trends for the period 2000 to 2016, Atmos. Chem. Phys., 17, 10675–10690, https://doi.org/10.5194/acp-17-10675-2017, 2017.

Tsou, J. J., Connor, B. J., Parrish, A., McDermid, I. S., and Chu, W. P.: Ground-based microwave monitoring of middle atmosphere ozone: Comparison to lidar and Stratospheric and Gas Experiment II satellite observations, J. Geophys. Res., 100, 3005, https://doi.org/10.1029/94JD02947, 1995.

Tummon, F., Hassler, B., Harris, N. R. P., Staehelin, J., Steinbrecht, W., Anderson, J., Bodeker, G. E., Bourassa, A., Davis, S. M., Degenstein, D., Frith, S. M., Froidevaux, L., Kyrölä, E., Laine, M., Long, C., Penckwitt, A. A., Sioris, C. E., Rosenlof, K. H., Roth, C., Wang, H.-J., and Wild, J.: Intercomparison of vertically resolved merged satellite ozone data sets: interannual variability and long-term trends, Atmos. Chem. Phys., 15, 3021–3043, https://doi.org/10.5194/acp-15-3021-2015, 2015.

Ulaby, F. and Long, D.: Microwave Radar and Radiometric Remote Sensing, chaps. 6–7, University of Michigan Press, 226–320, https://doi.org/10.3998/0472119356, 2014.

University of Bern: Bern Open Repository and Information System BORIS, https://boris-portal.unibe.ch/cris/project/pj00023, last access: 27 June 2022.

von der Gathen, P., Kivi, R., Wohltmann, I., Salawitch, R. J., and Rex, M.: Climate change favours large seasonal loss of Arctic ozone, Nat. Commun., 12, 1–17, https://doi.org/10.1038/s41467-021-24089-6, 2021.

Waters, J., Froidevaux, L., Harwood, R., Jarnot, R., Pickett, H., Read, W., Siegel, P., Cofield, R., Filipiak, M., Flower, D., Holden, J., Lau, G., Livesey, N., Manney, G., Pumphrey, H., Santee, M., Wu, D., Cuddy, D., Lay, R., Loo, M., Perun, V., Schwartz, M., Stek, P., Thurstans, R., Boyles, M., Chandra, K., Chavez, M., Chen, G.-S., Chudasama, B., Dodge, R., Fuller, R., Girard, M., Jiang, J., Jiang, Y., Knosp, B., LaBelle, R., Lam, J., Lee, K., Miller, D., Oswald, J., Patel, N., Pukala, D., Quintero, O., Scaff, D., Van Snyder, W., Tope, M., Wagner, P., and Walch, M.: The Earth observing system microwave limb sounder (EOS MLS) on the aura Satellite, IEEE T. Geosci. Remote, 44, 1075–1092, https://doi.org/10.1109/TGRS.2006.873771, 2006.

Ziemke, J. R., Labow, G. J., Kramarova, N. A., McPeters, R. D., Bhartia, P. K., Oman, L. D., Frith, S. M., and Haffner, D. P.: A global ozone profile climatology for satellite retrieval algorithms based on Aura MLS measurements and the MERRA-2 GMI simulation, Atmos. Meas. Tech., 14, 6407–6418, https://doi.org/10.5194/amt-14-6407-2021, 2021.

5 | Spectrometer assessment for ozone microwave radiometer

The Acqiris AC240 used in GROMOS and SOMORA is a digital spectrometer initially developed in Switzerland during the 2000s for radio astronomy (Benz et al., 2005). It was one of the first commercially available real-time spectrometer used for atmospheric remote sensing in microwave radiometry and, at the time, this novel digital spectrometer presented quite an improvement compared to the previous spectrometer types (Müller et al., 2009).

Despite being widely used in microwave radiometry, the full characterization of the AC240 spectroscopic performance remains largely unknown. During the decade 2010-2020, some publications reported a persistent bias from ozone and water vapour time series measured with the AC240 and installed on different instruments, without finding any satisfying explanations for the bias (Nedoluha et al., 2011; Tschanz et al., 2013; Orte et al., 2019). This suspicious bias motivated further investigations and a measurement campaign was performed in collaboration between the IAP of the University of Bern and the U.S. Naval Research Laboratory (NRL) during the design of a new radiometer front-end for the Microwave Ozone Profiling Instrument (MOPI) (Kotiranta et al., 2019). This chapter summarizes the bias investigations done with the data collected during this measurement campaign and shows the resulting study published in Sauvageat et al., 2020.

Using the newly developed front-end for MOPI, the measurement campaign was setup to compare the AC240 against two other high-resolution digital real-time spectrometers. For 6 months, from January to June 2019, parallel measurements of the ozone emission line at 110.836 GHz from the three spectrometers were recorded. Hot-cold calibration was performed with an ambient target and liquid nitrogen (LN_2). Preliminary results from this campaign were shown in Murk and Kotiranta, 2019 who found that the AC240 was biased compared to the other, more recent digital spectrometers.

These preliminary results were the starting point of my study. The main goal was to investigate in greater details the observed bias and to characterize its influence on atmospheric trace gases retrievals, in particular ozone. As GROMOS and SOMORA use the AC240 since 2009, the hope was to better understand the bias of this spectrometer to provide a correction to the ozone time measured since 2009 on these two instruments.

In this study, we therefore investigated the sensitivity of the bias to the atmospheric conditions and found that the bias is caused by multiples sources. Among them, non-linearities in the characteristic curve of the AC240 produce a broadband, but small bias compared to the two other spectrometers. A larger and more important bias originates from some sort of spectral leakage in the AC240. This spectral bias is more problematic because it results in a scaling of the observed atmospheric emission and therefore directly impacts the retrieval of ozone profile. In fact, a bias of $\sim 10\%$ was found on ozone profile retrieved from the AC240 compared to the other spectrometers.

Although we were not able to identify the source of such leakage, we were able to reproduce it quite accurately with a remarkably simple correction scheme. It consists of a scaling of the observed spectrum with a factor of $\sim 8\%$ which succeeds at correcting the bias of the ozone profiles retrieved from the AC240. At the time of this study, we tried to reproduce the bias with laboratory measurements with limited success. We could observe some spectral leakage from

the AC240 in the measurements but with a significantly lower amplitude that the bias observed during the measurement campaign.

Since this publication, I have continued the investigations of the spectral bias on the AC240. Notably, I have compared the GROMOS instrument with co-located measurements from the Wind Radiometer for Campaigns (WIRA-C). WIRA-C is a campaign wind radiometer which also observed the ozone emission line at 142 GHz. It was placed on the roof of the University of Bern, next to the GROMOS instrument in 2022. It uses a USRP X310 spectrometer while GROMOS still uses the AC240. Therefore, I have made some more parallel measurements between the two instruments and again observed a spectral bias from the AC240. The bias was of similar magnitude than the one observed during the MOPI campaign, with a spectral leakage of $\sim 10\%$ from the AC240 compared to the USRP measurements. These measurements are not published but they provided an additional confirmation that the spectral leakage of the AC240 is real and seems to impact all the AC240 spectrometers in a comparable way. In addition, two new, independent measurement studies reported a bias from the AC240 with similar amplitude, supporting the need to correct for it in further studies (e.g., Nedoluha et al., 2022; Bell and Murk, 2023). This is why I decided to apply this correction for the new extended time series of GROMOS (see Section 7.2.1).

5.1 Publication: Real-time spectrometers comparison

This study was the first one published in the frame of this thesis. I presented it at the 16$^{\text{th}}$ Specialist Meeting on Microwave Radiometry and Remote Sensing of the Environment (MICRORAD) in 2020. It was then published as a conference paper and finally as a peer-reviewed publication in the *IEEE Journal of Selected Topics in Applied Earth Observations and Remote Sensing*.

Citation of the conference paper:

Sauvageat, E., Kotiranta, M., Hocke, K., Gomez, R. M., Nedoluha, G., and Murk, A. (2020). "Comparison of three high resolution real-time spectrometers for microwave ozone profiling instruments". In: *2020 16th Specialist Meeting on Microwave Radiometry and Remote Sensing for the Environment (MicroRad)*, pp. 1–4. DOI: 10.1109/MicroRad49612.2020.9342608.

Citation of the peer-reviewed publication:

Sauvageat, E., Albers, R., Kotiranta, M., Hocke, K., Gomez, R. M., Nedoluha, G. E., and Murk, A. (2021). "Comparison of Three High Resolution Real-Time Spectrometers for Microwave Ozone Profiling Instruments". In: *IEEE Journal of Selected Topics in Applied Earth Observations and Remote Sensing* 14, pp. 10045–10056. DOI: 10.1109/JSTARS.2021.3114446.

IEEE JOURNAL OF SELECTED TOPICS IN APPLIED EARTH OBSERVATIONS AND REMOTE SENSING, VOL. 14, 2021 10045

Comparison of Three High Resolution Real-Time Spectrometers for Microwave Ozone Profiling Instruments

Eric Sauvageat, Roland Albers, Mikko Kotiranta, Klemens Hocke, R. Michael Gomez, Gerald E. Nedoluha, and Axel Murk

***Abstract*—In this contribution, we present a comparison of three digital real-time spectrometers used in passive remote sensing of ozone and other trace gases in the middle atmosphere. During a period of six months, we connected the spectrometers to the same radiometric front-end to perform parallel observations of the ozone emission line at 110.836 GHz. This allowed us to better characterize a bias previously observed on the integrated spectra of the Acqiris AC240, a widely used digital spectrometer which has been used for more than a decade in many operational microwave radiometers. We investigated the bias under different atmospheric conditions and found that it is caused by multiple sources. Nonlinearities in the calibration are responsible for part of the bias, but a larger contribution stems from a second effect in the AC240. Although this error source is still partly unexplained, we found that a simple correction scheme simulating a spectral leakage can be applied to the integrated spectra of the AC240 and worked well on our range of observations. We also show that by applying our bias correction to the spectra, we can correct the bias in the ozone retrievals. There is still a need for further measurements to validate this approximate correction, but it could help to correct the numerous time series of ozone and other atmospheric constituents recorded by the AC240.**

***Index Terms*—Atmospheric measurements, digital real-time spectrometers, microwave radiometry, microwave spectroscopy, ozone, remote sensing, water vapor.**

I. Introduction

MICROWAVE ground-based radiometers provide continuous, all-weather observations of many constituents in the atmosphere. Compared to satellites, they have a high temporal resolution and are therefore important for estimating long-term trends in atmospheric gas concentrations and for cross validating satellite observations. In particular, they have been used successfully for monitoring ozone, water vapor, temperature, carbon monoxide, and winds in the middle atmosphere [1]–[4].

These instruments are particularly well suited for the observation of ozone in the stratosphere (the so-called "ozone layer") and in the lower mesosphere, i.e., from approximately 20 to 70 km altitude. Thanks to multiple ozone transition lines in the microwave frequency range and to the pressure broadening mechanism, it is possible to retrieve the vertical ozone mixing ratio profile in the stratosphere and the lower mesosphere through the so-called inversion problem [5]. Therefore, microwave radiometers have been used for ozone profiling in a variety of locations, especially since the Montreal Protocol (1987). Following the ban of the ozone depleting substances, the assessment of ozone recovery in the middle atmosphere has become a key scientific topic [6]. Due to their long lasting time series and their nearly continuous sampling capabilities, microwave ozone radiometers are important instruments to assess the ozone trends of the last two decades.

Today, most microwave radiometers for middle atmospheric sounding are using high-resolution real-time spectrometers to extract the spectral information from the atmospheric radio frequency (RF) signal. In the last decade, real-time digital spectrometers have progressively replaced the older acousto-optical (AOS), chirp-transform or filter bank (FB) spectrometers in radio astronomy and atmospheric remote sensing. Initially designed for radio astronomy, the Acqiris AC240 was the first commercially available spectrometer used in atmospheric profiling radiometers [7], [8]. Since then, it has been used in many instruments worldwide, in particular in ozone, temperature, and water vapor profiling radiometers. Despite the numerous time series collected with the AC240, its spectroscopic performance remains largely unknown and has not yet been quantified.

Different publications have shown a persistent negative bias in the time series derived from the AC240 compared to other datasets, but its origin has yet to be determined [9]–[12]. It concerns both ozone and water vapour instruments, which for most of them, are operated in the frame of the Network for the Detection of Atmospheric Composition Change (NDACC) [13]. Despite generally high uncertainties on passive radiometric observations, this persistent bias has raised some questions about the AC240 and some users have expressed the need for a more thorough investigation of the influence of this back-end on the measurements.

Manuscript received May 30, 2021; revised August 25, 2021; accepted September 15, 2021. Date of publication September 22, 2021; date of current version October 15, 2021. The work of R. Michael Gomez and Gerald E. Nedoluha was supported in paty by NASA under the Upper Atmosphere Research Program and in part by the Office of Naval Research. (*Corresponding author: Eric Sauvageat.)*

Eric Sauvageat, Klemens Hocke, and Axel Murk are with the Institute of Applied Physics and the Oeschger Centre for Climate Change Research, University of Bern, 3012 Bern, Switzerland (e-mail: eric.sauvageat@iap.unibe.ch; klemens.hocke@iap.unibe.ch; axel.murk@iap.unibe.ch).

Roland Albers and Mikko Kotiranta are with the Institute of Applied Physics, University of Bern, 3012 Bern, Switzerland (e-mail: roland.albers@iap.unibe.ch; mikko.kotiranta@iap.unibe.ch).

R. Michael Gomez and Gerald E. Nedoluha are with the Remote Sensing Division, U.S. Naval Research Laboratory, Washington, DC 20375 USA (e-mail: mike.gomez@nrl.navy.mil; gerald.nedoluha@nrl.navy.mil).

Digital Object Identifier 10.1109/JSTARS.2021.3114446

Parallel measurements of atmospheric emission lines with different back-ends enable us to characterize their spectroscopic performance and quantify their influence on the atmospheric profiles. The only studies comparing the AC240 with other spectrometers were done at the time when the AC240 replaced older FB and AOS back-ends in some ozone radiometers, with the goal to homogenize the time series (using the AC240 as the reference) [14], [15]. These studies both show an altitude dependent bias (with a globally negative trend) from the time series derived from the AC240 compared to the older spectrometers. However, it has to be noted that the change from an FB or AOS to a high resolution FFT spectrometer also has other impacts on the time series (e.g., from the change in bandwidth or spectral resolution) that can influence the results of such comparisons significantly.

This study aims at presenting a first intercomparison between digital real-time spectrometers used in passive microwave remote sensing, including the AC240 and two state-of-the-art spectrometers. We compared the influence of these three digital back-ends on radiometric observations of the ozone emission line at 110.836 GHz. We organized a measurement campaign between January and June 2019 at the University of Bern and conducted a first set of analysis described in [16] and [17]. First results from this campaign suggested that the calibrated spectra from the AC240 was systematically biased, measuring a smaller ozone line amplitude and a different slope compared to the more recent spectrometers. To better characterize these discrepancies, we expanded on the previous analysis by investigating the sensitivity of the bias to the weather conditions and by quantifying its impact on the retrieved ozone profiles. We evaluated the effect of a simple correction scheme on the integrated spectra and the middle-atmospheric ozone profiles. In addition, we conducted new laboratory tests aiming to confirm the observed bias and help understand its origin.

The rest of this article is organized as follows. Section II describes the instrumental setup that was used during the measurement campaign and for the laboratory tests. Section III describes the measurement campaign and the associated data processing, from the calibration to the ozone retrievals. It presents and discusses the results of the campaign and their limitations. A discussion of the bias origin is made in Section IV, together with the latest laboratory investigations that we conducted to better understand it. Finally, a brief conclusion and outlook are presented in Section V.

II. Instrumental Setup

The microwave ozone profiling instruments (MOPI) are a series of ground-based radiometers operated by the United States Naval Research Laboratory (NRL) in the frame of NDACC. Since 1995, the MOPI instruments are monitoring ozone in the middle-atmosphere above Mauna Loa, Hawaii, and Lauder New Zealand [2].

As a front-end for our measurement campaign, we have used MOPI 5, which is a new, room temperature receiver designed at the Institute of Applied Physics (IAP) at the University of Bern as a replacement of the current MOPI cryogenic receiver. MOPI 5 is a single side band heterodyne receiver designed for the observation of the thermal emission line of ozone at 110.836 GHz. It uses state-of-art frond-end components and works at room temperature with a single side band noise temperature of around 550 K. A more thorough description of the MOPI 5 receiver can be found in [18].

A. Spectrometers

In most radiometers, the radio frequency (RF) signal is down-converted and processed before being analyzed by a spectrometer. Within the spectrometer, different techniques exist to extract the spectral information from the RF signal. With the increase of computational capacity in the last two decades, most spectrometers are now using digital signal processing methods: the RF signal is sampled by a fast analog-to-digital converter (ADC) and fed to a field programmable gate array (FPGA) processor that calculates the spectral components of the signal in real-time.

The Acqiris AC240 was the first commercial fast Fourier transform (FFT) spectrometer used for atmospheric remote sensing. It was developed in 2005 in a collaboration between the company Acqiris and Swiss universities [7], [8]. Since then, it has been widely used in middle atmospheric studies, for ozone, water vapor or temperature profiling around the world.

At the time of the AC240 development, the available FPGA resources did not allow to calculate the FFT on the full 1 GHz bandwidth without small truncation errors. It results in small but noticeable artifacts, especially when higher integration times are needed, which is often the case for ozone profiling instruments. For this reason, the AC240 has now been replaced by the Acqiris U5303 A, which features an improved dynamic range, a larger bandwidth and does not suffer from numerical truncation errors anymore [19].

For this study, we used a U5303 A with a customized spectrometer firmware developed in a collaboration between IAP, Acqiris, and other Swiss universities (simply U5303 from now on). It processes a 1.6 GHz bandwidth and includes some advanced features such as I/Q signal processing with amplitude and phase correction as well as cross correlation that we did not use for our measurements. It also uses a polyphase filter bank (PFB) algorithm, which improves the channel response compared to the FFT algorithm without significant loss of sensitivity [16]. Fig. 1 shows the measured channel responses of the AC240 (FFT) and the U5303 (PFB). Compared to the FFT, which follows very closely the expected $|\operatorname{sinc}(x)|^2$ behavior, the PFB shows much faster sidelobe roll-off and a much better channel separation.

Together with the two Acqiris spectrometers, we have used the USRP X310 from Ettus Research, which is a software defined radio (SDR) receiver [20]. For this study, it was used with a customized FFT spectrometer firmware, processing a 200 MHz bandwidth around the ozone line frequency. As an option, the USRP bandwidth can be extended by frequency switching to observe a broader spectral region, and therefore to get profiling capabilities at lower altitudes [21]. For instance, this spectrometer is now operated in our two wind monitoring radiometers observing the ozone emission line at 142 GHz [22]. The main characteristics of the spectrometers used in this study are shown

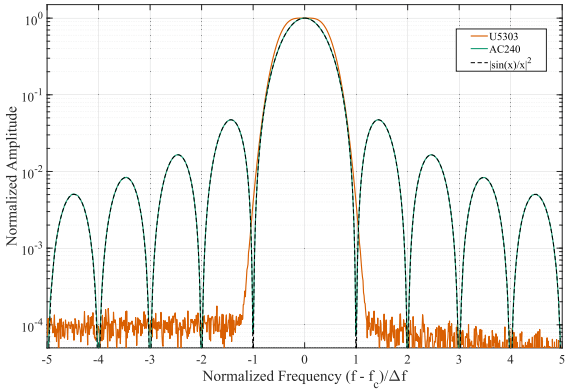

Fig. 1. Measured channel responses of the AC240 and the U5303. The amplitude is normalized to the center channel and the frequency axis is normalized with the channel spacing for both spectrometers. The black dashed line (superimposed to the green line) is the theoretical channel response for an FFT spectrometer with a rectangular window function.

TABLE I
DIGITAL SPECTROMETERS USED IN THIS STUDY

Model	Bandwidth	ADC	Δf	Type
AC240 Acqiris	1000 MHz	8 bits	61.04 kHz	FFT
U5303 Acqiris	1600 MHz	12 bits	97.66 kHz	PFB
USRP Ettus	200 MHz	14 bits	12.21 kHz	FFT

in Table I. A more detailed comparison of the spectrometers and how they were connected to the front-end can be found in [16].

III. Measurement Campaign

Between January and June 2019, we operated a test instrument based on the MOPI 5 receiver (denoted simply MOPI 5 from now on) on the roof of one of the buildings of the University of Bern (47°N) in Switzerland [18]. As back-ends, the AC240, U5303 and USRP were connected in parallel to the instrument and provided simultaneous observations of the atmospheric ozone emission line at 110.836 GHz at an elevation angle of 40°. The radiometer was calibrated by switching continuously between the atmospheric signal, an ambient temperature calibration target and a liquid nitrogen (LN2) cold target. If we neglect the time needed for technical maintenance, MOPI 5 provided more than 350 h of parallel observations with the three spectrometers. Despite the laborious manual refilling of the liquid nitrogen target, the observations covered a broad range of atmospheric conditions distributed mostly over four months (January to April). An example of the time series recorded during the month of February is shown in Fig. 2.

A. Calibration and Integration

To investigate the bias between the calibrated spectra of the AC240 and the two other back-ends previously described in [16], we have devised new harmonized calibration and integration routines for the three spectrometers. They use a hot–cold calibration scheme and compute 10 min averaged brightness temperature spectra for each spectrometer. Based on a set of

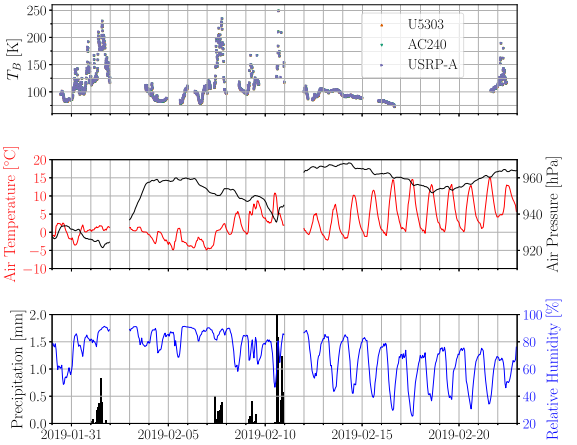

Fig. 2. Time series with 10 min averaged brightness temperature (T_B) from the 3 spectrometers (top panel), hourly averaged air pressure and temperature (middle panel), and precipitation and relative humidity (bottom panel) recorded in Bern.

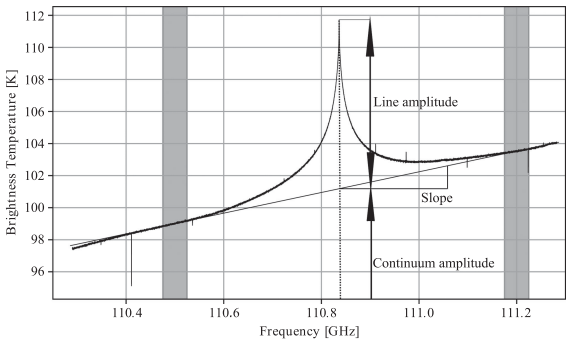

Fig. 3. Sketch of the parameters used for the bias description. The shaded area show the frequency bands used to fit the slope of the spectra. The continuum amplitude ($T_{B,c}$) is the brightness temperature at which the fitted slope crosses the line center frequency. The line amplitude ($T_{B,l}$) is the difference between the emission peak and the continuum amplitude.

additional parameters (noise temperature spectrum, number of spectra for each target, etc.), this new routine identifies the periods where technical problems occurred on the instrument and flags the corresponding calibrated spectra. It enables one to sort out the spectra of dubious quality before integration.

To improve our understanding of the bias, we decided to investigate the relationship between the bias and the atmospheric opacity. At microwave frequencies increases in tropospheric water vapor are the main cause of increasing opacity, and hence increasing continuum brightness temperature and decreasing stratospheric ozone line strength. In the case of the MOPI 5 observations at 110.836 GHz, the oxygen emission band at 118 GHz additionally induces a characteristic slope in the calibrated spectrum, with a brightness temperature increasing towards higher frequencies (see Fig. 3). Therefore, it is possible to compute the tropospheric opacity observed during each calibration cycle from its mean spectral brightness temperature $T_{B,mean}$ using the method described in [23]. It enables sorting of

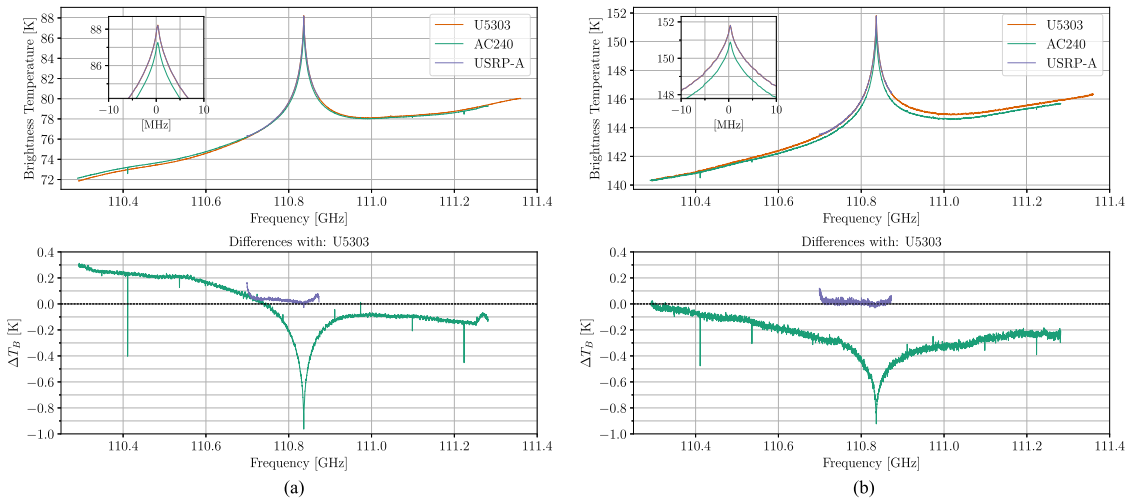

Fig. 4. Comparison of the integrated spectra recorded from the three spectrometers in February 2019 for two brightness temperature bins, corresponding to two different atmospheric opacities. The details of the calibration and integration processes are described in the text. (a) Low atmospheric opacity: $T_{B,mean} < 80$ K. (b) High atmospheric opacity: 140 K $< T_{B,mean} <$ 150 K.

the calibrated spectra based on their tropospheric opacity before integration. Note that in order to get meaningful results, integrating the same calibration cycles from the three spectrometers is required.

Taking the U5303 as the reference, we computed the mean calibrated brightness temperature from the central channels for each spectrum and collated the calibrated spectra into different brightness temperature (T_B) bins before integration. For the February time period, it resulted in 15 different T_B bins, with $T_{B,mean}$ ranging from 75 to 210 K. Note that we used the same integration periods for the three spectrometers but that the integration time for each T_B bin is different as the number of calibrated spectra belonging to each bin is different.

B. Bias Description and Correction

Fig. 4 shows a comparison of the integrated spectra from the three spectrometers for two different T_B bins (out of 15) recorded during the month of February. On the February time period, the integrated spectra from the USRP and the U5303 agree very well, with an averaged brightness temperature difference $|\Delta T_B| < 20$ mK at the frequency line center (± 25 MHz) for all bins. On the contrary, the AC240 shows a systematic negative bias at the line center ($|\Delta T_B| > 0.4$ K at all bins) and a different spectral slope, which confirms the bias previously observed on the daily spectra by [16]. In addition, the negative bias at the line center and the slope difference on the AC240 are more pronounced at lower tropospheric opacity [see Fig. 4(a)] compared to the higher tropospheric opacity case [see Fig. 4(b)]. The differences shown in Fig. 4 underline the significance of the bias seen on the AC240 but they do not enable identification of its potential sources.

In order to get a better description of the bias observed on the AC240, we computed the three parameters sketched in Fig. 3, i.e., line amplitude, slope, and continuum amplitude for each integrated spectrum. To study the relationship between the bias and the brightness temperature, we computed these parameters on hourly integrated spectra from the two broadband spectrometers. Compared to the spectra based on T_B bins, it allows us to get more data points and a constant integration time (1 h).

Fig. 5 shows the differences between the parameters evaluated for the U5303 and the AC240 hourly integrated spectra between January and April 2019. It confirms a certain consistency of the bias on the MOPI 5 time series and illustrates its dependency to the brightness temperature. Both the line amplitude and the slope biases follow a close to linear trend with the brightness temperature, which is in accordance with the first observations made from Fig. 4.

Whereas the line amplitude and slope biases have a similar shape, this is not the case for the continuum bias shown in Fig. 5(c). It suggests that the full bias might be a combination of multiple error sources.

Most radiometers assume a linear amplitude transfer characteristic between the calibration loads and the sky observation. It is usually a good approximation but never exactly true and any departure from linearity would result in a bias on the calibrated spectra. From now on, we will refer to this bias simply as "nonlinearities" to distinguish it from the other error sources. As a first order approximation, this nonlinearity is often taken into account by adding a quadratic term on the linear transfer characteristic. It results in a negligible bias when the observed spectrum matches the temperature of one of the calibration loads and in a maximum bias in between. In general, the calibration bias can be derived from a set of brightness measurements at different scene temperatures (as done in [24], [25]). In our case, we can make use of our parallel spectrometers and use the sky measurements directly. As both the U5303 and the USRP

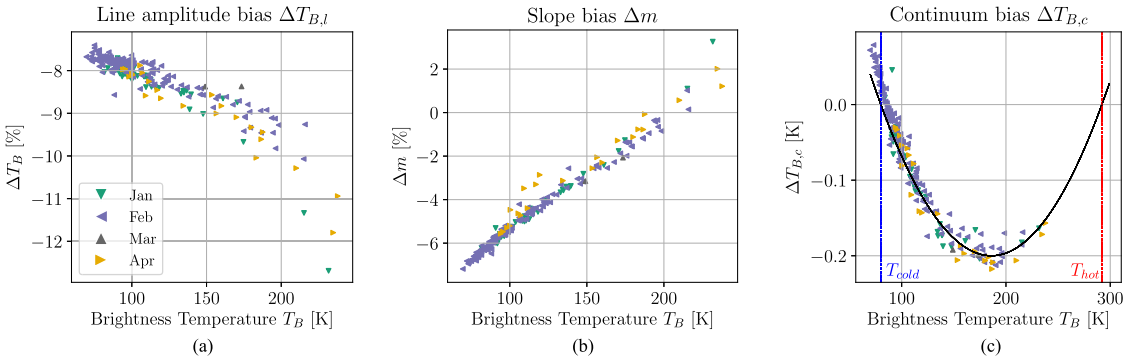

Fig. 5. Parameters from Fig. 3 computed on hourly integrated spectra between January and April 2019. All three panels show the difference between the parameters computed on the AC240 and the U5303 as a function of the mean brightness temperature of the integrated spectra. (a) Relative differences of the line amplitude bias. It is computed as a fraction of the line amplitude as defined in Fig. 3. For instance for $T_B = 100$ K, the line amplitude is ≈ 10 K so that the line amplitude bias is ≈ 0.8 K (or $\Delta T_{B,l} = 8\%$.) (b) Relative differences of the slope bias computed as a fraction of the fitted slope on the U5303. (c) Absolute differences in the continuum bias. The black line shows the modeled quadratic calibration bias that accounts for the nonlinearities.

correspond on the whole range of brightness temperature, we can consider their measurements as the true scene temperature and assume that the continuum bias seen in Fig. 5(c) arises from nonlinearities in the AC240. We can then apply a quadratic correction term to account for its nonlinear amplitude transfer characteristic.

The black line in Fig. 5(c) shows modeled nonlinearities resulting from such a quadratic correction term. It has been derived from the continuum difference between the AC240 and the U5303 ($\Delta T_{B,c}$), setting $\Delta T_{B,c} = 0$ at T_{cold} and T_{hot} and approximating a maximal continuum bias $\Delta T_{B,c} = -0.2$ K in between both calibration load temperatures at

$$T_B = \frac{T_{hot} + T_{cold}}{2} \approx 185\,\mathrm{K}. \tag{1}$$

With this simple assumption we are able to reproduce the continuum bias quite well, although our observations do not match the black line in Fig. 5(c) exactly. This might be explained by the fact that T_{hot} is assumed constant for the whole time series and maybe more importantly, because the mean brightness temperature (abscissa of Fig. 5) is actually computed around the line center, which means that it is a slight overestimation of the full spectrum averaged brightness temperature. Also, we would need more observations at higher brightness temperatures to accurately fit the maximal bias value but as a first estimation, this simple correction is able to correct quite accurately for the nonlinearities on the MOPI 5 measurements.

Although the nonlinearities can account for the continuum bias, they do not explain the line amplitude and slope biases. Looking at Fig. 6(a), we see that even though T_B is close to the cold load temperature ($T_B \approx 80$ K), the slope and line amplitude biases are significant, when they should be close to zero if they were only due to nonlinearities. Both seem to follow a close linear relationship with T_B with larger uncertainties at higher T_B. The growing spread of the data points with T_B is explained from the growing continuum emission (which is absorbing most of the ozone line features at higher T_B) combined to a lower number of observations at higher T_B.

The line amplitude and slope biases seem to be the results of a significant "spectral leakage" that would impact the AC240. We still do not understand what exactly could cause such a leakage (see section IV), but it resembles the result of a constant brightness temperature scaling on the AC240. Using a constant scaling factor and incorporating our modeled nonlinearities, we are able to provide a first order correction for the integrated spectra of the AC240

$$T_{B,corr} = \frac{1}{(1-\alpha)}(T_B - \alpha\overline{T_B} - \Delta T_{B,c}) \tag{2}$$

where $T_{B,corr}$ is the corrected brightness temperature spectrum, α is a scaling factor, $\overline{T_B}$ is the mean value of the measured spectrum calculated over the entire bandwidth of the AC240, and $\Delta T_{B,c}$ is the nonlinearity correction described above.

Fig. 6 shows the comparisons between the integrated spectra from the U5303 and the AC240 for two atmospheric opacities and three different cases: the original bias (green lines) and the corrected spectra using a constant scaling factor with (purple) and without (grey: $\Delta T_{B,c} = 0$) the nonlinearity correction. We see that (2) is able to reduce the bias between the AC240 and the U5303. The correction for nonlinearities limits the broadband bias observed when the brightness temperature moves away from the calibration load temperatures, whereas the scaling factor is effective at reducing the slope and the line center biases. We find that a constant scaling factor ($\alpha = 8\%$) works well for the range of brightness temperatures observed, not only for the month of February but also for the rest of the MOPI 5 observations.

To summarize, it seems that the full bias is a combination of nonlinearities and of a spectral leakage on the AC240. The nonlinearities can be modeled, corrected and it is essentially a broadband contribution to the spectrum which depends on the atmospheric conditions (or on $T_{B,mean}$). On the contrary, the fractional spectral bias seems to remain more or less independent of the atmospheric conditions because a constant scaling parameter is able to correct for the whole range of

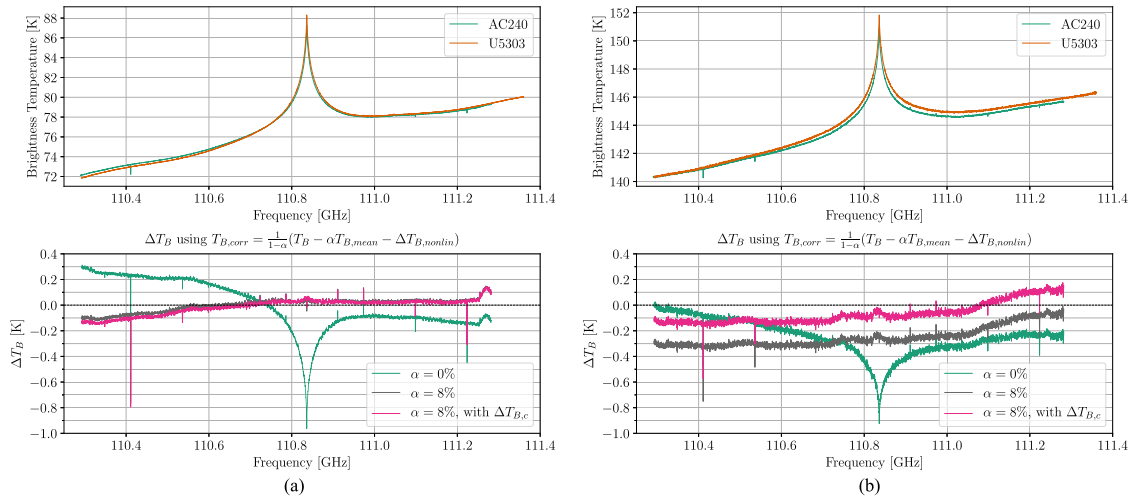

Fig. 6. Comparison of the AC240 and the U5303 integrated spectra recorded for two brightness temperature bins, corresponding to two different atmospheric opacities. The bottom panels show the absolute brightness temperature differences between the AC240 spectra before (green line as in Fig. 4) and after it is corrected according to (2). The grey curves do not account for nonlinearities ($\Delta T_{B,c} = 0$) whereas the purple ones show the full correction with modeled nonlinearities. (a) Low atmospheric opacity: $T_{B,mean} < 80$ K. (b) High atmospheric opacity: 140 K $< T_{B,mean} <$ 150 K.

atmospheric conditions. The fact that the line amplitude and slope biases evolve with T_B (see Fig. 5) might be related to the way these parameters are computed and it will need further studies to validate the dependency of the spectral bias on the atmospheric conditions. Note that the spectral leakage is much more significant for ozone retrievals than the nonlinearities: the former impacts the line amplitude and the slope of the spectrum directly while the latter is essentially a broadband contribution. The line amplitude bias is of particular concern because of its amplitude (≈ 8 to 9% at the line center) and its immediate impact on the retrieved ozone profile whereas the continuum and slope biases are usually fitted before or during the retrieval process.

C. Ozone Retrievals

To study the effect of the observed bias and its approximate correction on the atmospheric profiles, we performed ozone retrievals from the MOPI 5 integrated spectra. At microwave frequencies, the pressure broadening of thermal emission lines enables us to retrieve vertical profiles of atmospheric gases from passive radiometric observations at selected frequencies (e.g., 110.836 GHz for ozone). A retrieval consists at finding the best estimate of the real profile from the shape of the integrated spectra, the measurement errors, a set of *a priori* information, and a so-called forward model [5]. In microwave radiometry, the forward model is essentially a radiative transfer model that describes the physical relationship between the ozone profiles and the radiometric observations.

As for the calibration routine, we have devised a new routine to retrieve atmospheric ozone profiles from the MOPI 5 measurements at 110.836 GHz. As a forward model, we have used the latest version of the atmospheric radiative transfer simulator 2.4 (ARTS) [26]. It is a radiative transfer simulation software with a focus on the microwave region and it also includes some instrumental effects (e.g., channel response) on the simulated spectra. It simulates the atmospheric emission spectra at the radiometer location according to given atmospheric conditions (pressure, temperature, and atmospheric constituents). ARTS provides a large choice of predefined atmospheric scenarios that can be used as inputs for the forward model.

In this study, we used the Fascod climatology, more specifically its mid-latitude winter atmospheric scenario [27]. It is included in the ARTS package and provides all relevant atmospheric variables for the forward model. As *a priori* ozone profiles, we used a monthly climatology derived from the European Centre for Medium-Range Weather Forecasts (ECMWF) operational reanalysis extended by an AURA/MLS climatology above around 70 km (similarly as [14]). The spectroscopic parameters were taken from the high-resolution transmission molecular absorption database (HITRAN) [28]. Following the formalism of [5], the optimal estimation method is now integrated within the ARTS package itself, which enables the inversion of the integrated spectra directly within ARTS. This setup was used successfully in [21] for ozone retrievals at 142.175 GHz.

Water vapour is the main contributor to opacity at microwave frequencies and is mainly found in the troposphere. Therefore, its contribution to observation of middle-atmospheric ozone is essentially a broadband absorption of radiation emitted by the ozone molecules and it is often removed by a so-called tropospheric correction [23]. In our case, the water vapour continuum absorption was retrieved together with ozone directly from the integrated spectra. Also, due to the lack of standing wave attenuation techniques during the MOPI 5 campaign, we had to include some baseline features to the retrievals (polynomial and sinusoidal) to obtain converging results. As the

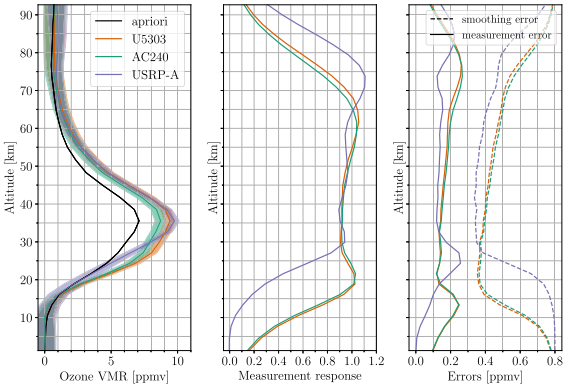

Fig. 7. Example of ozone retrievals from the three spectrometers for the integrated spectra shown in Fig. 4(a). The left panel shows the ozone volume mixing ratio (VMR) with its associated total error, the middle panel shows the measurement response (MR), and the right panel shows the smoothing and measurement errors from the retrievals (see text for details).

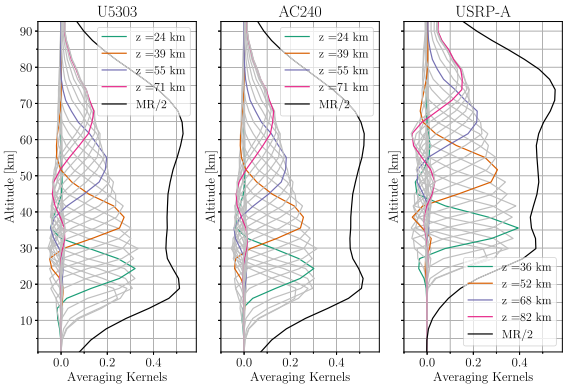

Fig. 8. Averaging kernels (AVKs, grey lines) and measurement responses (MR) corresponding to the ozone retrievals shown in Fig. 7 for the three spectrometers. For clarity, the MR has been divided by 2 (black lines) to be plotted together with the AVKs. We have highlighted some AVKs and labelled them with their corresponding altitude.

integration time was different for each integrated spectrum, it resulted in very different noise levels that had to be taken into account in each retrieval and therefore, the noise covariance matrix was adapted for each brightness temperature bin to get the best possible retrieval. Note that the rest of the retrieval setup (forward model, *a priori*, spectroscopy, etc.,) was identical for the three spectrometers.

Besides the ozone volume mixing ratio (VMR) profiles, the optimal estimation method provides diagnostic quantities that can be used to derive the averaging kernels (AVKs) or the uncertainty budget of the retrievals (see [5] for more details). The AVKs describe the sensitivity of the retrieval to changes in the true ozone profile and is used to compute the measurement response (MR). The MR is the sum of the AVKs for each altitude and quantifies the amount of information contained in the retrievals that is coming from the actual measurements at a given altitude (the remaining part is coming from the *a priori* profile). For instance, a MR over 0.8 indicates that the contribution of the radiometric measurements to the "optimal estimated" profile is higher than 80%, i.e., that the *a priori* contribution is less than 20%. In the case of ozone retrievals, the errors can be separated into three main components: the errors related to the forward model (neglected in the following because they are the same for the three spectrometers), the so-called smoothing error and the measurement error (or retrieval noise). The smoothing error arises from the limited spatial resolution of the microwave radiometer, which prevents resolving fine vertical structure in the profile. The measurement error is linked with uncertainties in the radiometric measurement (e.g., thermal noise). The sum of the smoothing and the measurement error is usually called the total error. A representative example of ozone VMR profiles retrieved from the different spectrometers is shown in Fig. 7 together with their respective measurement responses and retrieval errors characterization. Fig. 8 shows the corresponding AVKs for these specific retrievals, which correspond to the integrated spectra from the first T_B bin shown in Fig. 4(a).

D. Bias on the Ozone Profiles

To compare the ozone profiles retrieved from the three spectrometers, it is important to underline some of the features shown in Figs. 7 and 8. We see on these figures that the MRs from the AC240 and the U5303 are very similar whereas the MR from the USRP is quite different and seems shifted towards higher altitudes. It is explained by its smaller bandwidth and higher spectral resolution compared to the AC240 and the U5303 (see Table I), which enables the USRP to retrieve ozone profile from ≈ 30 to 80 km altitude (MR $\geqslant 80\%$ is often considered as a lower limit for meaningful retrievals, i.e., when the contribution from the *a priori* to the final profile is lower than 20%), whereas the AC240 and the U5303 have retrievals capabilities from ≈ 20 to 70 km. The declining MR of the USRP at low altitudes means that from 30 km downward, the retrieved ozone profile from the USRP is increasingly influenced by the *a priori* profile and so it explains the strong deviation of the USRP ozone profile from the AC240 and the U5303 below 30 km (see Fig. 7). Between 30 and 60 km, the retrieved profiles from the USRP and the U5303 are in good agreement (e.g., the mean relative difference between the ozone profiles is less than 3%), despite some remaining oscillations in some of the retrievals as discussed later. The AC240 and U5303 have similar retrieval capabilities (similar AVKs and MRs) so they can be compared directly. Between 20 and 60 km, the AC240 profile in Fig. 7 shows a strong negative ozone bias compared to the U5303, with close to 0.5 ppmv less ozone retrieved from the AC240 at the ozone peak around 35 km altitude.

To evaluate the effect of the spectral and nonlinearity corrections (2) on the ozone profiles, we also retrieved the corrected integrated spectra from the AC240 with the same retrieval routine. Focusing on the ozone difference between the two broadband spectrometers, Fig. 9 shows examples of the relative bias between the AC240 and the U5303 before and after applying the correction on the AC240 integrated spectra. Fig. 10 shows the relative ozone bias (averaged on 10 km altitude ranges) of

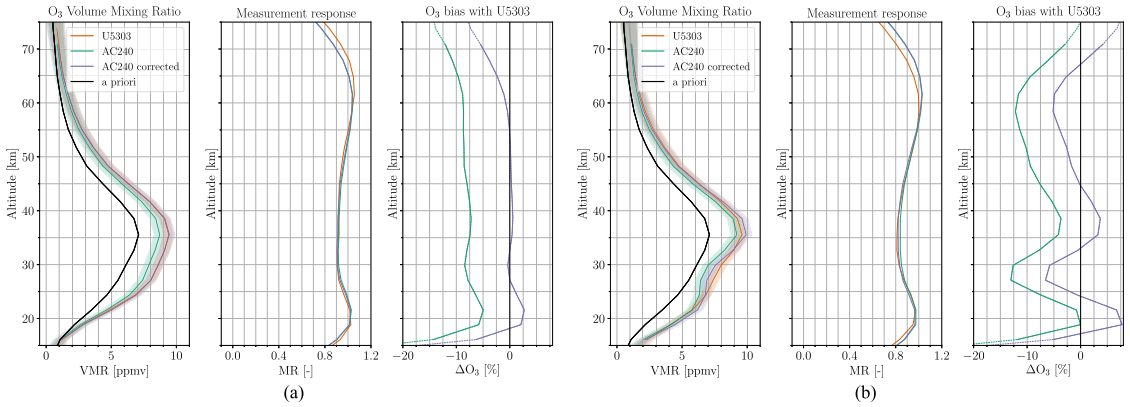

Fig. 9. Ozone retrievals from the integrated spectra of two different T_B bins for the U5303, the AC240, and the AC240 corrected using (2). For each T_B bin or atmospheric opacity case, the left panel shows the retrieved ozone profiles and the middle panel shows the measurement response. The right panel show the relative bias between the ozone profiles retrieved from the AC240 (with and without correction) and the U5303, taken as the reference. (a) Low atmospheric opacity: $T_{B,mean} < 80$ K. (b) High atmospheric opacity: 140 K $< T_{B,mean} <$ 150 K.

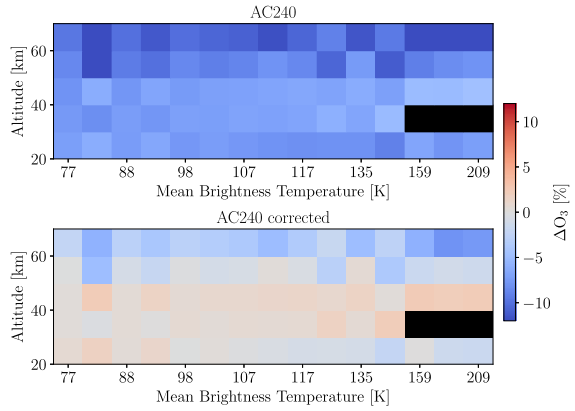

Fig. 10. Mean relative bias in ozone volume mixing ratio compared to the reference spectrometer (U5303) for all altitude ranges and brightness temperature bins (see Section III-A) of the February time period. The bins are labelled using their mean spectral brightness temperature $T_{B,mean}$. The upper panel shows the original bias of the AC240 spectrometer whereas the lower panel shows the remaining bias after correction with (2) of the AC240 integrated spectra prior to the retrieval. The black squares show the altitude ranges where the measurement responses is constantly lower than 80%.

the AC240 before (upper panel) and after (lower panel) the correction for all T_B bins in February. Compared to the U5303, it confirms that the AC240 has a systematic bias of 5% to 12% less ozone from 20 to 70 km altitude. More specifically, the ozone bias is more or less constant between 20 and 50 km and rises slightly above 50 km. Both Figs. 9 and 10 show that, after correction of the AC240 integrated spectra, the bias between this spectrometer and the U5303 is significantly reduced. It is the case for all T_B bins and for all altitude ranges, which is consistent with the systematic negative bias observed on the integrated spectra of the AC240.

As the ozone bias does not strongly depend on the brightness temperature bin (see Fig. 10), Table II presents the mean relative

TABLE II
MEAN RELATIVE BIAS ON THE OZONE PROFILES WITH CORRESPONDING ABSOLUTE VALUE (IN PPMV)

Altitude	**AC240 - U5303**	**AC240$_c$ - U5303**	**AC240 - AC240$_c$**
20-30 km	-7.50% (-0.52)	-0.21% (-0.01)	-7.30% (-0.50)
30-40 km	-6.94% (-0.64)	0.70% (0.06)	-7.59% (-0.71)
40-50 km	-6.63% (-0.41)	1.31% (0.08)	-7.79% (-0.49)
50-60 km	-9.23% (-0.27)	-1.28% (-0.04)	-8.05% (-0.23)
60-70 km	-11.02% (-0.17)	-4.11% (-0.08)	-7.20% (-0.11)

ozone bias (with corresponding absolute VMR bias [ppmv]) as a function of the altitude range. The effect of the spectral correction is highlighted by showing the ozone profile difference between the AC240 before and after applying the correction (AC240-AC240$_c$). As this column does not use the U5303 as the reference, it allows one to see the real impact of (2) on the ozone retrievals. It shows a more or less constant relative bias with altitude and means that the spectral correction has the same effect at all altitudes.

For some retrievals, we noticed oscillations on the resulting VMR profiles (see the right panel of Fig. 9) that we could not remove during the data processing. These oscillations are seen in the data of all three spectrometers and can be explained by a baseline ripple on the integrated spectra, which is mostly caused by standing waves form the LN2 target. In most operational monitoring radiometers this ripple is reduced with an optical path-length modulator, which was not available during this test campaign, resulting in noticeable baselines within the integrated spectra. The spectral noise differences between the spectrometers and the T_B bins also made the removal of these oscillations difficult, especially at higher tropospheric opacity, where the ozone line is increasingly absorbed by the water vapor continuum. In our opinion though, these oscillations are artificial and do not call the validity of the bias results into question. However, they may explain why we do not observe a trend in the ozone bias with the T_B bins and therefore, further investigation

is needed to provide any conclusions regarding the evolution of the ozone bias with brightness temperature.

To conclude, despite some technical difficulties during the retrieval processing, the second column of Table II provides a first quantification of the ozone profile bias originating from the AC240 while the fourth column quantifies the effect of the spectral and nonlinearity corrections (2) applied to the integrated spectra. The observed ozone bias is consistent with the spectral bias observed on the integrated spectra of the AC240 and its amplitude is quite large and might explain some of the biases seen in some ozone or water vapour time series derived from the AC240.

IV. Discussion

The MOPI 5 measurement campaign was quite limited in time and was primarily designed as a test setup for the comparison of digital back-ends. Whereas it provided a unique dataset for the identification of a spectral bias on the AC240, it sets some limitations on the retrieval capabilities and the amount of data collected during this measurement campaign. As an example, the need to manually refill the liquid nitrogen target during the campaign or the large spectral baselines did limit the amount of decent measurements quite significantly and explains why we mostly focused on the month of February in our study. Also, it did not enable us to understand the bias sources, nor to properly validate its successful correction. It results in a limited ability to extrapolate the MOPI 5 results to other instruments, atmospheric lines or different signal-to-noise ratios without further validation. Hereafter, we discuss our hypotheses and attempts to explain and reproduce the spectral bias on the integrated spectrum of the AC240.

A. Origins of the Bias

The systematic bias seen on the integrated spectra from the AC240 compared to the U5303 seems to have multiple sources. Whereas nonlinearities explains well the continuum difference, it fails to explain the spectral leakage leading to the line amplitude and slope biases. The line amplitude is especially problematic in the case of ozone monitoring because both the slope and continuum biases can be mostly accounted for in the retrieval by the tropospheric correction [23]. In case of nonlinearities, a simple tropospheric correction would still lead to a small error on the frequency line center but this effect should remain small compared to the effect of the spectral leakage.

To this day, we have investigated multiple possible explanations for the observed bias of the line amplitude. Laboratory measurements of the channel response with a swept continuous wave (CW) signal generator in Fig. 1 show that the AC240 follows closely the expected $|\operatorname{sinc}(x)|^2$ frequency response of an FFT with a rectangular window function. The convolution of this channel response with simulated ozone emission lines introduces only a negligible bias at the line center and it cannot explain the observed bias of the AC240. This theoretical channel response is also taken into account in the retrieval with ARTS, but its effect on the retrieved ozone profiles is negligible. The channel response measurements were also repeated with a much smaller amplitude of the swept CW signal added to a broadband noise background signal. Also in this case a behavior close to the expected $|\operatorname{sinc}(x)|^2$ response was observed, with only a small increase of the side lobe levels for very low signal to background power ratios (SBR).

B. Laboratory Tests

We attempted to recreate the bias of the AC240 to the U5303, using various power levels and SBRs. A CW signal was coupled with a wideband noise generator (NG) to create an approximation of an atmospheric emission line. The NG output was capped to 800 MHz using a lowpass filter and attenuated until the spectrometer counts were close to the atmospheric measurements. The CW was matched to the peak of a real absorption line and tuned to a frequency located at the center of a channel for both spectrometers simultaneously. In an effort to make the test more representative, the CW frequency was chosen to be as close to the location of the absorption line in the MOPI 5 measurements as possible. The output was split and read by both spectrometers in parallel. For the test the CW was cycled ON and OFF every 2 s and the measurements for each state averaged over the test duration. By computing the relative difference between the I_{on} (SG ON) and I_{off} (SG OFF) spectra for each spectrometer, any power leakage from the SG channel into the other channels should be visible. The relative difference is calculated as follows:

$$\Delta_{relative} = \frac{I_{on} - I_{off}}{I_{off}}. \tag{3}$$

This CW test did not show any spectral leakage from either spectrometer. The same test was repeated at other signal frequencies, power levels, and SBRs with similar results.

It could be still questioned whether these tests with a coherent CW source are sufficiently representative for the observation of an incoherent atmospheric emission line. For that reason we repeated these measurements with a narrow, band limited noise signal instead of the CW signal generator. It was generated using a second amplified noise diode, which was followed by a band pass filter with a 3 dB bandwidth of either 5 or 10 MHz. A programmable 70 dB step attenuator was used to switch between the "ON" and "OFF" cases, which were then added to the broadband noise background. The amplitude of the broadband noise background could be also changed with a second programmable attenuator to mimic the total power calibration of a real radiometer with a hot and a cold calibration load. Fig. 11 shows an example of a U5303 spectra for the background signal with and without the added narrow band noise, as well as with the 6 dB higher level for the "hot" calibration.

Fig. 12 shows the relative difference between the "ON" by "OFF" states of the band limited noise source calculated with (3). Outside of the narrow band signal the level of the relative difference remains close to zero for the U5303, whereas it increases noticeably for the AC240. This, along with a minor negative offset of the AC240 at the signal peak, is an indication of spectral leakage in the AC240. Given that we did not see this offset during the previous tests with CW signals, the overall increase in signal power (now spread across a multitude of channels) must be the key difference. We tested this by changing

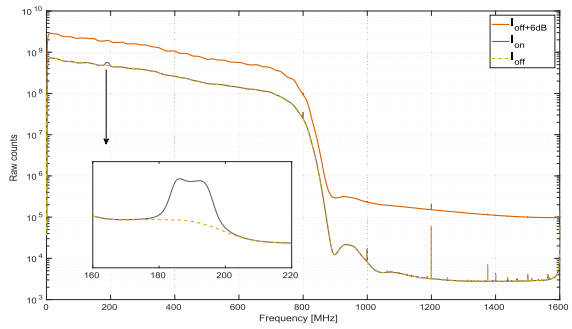

Fig. 11. Example for the three different kinds of spectra recorded during laboratory tests, showing U5303 only.

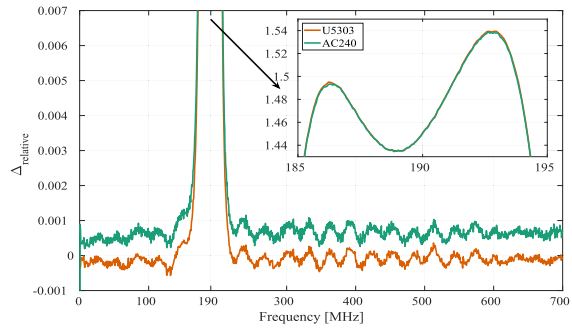

Fig. 12. Relative difference as computed with equation (3) for both U5303 and AC240. Signal frequency: 190 ± 5 MHz.

both the amplitude and width of the signal and could see that the magnitude of the spectral leakage could be reduced by either reducing the width or amplitude of the signal. While this is an indication for the origin of the bias, the magnitude of the leakage is still very small compared to the apparent correction factor for MOPI 5. It should also be considered that the SBR of the test was significantly higher (≈ 1.5) than for the MOPI 5 measurement campaign (0.05 or lower).

As previous tests only considered two spectra for comparison, the third test was designed to mimic the calibration process more closely. When considering a "hot" ($I_{off+6\,\mathrm{dB}}$) spectrum in addition to a "cold" (I_{off}) calibration spectrum and a synthetic atmospheric spectrum (I_{on}), a "calibrated" spectrum can be produced by

$$I_{cal} = \frac{I_{on} - I_{off}}{I_{off+6dB} - I_{off}}. \tag{4}$$

When comparing the I_{cal} spectra of the AC240 to the U5303 an offset of roughly -3% was visible in the narrow band signal which is consistent with the idea that power is leaking into other channels. Signal amplitude and width (by substituting a smaller bandpass filter) were varied to determine the effect on the offset. Neither change had a noticeable effect on the signal offset in percentage terms. However, the offset between AC240 and U5303 away from the signal changed. A noticeable, but small positive offset of the AC240 from the U5303 was observed in the measurement with the highest SBR (≈ 0.17), but disappeared for all other measurements. Possibly, the reduction in power and width of the signal reduced the magnitude of the spectral leakage to an extent where it was no longer noticeable. When examining the relative difference between only the "hot" and "cold" spectra, using (3) we could see a negative offset across the whole spectrum of similar magnitude as seen in the "calibrated" spectra. Meaning the offset in these tests could be caused by a nonlinearity of the AC240 instead of power leakage, however more tests are required to further investigate this effect and its relation to the spectral bias seen during the MOPI 5 measurement campaign.

V. Conclusion

The main goal of this contribution was to compare the influence of different digital spectrometers on passive microwave observations of middle-atmospheric ozone. It further investigated a systematic bias previously observed between the calibrated spectra recorded by the widely used AC240 and the more recent U5303 and USRP X310 digital spectrometers. The parallel observations obtained during a measurement campaign confirmed that the AC240 was consistently biased compared to the other two spectrometers. The bias is made up of a lower emission line amplitude and a different spectral slope compared to the U5303 which seems to be the results of a spectral leakage on the AC240. Attempts to reproduce the spectral bias in the laboratory were inconclusive. While we could find some evidence of spectral leakage of the AC240, its observed effect was too small to produce an offset matching the bias observed in the MOPI 5 measurements. Further tests are planned so the root cause of the bias can be determined. In addition, we have identified nonlinearities on this spectrometer, which induce dependency of the bias to the weather conditions (i.e., on the atmospheric opacity). We showed that the observed bias can be reduced significantly with a simple correction consisting of a constant scaling factor and by accounting for the nonlinearities.

We further investigated the effect of the bias on the ozone mixing ratio profiles by performing retrievals with the integrated spectra recorded by the three spectrometers. We observed a negative bias between 6.5 and 11% on the ozone profiles retrieved from the AC240 compared to the U5303 between 20 and 70 km altitudes. We also showed that the spectral correction applied on the integrated spectra can significantly reduce the ozone profile bias of the AC240.

The bias observed on the ozone profiles is considerable and might have large impacts on the time series recorded with the AC240. It could help explain the biases already reported with this spectrometer, not only for ozone, but also for water vapour observations. As the origin of the bias is not fully understood yet, further investigation is necessary before implementing the correction for other instruments or atmospheric lines. The AC240 is currently being replaced in several microwave radiometers and we are preparing parallel measurements with AC240/U5303

on a 142 GHz ozone radiometer and with AC240/USRP on a 22 GHz water vapour radiometers of NDACC. It should provide the required validation to extrapolate our approximate correction to the rest of the NDACC instruments that have used, or are still using, the AC240.

ACKNOWLEDGMENT

The authors would like to thank J. Hagen for his help to the retrievals as well as N. Jaussi, A. Luder, and T. Plüss for their technical expertise during the measurement campaign and the laboratory work. The authors also acknowledge the numerous developers that contributed to the free and open source tools used for the data analysis and visualization, in particular xarray [29], Matplotlib [30], Typhon, pyretrievals, and the ARTS community [26]. Eric Sauvageat, Klemens Hocke, and Axel Murk would like to acknowledge the support of the Oeschger Centre for Climate Change Research (OCCR).

REFERENCES

[1] Y. Calisesi, "The stratospheric ozone monitoring radiometer SOMORA: NDSC application document," *IAP Res. Rep*, vol. 11, pp. 53–54, 2003.

[2] G. E. Nedoluha, R. M. Bevilacqua, R. M. Gomez, D. L. Thacker, W. B. Waltman, and T. A. Pauls, "Ground-based measurements of water vapor in the middle atmosphere," *J. Geophysical Res.: Atmos.*, vol. 100, no. D2, pp. 2927–2939, 1995.

[3] R. M. Gomez, G. E. Nedoluha, H. L. Neal, and I. S. McDermid, "The fourth-generation water vapor millimeter-wave spectrometer," *Radio Sci.*, vol. 47, no. 1, pp. 1–11, 2012.

[4] R. Rüfenacht, N. Kämpfer, and A. Murk, "First middle-atmospheric zonal wind profile measurements with a new ground-based microwave doppler-spectro-radiometer," *Atmospheric Meas. Techn.*, vol. 5, no. 11, pp. 2647–2659, 2012.

[5] C. D. Rodgers, "Inverse methods for atmospheric sounding: Theory and practice," *World Sci.*, vol. 2, pp. 65–80, 2000.

[6] I. Petropavlovskikh, S. Godin-Beekmann, D. Hubert, R. Damadeo, B. Hassler, and V. Sofieva, "SPARC/IO3C/GAW report on long-term ozone trends and uncertainties in the stratosphere," Tech. Rep., Feb. 2019, *9th Assessment Report of the SPARC Project, Published by the International Project Office at DLR-IPA. Also: GAW Report No 241; WCRP Report 17*/ 2018. [Online]. Available: https://elib.dlr.de/126666/

[7] A. O. Benz *et al.*, "A broadband FFT spectrometer for radio and millimeter astronomy," *Astron. Astrophys.*, vol. 442, no. 2, pp. 767–773, 2005.

[8] S. Müller, A. Murk, C. Monstein, and N. Kämpfer, "Intercomparison of digital fast fourier transform and acoustooptical spectrometers for microwave radiometry of the atmosphere," *IEEE Trans. Geosci. Remote Sens.*, vol. 47, no. 7, pp. 2233–2239, Jul. 2009.

[9] G. E. Nedoluha, R. M. Gomez, B. C. Hicks, J. Helmboldt, R. M. Bevilacqua, and A. Lambert, "Ground-based microwave measurements of water vapor from the midstratosphere to the mesosphere," *J. Geophysical Res.: Atmos.*, vol. 116, no. D2, pp. 9–10, 2011.

[10] B. Tschanz, C. Straub, D. Scheiben, K. A. Walker, G. P. Stiller, and N. Kämpfer, "Validation of middle-atmospheric campaign-based water vapour measured by the ground-based microwave radiometer MIAWARA-C," *Atmospheric Meas. Techn.*, vol. 6, no. 7, pp. 1725–1745, 2013.
[Online]. Available: https://amt.copernicus.org/articles/6/1725/2013/

[11] L. Bernet *et al.*, "Ground-based ozone profiles over central Europe: Incorporating anomalous observations into the analysis of stratospheric ozone trend," *Atmospheric Chem. Phys.*, vol. 19, no. 7, pp. 4289–4309, 2019. [Online]. Available: https://acp.copernicus.org/articles/19/4289/2019/

[12] P. F. Orte *et al.*, "Analysis of a southern sub-polar short-term ozone variation event using a millimetre-wave radiometer," *Annales Geophysicae*, vol. 37, no. 4, pp. 613–629, 2019. [Online]. Available: https://angeo.copernicus.org/articles/37/613/2019/

[13] M. De Mazière *et al.*, "The network for the detection of atmospheric composition change (NDACC): History, status and perspectives," *Atmospheric Chem. Phys.*, vol. 18, no. 7, pp. 4935–4964, 2018. [Online]. Available: https://acp.copernicus.org/articles/18/4935/2018/

[14] S. Studer, K. Hocke, M. Pastel, S. Godin-Beekmann, and N. Kämpfer, "Intercomparison of stratospheric ozone profiles for the assessment of the upgraded GROMOS radiometer at bern," *Atmospheric Meas. Techn. Discuss.*, vol. 6, pp. 6097–6146, 2013.

[15] E. Maillard Barras *et al.*, "Study of the dependence of long-term stratospheric ozone trends on local solar time," *Atmospheric Chem. Phys.*, vol. 20, no. 14, pp. 8453–8471, 2020. [Online]. Available: https://acp.copernicus.org/articles/20/8453/2020/

[16] A. Murk and M. Kotiranta, "Characterization of digital real-time spectrometers for radio astronomy and atmospheric remote sensing," in *Proc. Int. Symp. Space THz Technol.*, Gothenburg, Sweden, vol. 15, 2019.

[17] E. Sauvageat, M. Kotiranta, K. Hocke, R. M. Gomez, G. Nedoluha, and A. Murk, "Comparison of three high resolution real-time spectrometers for microwave ozone profiling instruments," in *Proc. 16th Specialist Meeting Microw. Radiometry Remote Sens. Environ.,* 2020, pp. 1–4.

[18] M. Kotiranta, R. M. Gomez, G. Nedoluha, N. Kämpfer, and A. Murk, "Receiver development for the microwave ozone profiling instrument MOPI 5," in *Proc. IEEE Int. Geosci. Remote Sens. Symp.*, 2019, pp. 8952–8955.

[19] "Enhanced fast Fourier transform application on 12-bit high-speed data acquisition PCIe Card," Accessed: Nov. 5, 2021. [Online]. Available: https://acqiris.com

[20] "Ettus research, a national instruments brand," Accessed: Nov. 5, 2021. [Online]. Available: https://www.ettus.com/

[21] J. Hagen, A. Luder, A. Murk, and N. Kämpfer, "Frequency-Agile FFT spectrometer for microwave remote sensing applications," *Atmosphere*, vol. 11, no. 5, pp. 3–6, 2020. [Online]. Available: https://www.mdpi.com/2073-4433/11/5/490

[22] J. Hagen, A. Murk, R. Rüfenacht, S. Khaykin, A. Hauchecorne, and N. Kämpfer, "WIRA-C: A compact 142-GHz-radiometer for continuous middle-atmospheric wind measurements," *Atmospheric Meas. Techn.*, vol. 11, no. 9, pp. 5007–5024, 2018. [Online]. Available: https://amt.copernicus.org/articles/11/5007/2018/

[23] T. Ingold, R. Peter, and N. Kämpfer, "Weighted mean tropospheric temperature and transmittance determination at millimeter-wave frequencies for ground-based applications," *Radio Sci.*, vol. 33, no. 4, pp. 905–918, Jul. 1998.

[24] F. Weng *et al.*, "Calibration of Suomi national polar-orbiting partnership advanced technology microwave sounder," *J. Geophysical Res.: Atmos.*, vol. 118, no. 19, pp. 11–187, 2013.

[25] R. V. Leslie, W. J. Blackwell, A. Cunningham, M. DiLiberto, J. Eshbaugh, and I. A. Osaretin, "Pre-launch calibration of the NASA tropics constellation mission," in *Proc. IEEE 16th Specialist Meeting Microw. Radiometry Remote Sens. Environ.*, 2020, pp. 1–4.

[26] S. A. Buehler, J. Mendrok, P. Eriksson, A. Perrin, R. Larsson, and O. Lemke, "ARTS, the atmospheric radiative transfer simulator - version 2.2, the planetary toolbox edition," *Geoscientific Model Develop.*, vol. 11, no. 4, pp. 1537–1556, 2018. [Online]. Available: https://gmd.copernicus.org/articles/11/1537/2018/

[27] G. P. Anderson, S. A. Clough, F. Kneizys, J. H. Chetwynd, and E. P. Shettle, "AFGL atmospheric constituent profiles (0.120 km)," Air Force Geophysics Lab, Hanscom AFB, MA, USA, Tech. Rep., 1986.

[28] I. E. Gordon *et al.*, "The HITRAN2016 molecular spectroscopic database," *J. Quantitative Spectrosc. Radiative Transfer*, vol. 203, pp. 3–69, 2017.

[29] S. Hoyer and J. Hamman, "Xarray: ND labeled arrays and datasets in python," *J. Open Res. Softw.*, vol. 5, no. 1, p. 10, 2017.

[30] J. D. Hunter, "Matplotlib: A 2D graphics environment," *IEEE Ann. Hist. Comput.*, vol. 9, no. 3, pp. 90–95, May 2007.

Eric Sauvageat received the M.Sc. (Eng.) degree in energy management and sustainability from Ecole Polytechnique Fédérale de Lausanne, Lausanne, Switzerland, in 2018 and is currently working toward the Ph.D. degree in applied physics with the University of Bern, Bern, Switzerland.

His main research interests include microwave remote sensing and data analysis of atmospheric processes, with a focus on middle-atmospheric ozone.

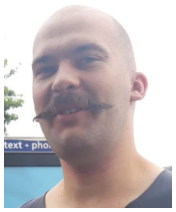

Roland Albers received the B.Eng. degree in aerospace engineering from Brunel University, London, U.K. in 2015, and the M.Sc. degree in astronautics and space engineering from Cranfield University, Milton Keynes, U.K., in 2016. He is currently working toward the Ph.D. degree in applied physics with the University of Bern, Bern, Switzerland.

He worked in the space industry on quasi-optical components. His research interests include space-borne radiometry, hardware design, and calibration.

Mikko Kotiranta received the M.Sc. (Tech.) degree (Hons.) in electrical engineering from the Helsinki University of Technology, Espoo, Finland, in 2008, and the Ph.D. degree in physics from the Goethe University of Frankfurt, Frankfurt am Main, Germany, in 2013.

He is currently with the Institute of Applied Physics, University of Bern, Bern, Switzerland, where he is engaged in the development of quasi-optical components and systems at millimeter and submillimeter wavelengths for atmospheric and astrophysical research.

Klemens Hocke received the venia legendi in atmospheric physics from the University of Bern, Bern, Switzerland, in 2011.

He is the leader of the Atmospheric Processes Group, Institute of Applied Physics, University of Bern. His interests include atmospheric dynamics, remote sensing, and data analysis of atmospheric water and stratospheric ozone.

R. Michael Gomez received the B.S. degree in physics from George Mason University, Fairfax, VA, USA, in 1991.

He is the Chief Engineer with the U.S. Naval Research Laboratory's microwave spectroscopy program. For the past 30 years, he has been developing microwave instrumentation for the investigation of atmospheric chemistry and dynamics. His research interests include hardware design, remote sensing applications, and atmospheric processes.

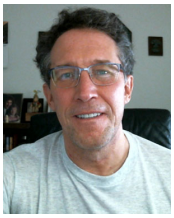

Gerald E. Nedoluha received the B.S. degree in physics from U.C. Berkeley, Berkeley, CA, USA, in 1983, and the Ph.D. degree in physics from the University of Illinois, Champaign, IL, USA, in 1990.

He is the Head of the Middle Atmospheric Physics Section with the U.S. Naval Research Laboratory, Washington, D.C., USA. He is also the Principle Investigator of a ground-based microwave spectroscopy program to conduct long-term measurements of H_2O, ClO, and O_3 in the middle atmosphere.

Axel Murk received the M.Sc. degree in physics from the Technical University of Munich, Munich, Germany, in 1995, and the Ph.D. degree in physics from the University of Bern, Bern, Switzerland, in 1999.

Since then, he has been involved in the development and characterization of millimeter- and submillimeter-wave instrumentation for different ground-based and space-borne projects. Since 2018, he is leading the IAP Microwave Physics Division with the University of Bern. His research interests include digital real-time spectrometers and the radiometric calibration of remote sensing instruments.

6 | Investigation of the ozone diurnal cycle over Switzerland

In the third and last study of my thesis, I investigated the ozone diurnal cycle over Switzerland using the harmonized time series of GROMOS and SOMORA. This chapter presents these investigations and summarises the results which were recently published in Sauvageat et al., 2023.

Middle-atmospheric ozone is subject to strong diurnal cycle with complex dependencies on the altitude, geographic location, sun insolation, temperature, chemistry, and dynamics. Therefore, it is important to account for it when comparing different observing systems or to compute accurate ozone trends, especially considering the uncertainties regarding the post-2000 stratospheric trends. Observations of the strato-mesospheric are rare though and passive ground-based MWRs are well suited for such observations as they are essentially the only few observing systems that can perform continuous, day and night ozone measurements in the middle atmosphere.

The bases for this study were developed in the frame of a Master thesis written at the IAP by Hou, 2022, for which I provided data and support for the analysis. After some good first results obtained by Hou, 2022, it was decided to continue the investigation of the strato-mesospheric ozone diurnal cycle with the unique setup offered by GROMOS and SOMORA. The idea was two-fold: first we wanted to see how well the diurnal cycle was represented in the recently harmonized time series of GROMOS and SOMORA. In fact, the diurnal cycle is a good test signal for models and retrieval algorithms. In the previous GROMOS ozone series, the diurnal cycle was either overestimated (Studer et al., 2013, focusing on the filter bank period) or missing some prominent features like the daytime stratospheric ozone maximum (Hocke K., personal communication for the FFTS period). As the ozone diurnal cycle measured by GROMOS was used as a reference in many ozone diurnal cycle study in the past decade (e.g. Parrish et al., 2014; Maillard Barras et al., 2020), it seemed important to better understand the reason of these discrepancies.

Therefore, I performed a similar analysis as Parrish et al., 2014 and investigated the monthly diurnal cycle above the mid-latitudes. The observations were compared against three model-based datasets, namely the recently published GEOS-GMI Diurnal Ozone Climatology (GDOC), (Frith et al., 2020), free-running simulation from the Whole Atmosphere Community Climate Model (WACCM) and simulations from the Belgian Assimilation System for Chemical ObsErvations (BASCOE). There is good agreement found between the harmonized series from GROMOS and SOMORA and against the three model-based dataset at most pressure levels and seasons. Most of the discrepancies seem to arise from the difference in vertical resolution between the two MWRs and the models. However, we also report a similar bias as Parrish et al., 2014 near the stratopause and similar delays in the onset of ozone depletion in the lower mesosphere, for which no explanation has been found yet.

The new harmonized time series from GROMOS and SOMORA offer a unique setup for observation of the ozone diurnal cycle, especially with regards to its short-term variability. In fact, in a modelling study based on WACCM, Schanz et al., 2014 identified regional variability of the ozone diurnal cycle which were attributed to regional anomalies in O_x, nitrogen oxides (NO_y) and temperature. For the first time, we present observations that confirm the existence

of short-term variability (in the order of days) of the ozone diurnal cycle during wintertime. The magnitude of the short-term variability exceeds the monthly or the inter-annual variability of the ozone diurnal cycle and is important to understand the regional ozone variability at short time scales. Also, it might be worth considering when accounting for the ozone diurnal cycle in dataset homogenization. Focusing on a case study during the winter 2014-2015, we can provide a plausible explanation for the observed variability, which is also well reproduced in the BASCOE simulations. Following the SSW of January 2015, irruption of polar air containing low abundance of nitrous oxide N_2O — the primary source of nitrogen oxides NO_x — caused a reduction in the ozone catalytic depletion cycle, therefore increasing the ozone production during daytime. It resulted in an increase of ~ 5 times of the diurnal cycle amplitude during a period of a few days. Short-term variability is also observed at period where no clear changes of NO_x is visible and therefore, there are also other reasons that can explain this variability. One possibility might be the short-term tidal variability which is relatively unexplored and unobserved yet but of high interest and could affect the ozone diurnal cycle. It was out of the scope of the publication to investigate all of them, but it is an area of research which deserves more investigations.

6.1 Publication: Ozone diurnal cycle over Switzerland

Following the Master thesis of Hou, 2022, some of these results were presented at the SPARC General Assembly in October 2022 and the full study has recently been published in *Atmospheric Chemistry and Physics*.

Citation:

Sauvageat, E., Hocke, K., Maillard Barras, E., Hou, S., Errera, Q., Haefele, A., and Murk, A. (2023). "Microwave radiometer observations of the ozone diurnal cycle and its short-term variability over Switzerland". In: *Atmospheric Chemistry and Physics* 23.13, pp. 7321–7345. DOI: 10.5194/acp-23-7321-2023.

Atmos. Chem. Phys., 23, 7321–7345, 2023
https://doi.org/10.5194/acp-23-7321-2023

Atmospheric Chemistry and Physics
Open Access
EGU

Microwave radiometer observations of the ozone diurnal cycle and its short-term variability over Switzerland

Eric Sauvageat[1,2], Klemens Hocke[1,2], Eliane Maillard Barras[3], Shengyi Hou[1], Quentin Errera[4], Alexander Haefele[3], and Axel Murk[1,2]

[1]Institute of Applied Physics, University of Bern, Bern, Switzerland
[2]Oeschger Centre for Climate Change Research, University of Bern, Bern, Switzerland
[3]Federal Office of Meteorology and Climatology MeteoSwiss, Payerne, Switzerland
[4]Royal Belgian Institute for Space Aeronomy (BIRA-IASB), Brussels, Belgium

Correspondence: Eric Sauvageat (eric.sauvageat@unibe.ch)

Received: 10 March 2023 – Discussion started: 28 March 2023
Revised: 24 May 2023 – Accepted: 5 June 2023 – Published: 4 July 2023

Abstract. In Switzerland, two ground-based ozone microwave radiometers are operated in the vicinity of each other (ca. 40 km): the GROund-based Millimeter-wave Ozone Spectrometer (GROMOS) in Bern (Institute of Applied Physics) and the Stratospheric Ozone MOnitoring RAdiometer (SOMORA) in Payerne (MeteoSwiss). Recently, their calibration and retrieval algorithms have been fully harmonized, and updated time series are now available since 2009. Using these harmonized ozone time series, we investigate and cross-validate the strato–mesospheric ozone diurnal cycle derived from the two instruments and compare it with various model-based datasets: the dedicated GEOS-GMI Diurnal Ozone Climatology (GDOC) based on the Goddard Earth Observing System (GEOS-5) general circulation model, the Belgian Assimilation System for Chemical ObsErvations (BASCOE) – a chemical transport model driven by ERA5 dynamics, and a set of free-running simulations from the Whole Atmosphere Community Climate Model (WACCM). Overall, the two instruments show very similar ozone diurnal cycles at all seasons and pressure levels, and the models compare well with each other. There is a good agreement between the models and the measurements at most seasons and pressure levels, and the largest discrepancies can be explained by the limited vertical resolution of the microwave radiometers. However, as in a similar study over Mauna Loa, some discrepancies remain near the stratopause, at the transition region between ozone daytime accumulation and depletion. We report similar delays in the onset of the modelled ozone diurnal depletion in the lower mesosphere.

Using the newly harmonized time series of GROMOS and SOMORA radiometers, we present the first observations of short-term (sub-monthly) ozone diurnal cycle variability at mid-latitudes. The short-term variability is observed in the upper stratosphere during wintertime, when the mean monthly cycle has a small amplitude and when the dynamics are more important. This is shown in the form of strong enhancements of the diurnal cycle, reaching up to 4–5 times the amplitude of the mean monthly cycle. We show that BASCOE is able to capture some of these events, and we present a case study of one such event following the minor sudden stratospheric warming of January 2015. Our analysis of this event supports the conclusions of a previous modelling study, attributing regional variability of the ozone diurnal cycle to regional anomalies in nitrogen oxide (NO_x) concentrations. However, we also find periods with an enhanced diurnal cycle that do not show much change in NO_x and where other processes might be dominant (e.g. atmospheric tides). Given its importance, we believe that the short-term variability of the ozone diurnal cycle should be further investigated over the globe, for instance using the BASCOE model.

Published by Copernicus Publications on behalf of the European Geosciences Union.

1 Introduction

Beyond its role in the protection of earth from harmful ultraviolet radiation, ozone is a key species in the energy balance of the middle atmosphere, strongly influencing the radiation budget and thermal state of the stratosphere and mesosphere. Following the success of the Montreal Protocol in 1987, full recovery of the ozone layer is expected for the 21st century with significant regional variability and uncertainties. In particular, there is a high degree of uncertainty about the lower stratospheric ozone recovery, and there is increasing observational evidence that ozone is still declining at some locations in the lower stratosphere (Ball et al., 2018; Maillard Barras et al., 2022a; Godin-Beekmann et al., 2022), without satisfactory explanation to date.

Ozone is a very reactive molecule involved in many (photo-)chemical reactions in the middle atmosphere. The set of pure oxygen photochemical reactions leading to the production and destruction of ozone was first described by Chapman (1930) and is known as the Chapman cycle. Together with catalytic depletion cycles involving many different species (NO_y, Cl_y, HO_y, etc.), they mostly drive the ozone amount in the middle atmosphere at multiple timescales. In particular, ozone concentrations are subject to complex diurnal cycle patterns depending on the geographic location, altitude, season, and other factors (Schanz et al., 2014), which makes it both important and difficult to fully take into account in models or observations.

The importance of the ozone diurnal cycle in the mesosphere has been recognized early through the use of photochemical models and from early measurements (e.g. Prather, 1981; Vaughan, 1982; Pallister and Tuck, 1983; Zommerfelds et al., 1989). Its main patterns are well known and have been successfully observed and modelled (Connor et al., 1994; Ricaud et al., 1991; Huang et al., 1997). In the stratosphere though, the ozone diurnal cycle is much weaker which makes accurate observations challenging. However, it needs to be taken into account when comparing different observing systems or to compute accurate trends (Bhartia et al., 2013; Maillard Barras et al., 2020). In recent years, there has been a renewed interest to improve the consideration of the diurnal variations of ozone and nitrogen oxides in satellite measurements (Frith et al., 2020; Schanz et al., 2021; Strode et al., 2022), partly because of the remaining uncertainties in post-2000 stratospheric ozone trends. For instance, Frith et al. (2020) used a modified version of the GEOS-5 model to produce a global, zonally averaged ozone diurnal climatology: the GEOS-GMI Diurnal Ozone Climatology (GDOC). The idea was to publish an easy-to-use climatology of scaling factors to account for ozone diurnal variability in intercomparison studies or for the creation of a merged ozone dataset. More recently, Strode et al. (2022) developed similar year-specific scaling factors for comparisons with the SAGE II-I/ISS measurements.

To validate such diurnal scaling factors, accurate observations are needed at different altitudes and locations. However, such observations remain relatively sparse and challenging, especially in the stratosphere where the ozone diurnal cycle amplitude is small. Also, many satellites are sun synchronous or use the sun as source, which limits their ability to derive full diurnal cycles. Some satellite-based ozone diurnal cycles have been successfully derived, however, from SAGE/ISS (Sakazaki et al., 2013, 2015) and from SABER on the Thermosphere Ionosphere Mesosphere Energetics and Dynamics (TIMED) satellite (Huang et al., 2010a). Although the satellite-based observations offer a global view on the ozone diurnal cycle, they do need to aggregate data in space or time to derive a diurnal cycle, therefore blurring any short-term or regional fluctuations in the cycle amplitude.

Passive microwave ground-based radiometers (MWRs) are well suited for ozone diurnal cycle observations, because they operate continuously and do not use the sun as a source. These instruments have been used successfully by different groups to monitor the diurnal cycle, not only in the mesosphere but also in the stratosphere (Connor et al., 1994; Schneider et al., 2005; Haefele et al., 2008; Parrish et al., 2014; Studer et al., 2014; Schranz et al., 2018). In the tropics, Parrish et al. (2014) derived detailed stratospheric ozone diurnal cycles over Mauna Loa from MWR measurements and compared them with satellite measurements and the Goddard Earth Observing System Chemistry Climate Model (GEOSCCM). They found a good agreement between the MWR and satellite observations as well as remaining discrepancies with the model in the upper stratosphere (3.2 to 1.8 hPa). In the polar region, Schranz et al. (2018) found larger discrepancies between MWR measurements and SD-WACCM simulations over Ny-Ålesund but only focused on a single year of measurements.

In this contribution, we derive updated ozone diurnal cycles over Switzerland from two co-located (ca. 40 km) ground-based MWRs between 2010 and 2022. The time series have recently been fully reprocessed with a harmonized algorithm (Sauvageat et al., 2022b), and they provide a unique set of measurements to study the ozone diurnal cycle and validate model simulations over the mid-latitudes. Compared to the three previous studies on ozone diurnal cycle over Switzerland (Zommerfelds et al., 1989; Haefele et al., 2008; Studer et al., 2014), this study combines the two MWRs over an extended time period (> 10 years) and focuses on the time where the two instruments used the same digital spectrometer (after 2009). The combination of the spectrometer update and of the recent harmonization extended the altitude range and improved the sensitivity of the ozone retrievals. We obtain significant improvements in the updated stratospheric ozone diurnal cycle measured by the GROund-based Millimeter-wave Ozone Spectrometer (GROMOS) in Bern. In fact, the study from Studer et al. (2014) showed overestimated diurnal cycle amplitude compared to the model simulations. Although it was focused on

the time period when GROMOS used a filter bank spectrometer (before 2009), we believe that part of the discrepancies were also due to the retrieval algorithm. Given that this instrument provided one of the main references for ozone diurnal cycle comparison studies over the mid-latitudes in the last decade, we believe that it is highly valuable to present in detail these updated results.

In fact, the objective of the present study is multiple. First we use the harmonized time series to derive the updated diurnal cycle above Switzerland and provide a comparative basis for different models at mid-latitudes. We especially aim at providing an additional validation for the dedicated GEOS-GMI Diurnal Ozone Climatology (GDOC), which has been published for use as a data analysis tool. In addition, we compare our measurements with two other types of model-based datasets: the Belgian Assimilation System for Chemical ObsErvations from Envisat (BASCOE) chemistry transport model (CTM) and the Whole Atmosphere Community Climate Model (WACCM) chemistry climate model (CCM). Finally, we present the first observations of short-term (sub-monthly) ozone diurnal variability and investigate the causes for such variations. We use the global, high-resolution simulations of BASCOE coupled with reanalysis data from ERA5 (Hersbach et al., 2020) to cross-validate our observations. We discuss a case study of the winter 2014–2015 and provide other examples where short-term fluctuations of the ozone diurnal cycle were observed.

The publication is organized as follows: Sect. 2 introduces the datasets and the methods used to compute the ozone diurnal cycle. Section 3 presents the results including the monthly ozone profile comparisons (Sect. 3.1), the intercomparisons of the monthly averaged ozone diurnal cycle over Bern (Sect. 3.2), and an example of observed short-term variability during the boreal winter 2014–2015 (Sect. 3.3). Finally, Sect. 4 presents a summary of the main results and some conclusions.

2 Materials and methods

In the following, we present succinctly the datasets and the methods used in our study. Regarding the datasets, we focus mostly on the microwave radiometer time series and on the main model characteristics, and we provide references for the reader for additional details. Also, we summarize the most important features and relevant publications for each dataset in Table 1.

2.1 Microwave ground-based radiometers

Microwave ground-based radiometers (MWRs) are passive remote sensing instruments that can be used to derive trace gas or temperature profiles in the atmosphere. MWRs measure the emission of atmospheric molecules in the microwave frequency range. Therefore, they do not rely on the sun for their observations and provide quite high temporal resolution and continuous sampling, which makes them an excellent candidate for diurnal cycle studies.

In Switzerland, two ozone microwave radiometers are operated close to each other (ca. 40 km) on the Swiss Plateau. The GROund-based Millimeter-wave Ozone Spectrometer (GROMOS) is operated by the Institute of Applied Physics (IAP) at the University of Bern (46.95° N, 7.44° E; 560 m a.s.l.) since 1994 and the Stratospheric Ozone MOnitoring RAdiometer (SOMORA) is operated by the Federal Office of Meteorology and Climatology MeteoSwiss in Payerne (46.82° N, 6.94° E; 491 m a.s.l.) since 2000. The two instruments have been designed at the IAP, have similar design, and use the rotational ozone emission line at 142.175 GHz to derive strato–mesospheric ozone profiles. Also, they have similar viewing geometries; both observe the sky at $\sim 40°$ elevation angle and experience similar atmospheric opacity conditions. Following discrepancies identified between the two instruments (Bernet et al., 2019; SPARC/IO3C/GAW, 2019), a complete harmonization of the data processing has recently been performed for GROMOS and SOMORA. It resulted in harmonized, continuous, hourly time series of strato–mesospheric ozone starting in 2009, which are now freely available (Sauvageat et al., 2022b).

The vertical resolution of the MWRs is quite coarse ($\sim$ 10 km up to 3 hPa and $\sim$ 15 km above), and the vertical extent of the ozone profile is from 60 to 0.02 hPa ($\sim$ 20 to 75 km), corresponding to the range where the a priori contribution to the retrieved profile is lower than 20 % (Fig. 1). The MWRs coarser vertical resolution needs to be taken into account for intercomparison with higher-resolution datasets (e.g. models), also for the diurnal cycle comparisons. The usual way is to apply a smoothing procedure to the higher-resolution dataset for the comparisons. In our study, we use the classical "averaging kernel smoothing" which essentially convolves the high-resolution dataset with the averaging kernels (AVKs) of the MWR retrieval using Eq. (1) (Rodgers and Connor, 2003). Equation (1) also applies the effect of the a priori contribution of the MWR retrievals onto the higher-resolved profile and is usually expressed as

$$\boldsymbol{x}_{\mathrm{c}} = \boldsymbol{x}_{\mathrm{a}} + \mathbf{A}(\boldsymbol{x} - \boldsymbol{x}_{\mathrm{a}}), \tag{1}$$

with $\boldsymbol{x}_{\mathrm{a}}$ being the a priori profile (derived from monthly WACCM profiles in our case), $\mathbf{A}$ the averaging kernel matrix, and $\boldsymbol{x}$ and $\boldsymbol{x}_{\mathrm{c}}$ respectively the original and convolved high-resolution profiles.

GROMOS and SOMORA essentially have the same sensitivity, allowing us to compare their observations directly. It can be seen by looking at the mean AVKs and the measurement contribution of the retrievals shown in Fig. 1. This also means that there is only little difference whether we use GROMOS or SOMORA AVKs for the smoothing procedure. In the following, all convolutions on the higher-resolution profiles are performed using the GROMOS AVKs. Figure 1 shows the mean AVKs of the full GROMOS and SOMORA

time series; however, for all the convolutions we use the appropriate monthly daytime or nighttime AVKs.

2.1.1 Satellite measurements

For validation purposes, we use measurements from the Microwave Limb Sounder (MLS) mounted on the Aura spacecraft (Waters et al., 2006). Since its launch in July 2004, the MLS instrument has been used extensively for trace gas observations and is one of the main measurement references for global ozone monitoring studies. More specifically, we use the latest ozone retrieval product (v5), following the screening guidelines provided in Livesey et al. (2022). The MLS ozone vertical resolution ranges from ~ 2.5 to ~ 5 km in the stratosphere and mesosphere, whereas its horizontal resolution ranges between 300 and 500 km. As spatial co-location criteria, we keep only measurements around Switzerland ($\pm 1.8°$ in latitude and $\pm 5°$ longitude). Aura overpasses Switzerland twice a day, at 02:20 and 13:10 LST (local solar time), thus providing the day-to-night ozone ratios but not the full diurnal cycle. In Sect. 3.3, we also show some measurements of temperature and nitrous oxide from MLS; however, as higher temporal resolution was needed for the short-term analysis, these were obtained with more relaxed co-location criteria ($\pm 3.6°$ latitude and $\pm 10°$ longitude) but following the same screening guidelines (Livesey et al., 2022).

2.2 Model-based datasets

2.2.1 GDOC

GEOS-GMI Diurnal Ozone Climatology (GDOC) is a model-based climatology of ozone diurnal cycle derived from the NASA Goddard Earth Observing System general circulation model, version 5 (GEOS-5). The goal of this climatology is to provide a simple data analysis tool to account for ozone diurnal variability, e.g. when comparing different satellite profiles.

For the production, GEOS-5 was run in replay mode constrained to 3-hourly MERRA-2 assimilated meteorological fields from January 2017 to December 2018 (see Orbe et al., 2017; Frith et al., 2020, and references therein for model details). As final product, the GDOC provides zonally averaged (on 5° latitude bands) ozone diurnal cycles from 90 to 0.3 hPa ($\sim$ 20 to 55 km) with equivalent vertical resolution of ~ 1 km and a time resolution of 30 min. The climatology is also available (on request) on original model levels but has not been evaluated below 30 hPa and above 0.3 hPa, which is the reason why we chose not to use it outside of this pressure range.

It provides monthly climatological ozone values as a function of local solar time (LST) normalized to midnight ozone values. The GDOC does not contain the original ozone profiles, which prevents the application of the averaging kernel smoothing procedure on this dataset. Consequently, we only show the original high-resolution profile from the GDOC dataset.

2.2.2 BASCOE

This study uses the chemistry transport model (CTM) simulation performed by the Belgian Assimilation System for Chemical ObsErvations (BASCOE; Errera and Fonteyn, 2001; Errera et al., 2008). The simulation covers the 2010–2020 period and is driven by 6-hourly wind and temperature fields taken from ERA5 (Hersbach et al., 2020), preprocessed in a similar set-up as described in Chabrillat et al. (2018) and Minganti et al. (2022). The simulation is performed with a time resolution of 30 min, a horizontal resolution of 2° in latitude and 2.5° in longitude, and 42 hybrid pressure levels from the surface to 0.01 hPa with a vertical resolution between 1 km in the lower stratosphere and 4 km in the lower mesosphere. The BASCOE model focuses on the calculation of the chemical composition of the stratosphere. It includes around 60 chemical species interacting through around 200 reactions (gas phase, photolysis, and heterogeneous) and a parametrization to account for the effect of sulfate aerosols and polar stratospheric clouds on the stratospheric composition (Huijnen et al., 2016). Background sulfate aerosols are taken from the Climate Model Intercomparison Project Phase 6 (CMIP6) recommendations, whereas surface emissions of long-lived species are taken from the "Historical Greenhouse Gas Concentrations" (HGGC) recommendations also produced for CMIP6 experiments (Meinshausen et al., 2017). The model provides a realistic composition of the stratosphere when compared to independent observations (see, for example, Prignon et al., 2021; Minganti et al., 2020, 2022). For this study, the model outputs have been interpolated at the location of Bern so that they can be compared with the two MWRs.

2.2.3 WACCM

We also use results from the Whole Atmosphere Community Climate Model (WACCM), version 4, in the configuration described by Schanz et al. (2021). WACCM is a fully coupled global chemistry climate model developed at the National Center for Atmospheric Research (NCAR) with a stratospheric chemistry module based on the Model of Ozone and Related Chemical Tracers (MOZART) (Kinnison et al., 2007). It simulates the atmosphere from the surface to $\sim$ 150 km altitude, with a vertical resolution between 1.1 and 2 km in the middle atmosphere. WACCM was run with a horizontal resolution of 4° latitude by 5° longitude, and for our study we use the closest grid point to both Bern and Payerne, which corresponds to 46° N and 5° E. The model was run with the pre-defined free-running "F 2000" scenario, simulating a perpetual year 2000 but without data nudging.

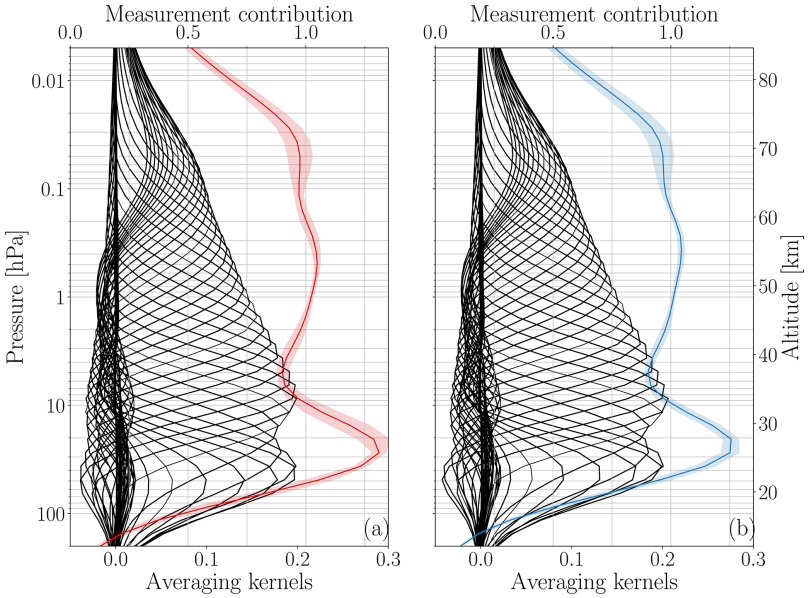

Figure 1. Mean averaging kernels and measurement contribution for **(a)** GROMOS and **(b)** SOMORA. The black lines are the averaging kernel at individual pressure levels, whereas the colour lines are the respective measurement contribution (see upper x axis). The shaded colour area shows the standard deviation of the measurement contribution.

Table 1. Summary of the datasets used in this study.

Dataset	Type	Coverage (horizontal, vertical)	Reference
GROMOS	MWR measurement	local, 60–0.02 hPa	Sauvageat et al. (2022b)
SOMORA	MWR measurement	local, 60–0.02 hPa	Sauvageat et al. (2022b)
MLS	Limb-sounding measurement	global, 261–0.001 hPa	Waters et al. (2006); Froidevaux et al. (2008)
GDOC	Model-based climatology	zonal, 30–0.3 hPa	Frith et al. (2020)
BASCOE	CTM	global, surface–0.05 hPa	Errera et al. (2008)
WACCM	CCM, free-running	global, surface–5.1×10^{-6} hPa	Garcia et al. (2007); Marsh et al. (2013)
ERA5	Reanalysis	global, surface–0.05 hPa	Hersbach et al. (2020)

2.3 Ozone profiles and day-to-night ratios

Before computing the ozone diurnal cycle from our different datasets, we first compare their monthly averaged ozone profiles during daytime and nighttime and compute their day-to-night ratios. We compare our two MWRs with MLS and BASCOE, all averaged over the time period 2010–2020, therefore removing most of the year-to-year variability. WACCM is not included in these comparisons for two reasons. First, we use the free-running WACCM simulations for a single year, and it would make no sense to compare it with the other datasets which are multi-year averages, especially in the wintertime when dynamics are an important modulator of the ozone amount. Second, the monthly averaged WACCM ozone profiles are actually used as a priori data for our MWR retrievals; therefore, they can not be used for validation against the retrieved MWR profiles.

For the ozone profile comparisons, we choose to use profiles whose time corresponds approximately to the MLS overpass times (02:20 and 13:10 LST). Therefore, we keep timestamps between 12:00 and 15:00 LST for the daytime profiles and between 01:00 and 04:00 LST for the nighttime profiles, regardless of the dataset. As explained in Sect. 2.1, we convolve the BASCOE simulations and the MLS measurements with monthly averaged daytime or nighttime GROMOS AVKs.

2.4 Ozone diurnal cycle

Similarly to the GDOC climatology, we choose to express the ozone diurnal cycle as ratio of ozone volume mixing ratios (VMRs) relative to the midnight value. To compute the reference midnight value ($O_{3,NT}$ in Eq. 1), we have used different time periods to reflect the different time resolu-

tions of the datasets. For the MWRs (∼ 1 h time resolution), we compute the midnight reference value by taking an average of two nighttime measurements between 23:00 and 01:00 LST. For WACCM and BASCOE (30 min time resolution), we use measurement between 00:00 and 01:00 LST, whereas the GDOC was normalized to the values between 23:45 to 00:15 LST (Frith et al., 2020).

For each hour and at each pressure level, we then compute the ratios to ozone at midnight using Eq. (2). To simplify the notation, we do not explicitly write the pressure dependence of all the terms.

$$\Delta O_3(h) = \frac{O_3 - O_{3,NT}}{O_{3,NT}} \quad (2)$$

To compare with the monthly GDOC climatology, we compute monthly averaged $\Delta O_3(h)$ from GROMOS, SOMORA, WACCM, and BASCOE. For each dataset, we use the available time series, i.e. 12 years of data for the two MWRs (2010–2022), 10 years for BASCOE (2010–2020), and the 1 year of the WACCM free-running model run. For the MWRs, we additionally filtered the time series to remove the measurements done at very high tropospheric opacity ($\tau > 1.5$), as they result in lower quality retrievals and can potentially contaminate the monthly averages. To some extent, it also helps to limit any seasonal bias arising due to the summertime higher opacity, although it is difficult to rule out this effect completely (e.g. see discussion on the effect of the opacity on GROMOS and SOMORA in Sauvageat et al. (2022b)). For the diurnal cycle, the effect of this filtering is not very large, and for the interested reader the unfiltered version is provided in the Supplement (Figs. S5 to S16).

We compute errors on the MWRs and BASCOE ozone diurnal cycles as standard error of the mean (SEM). For each month and LST hour, we compute the standard deviation of $\Delta O_3(h)$ and divide it by the square root of the number of ozone profiles available for each hour.

2.5 Short-term variability of the ozone diurnal cycle

In addition to monthly averaged ozone diurnal cycle, we also show observations of short-term (sub-monthly) variability of the ozone diurnal cycle. GROMOS and SOMORA provide a unique set-up for short-term ozone diurnal cycle observations, because they have continuous, hourly, co-located measurements. Therefore, we can use them to compute the ozone diurnal cycle on sub-monthly periods and cross-validate their measurements. Also, we use BASCOE simulations to compute the short-term variability of the ozone diurnal cycle over Switzerland and to investigate the cause of such variability.

In order to detect sub-monthly variations in the ozone diurnal cycle, we computed the day-to-night differences in ozone VMR for GROMOS, SOMORA, and BASCOE. More specifically, we compute the anomalies of the day-to-night differences (D_{O_3}) to a monthly climatology. As daily anomalies are too noisy, we average these differences on 5 d.

$$D_{O_3} = O_{3,DT} - O_{3,NT}[\text{ppmv}] \quad (3)$$

In this contribution, we focus on the winter 2014–2015 and use BASCOE and MLS data to investigate and discuss potential reasons explaining a specific event during this winter. For further studies, we provide along with this publication the full time series of D_{O_3} daily anomalies for GROMOS, SOMORA, and BASCOE.

3 Results and discussions

3.1 Monthly ozone profiles and day-to-night ratio

The comparisons of the monthly averaged ozone daytime and nighttime profiles and day-to-night ratios are shown in Fig. 2 for December and Fig. 3 for June as proxies for the winter and summer season. Figures A1 and A2 in Appendix A show similar comparisons for March and September, respectively. Similar comparisons but with respect to SOMORA MWR can be seen in the Supplement (Figs. S1 to S4). Overall we find a good agreement between measured ozone profiles (GROMOS, SOMORA, and MLS), with relative differences between the measured ozone profiles lower than 10 % up to 0.1 hPa. The differences between BASCOE and the MWR are within 15 % between 30 and 0.2 hPa, with slightly larger bias during the winter months. BASCOE notably underestimates ozone amounts in the upper stratosphere to lower mesosphere (up to ∼ 0.5 hPa) and overestimates ozone in the lower stratosphere, regardless of the month or the time of day. Above 0.2 hPa, the differences depend on the month considered, but the model tends to underestimate the daytime ozone profiles, leading to a small overestimation of the day-to-night depletion ratio over 0.2 hPa. The ozone deficit of BASCOE in the middle atmosphere is consistent with previous studies (Skachko et al., 2016) and could be due to an overestimation of NO_2 in the model simulations, thereby enhancing catalytic ozone destruction though the so-called "Crutzen" cycle (Crutzen, 1970). Note that this deficit of middle-atmospheric ozone is found in other models as well (see, for example, Fig. 3.1 in SPARC, 2010).

All datasets show the ozone daytime accumulation in the stratosphere and its transition to ozone daytime depletion around the stratopause (∼ 2–1 hPa). All datasets show stratospheric ozone accumulation during daytime (up to ∼ 1 hPa) with stronger amplitude during the summertime, and they all show the strong mesospheric ozone depletion during daytime, growing in amplitude with altitude. They agree quite well on the pressure at which peak accumulation and peak depletion occur. During summer, there is an excellent agreement between day-to-night ratios up ∼ 0.6 hPa. Above this pressure level, the GDOC climatology systematically underestimates the daytime ozone loss, leading to less negative day-to-night ratio than the other datasets. In the mesosphere,

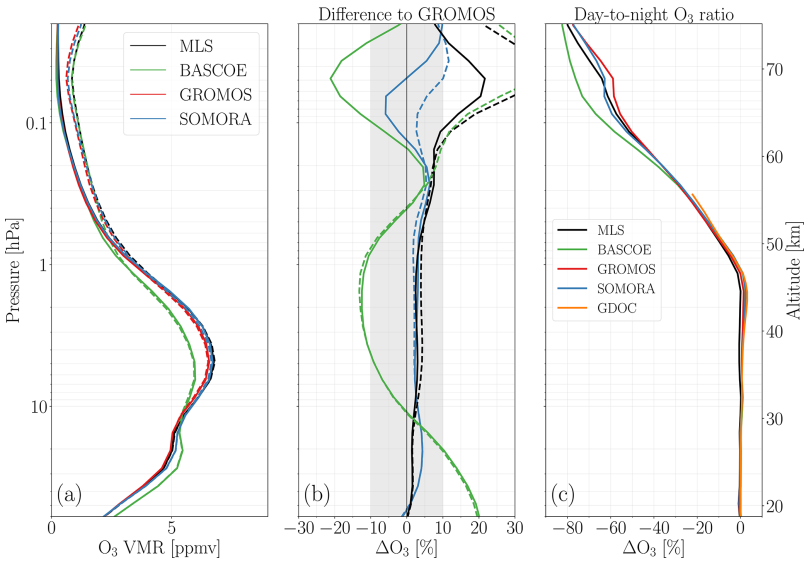

Figure 2. **(a)** Monthly averaged profiles, **(b)** relative differences ((X-GRO)/GRO), and **(c)** day-to-night ratios of ozone VMR above Switzerland in December. In panels **(a)** and **(b)**, the solid lines are the daytime profiles, whereas the dashed lines are the nighttime profiles.

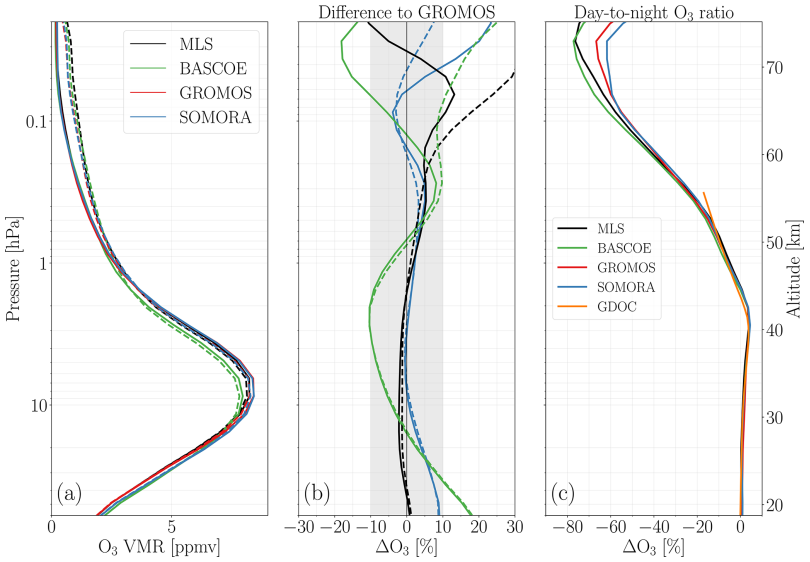

Figure 3. Same as Fig. 2 but for June.

BASCOE and MLS compare well with the MWRs up to 0.05 hPa, with day-to-night ratios in agreement within 15 %.

3.2 Comparison of monthly ozone diurnal cycle

Going beyond the day-to-night ratio, full monthly diurnal cycles over Switzerland are shown for summer and winter in Figs. 4 and 5 for the two MWRs and the three model-based datasets (Figs. B1 and B2 in Appendix B show similar results for spring and autumn, respectively). These figures show the ratios to ozone midnight values as a function of the LST between 60 and 0.02 hPa (respectively 30 and 0.3 hPa for GDOC). As mentioned previously, the monthly averages correspond to different time periods for each dataset: 2010–2022 for GROMOS and SOMORA, 2010–2020 for BAS-

COE, 2017–2018 for the GDOC, and 2000 perpetual year for WACCM. Also, AVK smoothing procedures have been applied to the WACCM and BASCOE dataset but not to the GDOC. The original version without any AVK smoothing can be seen for all datasets in the Supplement. For better visualization, we also show these diurnal cycles averaged over nine selected pressure ranges. This is shown in Figs. 6 and 7 for winter and summer (in Figs. B3 and B4 in Appendix B for spring and autumn). These figures show the original cycle from each dataset together with the AVK smoothed cycle, which enables us to clearly see the effect of the AVK smoothing procedure on the high-resolution datasets. In order to better compare the different months and datasets, Fig. 8 shows vertical profiles of the diurnal cycle amplitude for all months and datasets. Here, the amplitude is defined as the percentage change between the maximum and the minimum normalized ozone ratios (ΔO_3 as defined in Eq. 2) during the course of a day.

The new harmonized ozone time series from GROMOS and SOMORA have excellent agreement in ozone diurnal cycle. They agree well in patterns and amplitudes at all seasons and most altitudes. Some small discrepancies can be seen in summertime in the transition region (see, for example, July or August in Fig. 8); however, as shown in Sauvageat et al. (2022b), it is also the season where GROMOS and SOMORA experienced the larger discrepancies between their respective measurements. The two regimes of the ozone diurnal cycle are clearly visible in all datasets. Namely, the accumulation of ozone during daytime in the stratosphere and the depletion of ozone during daytime above $\sim$ 1 hPa are well captured by all datasets.

Among the model datasets, we observe most discrepancies of the diurnal cycle amplitude by the GDOC during wintertime in the upper stratosphere (see January or February in Fig. 8). To some extent, these discrepancies could be due to the temporal (different averaging periods) and longitudinal (zonal mean in GDOC) variability, which are both smoothed out in the GDOC. As mentioned by Frith et al. (2020), this is also the season where the ozone diurnal cycle is smaller and where the model uncertainties are higher. Below, we will present a summary of the differences between the MWRs and the models, focusing on different altitude regions and discuss in more details the reasons for the observed discrepancies.

3.2.1 Mesosphere ($p < 0.3$ hPa)

Overall, we observe a tendency of the models to overestimate the diurnal ozone depletion in the mesosphere. It is mostly noticeable above $\sim$ 0.1 hPa where the sensitivity values of the MWRs are decreasing and where the measurement error is growing fast. Therefore, even if the effect of the lower sensitivity should be included through the AVK smoothing, biases above this altitude should be considered with care. Note that at this altitude, BASCOE also has a limited vertical resolution as it only uses two pressure levels above 0.1 hPa. Considering the above limitations, we still observe quite a good agreement of the upper mesospheric diurnal cycle at all seasons. In agreement with Parrish et al. (2014) but in contradiction with the conclusions from Studer et al. (2014), we do not observe a significant seasonal variation of the mesospheric diurnal cycle amplitude. This is in better agreement with the model results, which show similar amplitude throughout the year.

3.2.2 Lower mesosphere (1–0.3 hPa)

In the lower mesosphere, we note a consistent bias between the models and the observations around sunrise: the diurnal ozone depletion observed by the MWRs consistently starts earlier than the models. It is true for most months and could be partly explained by differences in the vertical resolution (e.g. see Fig. 7 at 51 and 56 km). Interestingly, it does not seem to impact the sunset period, which rules out potential errors arising from the time conversion between the different datasets. This feature was also observed by Parrish et al. (2014) over Mauna Loa, and it seems to persist even after application of the AVKs (not for all months though), which gives us confidence that it does not result from the a priori data.

3.2.3 Stratopause region (3–1 hPa)

Around the stratopause, we can clearly see the complex transition region between the mesospheric diurnal depletion and the stratospheric accumulation. This is where we notice the largest biases between our different datasets. In fact, we observe discrepancies among the three model-based datasets and between the observations and the models. The biases around the stratopause (1–3 hPa) are similar to the ones reported by Parrish et al. (2014) and Haefele et al. (2008), i.e. differing behaviour in the pre-dawn hours and after sunrise. They are seen at all seasons during daytime and reach values up to 2 % differences among the models themselves (e.g. between 1 and 2 hPa in Fig. 7). Between the models and the MWRs, the biases are significantly reduced by the application of the AVK smoothing procedure, but we still note biases up to 2 % in this region.

As will be shown in Sect. 3.3, the upper stratosphere and lower mesosphere are also experiencing short-term variability of the ozone diurnal cycle, which can influence the monthly averaged cycle. In particular, the datasets produced using only a few specific years (i.e. WACCM or GDOC in our case) will be influenced by the short-term variability of these years, whereas it will be smoothed out in the MWR or the BASCOE datasets which are averaged on 10 years or more. As shown in Fig. S11 from the Supplement of Frith et al. (2020), although the inter-annual variability is generally limited below 5 hPa and during summer, inter-annual variations up to 5 % around 0.5–1 hPa can be seen during wintertime in the mid-latitudes. This supports the existence of

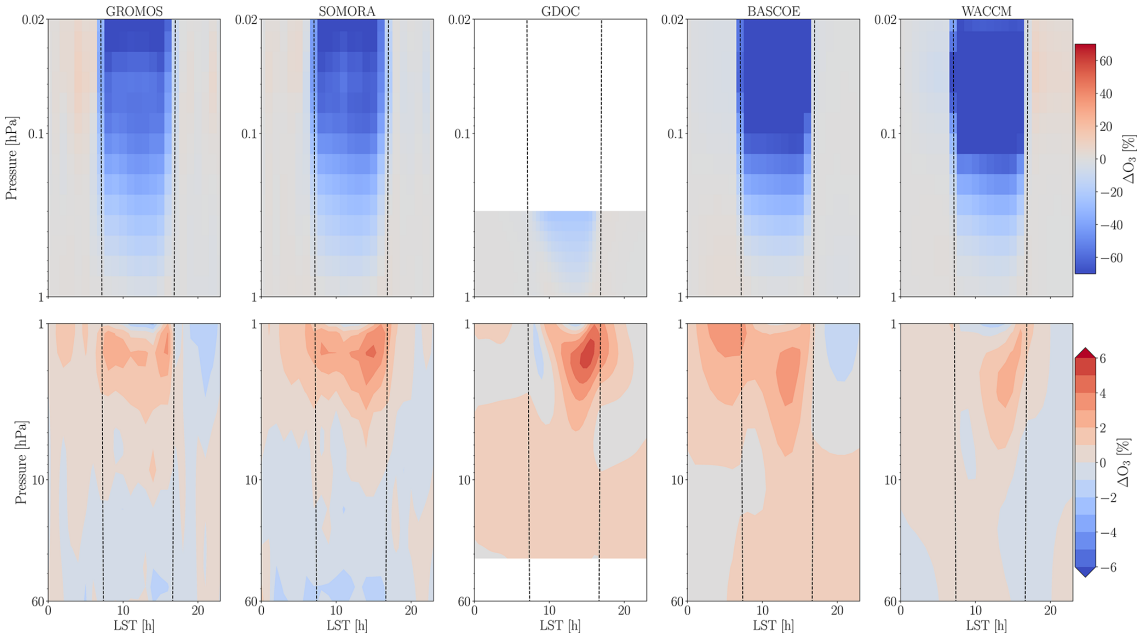

Figure 4. Monthly averaged ozone diurnal cycle over Switzerland in December as seen in GROMOS, SOMORA, GDOC, BASCOE, and WACCM datasets. Note that only the BASCOE and WACCM datasets have been convolved with the AVKs of GROMOS as explained in Sect. 2.1.

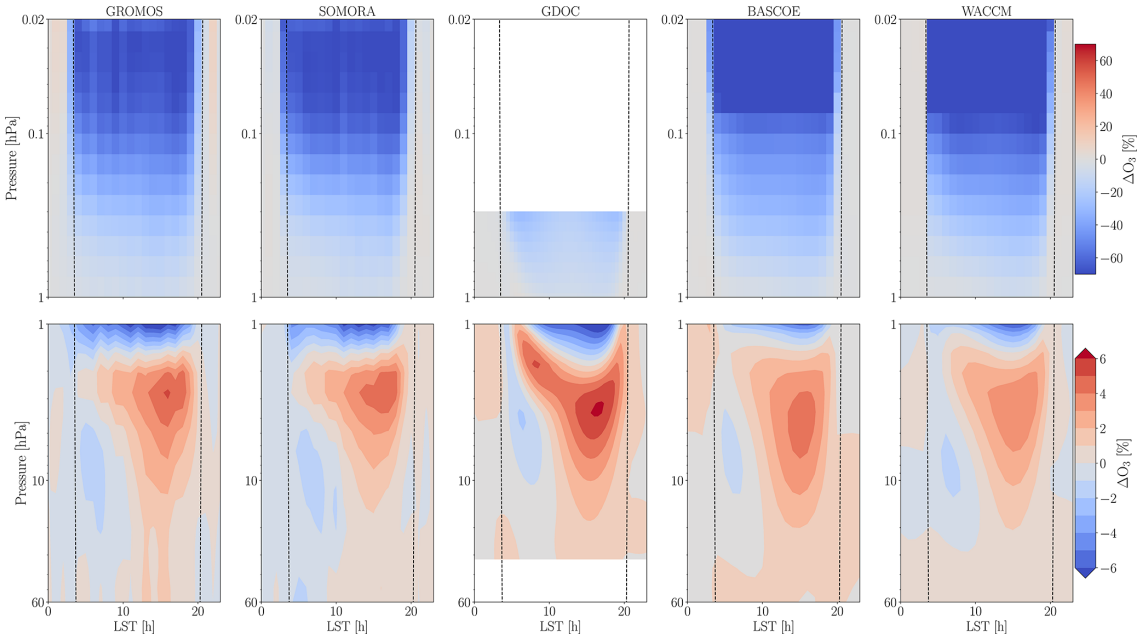

Figure 5. Same as Fig. 4 but for June.

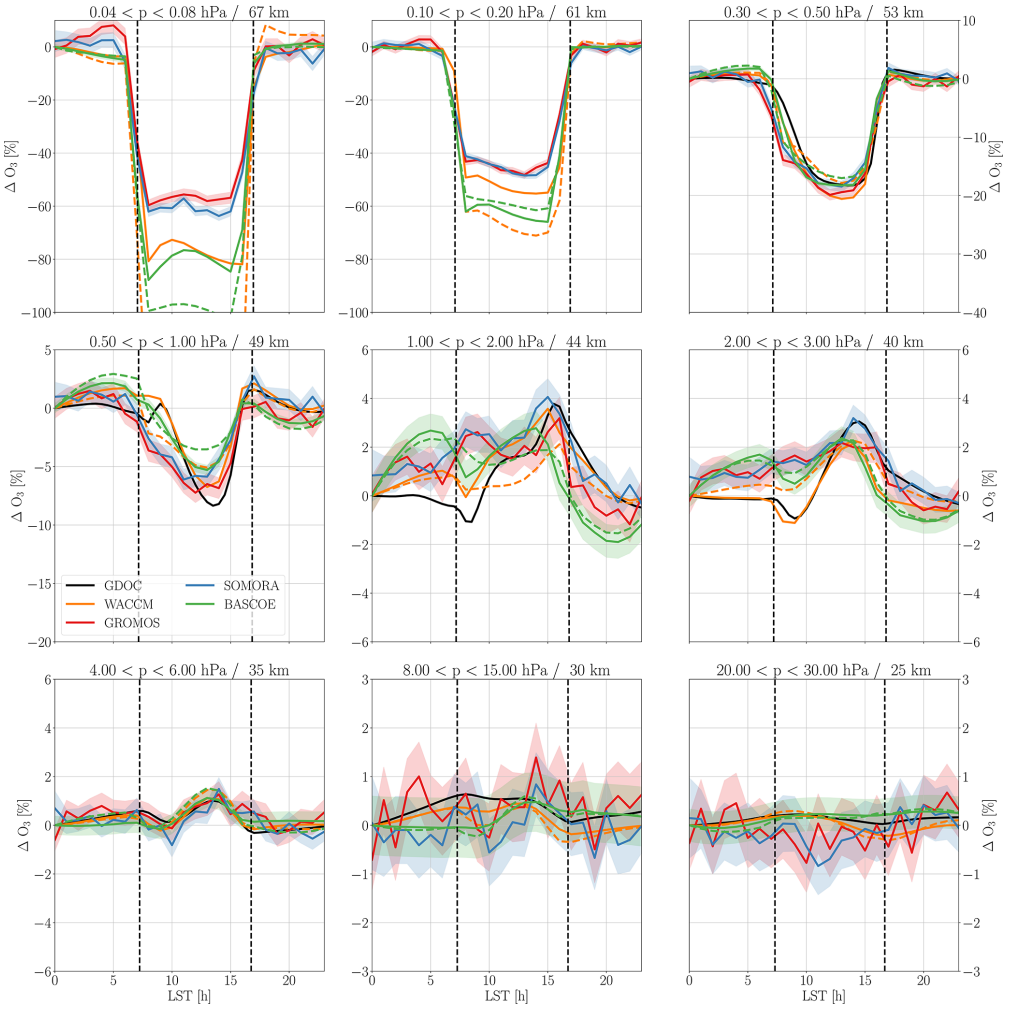

Figure 6. Monthly averaged ozone diurnal cycle over Switzerland at four selected pressure ranges in December. For BASCOE and WACCM, we show both the diurnal cycle before (solid lines) and after convolution (dashed lines) of the dataset with the AVKs of GROMOS. To account for the large changes in the diurnal cycle amplitude with altitude, the scale of the y axis is adapted for each sub-plot.

short-term variability in the ozone diurnal cycle and might therefore explain some of the remaining discrepancies near the stratopause region.

3.2.4 Middle and lower stratosphere (30–3 hPa)

In the middle and lower stratosphere, we observe the typical behaviour of the stratospheric ozone diurnal cycle: a small dip after sunrise followed by a gentle accumulation reaching a maximum in the late afternoon. The stratospheric cycle shows a high seasonal variability, with a maximum diurnal cycle amplitude around the summer solstice and lower diurnal variations during winter. In summer, we observe a peak amplitude of the ozone diurnal cycle of 3 %–4 % in the afternoon around 5 hPa in July, reducing to less than 2 % in the wintertime. For this reason, the dip after sunrise, attributed to rapid dissociation of NO_2 at sunrise (Pallister and Tuck, 1983), is mostly visible during the summer months. Note that this is a significant improvement compared to the previous retrievals of the GROMOS time series, where the dip was not observed and where the amplitude of the stratospheric cycle was high compared to the models (Fig. 6a and b in Studer et al., 2014). With the new time series, the amplitude of stratospheric ozone cycle is well captured by GROMOS and SOMORA at most seasons. In fact, most of the discrepancies that we observe in the middle stratosphere are the consequences of the limited vertical resolution of the MWRs,

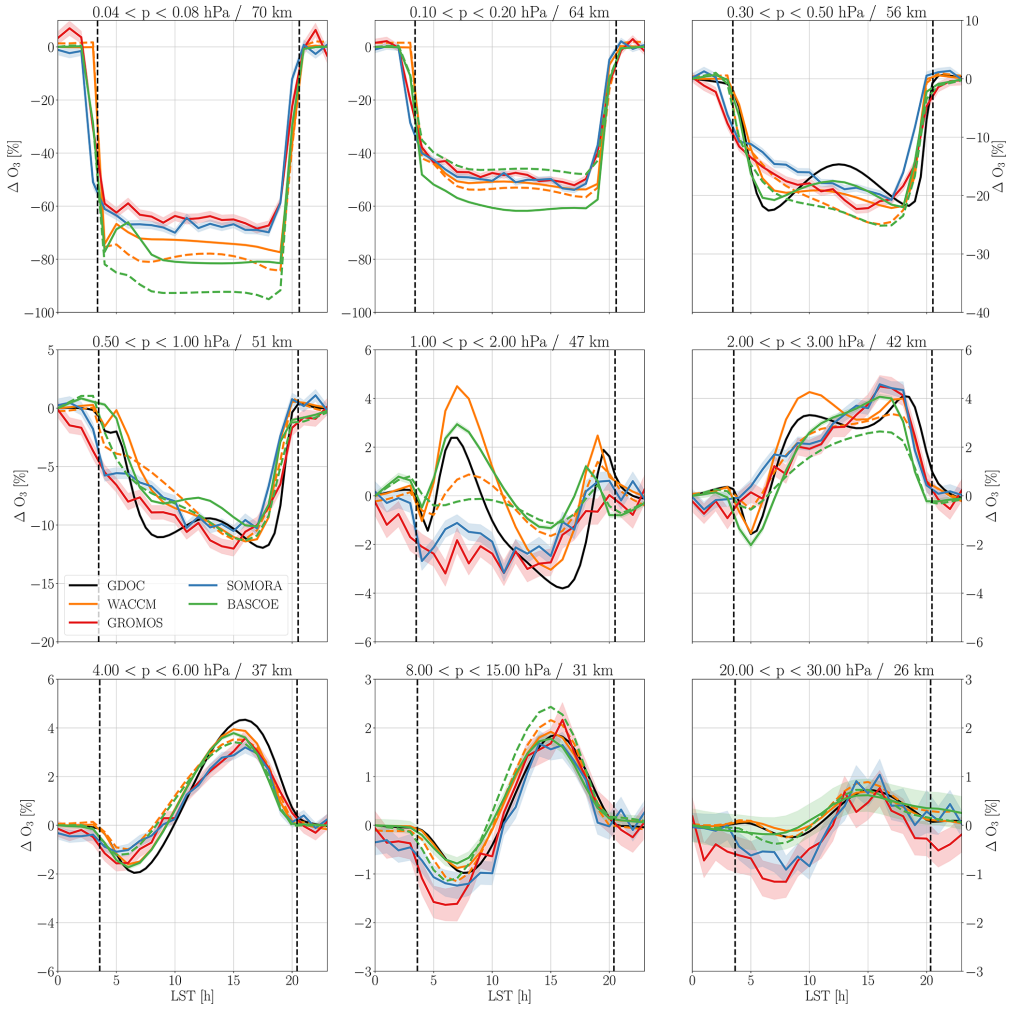

Figure 7. Same as Fig. 6 but for June.

whereas the differences of the lower stratosphere stay mostly within the error bars.

3.3 Short-term variability of the ozone diurnal cycle

In this section, we present the first measurements of short-term ozone diurnal cycle variability using the unique set-up offered by the co-located, hourly resolved measurements from GROMOS and SOMORA. To our knowledge, it is the first time that short-term variability of the ozone diurnal cycle is observed, and in the following we try to identify some of the reasons leading to such events, focusing on a case study from the boreal winter 2014–2015.

The upper panel in Fig. 9 shows the ozone concentration in the upper stratosphere from GROMOS, SOMORA, and BASCOE. From the ozone time series already, there are time periods where the ozone VMR shows some large fluctuations on a diurnal basis in a season where the mean ozone cycle is usually small (see Fig. 6, around 40 km). An example of such a case can be seen at the beginning of January 2015 (arrow in Fig. 9) or, for instance, at the end of January 2015. From the BASCOE time series, we can even identify other periods with enhanced cycles, which are not really seen as such in the MWR measurements. These are some examples of what we refer to as "short-term ozone diurnal cycle variability", generally lasting for a few days.

These enhancements can be better seen in Fig. 10, in the form of day-to-night D_{O_3} anomalies in the middle atmosphere (60–0.1 hPa). It shows similar patterns in GROMOS and SOMORA time series, with a large increase in D_{O_3} of

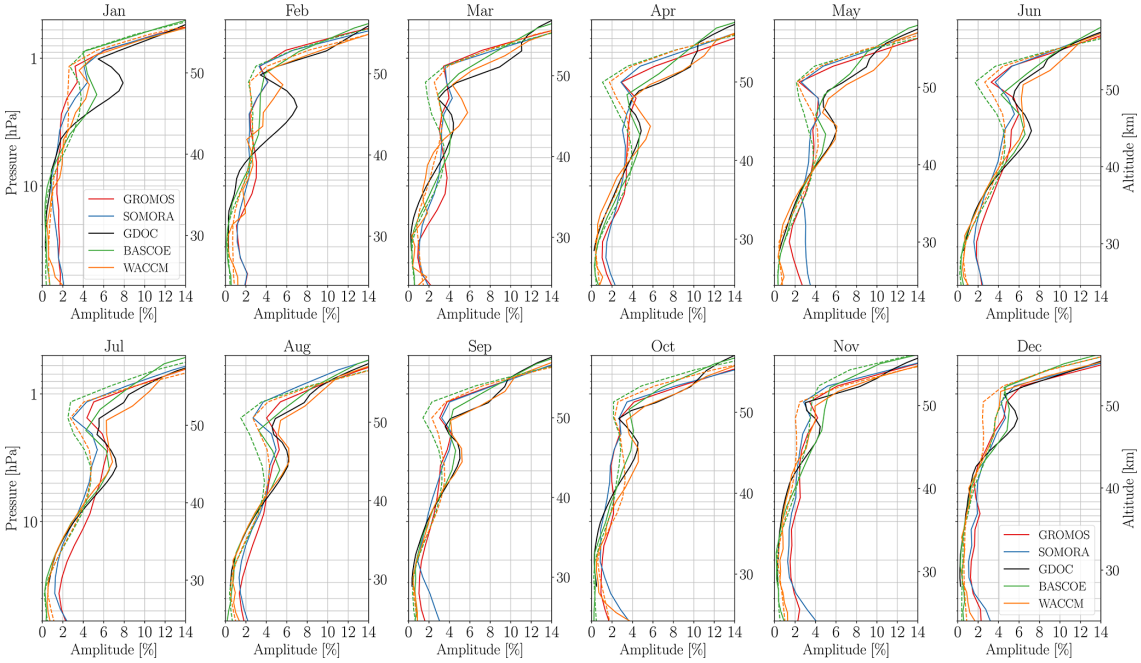

Figure 8. Monthly averaged vertical profiles of the ozone diurnal cycle amplitude. It shows the percentage change between the maximum and the minimum ozone ratio values. The dashed lines show the model results after convolution with the AVKs of GROMOS.

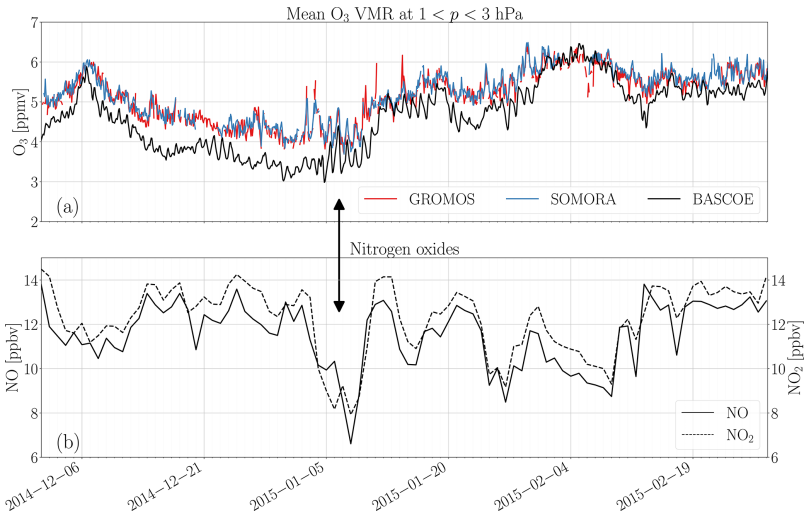

Figure 9. **(a)** Ozone VMR from GROMOS, SOMORA, and BASCOE during the boreal winter 2014–2015. **(b)** Nitrogen oxides (NO and NO_2) simulated by BASCOE. All quantities are averaged between 3 and 1 hPa and the ozone time series over 2 h time periods. NO_x values are shown as daily mean of nighttime (NO_2) and daytime (NO) values, respectively. The arrow highlights the period with an enhanced diurnal cycle.

around 1 hPa at the beginning of January 2015, followed by a secondary peak in the second half of the month. To some extent, BASCOE is also able to reproduce these two peaks in the ozone diurnal cycle, somehow limited to below 1 hPa and with limited vertical resolution.

Focusing on the upper stratosphere (3–1 hPa) where the anomalies are highest, Fig. 11 shows the temporal evolution of different quantities during the winter 2014–2015. In particular, Fig. 11b shows the day and nighttime ozone values. Focusing on the early January event, it can be seen that there is a consistent increase in daytime ozone from the three datasets, somehow delayed slightly in time in BASCOE compared to the MWRs. Such an increase is also visible during the second peak at the end of January for GROMOS and SOMORA and somehow less clearly in the BASCOE series. In terms of amplitude, this increase is substantial and corresponds approximately to 4 to 5 times the monthly averaged day-to-night difference in January, which is ~ 0.1 ppmv at this pressure level.

Corresponding to these peaks in D_{O_3} anomalies, sharp decreases in nitrogen oxides (NO_x) are simulated from BASCOE. In fact, the decrease affects both nitric oxide (NO) and nitrogen dioxide (NO_2). The two species are in photochemical balance during the day as NO mainly originates from photolysis of NO_2 during daytime and can react with ozone to give back NO_2, forming a major catalytic ozone depletion process in the middle atmosphere (Crutzen, 1970). In fact, the effect of NO_x on ozone maximizes between 20 and 45 km altitude ($\sim$ 50–1 hPa), corresponding well to the peaks of diurnal cycle enhancements seen in Fig. 10. To cross-validate these simulations, we also show some nitrous oxide (N_2O) measurements taken by the MLS instrument on board the Aura satellite in Fig. 11e. Also here, the early January peak is visible as a decrease in the N_2O measurement from MLS, which makes sense as N_2O is the main source of NO_x in this altitude region (McElroy and McConnell, 1971). Note that this is not the only event identified where such a behaviour can be seen. In fact, it seems that most winters seem to experience similar events (see, for example, similar plots for the boreal winter 2016–2017 shown in Appendix C).

In order to provide a more global picture and investigate the reasons for the N_2O decrease seen above central Europe in the MLS measurements, we investigated the dynamical situation of the Northern Hemisphere by looking at the ERA5 reanalysis data during this period. In fact, this event follows closely a sudden stratospheric warming (SSW) which took place in early January. It was a minor warming but with significant disturbances on middle-atmospheric chemistry and transport (Manney et al., 2015). In fact, Fig. 2 from Manney et al. (2015) shows how the polar vortex briefly split at the onset of the SSW, leading to a mixing of the air between the mid-latitudes and the poles in the upper stratosphere. Following this event, some filaments of polar air containing little ozone and N_2O reached central Europe as can be seen on the ozone map in Fig. 12. Such an irruption of polar air over Switzerland would explain the decrease in the N_2O MLS measurements seen in early January and might well explain the subsequent changes in NO_x and consequently in the ozone diurnal cycle.

Interestingly, we do not observe the strong ozone decrease associated with this filament of polar air reaching Bern, neither in the MWRs nor in the BASCOE time series. This could be a problem from the ERA5 reanalysis data as they do not feature any diurnal cycle at these altitudes and therefore might also lack the reaction of ozone to greater sun illumination (resulting in more ozone production and therefore increasing ozone amount in the low-ozone polar air which would be missed by the model). Even though this event might be considered a textbook example of such a dynamical event, we find it interesting to find such a coherent picture of a short-term event from a combination of ground-based measurements, chemistry transport model, satellite measurements, and reanalysis data.

In this publication, we focused on a specific case of short-term diurnal cycle variability related to NO_x changes in the upper stratosphere. However, in the MWRs and in the BASCOE time series, the short-term variability is not always associated with changes in NO_x concentration. Among the non-chemical processes that can impact the diurnal cycle amplitude, solar tides are important, both through vertical transport of O_x and through their modulation of temperature which can have a significant impact on ozone photochemistry (Schanz et al., 2014). Solar tides have periods of 1 solar day (24 h) or of its harmonics (e.g. 12 or 8 h) and can therefore impact the diurnal cycle as well, but generally their impact should be larger in the upper mesosphere and above (see, for example, Bjarnason et al., 1987; Huang et al., 2010b). However, Sakazaki et al. (2013) reported significant influence from tidal vertical transport at $\sim$ 35 km already; therefore, short-term tidal variability could induce some short-term variations of the ozone diurnal cycle in the upper stratosphere. The reciprocal is also true as variability of the stratospheric ozone thermal forcing can influence the generation of tides (Goncharenko et al., 2012). There have been studies on the tidal variability in the middle atmosphere, and it has been shown that solar tides are subject to a wide range of temporal variability, from intra-seasonal to short-term variability of a few days (Kopp et al., 2015; Baumgarten et al., 2018). It has also been shown that tides respond to SSW and can have nonlinear interactions with planetary and gravity waves. Hence, it is likely that a coupling exists between the tidal variability and the short-term variability observed in the ozone diurnal cycle, but it is difficult to conclude on any causal relation without additional data (e.g. high-resolution temperature or wind measurements).

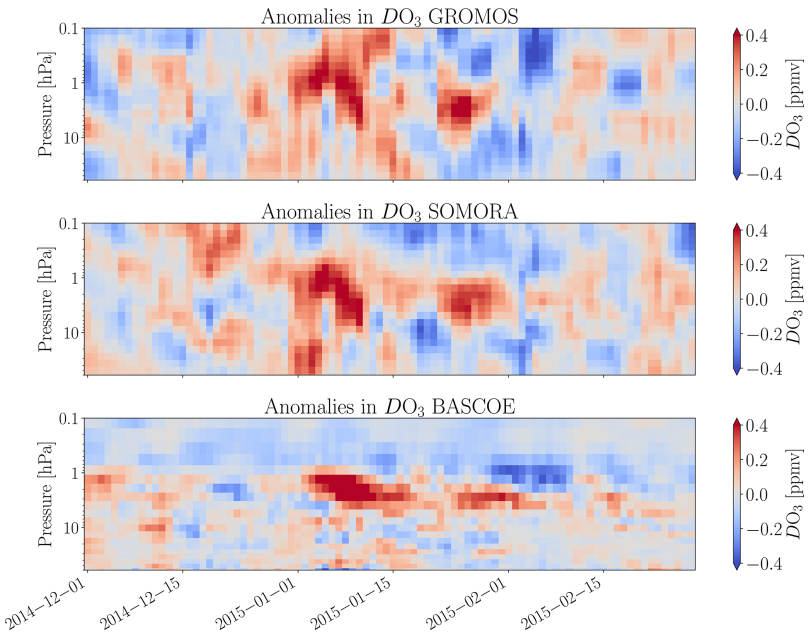

Figure 10. Anomalies in day–night D_{O_3} from GROMOS, SOMORA, and BASCOE during the boreal winter 2014–2015. For each dataset, we show the differences of D_{O_3} compared to a monthly climatology computed on the decade 2010–2020.

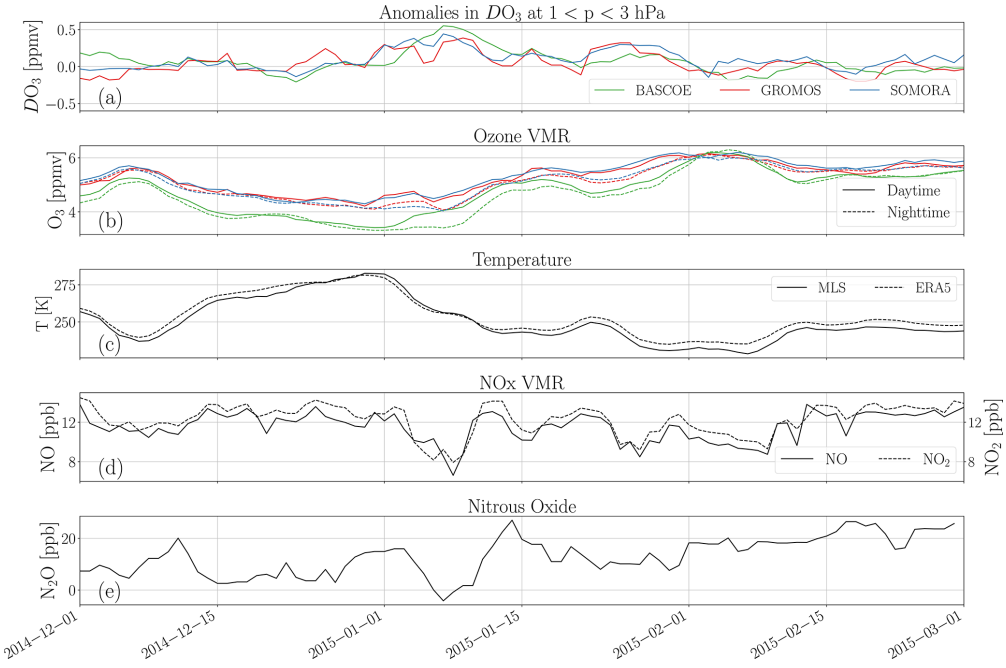

Figure 11. Time series of different quantities during the winter 2014–2015, all averaged between 3 and 1 hPa. Panel **(a)** shows the D_{O_3} anomalies, panel **(b)** shows the ozone VMR of the three dataset during daytime and nighttime, panel **(c)** shows temperature from MLS and ERA5, panel **(d)** shows NO and NO_2 as simulated by BASCOE, and panel **(e)** shows N_2O measurements from MLS.

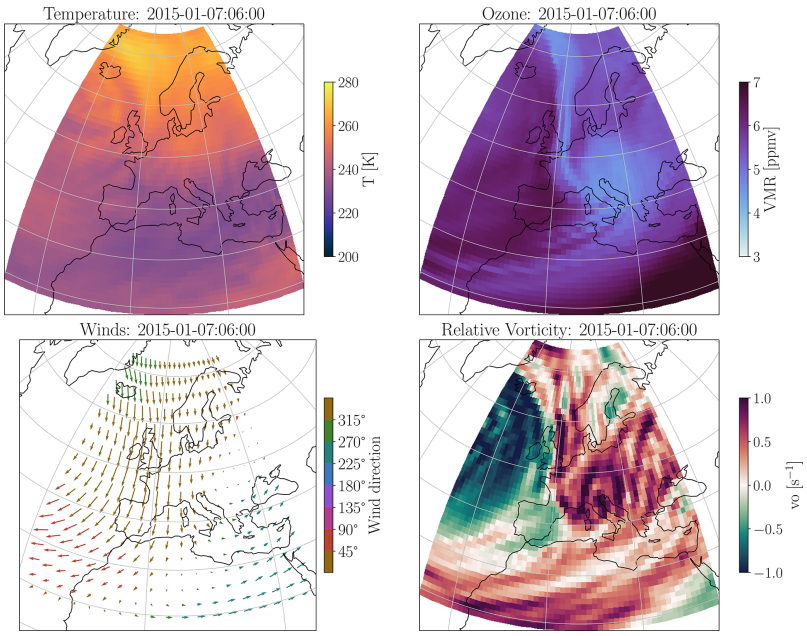

Figure 12. Situation over Europe in the upper stratosphere ∼ 5 hPa shortly after the minor SSW of early January 2015 as seen in the ERA5 reanalysis.

4 Conclusions

Using new harmonized ozone time series from two nearby microwave radiometers enables us to study in great detail the ozone diurnal cycle over Switzerland. With more than 11 years of parallel, independent measurements, these instruments provide a unique validation source for satellite and model-based datasets. We find that the recently published GDOC climatology compares well with our MWRs above Switzerland and agrees well with the WACCM and BASCOE models in the stratosphere and lower mesosphere. As reported by previous studies, we observe some remaining discrepancies between our observations and the models near the stratopause, in the transition region between ozone daytime accumulation and depletion. The discrepancies remain small and are significant only during summertime, where the diurnal cycle is stronger, providing better signal-to-noise ratio for the observations. Some of our results contradict a previous study also based on the GROMOS instrument (Studer et al., 2014), now providing a better agreement of the ozone diurnal cycle compared to model-based datasets but also compared to another previous MWR diurnal cycle study (Parrish et al., 2014). These updated results motivated the present study, and they are a consequence of the spectrometer change and of the recent harmonization of the calibration and retrieval routines of GROMOS and SOMORA (Sauvageat et al., 2022b).

For the first time, short-term variations of the ozone diurnal cycle could be detected in two co-located MWR time series, highlighting the value of ground-based radiometric measurements to monitor the short-term dynamics and photochemistry in the middle atmosphere. The quantification of these variations is limited by the rapidly increasing measurement noise; however, some enhancements of the diurnal cycle are clearly visible in the upper stratosphere during wintertime, where the diurnal cycle is otherwise very small. Compared to the averaged monthly diurnal cycle, we find an enhancement of 4–5 times the monthly mean diurnal cycle amplitude lasting for a few days. In fact, the observed short-term variability of the ozone diurnal cycle seems much higher than its intra-seasonal (month-to-month) or inter-annual variability during wintertime.

Regional (longitudinal) variability of the stratospheric ozone diurnal cycle has previously been identified by Schanz et al. (2014) in a model-based study from WACCM. They attributed the regional variability to changes in temperature (atmospheric tides), O_x, and NO_y. Our study supports that, in some cases, short-term variability in the ozone diurnal cycle can be attributed to changes in NO_x concentrations through dynamical transport. In other cases, other processes might be acting to modify the amplitude of the ozone diurnal cycle, e.g. changes in atmospheric tides. Our study also shows that a CTM like BASCOE is able to simulate the changes in the ozone diurnal cycle amplitude due to changes in NO_x. In view of its significance, we believe that the reasons and importance of the short-term variability of the diurnal cycle should be further investigated globally with BASCOE.

It is beyond the scope of this publication to provide comprehensive analysis of this phenomenon, but we aim at bringing some new data to better understand stratospheric ozone diurnal cycle variability. It seems to be of particular interest in views of the recent studies aiming at better accounting for the stratospheric ozone diurnal variability in satellite datasets (e.g. Frith et al., 2020; Strode et al., 2022; Natarajan et al., 2023). Note that we focused our analysis on the upper stratosphere, where the short-term variability was most visible in our observations, but short-term variations are not limited to this region. In fact, our observations indicate that the variability is also present in the mesosphere and the lower stratosphere, where the role of NO_x is less important and where other processes likely dominate. To conclude, more work is definitely needed to assess the importance of the short-term variability of the ozone diurnal cycle and confirm the potential role of other mechanisms influencing it.

Appendix A: Monthly ozone profile comparisons

A1 Additional plots for spring and autumn

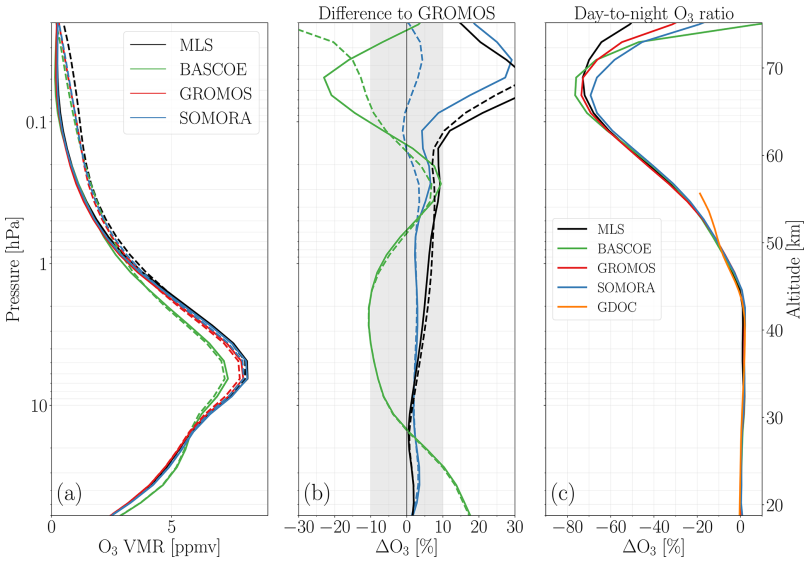

Figure A1. Same as Fig. 2 but for March.

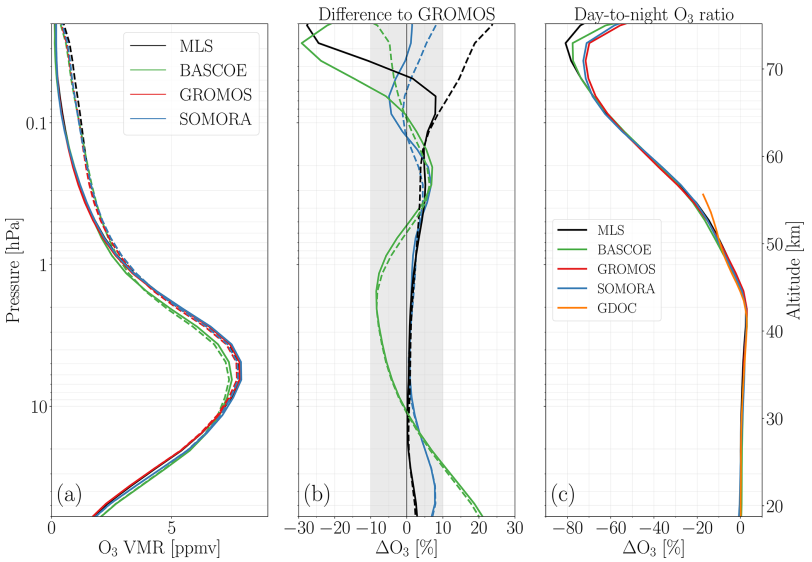

Figure A2. Same as Fig. 2 but for September.

Appendix B: Monthly diurnal cycle

B1 Additional plots for spring and autumn

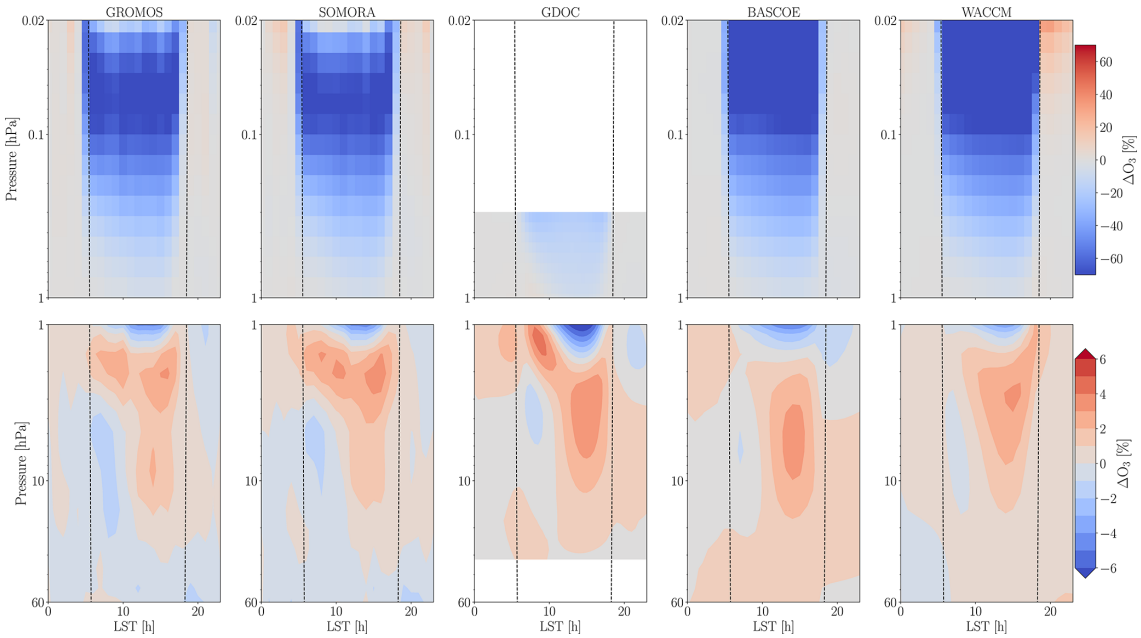

Figure B1. Same as Fig. 4 but for March.

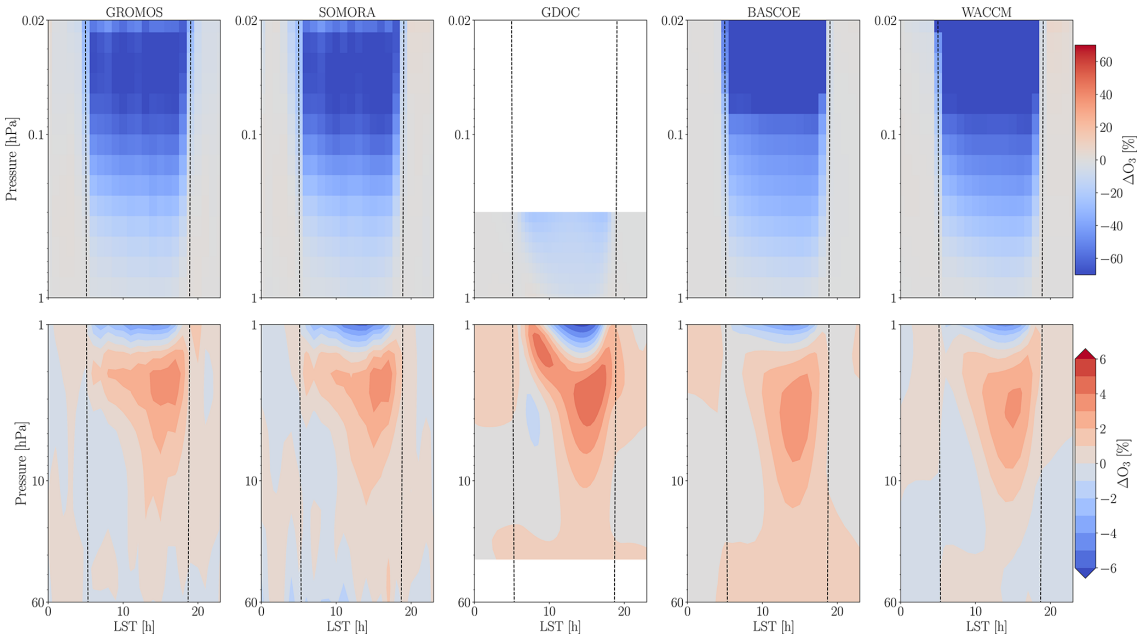

Figure B2. Same as Fig. 4 but for September.

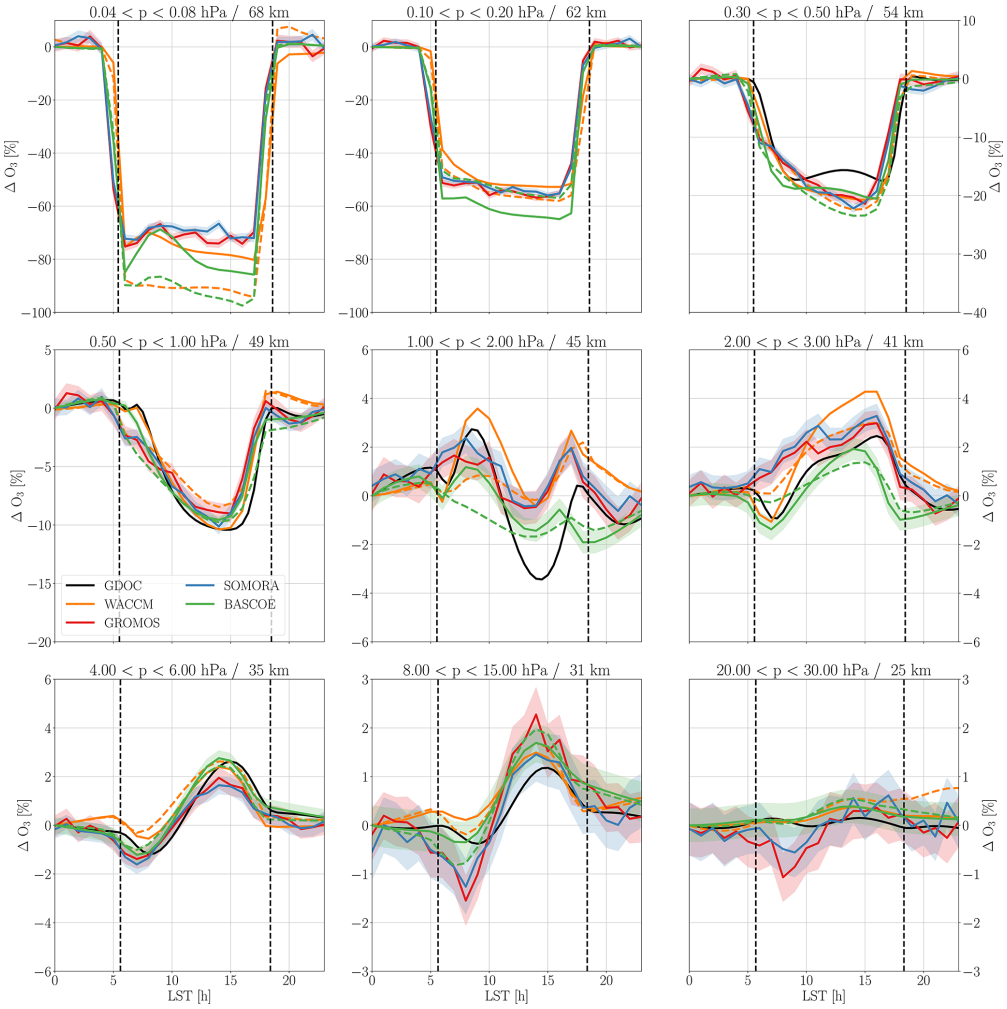

Figure B3. Same as Fig. 6 but for March.

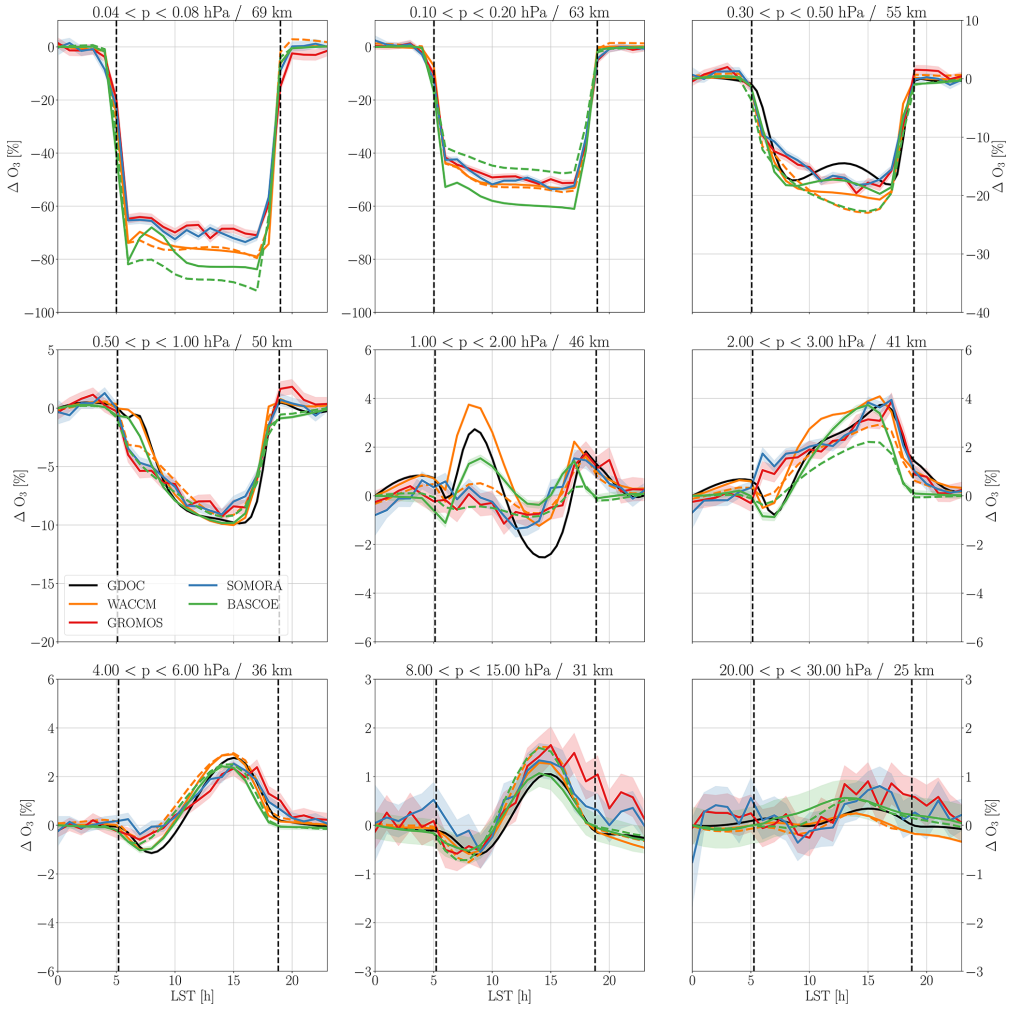

Figure B4. Same as Fig. 6 but for September.

Appendix C: Short-term variability

C1 Short-term

In this section, we show measurements and simulations of the short-term variability during the boreal winter 2016–2017. Although more work is needed to unravel the complete picture of this winter, it shows another example of diurnal cycle enhancement associated with a sharp decrease in nitrogen oxides in the upper stratosphere.

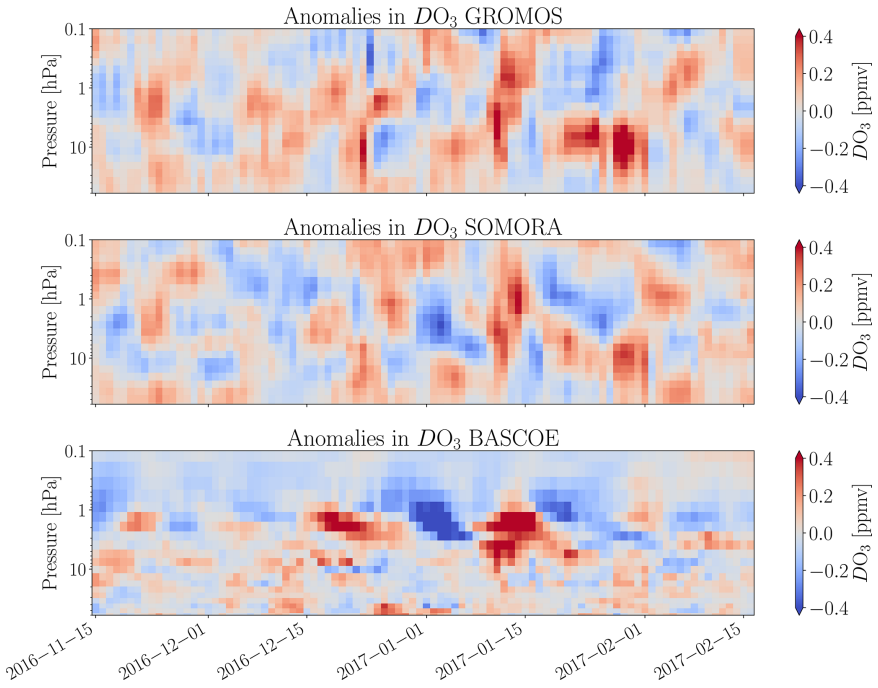

Figure C1. Anomalies in day–night D_{O_3} from GROMOS, SOMORA, and BASCOE during the boreal winter 2016–2017. For each dataset, we show the differences of D_{O_3} compared to a monthly climatology computed on the decade 2010–2020.

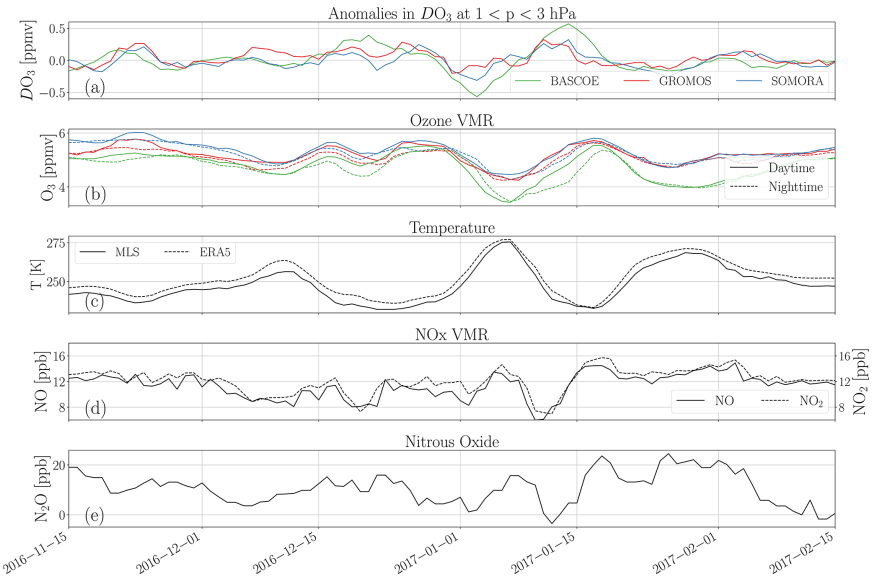

Figure C2. Time series of different quantities during the winter 2016–2017, all averaged between 3 and 1 hPa. Panel **(a)** shows the D_{O_3} anomalies, panel **(b)** shows the ozone VMR of the three dataset during daytime and nighttime, panel **(c)** shows temperature from MLS and ERA5, panel **(d)** shows NO and NO_2 as simulated by BASCOE, and panel **(e)** shows N_2O measurements from MLS.

Code and data availability. The GROMOS and SOMORA level-2 data are available from the Bern Open Repository and Information System in the form of yearly netCDF files (https://doi.org/10.48620/65, Sauvageat et al., 2022a; https://doi.org/10.48620/119, Maillard Barras et al., 2022b). The recently harmonized calibration and retrieval routines are freely available at https://doi.org/10.5281/zenodo.6799357 (Sauvageat, 2022). The data and analysis code reproducing the results presented in this paper are freely available. MLS v5 data (Schwartz et al., 2020) are available from the NASA Goddard Space Flight Center Earth Sciences Data and Information Services Center (GES DISC): https://doi.org/10.5067/Aura/MLS/DATA2516. The ERA5 dataset (https://doi.org/10.24381/cds.143582cf, Hersbach et al., 2020, 2017) was downloaded from the Copernicus Climate Change Service (C3S) Climate Data Store. The CMIP6 recommendations for sulfate aerosols used in BASCOE are available at ftp://iacftp.ethz.ch/pub_read/luo/CMIP6/ (last access: 27 June 2023).

Supplement. The supplement related to this article is available online at: https://doi.org/10.5194/acp-23-7321-2023-supplement.

Author contributions. ES carried out the data analysis, analysed the results, and prepared the manuscript. KH conceived the project and contributed to the interpretation of the results. EMB provided the SOMORA data and contributed to the interpretation of the results. SH performed a preliminary study within the frame of his Master's thesis. QE performed the BASCOE simulation and provided valuable help on the interpretation of all model results. AH and AM contributed to the interpretation of the results. All of the authors discussed the scientific findings and provided valuable feedback for the manuscript editing.

Competing interests. The contact author has declared that none of the authors has any competing interests.

Disclaimer. Publisher's note: Copernicus Publications remains neutral with regard to jurisdictional claims in published maps and institutional affiliations.

Special issue statement. This article is part of the special issue "Atmospheric ozone and related species in the early 2020s: latest results and trends (ACP/AMT inter-journal SI)". It is not associated with a conference.

Acknowledgements. The authors would like to acknowledge all the people involved in the design and operation of GROMOS and SOMORA. Also, they would like to thank the developers of the Atmospheric Radiative Transfer Simulator (Buehler et al., 2018), version 2.4 and their precious support to set up the ozone retrievals. In addition, we thank the numerous contributors to the free and open source software packages used for the data analysis, in particular xarray, matplotlib, Typhon and pyretrieval.

Financial support. This work has been supported by MeteoSwiss and the Swiss Global Atmospheric Watch programme.

Review statement. This paper was edited by Farahnaz Khosrawi and reviewed by two anonymous referees.

References

Ball, W. T., Alsing, J., Mortlock, D. J., Staehelin, J., Haigh, J. D., Peter, T., Tummon, F., Stübi, R., Stenke, A., Anderson, J., Bourassa, A., Davis, S. M., Degenstein, D., Frith, S., Froidevaux, L., Roth, C., Sofieva, V., Wang, R., Wild, J., Yu, P., Ziemke, J. R., and Rozanov, E. V.: Evidence for a continuous decline in lower stratospheric ozone offsetting ozone layer recovery, Atmos. Chem. Phys., 18, 1379–1394, https://doi.org/10.5194/acp-18-1379-2018, 2018.

Baumgarten, K., Gerding, M., Baumgarten, G., and Lübken, F.-J.: Temporal variability of tidal and gravity waves during a record long 10-day continuous lidar sounding, Atmos. Chem. Phys., 18, 371–384, https://doi.org/10.5194/acp-18-371-2018, 2018.

Bernet, L., von Clarmann, T., Godin-Beekmann, S., Ancellet, G., Maillard Barras, E., Stübi, R., Steinbrecht, W., Kämpfer, N., and Hocke, K.: Ground-based ozone profiles over central Europe: incorporating anomalous observations into the analysis of stratospheric ozone trends, Atmos. Chem. Phys., 19, 4289–4309, https://doi.org/10.5194/acp-19-4289-2019, 2019.

Bhartia, P. K., McPeters, R. D., Flynn, L. E., Taylor, S., Kramarova, N. A., Frith, S., Fisher, B., and DeLand, M.: Solar Backscatter UV (SBUV) total ozone and profile algorithm, Atmos. Meas. Tech., 6, 2533–2548, https://doi.org/10.5194/amt-6-2533-2013, 2013.

Bjarnason, G. G., Solomon, S., and Garcia, R. R.: Tidal influences on vertical diffusion and diurnal variability of ozone in the mesosphere, J. Geophys. Res.-Atmos., 92, 5609–5620, https://doi.org/10.1029/JD092iD05p05609, 1987.

Buehler, S. A., Mendrok, J., Eriksson, P., Perrin, A., Larsson, R., and Lemke, O.: ARTS, the Atmospheric Radiative Transfer Simulator – version 2.2, the planetary toolbox edition, Geosci. Model Dev., 11, 1537–1556, https://doi.org/10.5194/gmd-11-1537-2018, 2018.

Chabrillat, S., Vigouroux, C., Christophe, Y., Engel, A., Errera, Q., Minganti, D., Monge-Sanz, B. M., Segers, A., and Mahieu, E.: Comparison of mean age of air in five reanalyses using the BASCOE transport model, Atmos. Chem. Phys., 18, 14715–14735, https://doi.org/10.5194/acp-18-14715-2018, 2018.

Chapman, S.: A theory of the upper-atmospheric ozone, Memoirs of the Royal Meteorological Society, 3, https://www.rmets.org/sites/default/files/papers/chapman-memoirs.pdf (last access: 27 June 2023), 1930.

Connor, B. J., Siskind, D. E., Tsou, J., Parrish, A., and Remsberg, E. E.: Ground-based microwave observations of ozone in the upper stratosphere and mesosphere, J. Geophys. Res.-Atmos., 99, 16757–16770, https://doi.org/10.1029/94JD01153, 1994.

Crutzen, P. J.: The influence of nitrogen oxides on the atmospheric ozone content, Q. J. Roy. Meteor. Soc., 96, 320–325, https://doi.org/10.1002/qj.49709640815, 1970.

Errera, Q. and Fonteyn, D.: Four-dimensional variational chemical assimilation of CRISTA stratospheric measurements, J. Geophys. Res.-Atmos., 106, 12253–12265, https://doi.org/10.1029/2001JD900010, 2001.

Errera, Q., Daerden, F., Chabrillat, S., Lambert, J. C., Lahoz, W. A., Viscardy, S., Bonjean, S., and Fonteyn, D.: 4D-Var assimilation of MIPAS chemical observations: ozone and nitrogen dioxide analyses, Atmos. Chem. Phys., 8, 6169–6187, https://doi.org/10.5194/acp-8-6169-2008, 2008.

Frith, S. M., Bhartia, P. K., Oman, L. D., Kramarova, N. A., McPeters, R. D., and Labow, G. J.: Model-based climatology of diurnal variability in stratospheric ozone as a data analysis tool, Atmos. Meas. Tech., 13, 2733–2749, https://doi.org/10.5194/amt-13-2733-2020, 2020.

Froidevaux, L., Jiang, Y. B., Lambert, A., Livesey, N. J., Read, W. G., Waters, J. W., Browell, E. V., Hair, J. W., Avery, M. A., McGee, T. J., Twigg, L. W., Sumnicht, G. K., Jucks, K. W., Margitan, J. J., Sen, B., Stachnik, R. A., Toon, G. C., Bernath, P. F., Boone, C. D., Walker, K. A., Filipiak, M. J., Harwood, R. S., Fuller, R. A., Manney, G. L., Schwartz, M. J., Daffer, W. H., Drouin, B. J., Cofield, R. E., Cuddy, D. T., Jarnot, R. F., Knosp, B. W., Perun, V. S., Snyder, W. V., Stek, P. C., Thurstans, R. P., and Wagner, P. A.: Validation of Aura Microwave Limb Sounder stratospheric ozone measurements, J. Geophys. Res.-Atmos., 113, D15S20, https://doi.org/10.1029/2007JD008771, 2008.

Garcia, R. R., Marsh, D. R., Kinnison, D. E., Boville, B. A., and Sassi, F.: Simulation of secular trends in the middle atmosphere, 1950–2003, J. Geophys. Res.-Atmos., 112, D09301, https://doi.org/10.1029/2006JD007485, 2007.

Godin-Beekmann, S., Azouz, N., Sofieva, V. F., Hubert, D., Petropavlovskikh, I., Effertz, P., Ancellet, G., Degenstein, D. A., Zawada, D., Froidevaux, L., Frith, S., Wild, J., Davis, S., Steinbrecht, W., Leblanc, T., Querel, R., Tourpali, K., Damadeo, R., Maillard Barras, E., Stübi, R., Vigouroux, C., Arosio, C., Nedoluha, G., Boyd, I., Van Malderen, R., Mahieu, E., Smale, D., and Sussmann, R.: Updated trends of the stratospheric ozone vertical distribution in the 60° S–60° N latitude range based on the LOTUS regression model , Atmos. Chem. Phys., 22, 11657–11673, https://doi.org/10.5194/acp-22-11657-2022, 2022.

Goncharenko, L. P., Coster, A. J., Plumb, R. A., and Domeisen, D. I. V.: The potential role of stratospheric ozone in the stratosphere-ionosphere coupling during stratospheric warmings, Geophys. Res. Lett., 39, L08101, https://doi.org/10.1029/2012GL051261, 2012.

Haefele, A., Hocke, K., Kämpfer, N., Keckhut, P., Marchand, M., Bekki, S., Morel, B., Egorova, T., and Rozanov, E.: Diurnal changes in middle atmospheric H_2O and O_3: Observations in the Alpine region and climate models, J. Geophys. Res.-Atmos., 113, D17303, https://doi.org/10.1029/2008JD009892, 2008.

Hersbach, H., Bell, B., Berrisford, P., Hirahara, S., Horányi, A., Muñoz-Sabater, J., Nicolas, J., Peubey, C., Radu, R., Schepers, D., Simmons, A., Soci, C., Abdalla, S., Abellan, X., Balsamo, G., Bechtold, P., Biavati, G., Bidlot, J., Bonavita, M., De Chiara, G., Dahlgren, P., Dee, D., Diamantakis, M., Dragani, R., Flemming, J., Forbes, R., Fuentes, M., Geer, A., Haimberger, L., Healy, S., Hogan, R.J., Hólm, E., Janisková, M., Keeley, S., Laloyaux, P., Lopez, P., Lupu, C., Radnoti, G., de Rosnay, P., Rozum, I., Vamborg, F., Villaume, S., and Thépaut, J.-N.: Complete ERA5 from 1940: Fifth generation of ECMWF atmospheric reanalyses of the global climate, Copernicus Climate Change Service (C3S) Data Store (CDS) [data set], https://doi.org/10.24381/cds.143582cf, 2017.

Hersbach, H., Bell, B., Berrisford, P., Hirahara, S., Horányi, A., Muñoz-Sabater, J., Nicolas, J., Peubey, C., Radu, R., Schepers, D., Simmons, A., Soci, C., Abdalla, S., Abellan, X., Balsamo, G., Bechtold, P., Biavati, G., Bidlot, J., Bonavita, M., De Chiara, G., Dahlgren, P., Dee, D., Diamantakis, M., Dragani, R., Flemming, J., Forbes, R., Fuentes, M., Geer, A., Haimberger, L., Healy, S., Hogan, R. J., Hólm, E., Janisková, M., Keeley, S., Laloyaux, P., Lopez, P., Lupu, C., Radnoti, G., de Rosnay, P., Rozum, I., Vamborg, F., Villaume, S., and Thépaut, J.-N.: The ERA5 global reanalysis, Q. J. Roy. Meteor. Soc., 146, 1999–2049, https://doi.org/10.1002/qj.3803, 2020.

Huang, F. T., Reber, C. A., and Austin, J.: Ozone diurnal variations observed by UARS and their model simulation, J. Geophys. Res.-Atmos., 102, 12971–12985, https://doi.org/10.1029/97JD00461, 1997.

Huang, F. T., Mayr, H. G., Russell III, J. M., and Mlynczak, M. G.: Ozone diurnal variations in the stratosphere and lower mesosphere, based on measurements from SABER on TIMED, J. Geophys. Res.-Atmos., 115, D24308, https://doi.org/10.1029/2010JD014484, 2010a.

Huang, F. T., McPeters, R. D., Bhartia, P. K., Mayr, H. G., Frith, S. M., Russell III, J. M., and Mlynczak, M. G.: Temperature diurnal variations (migrating tides) in the stratosphere and lower mesosphere based on measurements from SABER on TIMED, J. Geophys. Res.-Atmos., 115, D16121, https://doi.org/10.1029/2009JD013698, 2010b.

Huijnen, V., Flemming, J., Chabrillat, S., Errera, Q., Christophe, Y., Blechschmidt, A.-M., Richter, A., and Eskes, H.: C-IFS-CB05-BASCOE: stratospheric chemistry in the Integrated Forecasting System of ECMWF, Geosci. Model Dev., 9, 3071–3091, https://doi.org/10.5194/gmd-9-3071-2016, 2016.

Kinnison, D. E., Brasseur, G. P., Walters, S., Garcia, R. R., Marsh, D. R., Sassi, F., Harvey, V. L., Randall, C. E., Emmons, L., Lamarque, J. F., Hess, P., Orlando, J. J., Tie, X. X., Randel, W., Pan, L. L., Gettelman, A., Granier, C., Diehl, T., Niemeierm U., and Simmons, A. J.: Sensitivity of chemical tracers to meteorological parameters in the MOZART-3 chemical transport model, J. Geophys. Res.-Atmos., 112, D20302, https://doi.org/10.1029/2006JD007879, 2007.

Kopp, M., Gerding, M., Höffner, J., and Lübken, F.-J.: Tidal signatures in temperatures derived from daylight lidar soundings above Kühlungsborn (54° N, 12° E), J. Atmos. Sol.-Terr. Phy., 127, 37–50, https://doi.org/10.1016/j.jastp.2014.09.002, 2015.

Livesey, N. J., Read, W. G., Wagner, P. A., Froidevaux, L., Santee, M. L., Schwartz, M. J., Lambert, A., Valle, L. F. M., Pumphrey, H. C., Manney, G. L., Fuller, R. A., Jarnot, R. F., Knosp, B. W., and Lay, R. R.: Earth Observing System (EOS) Aura Microwave Limb Sounder (MLS) Version 5.0x Level 2 and 3 data quality and description document., Tech. Rep., https://mls.jpl.nasa.gov/eos-aura-mls/data-documentation, last access: 30 December 2022.

Maillard Barras, E., Haefele, A., Nguyen, L., Tummon, F., Ball, W. T., Rozanov, E. V., Rüfenacht, R., Hocke, K., Ber-

net, L., Kämpfer, N., Nedoluha, G., and Boyd, I.: Study of the dependence of long-term stratospheric ozone trends on local solar time, Atmos. Chem. Phys., 20, 8453–8471, https://doi.org/10.5194/acp-20-8453-2020, 2020.

Maillard Barras, E., Haefele, A., Stübi, R., Jouberton, A., Schill, H., Petropavlovskikh, I., Miyagawa, K., Stanek, M., and Froidevaux, L.: Dynamical linear modeling estimates of long-term ozone trends from homogenized Dobson Umkehr profiles at Arosa/-Davos, Switzerland, Atmos. Chem. Phys., 22, 14283–14302, https://doi.org/10.5194/acp-22-14283-2022, 2022a.

Maillard Barras, E., Sauvageat, E., Hocke, K., Murk, A., and Haefele, A.: Harmonized middle atmospheric ozone time series from SOMORA, BORIS Portal [data set], https://doi.org/10.48620/119, 2022b.

Manney, G. L., Lawrence, Z. D., Santee, M. L., Read, W. G., Livesey, N. J., Lambert, A., Froidevaux, L., Pumphrey, H. C., and Schwartz, M. J.: A minor sudden stratospheric warming with a major impact: Transport and polar processing in the 2014/2015 Arctic winter, Geophys. Res. Lett., 42, 7808–7816, https://doi.org/10.1002/2015GL065864, 2015.

Marsh, D. R., Mills, M. J., Kinnison, D. E., Lamarque, J.-F., Calvo, N., and Polvani, L. M.: Climate Change from 1850 to 2005 Simulated in CESM1(WACCM), J. Climate, 26, 7372–7391, https://doi.org/10.1175/JCLI-D-12-00558.1, 2013.

McElroy, M. B. and McConnell, J. C.: Nitrous Oxide: A Natural Source of Stratospheric NO, J. Atmos. Sci., 28, 1095–1098, https://doi.org/10.1175/1520-0469(1971)028<1095:NOANSO>2.0.CO;2, 1971.

Meinshausen, M., Vogel, E., Nauels, A., Lorbacher, K., Meinshausen, N., Etheridge, D. M., Fraser, P. J., Montzka, S. A., Rayner, P. J., Trudinger, C. M., Krummel, P. B., Beyerle, U., Canadell, J. G., Daniel, J. S., Enting, I. G., Law, R. M., Lunder, C. R., O'Doherty, S., Prinn, R. G., Reimann, S., Rubino, M., Velders, G. J. M., Vollmer, M. K., Wang, R. H. J., and Weiss, R.: Historical greenhouse gas concentrations for climate modelling (CMIP6), Geosci. Model Dev., 10, 2057–2116, https://doi.org/10.5194/gmd-10-2057-2017, 2017.

Minganti, D., Chabrillat, S., Christophe, Y., Errera, Q., Abalos, M., Prignon, M., Kinnison, D. E., and Mahieu, E.: Climatological impact of the Brewer–Dobson circulation on the N_2O budget in WACCM, a chemical reanalysis and a CTM driven by four dynamical reanalyses, Atmos. Chem. Phys., 20, 12609–12631, https://doi.org/10.5194/acp-20-12609-2020, 2020.

Minganti, D., Chabrillat, S., Errera, Q., Prignon, M., Kinnison, D. E., Garcia, R. R., Abalos, M., Alsing, J., Schneider, M., Smale, D., Jones, N., and Mahieu, E.: Evaluation of the N_2O Rate of Change to Understand the Stratospheric Brewer-Dobson Circulation in a Chemistry-Climate Model, J. Geophys. Res.-Atmos., 127, e2021JD036390, https://doi.org/10.1029/2021JD036390, 2022.

Natarajan, M., Damadeo, R., and Flittner, D.: Solar occultation measurement of mesospheric ozone by SAGE III/ISS: impact of variations along the line of sight caused by photochemistry, Atmos. Meas. Tech., 16, 75–87, https://doi.org/10.5194/amt-16-75-2023, 2023.

Orbe, C., Oman, L. D., Strahan, S. E., Waugh, D. W., Pawson, S., Takacs, L. L., and Molod, A. M.: Large-Scale Atmospheric Transport in GEOS Replay Simulations, J. Adv. Model. Earth Sy., 9, 2545–2560, https://doi.org/10.1002/2017MS001053, 2017.

Pallister, R. C. and Tuck, A. F.: The diurnal variation of ozone in the upper stratosphere as a test of photochemical theory, Q. J. Roy. Meteor. Soc., 109, 271–284, https://doi.org/10.1002/qj.49710946002, 1983.

Parrish, A., Boyd, I. S., Nedoluha, G. E., Bhartia, P. K., Frith, S. M., Kramarova, N. A., Connor, B. J., Bodeker, G. E., Froidevaux, L., Shiotani, M., and Sakazaki, T.: Diurnal variations of stratospheric ozone measured by ground-based microwave remote sensing at the Mauna Loa NDACC site: measurement validation and GEOSCCM model comparison, Atmos. Chem. Phys., 14, 7255–7272, https://doi.org/10.5194/acp-14-7255-2014, 2014.

Prather, M. J.: Ozone in the upper stratosphere and mesosphere, J. Geophys. Res. 86, 5325, https://doi.org/10.1029/JC086iC06p05325, 1981.

Prignon, M., Chabrillat, S., Friedrich, M., Smale, D., Strahan, S. E., Bernath, P. F., Chipperfield, M. P., Dhomse, S. S., Feng, W., Minganti, D., Servais, C., and Mahieu, E.: Stratospheric Fluorine as a Tracer of Circulation Changes: Comparison Between Infrared Remote-Sensing Observations and Simulations With Five Modern Reanalyses, J. Geophys. Res., 126, e2021JD034995, https://doi.org/10.1029/2021JD034995, 2021.

Ricaud, P., Brillet, J., De La Noe, J., and Parisot, J. P.: Diurnal and seasonal variations of stratomesospheric ozone: Analysis of ground-based microwave measurements in Bordeaux, France, J. Geophys. Res.-Atmos., 96, 18617–18629, https://doi.org/10.1029/91JD01871, 1991.

Rodgers, C. D. and Connor, B. J.: Intercomparison of remote sounding instruments, J. Geophys. Res.-Atmos., 108, 4116, https://doi.org/10.1029/2002JD002299, 2003.

Sakazaki, T., Fujiwara, M., Mitsuda, C., Imai, K., Manago, N., Naito, Y., Nakamura, T., Akiyoshi, H., Kinnison, D., Sano, T., Suzuki, M., and Shiotani, M.: Diurnal ozone variations in the stratosphere revealed in observations from the Superconducting Submillimeter-Wave Limb-Emission Sounder (SMILES) on board the International Space Station (ISS), J. Geophys. Res.-Atmos., 118, 2991–3006, https://doi.org/10.1002/jgrd.50220, 2013.

Sakazaki, T., Shiotani, M., Suzuki, M., Kinnison, D., Zawodny, J. M., McHugh, M., and Walker, K. A.: Sunset–sunrise difference in solar occultation ozone measurements (SAGE II, HALOE, and ACE–FTS) and its relationship to tidal vertical winds, Atmos. Chem. Phys., 15, 829–843, https://doi.org/10.5194/acp-15-829-2015, 2015.

Sauvageat, E.: GROMORA-harmo: calibration and retrieval code for Swiss ozone microwave radiometers, version 2.0, Zenodo [code], https://doi.org/10.5281/zenodo.6799357, 2022.

Sauvageat, E., Hocke, K., Maillard Barras, E., Haefele, A., and Murk, A.: Harmonized middle atmospheric ozone time series from GROMOS, BORIS Portal [data set], https://doi.org/10.48620/65, 2022a.

Sauvageat, E., Maillard Barras, E., Hocke, K., Haefele, A., and Murk, A.: Harmonized retrieval of middle atmospheric ozone from two microwave radiometers in Switzerland, Atmos. Meas. Tech., 15, 6395–6417, https://doi.org/10.5194/amt-15-6395-2022, 2022b.

Schanz, A., Hocke, K., and Kämpfer, N.: Daily ozone cycle in the stratosphere: global, regional and seasonal behaviour modelled

with the Whole Atmosphere Community Climate Model, Atmos. Chem. Phys., 14, 7645–7663, https://doi.org/10.5194/acp-14-7645-2014, 2014.

Schanz, A., Hocke, K., Kämpfer, N., Chabrillat, S., Inness, A., Palm, M., Notholt, J., Boyd, I., Parrish, A., and Kasai, Y.: The Diurnal Variation in Stratospheric Ozone from MACC Reanalysis, ERA-Interim, WACCM, and Earth Observation Data: Characteristics and Intercomparison, Atmosphere, 12, 625, https://doi.org/10.3390/atmos12050625, 2021.

Schneider, N., Selsis, F., Urban, J., Lezeaux, O., Noé, J. D. L., and Ricaud, P.: Seasonal and Diurnal Ozone Variations: Observations and Modeling, J. Atmos. Chem., 50, 25–47, https://doi.org/10.1007/s10874-005-1172-z, 2005.

Schranz, F., Fernandez, S., Kämpfer, N., and Palm, M.: Diurnal variation in middle-atmospheric ozone observed by ground-based microwave radiometry at Ny-Ålesund over 1 year, Atmos. Chem. Phys., 18, 4113–4130, https://doi.org/10.5194/acp-18-4113-2018, 2018.

Schwartz, M., Froidevaux, L., Livesey, N., and Read, W.: MLS/Aura Level 2 Ozone (O_3) Mixing Ratio V005, Goddard Earth Sciences Data and Information Services Center (GES DISC) [data set], https://doi.org/10.5067/Aura/MLS/DATA2516, 2020.

Skachko, S., Ménard, R., Errera, Q., Christophe, Y., and Chabrillat, S.: EnKF and 4D-Var data assimilation with chemical transport model BASCOE (version 05.06), Geosci. Model Dev., 9, 2893–2908, https://doi.org/10.5194/gmd-9-2893-2016, 2016.

SPARC: SPARC CCMVal Report on the Evaluation of Chemistry-Climate Models, in: SPARC Report, edited by: Eyring, V., Shepherd, T. G., and Waugh, D. W., SPARC Report No. 5, WCRP-30/2010, WMO/TD – No. 40, https://www.sparc-climate.org/publications/sparc-reports/ (last access: 27 June 2023), 2010.

SPARC/IO3C/GAW: SPARC/IO3C/GAW Report on Long-term Ozone Trends and Uncertainties in the Stratosphere, in: SPARC Report, edited by: Petropavlovskikh, I., Godin-Beekmann, S., Hubert, D., Damadeo, R., Hassler, B., and Sofieva, V., SPARC Report No. 9, GAW Report No. 241, WCRP-17/2018, https://doi.org/10.17874/f899e57a20b, 2019.

Strode, S. A., Taha, G., Oman, L. D., Damadeo, R., Flittner, D., Schoeberl, M., Sioris, C. E., and Stauffer, R.: SAGE III/ISS ozone and NO_2 validation using diurnal scaling factors, Atmos. Meas. Tech., 15, 6145–6161, https://doi.org/10.5194/amt-15-6145-2022, 2022.

Studer, S., Hocke, K., Schanz, A., Schmidt, H., and Kämpfer, N.: A climatology of the diurnal variations in stratospheric and mesospheric ozone over Bern, Switzerland, Atmos. Chem. Phys., 14, 5905–5919, https://doi.org/10.5194/acp-14-5905-2014, 2014.

Vaughan, G.: Diurnal variation of mesospheric ozone, Nature, 296, 133–135, https://doi.org/10.1038/296133a0, 1982.

Waters, J., Froidevaux, L., Harwood, R., Jarnot, R., Pickett, H., Read, W., Siegel, P., Cofield, R., Filipiak, M., Flower, D., Holden, J., Lau, G., Livesey, N., Manney, G., Pumphrey, H., Santee, M., Wu, D., Cuddy, D., Lay, R., Loo, M., Perun, V., Schwartz, M., Stek, P., Thurstans, R., Boyles, M., Chandra, K., Chavez, M., Chen, G.-S., Chudasama, B., Dodge, R., Fuller, R., Girard, M., Jiang, J., Jiang, Y., Knosp, B., LaBelle, R., Lam, J., Lee, K., Miller, D., Oswald, J., Patel, N., Pukala, D., Quintero, O., Scaff, D., Van Snyder, W., Tope, M., Wagner, P., and Walch, M.: The Earth observing system microwave limb sounder (EOS MLS) on the Aura Satellite, IEEE T. Geosci. Remote, 44, 1075–1092, https://doi.org/10.1109/TGRS.2006.873771, 2006.

Zommerfelds, W. C., Kunzi, K. F., Summers, M. E., Bevilacqua, R. M., Strobel, D. F., Allen, M., and Sawchuck, W. J.: Diurnal variations of mesospheric ozone obtained by ground-based microwave radiometry, J. Geophys. Res.-Atmos., 94, 12819–12832, https://doi.org/10.1029/JD094iD10p12819, 1989.

7 | Conclusions and Outlook

7.1 Concluding remarks

In this dissertation, I presented the work done to improve the quality of ozone time series measured by two Swiss microwave radiometers: GROMOS, operated at the IAP in Bern and SOMORA, operated at MeteoSwiss in Payerne. The data processing of the two instruments underwent a full harmonization, yielding new calibration and retrieval routines and new time series of middle-atmospheric ozone for both instruments from 2009 until today.

The new harmonized ozone retrievals now yield accurate ozone time series which are important for long-term ozone trends over Switzerland and provide consolidated validation datasets for satellite-based measurements. The new time series should enable reliable trend studies and are ready to be used in LOTUS phase 3, which started recently (2023-2025). In fact, the consistency between ground- and satellite-based observations is one of the focus areas identified for this new phase of LOTUS, in preparation for the next WMO Ozone Assessment in 2026. Because of the discrepancies between GROMOS and SOMORA, only the trends computed from SOMORA were shown in the Ozone Assessment 2022 (WMO, 2022). The hope is that this work will contribute to improving the quality and reliability of long-term strato–mesospheric ozone measurements.

Overall, the harmonized ozone time series from GROMOS and SOMORA show an improved agreement compared to the older series and validate well against external, satellite-based datasets. Mean relative differences between GROMOS, SOMORA and MLS are mostly lower than 10% between 50 and 0.1 hPa ($\sim 22 - 65$ km) and lower than 5% in the mid- and upper stratosphere ($\sim 30 - 50$ km). A careful documentation was produced which can be found along the time series (Sauvageat et al., 2022a; Maillard Barras et al., 2022b) and should help explain most of the spurious periods remaining on the two time series. The outputs of the routine have also been harmonized, making further studies using the two series easier. For now, only the GROMOS dataset starting in 2009 has been uploaded to NDACC but the extended, homogenized time series should follow soon (see Section 7.2.1).

I also investigated the performance of the digital spectrometer used in GROMOS and SOMORA: the Acqiris AC240. The AC240 was suspected to introduce a systematic bias in the atmospheric profiles retrieved from its measured spectra. The AC240 was compared against two other, more recent spectrometers to assess the bias under a wide range of atmospheric conditions and in the laboratory. Our investigations revealed that the AC240 suffers from a systematic spectral bias, which has a considerable influence on the retrieved ozone profiles, yielding a negative bias in the order of 10% compared to the two other spectrometers. We showed that a simple mathematical correction can be applied on the calibrated spectra to account for this bias but unfortunately, it was not possible to reproduce the bias in the laboratory and its origin remains unclear to this day. As mentioned in Chapter 5 though, similar bias amplitudes were observed in independent measurements, giving us confidence that the bias is real and should be accounted for in any time series measured with the AC240.

Finally, I used the harmonized time series of GROMOS and SOMORA to derive new strato–mesospheric ozone diurnal cycles over Switzerland. Compared to the last study on this topic

done with older GROMOS data, the stratospheric diurnal cycle amplitudes are now in better agreement against different model-based datasets. For the first time, we also measured short-term (in the order of days) variations in the upper stratospheric diurnal cycle during winter, exceeding its interannual variability. In a case study, I showed that this short-term variability is caused by meridional transport of air with low NO_x abundance, leading to an increased accumulation of ozone during daytime. It confirms certain model results obtained by Schanz et al., 2014, and opens the way to many interesting new research questions, such as the occurrence and significance of this variability on satellite homogenization studies, or the importance of short-term tidal variability in the middle atmosphere.

7.2 Outlook

In this section, before presenting some general recommendation on future works that could build upon this thesis, I would like to begin with a few remarks on the ongoing extension of the GROMOS and SOMORA ozone time series to the pre-2009 period, as this is of primary importance to establish new, harmonized ozone long-term trends.

7.2.1 Extension and homogenization of GROMOS and SOMORA time series

At first, the harmonization of the calibration and retrieval routines focused on the post-2009 period, when the two instruments used the same digital spectrometer (i.e., the AC240): this is the *version 2* of the time series which led to all the results presented in this dissertation. However, to compute truly long-term ozone trends, there is a need to extend the harmonization to the period before 2009 for the two instruments and to homogenize the complete time series. By homogenization, it is meant the careful treatment of the transition period, during which the spectrometer was updated. To do this homogenization without introducing jumps in the series, different strategies exist depending on the research interest but in any cases, it should be based on the period 2009-2011, where the older and the AC240 spectrometers were measuring in parallel, on both instruments.

The reprocessing of the GROMOS time series with the harmonized algorithms has now been completed back to 1994, which marks the start of the operational monitoring with this instrument. After correction of the AC240 bias for the post-2009 period, the average difference between the older filter banks and the AC240 between 2009 and 2011 was lower than 5% in the stratosphere and lower than 10% in the lower mesosphere with no clear seasonal variations. Therefore, a simple homogenization procedure can be applied to the GROMOS time series, simply removing the mean difference computed during the transition period from the filter banks retrieved profiles. This is similar as previously done by Moreira et al., 2015 and yields the full GROMOS time series (*version 3*) shown in Fig. 1.6. A similar work is ongoing on SOMORA at MeteoSwiss and should be completed soon.

At this point, I would like to point out that the correction for the AC240 bias for the post-2009 period on GROMOS yields an excellent agreement with the older filter bank spectrometer series but also degrades the agreement of the GROMOS time series against MLS. It was expected as the GROMOS time series version 2 agreed so well with MLS and as the spectral bias produces an error of around 10% on the ozone profile. As this bias is constant with time, it should not impact any trends derived from properly homogenized time series, but it will definitely need further investigations.

7.2.2 Recommendations for future work

Long-term ozone trends from GROMOS and SOMORA are of interest for the stratospheric ozone community. Although the new trends have not been computed yet, the new harmonized

ozone time series should enable the community to compute reliable ozone trends from GROMOS and SOMORA. However, it is worth keeping in mind that, while the post-2009 times series have been properly documented and validated against satellite datasets, it is not the case yet with the pre-2009 time series and it would be valuable to extend the validation to the pre-2009 series as well. Notably, some anomalous periods are still present after harmonization of the GROMOS time series slightly before 2000.

Regarding the bias of the AC240, new measurement campaigns are now in progress to further improve the understanding of the spectral bias. Namely, parallel measurements of the AC240 with other spectrometers are now ongoing on GROMOS and MIAWARA at the IAP. MeteoSwiss is planning to upgrade the SOMORA spectrometer and plan for parallel measurements as well.

On the strato–mesospheric ozone diurnal cycle, there are many remaining questions, especially on the cause of the observed short-term variability. Whereas the study presented in this dissertation was limited to a particular case study, there are now many possibilities to go beyond and investigate any systematic behind the short-term variability.

To summarise, below are my main suggestions for the continuation of the GROMORA project or for future studies:

- Finalize and validate the full homogenized time series of GROMOS (1994–now) and SOMORA (2000–now)
- Compute updated ozone trends from GROMOS and SOMORA
- Provide further validation and improve the understanding of the AC240 spectral bias from the multiple parallel measurement campaign in progress or to come.
- Investigate in more details the short-term variability of the ozone diurnal cycle, e.g. with BASCOE. The simulations can be combined with the recently harmonized co-located temperature measurements from the temperature radiometer (TEMPERA), for instance to study potential influence of short-term tidal variability.
- Investigate and monitor the effects of the development of 5G mobile network on GROMOS. In fact, we recently discovered radio frequency interferences (RFIs) affecting GROMOS which are believed to originate from the increasing use of 5G frequencies in Switzerland (the IF of GROMOS is in the centre of a recently allocated 5G band). If needed, the adoption of RFI mitigation strategies, widely used in satellite microwave radiometry, should be investigated.

Acknowledgment

Too many people contributed to the completion of my PhD thesis and to mention all of them without forgetting someone important would be delusional. Therefore, I would like to express my gratitude to all those who supported me in any way to reach this point, and I would especially like to thank:

Axel Murk and Klemens Hocke, who both in their very own way, guided me smoothly through the discovery of microwave remote sensing and of the middle atmosphere. Their motivation to share their expertise and their full support for my way of working were the key to the successful completion of my thesis.

Eliane Maillard Barras for her support, patience, and the many hours of interesting discussions and to Alexander Haefele for trusting me since the beginning.

Rolf Rüfenacht for always sharing with me excellent tips for my career plans.

Jonas Hagen, Andres Luder, and Tobias Plüss for providing me with a bit of proper IT education and for their precious help on instrumental aspects. And to all the people that contributed to keep GROMOS and SOMORA alive and operational all these years.

Beatrice Thut and Simone Corry for their kindness and their patience to deal with my carelessness in administrative matters.

The ARTS community for their work and availability and to the rest of the open-source community, especially around Python (numpy, matplotlib, xarray, ...).

The rest of the microwave group, including Roland, Witali, Yue, Leonie, Alistair, and all the others for sharing the good (and bad) times during the last 4 years.

My family, friends, and roomates who supported me since day 1 and always encouraged me to follow my path.

Audrey, pour rester fidèle à elle-même, pour sa confiance et pour son soutien sans faille dans mes projets les plus fous. Merci !

Bibliography

Ancellet, G. et al. (2022). "Homogenization of the Observatoire de Haute Provence electrochemical concentration cell (ECC) ozonesonde data record: comparison with lidar and satellite observations". In: *Atmospheric Measurement Techniques* 15.10, pp. 3105–3120. DOI: 10.5194/amt-15-3105-2022.

Anderson, J. et al. (2000). "Halogen Occultation Experiment confirmation of stratospheric chlorine decreases in accordance with the Montreal Protocol". In: *Journal of Geophysical Research: Atmospheres* 105.D4, pp. 4483–4490. DOI: 10.1029/1999JD901075.

Arblaster, J.M., and N.P Gillett (Lead Authors) et al. (2014). "Stratospheric ozone changes and climate". In: *Scientific Assessment of Ozone Depletion: 2014*. Geneva, Switzerland: Global Ozone Research and Monitoring Project - Report No. 55. Chap. 4.

Ball, W. T. et al. (2018). "Evidence for a continuous decline in lower stratospheric ozone offsetting ozone layer recovery". In: *Atmospheric Chemistry and Physics* 18.2, pp. 1379–1394. DOI: 10.5194/acp-18-1379-2018.

Bates, D. R. and Nicolet, M. (1950). "The photochemistry of atmospheric water vapor". In: *Journal of Geophysical Research (1896-1977)* 55.3, pp. 301–327. DOI: 10.1029/JZ055i003p00301.

Bell, A. B. and Murk, A. (2023). *Monitoring of Middle Atmospheric Water Vapour*. DOI: 10.48350/183553.

Benz, A. O. et al. (2005). "A broadband FFT spectrometer for radio and millimeter astronomy". In: *Astronomy & Astrophysics* 442.2, pp. 767–773. DOI: 10.1051/0004-6361:20053568.

Bernet, L. (2020). "Detecting trends of stratospheric ozone and tropospheric water vapour at mid-latitudes using measurements from multiple techniques". PhD thesis. Bern. URL: http://boristheses.unibe.ch/2410/.

Bernet, L. et al. (2019). "Ground-based ozone profiles over central Europe: incorporating anomalous observations into the analysis of stratospheric ozone trends". In: *Atmospheric Chemistry and Physics* 19.7, pp. 4289–4309. DOI: /10.5194/acp-19-4289-2019.

Bhartia, P. K. et al. (2013). "Solar Backscatter UV (SBUV) total ozone and profile algorithm". In: *Atmospheric Measurement Techniques* 6.10, pp. 2533–2548. DOI: 10.5194/amt-6-2533-2013.

Boyd, I. S. et al. (2007). "Ground-based microwave ozone radiometer measurements compared with Aura-MLS v2.2 and other instruments at two Network for Detection of Atmospheric Composition Change sites". In: *Journal of Geophysical Research: Atmospheres* 112.D24. DOI: 10.1029/2007JD008720.

Brasseur, G. and Solomon, S. (2005). *Aeronomy of the Middle Atmosphere: Chemistry and Physics of the Stratosphere and Mesosphere*. 3rd revised and enlarged. Vol. 32. Atmospheric and oceanographic sciences library. Dordrecht: Springer Netherlands. ISBN: 978-1-4020-3284-4. DOI: 10.1007/1-4020-3824-0_3.

Brewer, A. (1949). "Evidence for a world circulation provided by the measurements of helium and water vapour distribution in the stratosphere". In: *Quarterly Journal of the Royal Meteorological Society* 75.326, pp. 351–363. DOI: 10.1002/qj.49707532603.

Brönnimann, S. (2022). "Century-long column ozone records show that chemical and dynamical influences counteract each other". In: *Communications Earth & Environment* 3.143. DOI: 10.1038/s43247-022-00472-z.

Buehler, S. A. et al. (2005). "ARTS, the atmospheric radiative transfer simulator". In: *Journal of Quantitative Spectroscopy and Radiative Transfer* 91.1, pp. 65–93. DOI: 10.1016/j.jqsrt.2004.05.051.

Buehler, S. A. et al. (2018). "ARTS, the Atmospheric Radiative Transfer Simulator - Version 2.2, the planetary toolbox edition". eng. In: *Geoscientific Model Development* 11.4, pp. 1537–1556. DOI: 10.5194/gmd-11-1537-2018.

Butchart, N. (2014). "The Brewer-Dobson circulation". In: *Reviews of Geophysics* 52.2, pp. 157–184. DOI: 10.1002/2013RG000448.

Calisesi, Y., Hocke, K., and Kämpfer, N. (2005a). "The natural variability of stratospheric and mesospheric ozone as observed over Switzerland by a ground-based microwave remote sensor". In: *Memorie della Societ Astronomica Italiana, Journal of the Italian Astronomical Society* 76.4, pp. 937–940.

Calisesi, Y. (2003). *The Stratospheric Ozone Monitoring Radiometer SOMORA: NDSC Application Document*. IAP Research Report 2003-11. Bern, Switzerland: Institut für angewandte Physik, Universität Bern.

Calisesi, Y., Soebijanta, V. T., and Oss, R. v. (2005b). "Regridding of remote soundings: Formulation and application to ozone profile comparison". In: *Journal of Geophysical Research: Atmospheres* 110 (D23). DOI: 10.1029/2005JD006122.

Calisesi, Y., Wernli, H., and Kämpfer, N. (2001). "Midstratospheric ozone variability over Bern related to planetary wave activity during the winters 1994–1995 to 1998–1999". In: *Journal of Geophysical Research: Atmospheres* 106 (D8), pp. 7903–7916. DOI: 10.1029/2000JD900710.

Chapman, S. (1930). "A theory of the upper-atmospheric ozone". In: *Memoirs of the Royal Meteorological Society* 3.26. URL: https://www.rmets.org/sites/default/files/papers/chapman-memoirs.pdf.

Connor, B. J. et al. (1994). "Ground-based microwave observations of ozone in the upper stratosphere and mesosphere". In: *Journal of Geophysical Research: Atmospheres* 99.D8, pp. 16757–16770. DOI: 10.1029/94JD01153.

Crutzen, P. J. (1970). "The influence of nitrogen oxides on the atmospheric ozone content". In: *Quarterly Journal of the Royal Meteorological Society* 96.408, pp. 320–325. DOI: 10.1002/qj.49709640815.

De Mazière, M. et al. (2018). "The Network for the Detection of Atmospheric Composition Change (NDACC): history, status and perspectives". In: *Atmospheric Chemistry and Physics* 18.7, pp. 4935–4964. DOI: 10.5194/acp-18-4935-2018.

Dobson, G. M. B. (1956). "Origin and distribution of the polyatomic molecules in the atmosphere". In: *Proceedings of the Royal Society of London. A* 236.1205, pp. 187–193. DOI: 10.1098/rspa.1956.0127.

Dobson, G. M. B. and Harrison, D. (1926). "Measurements of the amount of ozone in the Earth's atmosphere and its relation to other geophysical conditions". In: *Proceedings of the Royal Society of London. A* 110.756, pp. 660–693. DOI: 10.1098/rspa.1926.0040.

Dumitru, M. et al. (2006). "Comparison and validation studies related to ground-based microwave observations of ozone in the stratosphere and mesosphere". In: *Journal of Atmospheric and Solar-Terrestrial Physics* 68.7, pp. 745–756. DOI: 10.1016/j.jastp.2005.11.001.

Eriksson, P. et al. (2011). "ARTS, the atmospheric radiative transfer simulator, version 2". In: *Journal of Quantitative Spectroscopy and Radiative Transfer* 112.10, pp. 1551–1558. DOI: 10.1016/j.jqsrt.2011.03.001.

Eriksson, P., Jiménez, C., and Buehler, S. A. (2005). "Qpack, a general tool for instrument simulation and retrieval work". In: *Journal of Quantitative Spectroscopy and Radiative Transfer* 91.1, pp. 47–64. DOI: 10.1016/j.jqsrt.2004.05.050.

Eriksson, P. et al. (2006). "Efficient forward modelling by matrix representation of sensor responses". In: *International Journal of Remote Sensing* 27.9, pp. 1793–1808. DOI: 10.1080/01431160500447254.

Eyring, V. et al. (2010). "Multi-model assessment of stratospheric ozone return dates and ozone recovery in CCMVal-2 models". In: *Atmospheric Chemistry and Physics* 10.19, pp. 9451–9472. DOI: 10.5194/acp-10-9451-2010.

Farman, J. C., Gardiner, B. G., and Shanklin, J. D. (1985). "Large losses of total ozone in Antarctica reveal seasonal ClOx/NOx interaction". In: *Nature* 315.6016, pp. 207–210.

Flury, T. et al. (2009). "Ozone depletion, water vapor increase, and PSC generation at midlatitudes by the 2008 major stratospheric warming". In: *Journal of Geophysical Research: Atmospheres* 114.D18. DOI: 10.1029/2009JD011940.

Frith, S. M. et al. (2020). "Model-based climatology of diurnal variability in stratospheric ozone as a data analysis tool". In: *Atmospheric Measurement Techniques* 13.5, pp. 2733–2749. DOI: 10.5194/amt-13-2733-2020.

Froidevaux, L. et al. (2008). "Validation of Aura Microwave Limb Sounder stratospheric ozone measurements". In: *Journal of Geophysical Research: Atmospheres* 113.D15. DOI: 10.1029/2007JD008771.

Garcia, R. R. and Solomon, S. (1985). "The effect of breaking gravity waves on the dynamics and chemical composition of the mesosphere and lower thermosphere". In: *Journal of Geophysical Research: Atmospheres* 90 (D2), pp. 3850–3868. DOI: 10.1029/JD090iD02p03850.

Gathen, P. von der et al. (2021). "Climate change favours large seasonal loss of Arctic ozone". In: *Nature Communications* 12.1, pp. 1–17. DOI: 10.1038/s41467-021-24089-6.

Godin-Beekmann, S. et al. (2022). "Updated trends of the stratospheric ozone vertical distribution in the 60°S–60°N latitude range based on the LOTUS regression model". In: *Atmospheric Chemistry and Physics* 22.17, pp. 11657–11673. DOI: 10.5194/acp-22-11657-2022.

Gordon, I. et al. (2022). "The HITRAN2020 molecular spectroscopic database". In: *Journal of Quantitative Spectroscopy and Radiative Transfer* 277, p. 107949. DOI: 10.1016/j.jqsrt.2021.107949.

Haefele, A. et al. (2008). "Diurnal changes in middle atmospheric H2O and O3: Observations in the Alpine region and climate models". In: *Journal of Geophysical Research: Atmospheres* 113.D17. DOI: 10.1029/2008JD009892.

Hagen, J. et al. (2018). "WIRA-C: a compact 142-GHz-radiometer for continuous middle-atmospheric wind measurements". In: *Atmospheric Measurement Techniques* 11.9, pp. 5007–5024. DOI: 10.5194/amt-11-5007-2018.

Han, Y. and Westwater, E. (2000). "Analysis and improvement of tipping calibration for ground-based microwave radiometers". In: *IEEE Transactions on Geoscience and Remote Sensing* 38.3, pp. 1260–1276. DOI: 10.1109/36.843018.

Hassler, B. et al. (2014). "Past changes in the vertical distribution of ozone–Part 1: Measurement techniques, uncertainties and availability". In: *Atmospheric Measurement Techniques* 7.5, pp. 1395–1427. DOI: 10.5194/amt-7-1395-2014.

Hassler, B. and Young, P. J. (Lead Authors) et al. (2022). "Update on Global Ozone: Past, Present, and Future, Chapter 3". In: *Scientific Assessment of Ozone Depletion: 2022*. GAW Report No. 278, WMO Geneva.

Herman, J. R. (1979). "The response of stratospheric constituents to a solar eclipse, sunrise, and sunset". In: *Journal of Geophysical Research: Oceans* 84.C7, pp. 3701–3710. DOI: 10.1029/JC084iC07p03701.

Hocke, K. et al. (2006). "Temporal variance of lower mesospheric ozone over Switzerland during winter 2000/2001". In: *Geophysical Research Letters* 33.9. DOI: 10.1029/2005GL025496.

Hocke, K. et al. (2007). "Comparison and synergy of stratospheric ozone measurements by satellite limb sounders and the ground-based microwave radiometer SOMORA". In: *Atmospheric Chemistry and Physics* 7.15, pp. 4117–4131. DOI: 10.5194/acp-7-4117-2007.

Hocke, K. et al. (2017). "An Atlantic streamer in stratospheric ozone observations and SD-WACCM simulation data". In: *Atmospheric Chemistry and Physics* 17.5, pp. 3445–3452. DOI: 10.5194/acp-17-3445-2017.

Hou, S. (2022). "The diurnal ozone variation in the middle atmosphere observed by microwave radiometers in Switzerland". Master Thesis. Philosophisch-Naturwissenschaftliche Fakultät, Universität Bern, Switzerland.

Huang, F. T., Reber, C. A., and Austin, J. (1997). "Ozone diurnal variations observed by UARS and their model simulation". In: *Journal of Geophysical Research: Atmospheres* 102.D11, pp. 12971–12985. DOI: 10.1029/97JD00461.

Hubert, D. et al. (2016). "Ground-based assessment of the bias and long-term stability of 14 limb and occultation ozone profile data records". In: *Atmospheric Measurement Techniques* 9.6, pp. 2497–2534. DOI: 10.5194/amt-9-2497-2016.

Ingold, T., Peter, R., and Kämpfer, N. (1998). "Weighted mean tropospheric temperature and transmittance determination at millimeter-wave frequencies for ground-based applications". In: *Radio Science* 33.4, pp. 905–918. DOI: 10.1029/98RS01000.

Janssen, M. A. (1993). *Atmospheric remote sensing by microwave radiometry*. Ed. by M. A. Janssen. Wiley series in remote sensing. Wiley. ISBN: 0-471-62891-3.

Kopp, G. et al. (2002). "Evolution of ozone and ozone-related species over Kiruna during the SOLVE/THESEO 2000 campaign retrieved from ground-based millimeter-wave and infrared observations". In: *Journal of Geophysical Research: Atmospheres* 107.D5, SOL 51-1-SOL 51–12. DOI: 10.1029/2001JD001064.

Kotiranta, M. et al. (2019). "Receiver Development for the Microwave Ozone Profiling Instrument MOPI 5". In: *2019 IEEE International Geoscience and Remote Sensing Symposium*, pp. 8952–8955. DOI: 10.1109/IGARSS.2019.8898498.

Krochin, W. et al. (2022). "Continuous temperature soundings at the stratosphere and lower mesosphere with a ground-based radiometer considering the Zeeman effect". In: *Atmospheric Measurement Techniques* 15.7, pp. 2231–2249. DOI: 10.5194/amt-15-2231-2022.

Lahoz, W. A. et al. (2007). "Data assimilation of stratospheric constituents: a review". In: *Atmospheric Chemistry and Physics* 7.22, pp. 5745–5773. DOI: 10.5194/acp-7-5745-2007.

Livesey, N. J. et al. (2008). "Validation of Aura Microwave Limb Sounder O3 and CO observations in the upper troposphere and lower stratosphere". In: *Journal of Geophysical Research: Atmospheres* 113.D15. DOI: 10.1029/2007JD008805.

Livesey, N. J. et al. (2022). *Earth Observing System (EOS) Aura Microwave Limb Sounder (MLS) Version 5.0x Level 2 and 3 data quality and description document*. Tech. rep. last access: 21 June 2023. URL: https://mls.jpl.nasa.gov/eos-aura-mls/data-documentation.

Lobsiger, E. (1987). "Ground-based microwave radiometry to determine stratospheric and mesospheric ozone profiles". In: *Journal of Atmospheric and Terrestrial Physics* 49.5, pp. 493–501. DOI: 10.1016/0021-9169(87)90043-2.

Lobsiger, E., Künzi, K., and Dütsch, H. (1984). "Comparison of stratospheric ozone profiles retrieved from microwave-radiometer and Dobson-spectrometer data". In: *Journal of Atmospheric and Terrestrial Physics* 46.9, pp. 799–806. DOI: 10.1016/0021-9169(84)90060-6.

Maillard Barras, E., Ruffieux, D., and Hocke, K. (2009). "Stratospheric ozone profiles over Switzerland measured by SOMORA, ozonesonde and MLS/AURA satellite". In: *International Journal of Remote Sensing* 30.15, pp. 4033–4041. DOI: 10.1080/01431160902821890.

Maillard Barras, E. et al. (2022a). "Dynamical linear modeling estimates of long-term ozone trends from homogenized Dobson Umkehr profiles at Arosa/Davos, Switzerland". In: *Atmospheric Chemistry and Physics* 22.21, pp. 14283–14302. DOI: 10.5194/acp-22-14283-2022.

Maillard Barras, E. et al. (2020). "Study of the dependence of long-term stratospheric ozone trends on local solar time". In: *Atmospheric Chemistry and Physics* 20.14, pp. 8453–8471. DOI: 10.5194/acp-20-8453-2020.

Maillard Barras, E. et al. (2022b). *Harmonized middle atmospheric ozone time series from SOMORA*. DOI: 10.48620/119.

Maillard Barras, E. et al. (2022c). *Harmonized middle atmospheric ozone time series from SOMORA*. Bern. DOI: 10.48620/119.

Manney, G. L. et al. (2011). "Unprecedented Arctic ozone loss in 2011". In: *Nature* 478.7370, pp. 469–475. DOI: 10.1038/nature10556.

Manney, G. L. et al. (2015). "A minor sudden stratospheric warming with a major impact: Transport and polar processing in the 2014/2015 Arctic winter". In: *Geophysical Research Letters* 42.18, pp. 7808–7816. DOI: 10.1002/2015GL065864.

Manney, G. L. et al. (2020). "Record-Low Arctic Stratospheric Ozone in 2020: MLS Observations of Chemical Processes and Comparisons With Previous Extreme Winters". In: *Geophysical Research Letters* 47.16. DOI: 10.1029/2020GL089063.

McPeters, R. D. et al. (2013). "The version 8.6 SBUV ozone data record: An overview". In: *Journal of Geophysical Research: Atmospheres* 118.14, pp. 8032–8039. DOI: 10.1002/jgrd.50597.

Molina, M. J. and Rowland, F. S. (1974). "Stratospheric sink for chlorofluoromethanes: chlorine atom-catalysed destruction of ozone". In: *Nature* 249.5460, pp. 810–812. DOI: 10.1038/249810a0.

Moreira, L. et al. (2015). "Trend analysis of the 20-year time series of stratospheric ozone profiles observed by the GROMOS microwave radiometer at Bern". In: *Atmospheric Chemistry and Physics* 15.19, pp. 10999–11009. DOI: 10.5194/acp-15-10999-2015.

Moreira, L. et al. (2016). "The natural oscillations in stratospheric ozone observed by the GROMOS microwave radiometer at the NDACC station Bern". In: *Atmospheric Chemistry and Physics* 16.16, pp. 10455–10467. DOI: 10.5194/acp-16-10455-2016.

Moreira, L., Hocke, K., and Kämpfer, N. (2018). "Short-term stratospheric ozone fluctuations observed by GROMOS microwave radiometer at Bern". In: *Earth, Planets and Space* 70.1, p. 8. DOI: 10.1186/s40623-017-0774-4.

Müller, S. et al. (2009). "Intercomparison of Digital Fast Fourier Transform and Acoustooptical Spectrometers for Microwave Radiometry of the Atmosphere". In: *IEEE Transactions on Geoscience and Remote Sensing* 47.7, pp. 2233–2239. DOI: 10.1109/TGRS.2009.2013695.

Murk, A. and Kotiranta, M. (2019). "Characterization of Digital Real-Time Spectrometers for Radio Astronomy and Atmospheric Remote Sensing". In: *Proceedings of the International Symposium on Space THz Technology, Gothenburg, Sweden*. Vol. 15. URL: https://www.nrao.edu/meetings/isstt/papers/2019/2019139142.pdf.

NASA (2023). *NASA Ozone Watch*. Last accessed: 21 June 2023. URL: https://ozonewatch.gsfc.nasa.gov/.

Nedoluha, G. E. et al. (1995). "Ground-based measurements of water vapor in the middle atmosphere". In: *Journal of Geophysical Research: Atmospheres* 100.D2, pp. 2927–2939. DOI: 10.1029/94JD02952.

Nedoluha, G. E. et al. (2011). "Ground-based microwave measurements of water vapor from the midstratosphere to the mesosphere". In: *Journal of Geophysical Research: Atmospheres* 116.D2. DOI: 10.1029/2010JD014728.

Nedoluha, G. E. et al. (2022). "Measurements of Mesospheric Water Vapor From 1992 to 2021 at Three Stations From the Network for the Detection of Atmospheric Composition Change". In: *Journal of Geophysical Research: Atmospheres* 127.21, e2022JD037227. DOI: 10.1029/2022JD037227. (Visited on 11/15/2022).

Newman, P. A. et al. (2009). "What would have happened to the ozone layer if chlorofluorocarbons (CFCs) had not been regulated?" In: *Atmospheric Chemistry and Physics* 9.6, pp. 2113–2128. DOI: 10.5194/acp-9-2113-2009.

Nyquist, H. (1928). "Thermal agitation of electric charge in conductors". In: *Physical review* 32.1, p. 110. DOI: 10.1103/PhysRev.32.110.

Orte, P. F. et al. (2019). "Analysis of a southern sub-polar short-term ozone variation event using a millimetre-wave radiometer". In: *Annales Geophysicae* 37.4, pp. 613–629. DOI: 10.5194/angeo-37-613-2019.

Pallister, R. C. and Tuck, A. F. (1983). "The diurnal variation of ozone in the upper stratosphere as a test of photochemical theory". In: *Quarterly Journal of the Royal Meteorological Society* 109.460, pp. 271–284. DOI: 10.1002/qj.49710946002.

Palm, M. et al. (2010). "The ground-based MW radiometer OZORAM on Spitsbergen – description and status of stratospheric and mesospheric O_3-measurements". In: *Atmospheric Measurement Techniques* 3.6, pp. 1533–1545. DOI: 10.5194/amt-3-1533-2010.

Parrish, A. (1994). "Millimeter-wave remote sensing of ozone and trace constituents in the stratosphere". In: *Proceedings of the IEEE* 82.12, pp. 1915–1929. DOI: 10.1109/5.338079.

Parrish, A. et al. (1988). "A ground-based technique for millimeter wave spectroscopic observations of stratospheric trace constituents". In: *Radio Science* 23.2, pp. 106–118. DOI: 10.1029/RS023i002p00106.

Parrish, A. et al. (1992). "Ground-based microwave monitoring of stratospheric ozone". In: *Journal of Geophysical Research: Atmospheres* 97.D2, pp. 2541–2546. DOI: 10.1029/91JD02914.

Parrish, A. et al. (2014). "Diurnal variations of stratospheric ozone measured by ground-based microwave remote sensing at the Mauna Loa NDACC site: measurement validation and GEOSCCM model comparison". In: *Atmospheric Chemistry and Physics* 14.14. Publisher: Copernicus GmbH, pp. 7255–7272. DOI: 10.5194/acp-14-7255-2014.

Perrin, A. et al. (2005). "Molecular Line Parameters for the "MASTER" (Millimeter Wave Acquisitions for Stratosphere/Troposphere Exchange Research) Database". In: *Journal of Atmospheric Chemistry* 51.2, pp. 161–205. DOI: 10.1007/s10874-005-7185-9.

Peter, R. (1997). *The Ground-based Millimeter-wave Ozone Spectrometer - GROMOS*. IAP Research Report 97-13. Bern, Switzerland: Institute of Applied Physics, University of Bern.

Petropavlovskikh, I. et al. (2019). *SPARC/IO3C/GAW Report on Long-term Ozone Trends and Uncertainties in the Stratosphere*. Tech. rep. 9th assessment report of the SPARC project, published by the International Project Office at DLR-IPA. also: GAW Report No. 241; WCRP Report 17/2018. URL: https://elib.dlr.de/126666/.

Prather, M. J. (1981). "Ozone in the upper stratosphere and mesosphere". In: *Journal of Geophysical Research* 86.C6, p. 5325. DOI: 10.1029/JC086iC06p05325.

Raffalski, U. et al. (2005). "Evolution of stratospheric ozone during winter 2002/2003 as observed by a ground-based millimetre wave radiometer at Kiruna, Sweden". In: *Atmospheric Chemistry and Physics* 5.5, pp. 1399–1407. DOI: 10.5194/acp-5-1399-2005.

Ravishankara, A. R., Daniel, J. S., and Portmann, R. W. (2009). "Nitrous Oxide N_2O): The Dominant Ozone-Depleting Substance Emitted in the 21st Century". In: *Science* 326.5949, pp. 123–125. DOI: 10.1126/science.1176985.

Ricaud, P. et al. (1991). "Diurnal and seasonal variations of stratomesospheric ozone: Analysis of ground-based microwave measurements in Bordeaux, France". In: *Journal of Geophysical Research: Atmospheres* 96.D10, pp. 18617–18629. DOI: 10.1029/91JD01871.

Rindlisbacher, T. (1999). "SOMORA - Ein mikrowellen-Radiometer fur das Monitoring von stratospharischem Ozon". Diploma Thesis. Institude of Applied Physics, University of Bern.

Rodgers, C. D. (1976). "Retrieval of atmospheric temperature and composition from remote measurements of thermal radiation". In: *Reviews of Geophysics* 14.4, p. 609. DOI: 10.1029/RG014i004p00609.

Rodgers, C. D. (2000). *Inverse Methods for Atmospheric Sounding: Theory and Practice*. World Scientific. ISBN: 978-981-02-2740-1.

Rodgers, C. D. and Connor, B. J. (2003). "Intercomparison of remote sounding instruments". In: *Journal of Geophysical Research: Atmospheres* 108.D3. DOI: 10.1029/2002JD002299.

Rosenkranz, P. W. (1998). "Water vapor microwave continuum absorption: A comparison of measurements and models". In: *Radio Science* 33.4, pp. 919–928. DOI: 10.1029/98RS01182.

Rüfenacht, R., Kämpfer, N., and Murk, A. (2012). "First middle-atmospheric zonal wind profile measurements with a new ground-based microwave Doppler-spectro-radiometer". In: *Atmospheric Measurement Techniques* 5.11, pp. 2647–2659. DOI: 10.5194/amt-5-2647-2012.

Ryan, N. J. et al. (2016). "Ozone profiles above Kiruna from two ground-based radiometers". In: *Atmospheric Measurement Techniques* 9.9, pp. 4503–4519. DOI: 10.5194/amt-9-4503-2016.

Sakazaki, T. et al. (2013). "Diurnal ozone variations in the stratosphere revealed in observations from the Superconducting Submillimeter-Wave Limb-Emission Sounder (SMILES) on board the International Space Station (ISS)". In: *Journal of Geophysical Research: Atmospheres* 118.7, pp. 2991–3006. DOI: 10.1002/jgrd.50220.

Salawitch, R. J. (Lead Author) et al. (2023). "Twenty Questions and Answers About the Ozone Layer: 2022 Update". In: *Scientific Assessment of Ozone Depletion: 2022, 75 pp.* World Meteorological Organization, Geneva, Switzerland.

Sauvageat, E. (2022a). *GROMORA-harmo: calibration and retrieval code for Swiss ozone microwave radiometers*. Version 2. DOI: 10.5281/zenodo.6799357.

Sauvageat, E. et al. (2023). "Microwave radiometer observations of the ozone diurnal cycle and its short-term variability over Switzerland". In: *Atmospheric Chemistry and Physics* 23.13, pp. 7321–7345. DOI: 10.5194/acp-23-7321-2023.

Sauvageat, E. (2021). *Calibration routine for ground-based passive microwave radiometer: a user guide*. Research Report No. 2021-01-MW. Institute of Applied Physics, University of Bern. DOI: 10.48350/164418.

— (2022b). *Harmonized ozone profile retrievals from GROMOS and SOMORA*. Research Report No. 2022-01-MW. Institute of Applied Physics, University of Bern. DOI: 10.48350/170121.

Sauvageat, E. et al. (2020). "Comparison of three high resolution real-time spectrometers for microwave ozone profiling instruments". In: *2020 16th Specialist Meeting on Microwave Radiometry and Remote Sensing for the Environment (MicroRad)*, pp. 1–4. DOI: 10.1109/MicroRad49612.2020.9342608.

Sauvageat, E. et al. (2021). "Comparison of Three High Resolution Real-Time Spectrometers for Microwave Ozone Profiling Instruments". In: *IEEE Journal of Selected Topics in Applied Earth Observations and Remote Sensing* 14, pp. 10045–10056. DOI: 10.1109/JSTARS.2021.3114446.

Sauvageat, E. et al. (2022a). *Harmonized middle atmospheric ozone time series from GROMOS*. DOI: 10.48620/65.

Sauvageat, E. et al. (2022b). "Harmonized retrieval of middle atmospheric ozone from two microwave radiometers in Switzerland". In: *Atmospheric Measurement Techniques* 15.21, pp. 6395–6417. DOI: 10.5194/amt-15-6395-2022.

Schanz, A., Hocke, K., and Kämpfer, N. (2014). "Daily ozone cycle in the stratosphere: global, regional and seasonal behaviour modelled with the Whole Atmosphere Community Climate Model". In: *Atmospheric Chemistry and Physics* 14.14, pp. 7645–7663. DOI: 10.5194/acp-14-7645-2014.

Schanz, A. et al. (2021). "The Diurnal Variation in Stratospheric Ozone from MACC Reanalysis, ERA-Interim, WACCM, and Earth Observation Data: Characteristics and Intercomparison". In: *Atmosphere* 12.5, p. 625. DOI: 10.3390/atmos12050625.

Scheiben, D. et al. (2012). "Observations of middle atmospheric H_2O and O_3 during the 2010 major sudden stratospheric warming by a network of microwave radiometers". In: *Atmospheric Chemistry and Physics* 12.16, pp. 7753–7765. DOI: 10.5194/acp-12-7753-2012.

Schranz, F. et al. (2018). "Diurnal variation in middle-atmospheric ozone observed by ground-based microwave radiometry at Ny-Ålesund over 1 year". In: *Atmospheric Chemistry and Physics* 18.6, pp. 4113–4130. DOI: 10.5194/acp-18-4113-2018.

Schranz, F. et al. (2019). "Investigation of Arctic middle-atmospheric dynamics using 3 years of H $_2$ O and O $_3$ measurements from microwave radiometers at Ny-Ålesund". In: *Atmospheric Chemistry and Physics* 19.15, pp. 9927–9947. DOI: 10.5194/acp-19-9927-2019.

Shepherd, T. G. (2000). "The middle atmosphere". In: *Journal of Atmospheric and Solar-Terrestrial Physics* 62.17, pp. 1587–1601. DOI: 10.1016/S1364-6826(00)00114-0.

Shi, G. et al. (2023). "Ozone and water vapor variability in the polar middle atmosphere observed with ground-based microwave radiometers". In: *EGUsphere* 2023, pp. 1–30. DOI: 10.5194/egusphere-2023-149.

Solomon, P. et al. (2006). "Rise and decline of active chlorine in the stratosphere". In: *Geophysical Research Letters* 33.18. DOI: 10.1029/2006GL027029.

Solomon, S. et al. (1986). "On the depletion of Antarctic ozone". In: *Nature* 321.6072, pp. 755–758. DOI: 10.1038/321755a0.

Solomon, S. (1999). "Stratospheric ozone depletion: A review of concepts and history". In: *Reviews of Geophysics* 37.3, pp. 275–316. DOI: 10.1029/1999RG900008.

Solomon, S. et al. (2016). "Emergence of healing in the Antarctic ozone layer". In: *Science* 353.6296, pp. 269–274. DOI: 10.1126/science.aae0061.

SPARC/IO3C/GAW (2019). "SPARC/IO3C/GAW Report on Long-term Ozone Trends and Uncertainties in the Stratosphere". In: ed. by I. Petropavlovskikh et al. SPARC Report No. 9, GAW Report No. 241, WCRP-17/2018. DOI: 10.17874/f899e57a20b.

Staehelin, J., Kegel, R., and Harris, N. R. P. (1998). "Trend analysis of the homogenized total ozone series of Arosa (Switzerland), 1926–1996". In: *Journal of Geophysical Research: Atmospheres* 103.D7, pp. 8389–8399. DOI: 10.1029/97JD03650.

Steinbrecht, W. et al. (2017). "An update on ozone profile trends for the period 2000 to 2016". In: *Atmospheric Chemistry and Physics* 17.17, pp. 10675–10690. DOI: 10.5194/acp-17-10675-2017.

Stolarski, R. S. and Cicerone, R. J. (1974). "Stratospheric Chlorine: a Possible Sink for Ozone". In: *Canadian Journal of Chemistry* 52.8, pp. 1610–1615. DOI: 10.1139/v74-233.

Strode, S. A. et al. (2022). "SAGE III/ISS ozone and NO_2 validation using diurnal scaling factors". In: *Atmospheric Measurement Techniques* 15.20, pp. 6145–6161. DOI: 10.5194/amt-15-6145-2022.

Studer, S. et al. (2013). "Intercomparison of stratospheric ozone profiles for the assessment of the upgraded GROMOS radiometer at Bern". In: *Atmospheric Measurement Techniques Discussions* 6, pp. 6097–6146. DOI: 10.5194/amtd-6-6097-2013.

Studer, S. et al. (2014). "A climatology of the diurnal variations in stratospheric and mesospheric ozone over Bern, Switzerland". In: *Atmospheric Chemistry and Physics* 14.12, pp. 5905–5919. DOI: 10.5194/acp-14-5905-2014.

Tschanz, B. et al. (2013). "Validation of middle-atmospheric campaign-based water vapour measured by the ground-based microwave radiometer MIAWARA-C". In: *Atmospheric Measurement Techniques* 6.7, pp. 1725–1745. DOI: 10.5194/amt-6-1725-2013.

Tsou, J. J. et al. (1995). "Ground-based microwave monitoring of middle atmosphere ozone: Comparison to lidar and Stratospheric and Gas Experiment II satellite observations". In: *Journal of Geophysical Research* 100.D2, p. 3005. DOI: 10.1029/94JD02947.

Tummon, F. et al. (2015). "Intercomparison of vertically resolved merged satellite ozone data sets: interannual variability and long-term trends". In: *Atmospheric Chemistry and Physics* 15.6, pp. 3021–3043. DOI: 10.5194/acp-15-3021-2015.

Ulaby, F. and Long, D. (2014). *Microwave Radar and Radiometric Remote Sensing*. University of Michigan Press. Chap. 7, pp. 262–320. ISBN: 978-0-472-11935-6. DOI: 10.3998/0472119356.

Vasic, V. (2005). *Homogenisation of ozone series measured by mw-radiometers over Bern and Payerne*. IAP Research Report 2005-06-MW. Bern, Switzerland: Institute of Applied Physics, University of Bern.

Vaughan, G. (1982). "Diurnal variation of mesospheric ozone". In: *Nature* 296.5853, pp. 133–135. DOI: 10.1038/296133a0.

Velders, G. J. M. et al. (2007). "The importance of the Montreal Protocol in protecting climate". In: *Proceedings of the National Academy of Sciences* 104.12, pp. 4814–4819. DOI: 10.1073/pnas.0610328104.

Villamayor, J. et al. (2023). "Very short-lived halogens amplify ozone depletion trends in the tropical lower stratosphere". In: *Nature Climate Change* 13.554-560. DOI: 10.1038/s41558-023-01671-y.

Wallace, J. M. and Hobbs, P. V. (2006). *Atmospheric Science: an Introductory Survey*. Second Edition. Vol. 92. Elsevier. ISBN: 978-0-12-732951-2. DOI: 10.1016/C2009-0-00034-8.

Waters, J. et al. (2006). "The Earth observing system microwave limb sounder (EOS MLS) on the Aura Satellite". In: *IEEE Transactions on Geoscience and Remote Sensing* 44.5, pp. 1075–1092. DOI: 10.1109/TGRS.2006.873771.

WMO (2022). In: *Scientific Assessment of Ozone Depletion: 2022*. World Meteorological Organization, GAW Report No. 278, 509 pp., WMO Geneva.

Ziemke, J. R. et al. (2021). "A global ozone profile climatology for satellite retrieval algorithms based on Aura MLS measurements and the MERRA-2 GMI simulation". In: *Atmospheric Measurement Techniques* 14.10, pp. 6407–6418. DOI: 10.5194/amt-14-6407-2021.

Zommerfelds, W. C. et al. (1989). "Diurnal variations of mesospheric ozone obtained by ground-based microwave radiometry". In: *Journal of Geophysical Research: Atmospheres* 94.D10, pp. 12819–12832. DOI: 10.1029/JD094iD10p12819.

A | Additional tables and plots

This chapter presents some additional materials related to the new harmonized calibration and retrieval algorithms of GROMOS and SOMORA.

A.1 Ozone a priori data

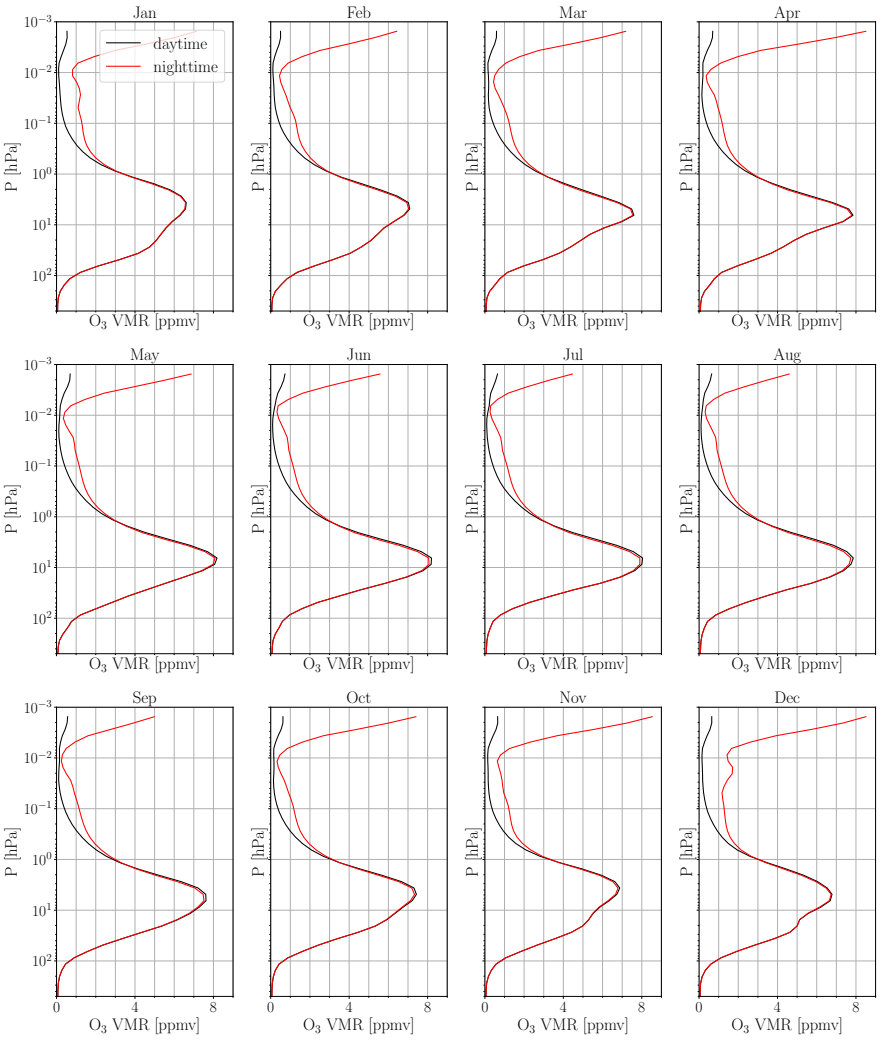

FIGURE A.1: Monthly day and nightime a priori profiles used in the GROMORA retrievals.

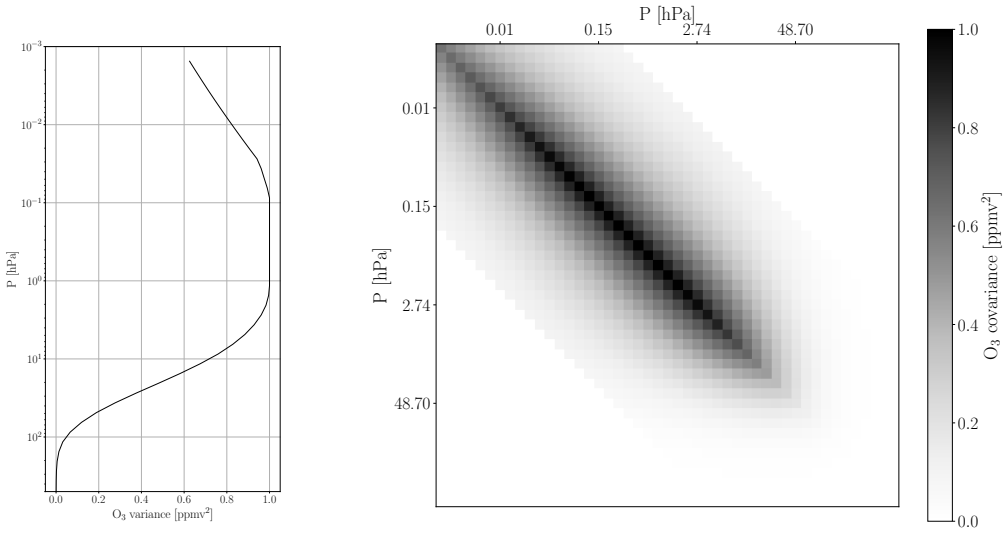

FIGURE A.2: Ozone a priori covariance matrix used for the GROMORA retrievals. Left: Diagonal variance profile. Right: 2D representation of the full covariance matrix against pressure levels.

A.2 Yearly diagnostics

Example of yearly diagnostics plots for the harmonized calibration and retrieval algorithms.

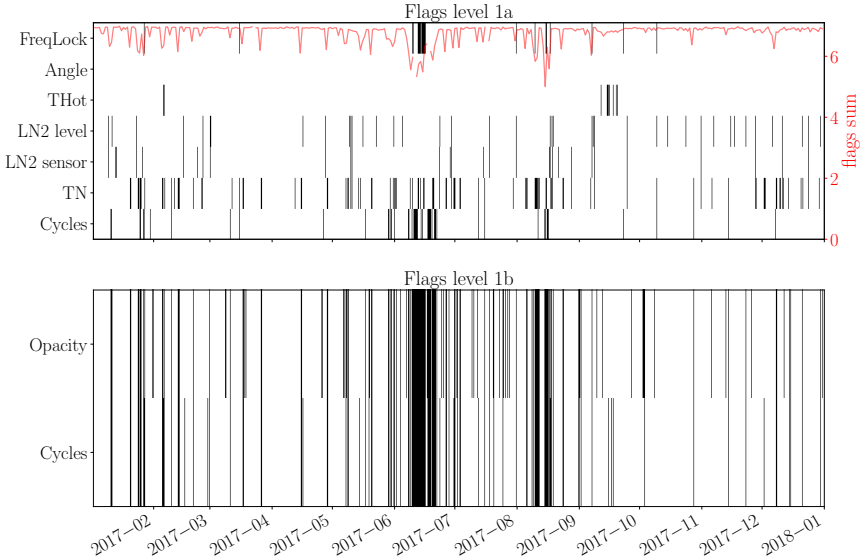

FIGURE A.3: Standard set of flags defined for the level 1. The top panel shows the flags for the calibrated spectra and the bottom one for the integrated spectra for GROMOS. For the meaning of the different flags, see Sauvageat, 2021

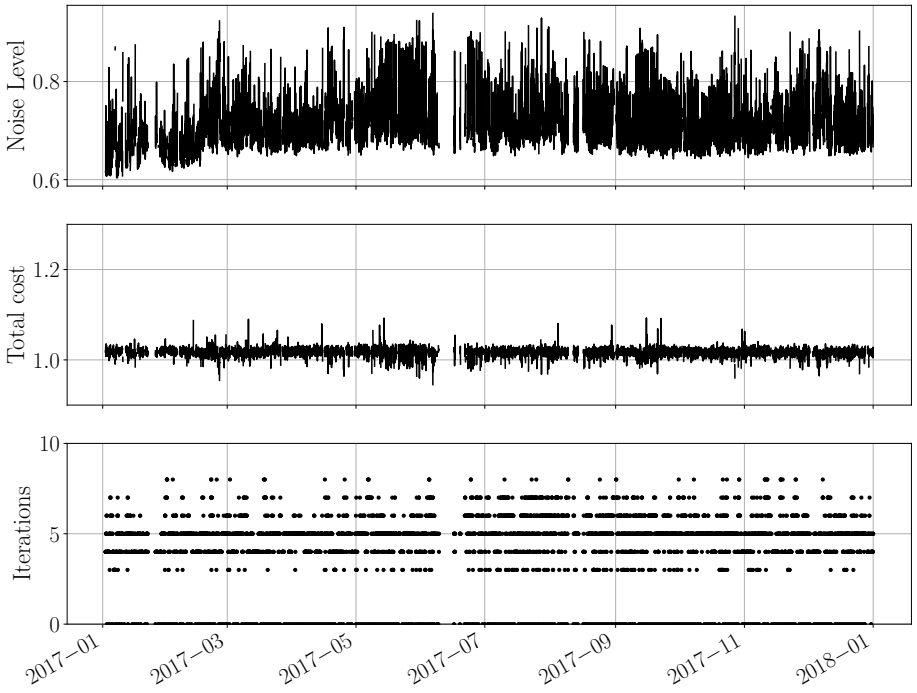

FIGURE A.4: Yearly concatenated diagnostic plots for GROMOS. It shows the noise level of the spectra (top), the final value of the cost function for each retrieval (middle), and the number of iterations performed before convergence of the OEM algorithm.

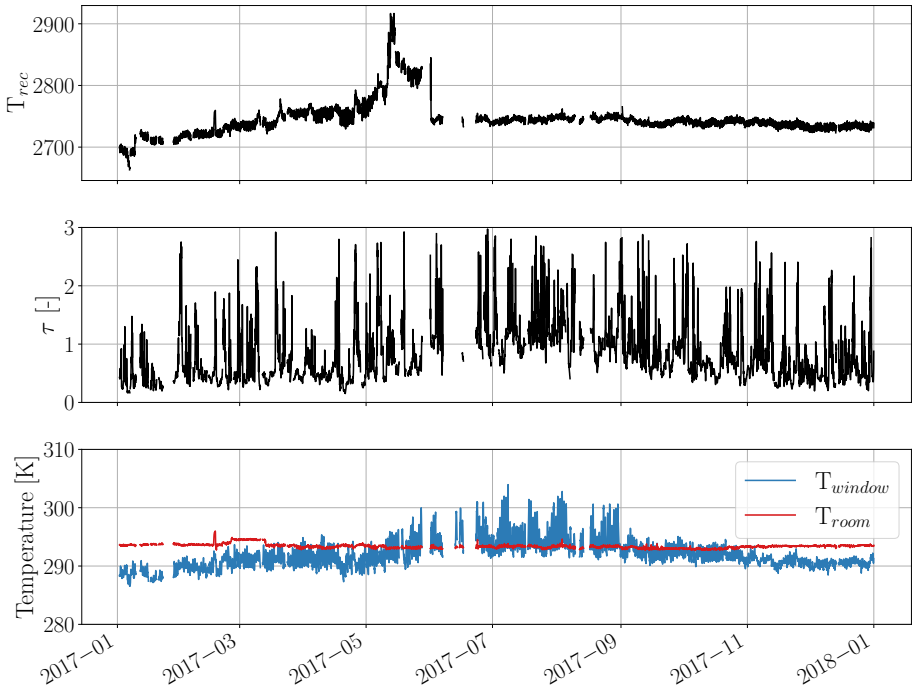

FIGURE A.5: Yearly concatenated diagnostic plots for GROMOS. It shows the receiver noise temperature (top), the atmospheric opacity (middle), the room temperature and the window temperature through which the instrument observe (bottom).

B | Miscellaneous

B.1 List of publications

Peer-reviewed articles and conference papers:

Sauvageat, E., Maillard Barras, E., Hocke, K., Haefele, A., and Murk, A. (2022b). "Harmonized retrieval of middle atmospheric ozone from two microwave radiometers in Switzerland". In: *Atmospheric Measurement Techniques* 15.21, pp. 6395–6417. DOI: 10.5194/amt-15-6395-2022.

Sauvageat, E., Albers, R., Kotiranta, M., Hocke, K., Gomez, R. M., Nedoluha, G. E., and Murk, A. (2021a). "Comparison of Three High Resolution Real-Time Spectrometers for Microwave Ozone Profiling Instruments". In: *IEEE Journal of Selected Topics in Applied Earth Observations and Remote Sensing* 14, pp. 10045–10056. DOI: 10.1109/JSTARS.2021.3114446.

Sauvageat, E., Hocke, K., Maillard Barras, E., Hou, S., Errera, Q., Haefele, A., and Murk, A. (2023). "Microwave radiometer observations of the ozone diurnal cycle and its short-term variability over Switzerland". In: *Atmospheric Chemistry and Physics* 23.13, pp. 7321–7345. DOI: 10.5194/acp-23-7321-2023.

Sauvageat, E., Kotiranta, M., Hocke, K., Gomez, R. M., Nedoluha, G., and Murk, A. (2020a). "Comparison of three high resolution real-time spectrometers for microwave ozone profiling instruments". In: *2020 16th Specialist Meeting on Microwave Radiometry and Remote Sensing for the Environment (MicroRad)*, pp. 1–4. DOI: 10.1109/MicroRad49612.2020.9342608.

Hocke, K., **Sauvageat, E.**, and Bernet, L. (2023). "Response of Total Column Ozone at High Latitudes to Sudden Stratospheric Warmings". In: *Atmosphere* 14.3. DOI: 10.3390/atmos14030450.

Wang, W., Murk, A., **Sauvageat, E.**, Fan, W., Dätwyler, C., Hervo, M., Haefele, A., and Hocke, K. (2023). "An Indoor Microwave Radiometer for Measurement of Tropospheric Water". In: *IEEE Transactions on Geoscience and Remote Sensing* 61, pp. 1–13. DOI: 10.1109/TGRS.2023.3261067.

Shi, G., Krochin, W., **Sauvageat, E.**., and Stober, G. (2023). "Ozone and water vapor variability in the polar middle atmosphere observed with ground-based microwave radiometers". In: *EGUsphere* 2023, pp. 1–30. DOI: 10.5194/egusphere-2023-149.

Reports, code, and datasets:

Sauvageat, E. (2021). *Calibration routine for ground-based passive microwave radiometer: a user guide*. Research Report No. 2021-01-MW. Institute of Applied Physics, University of Bern. DOI: 10.48350/164418.

Sauvageat, E. (2022b). *Harmonized ozone profile retrievals from GROMOS and SOMORA*. Research Report No. 2022-01-MW. Institute of Applied Physics, University of Bern. DOI: 10.48350/170121.

Sauvageat, E., Murk, A., Hocke, K., Maillard Barras, E., and Haefele, A. (2022a). *Harmonized middle atmospheric ozone time series from GROMOS*. Bern. DOI: 10.48620/65.

Maillard Barras, E., **Sauvageat, E.**, Murk, A., Hocke, K., and Haefele, A. (2022c). *Harmonized middle atmospheric ozone time series from SOMORA*. Bern. DOI: 10.48620/119.

Sauvageat, E. (2022a). *GROMORA-harmo: calibration and retrieval code for Swiss ozone microwave radiometers*. Version 2. DOI: 10.5281/zenodo.6799357.

Selected talks:

Sauvageat, E., Hou, S., Maillard Barras, E., Hocke, K., Haefele, A., and Murk, A. (2022d). *Ozone diurnal cycle in the middle atmosphere over Switzerland observed by two microwave radiometry*. Talk at SPARC General Assembly, Reading, United Kingdom.

Sauvageat, E. (2022c). *Microwave ozone radiometry in Switzerland*. Online talk at NDACC Microwave Group Meeting 2022.

Sauvageat, E., Maillard Barras, E., Hocke, K., Haefele, A., and Murk, A. (2022c). *Long-term harmonized ozone profiles in the middle atmosphere over Switzerland*. Talk at EGU General Assembly 2022, Vienna, Austria.

Sauvageat, E., Hagen, J., Kotiranta, M., Hocke, K., Gomez, M., Nedoluha, G., and Murk, A. (2020b). *Comparison of three high resolution real-time spectrometers for microwave ozone profiling instruments*. Online talk at 16th Specialist Meeting on Microwave Radiometry and Remote Sensing of the Environment, Florence, Italy.

Sauvageat, E. (2020). *GROSOM and MOPI 5: towards an improved quality of ozone time series derived from passive ground based radiometers*. Online talk at Seminar in Microwave Physics and Atmospheric Physics, Bern, Switzerland.

Sauvageat, E., Maillard Barras, E., Hocke, K., Haefele, A., and Murk, A. (2021b). *Harmonized retrieval of middle atmospheric ozone from two microwave radiometers in Switzerland*. Online talk and poster at the 2021 Quadriennial Ozone Symposium.

For a complete and updated list:

B.2 Declaration of consent

Erklärung

gemäss Art. 18 PromR Phil.-nat. 2019

Name/Vorname:	Eric Sauvageat
Matrikelnummer:	12-822-813
Studiengang:	Physik Bachelor ☐ Master ☐ Dissertation ☒
Titel der Arbeit:	Harmonized microwave radiometer observations of middle-atmospheric ozone over Switzerland
Leiter der Arbeit:	Dr. Axel Murk & PD Dr. Klemens Hocke

Ich erkläre hiermit, dass ich diese Arbeit selbständig verfasst und keine anderen als die angegebenen Quellen benutzt habe. Alle Stellen, die wörtlich oder sinngemäss aus Quellen entnommen wurden, habe ich als solche gekennzeichnet. Mir ist bekannt, dass andernfalls der Senat gemäss Artikel 36 Absatz 1 Buchstabe r des Gesetzes über die Universität vom 5. September 1996 und Artikel 69 des Universitätsstatuts vom 7. Juni 2011 zum Entzug des Doktortitels berechtigt ist.

Für die Zwecke der Begutachtung und der Überprüfung der Einhaltung der Selbständigkeitserklärung bzw. der Reglemente betreffend Plagiate erteile ich der Universität Bern das Recht, die dazu erforderlichen Personendaten zu bearbeiten und Nutzungshandlungen vorzunehmen, insbesondere die Doktorarbeit zu vervielfältigen und dauerhaft in einer Datenbank zu speichern sowie diese zur Überprüfung von Arbeiten Dritter zu verwenden oder hierzu zur Verfügung zu stellen.

Bern, den 24. June 2023

Eric Sauvageat

Unterschrift